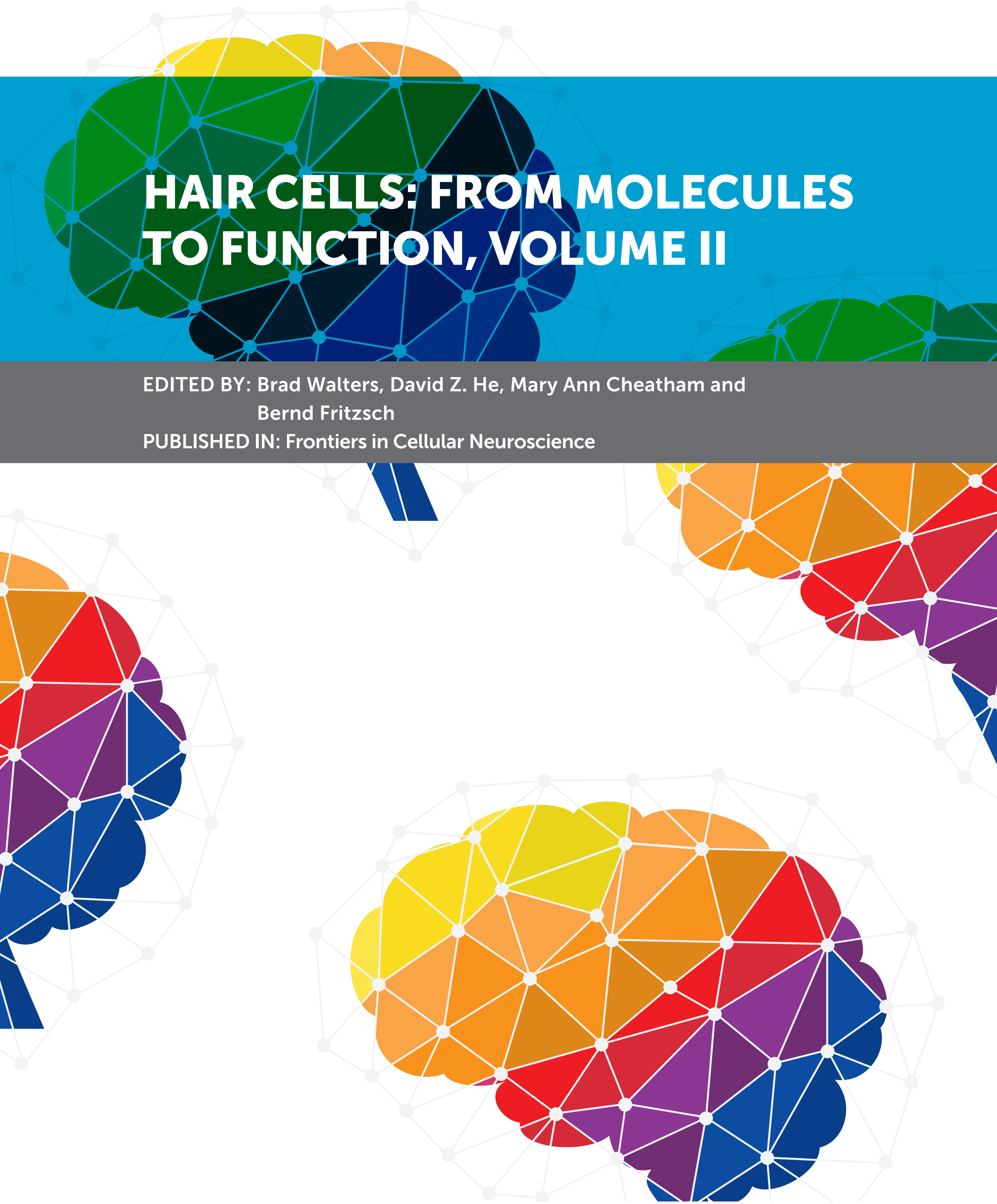

HAIR CELLS: FROM MOLECULES TO FUNCTION, VOLUME II

EDITED BY: Brad Walters, David Z. He, Mary Ann Cheatham and
Bernd Fritzsch

PUBLISHED IN: Frontiers in Cellular Neuroscience

frontiers Research Topics

ISSN 1664-8714
ISBN 978-2-83250-607-3
DOI 10.3389/978-2-83250-607-3

About Frontiers

Frontiers is more than just an open-access publisher of scholarly articles: it is a pioneering approach to the world of academia, radically improving the way scholarly research is managed. The grand vision of Frontiers is a world where all people have an equal opportunity to seek, share and generate knowledge. Frontiers provides immediate and permanent online open access to all its publications, but this alone is not enough to realize our grand goals.

Frontiers Journal Series

The Frontiers Journal Series is a multi-tier and interdisciplinary set of open-access, online journals, promising a paradigm shift from the current review, selection and dissemination processes in academic publishing. All Frontiers journals are driven by researchers for researchers; therefore, they constitute a service to the scholarly community. At the same time, the Frontiers Journal Series operates on a revolutionary invention, the tiered publishing system, initially addressing specific communities of scholars, and gradually climbing up to broader public understanding, thus serving the interests of the lay society, too.

Dedication to Quality

Each Frontiers article is a landmark of the highest quality, thanks to genuinely collaborative interactions between authors and review editors, who include some of the world's best academicians. Research must be certified by peers before entering a stream of knowledge that may eventually reach the public - and shape society; therefore, Frontiers only applies the most rigorous and unbiased reviews.
Frontiers revolutionizes research publishing by freely delivering the most outstanding research, evaluated with no bias from both the academic and social point of view.
By applying the most advanced information technologies, Frontiers is catapulting scholarly publishing into a new generation.

What are Frontiers Research Topics?

Frontiers Research Topics are very popular trademarks of the Frontiers Journals Series: they are collections of at least ten articles, all centered on a particular subject. With their unique mix of varied contributions from Original Research to Review Articles, Frontiers Research Topics unify the most influential researchers, the latest key findings and historical advances in a hot research area! Find out more on how to host your own Frontiers Research Topic or contribute to one as an author by contacting the Frontiers Editorial Office: frontiersin.org/about/contact

HAIR CELLS: FROM MOLECULES TO FUNCTION, VOLUME II

Topic Editors:
Brad Walters, University of Mississippi Medical Center, United States
David Z. He, Creighton University, United States
Mary Ann Cheatham, Northwestern University, United States
Bernd Fritzsch, The University of Iowa, United States

Citation: Walters, B., He, D. Z., Cheatham, M. A., Fritzsch, B., eds. (2022).
Hair Cells: From Molecules to Function, Volume II. Lausanne: Frontiers Media SA.
doi: 10.3389/978-2-83250-607-3

Table of Contents

frontiers | Frontiers in Cellular Neuroscience

TYPE Editorial
PUBLISHED 13 October 2022
DOI 10.3389/fncel.2022.1046646

OPEN ACCESS

EDITED AND REVIEWED BY
Marie-Ève Tremblay,
University of Victoria, Canada

*CORRESPONDENCE
Bradley J. Walters
bwalters2@umc.edu

SPECIALTY SECTION
This article was submitted to
Non-Neuronal Cells,
a section of the journal
Frontiers in Cellular Neuroscience

RECEIVED 16 September 2022
ACCEPTED 29 September 2022
PUBLISHED 13 October 2022

CITATION
Cheatham MA, Fritzsch B, He DZ and
Walters BJ (2022) Editorial: Hair cells:
From molecules to function, volume II.
Front. Cell. Neurosci. 16:1046646.
doi: 10.3389/fncel.2022.1046646

Editorial: Hair cells: From molecules to function, volume II

Mary Ann Cheatham[1], Bernd Fritzsch[2,3], David Z. He[4] and Bradley J. Walters[5]*

[1]The Knowles Hearing Center, Communication Sciences and Disorders, Northwestern University, Evanston, IL, United States, [2]Department of Biology, The University of Iowa, Iowa City, IA, United States, [3]Department of Otolaryngology, The University of Iowa, Iowa City, IA, United States, [4]Department of Biomedical Sciences, Creighton University, Omaha, NE, United States, [5]Department of Otolaryngology - Head and Neck Surgery, University of Mississippi Medical Center, Jackson, MS, United States

KEYWORDS

cochlea, vestibular system, hearing, balance, auditory, supporting cell, hair cell

Editorial on the Research Topic
Hair cells: From molecules to function, volume II

Now that the human genome has been sequenced (International Human Genome Sequencing Consortium, 2004; Nurk et al., 2022), genetic medicine is growing rapidly (Miller, 1992) and there is no reason that hearing health should not be a part of this movement. Although the opportunities for dealing with hearing loss and deafness have never been more compelling, we must define underlying disease mechanisms and identify biomarkers for patient susceptibility. This effort requires a better characterization of the normal system and how it develops in order to provide a foundation for learning how the system can be repaired and how hearing loss can be ameliorated.

This second volume continues to expand our knowledge of hair cell structure and specifically the hair bundle at the apical end of the sensory receptor cells in the inner ear. O'Donnel and Zheng report that *Camsap3*, a microtubule minus-end regulator, is required to form the kinocilia. While kinocilia do not persist after development in auditory hair cells, they are retained in adult vestibular hair cells and contribute to bundle movement and mechanotransduction. Kinocilia in conditional *Camsap3* knockout mice lack the central microtubule pair that characterizes the "9+2" configuration in primary cilia. The kinocilia are also shorter, which suggests that CAMSAP3 may be required for the development and maintenance of these long cytoskeletal structures on vestibular hair cells. Another paper by Liu and Zhao studied the glutaredoxin domain-containing cysteine-rich family of proteins implicated in DFNB25/101. Their previous work showed that GRXCR2 is required for localizing taperin at the base of the stereocilia. Although mice lacking GRXCR2 are deaf and their hair bundles disorganized, the phenotype was rescued by reducing taperin expression. The current report indicates that GRXCR1 is also important for stereocilia morphogenesis, but it is distributed all along the stereocilia. In contrast to GRXCR2, it does not bind taperin. Hence, the change in hair bundle morphology and the hearing loss in *Grxcr1*-deficient mice are not rescued by decreasing taperin expression. Qi et al. investigated complement C1q Like 1 (C1QL1), which enables signaling receptor binding activity and is involved in formation and maintenance of synapse structure (Kakegawa et al., 2015; Sigoillot et al., 2015). This gene is of interest given that *C1ql1* knockout mice exhibit progressive hearing loss and OHC death. Although the number of auditory nerve fibers innervating inner and outer hair cells (IHCs, OHCs) decreases, the spiral ganglion neurons and the thickness of the myelin sheath are wildtype-like. In addition, the morphology, number, and function of IHCs are not affected in *C1ql1* knockout mice consistent with preferential expression of this gene in OHCs (Li et al., 2018). Based on these results, it is suggested that *C1ql1* may play a role in age-related hearing loss and/or the greater susceptibility of OHCs to various insults.

Hair cell regeneration was also addressed in this collection, with the aim of eventually recreating new, functional hair cells. In one report, a new zebrafish model was developed where the human diphtheria toxin receptor (hDTR) is expressed only in hair cells (Jimenez et al.). This approach allows for *in vivo* hair cell ablation in embryonic or adult zebrafish. In contrast to aminoglycoside administration or noise exposure, the injection of DT produces a synchronous destruction of all hair cells with limited effects on neighboring inner ear cells. Characterization of dose responses and the time course of regenerative responses are also documented. In the mammalian cochlea, Heuermann et al. report that regenerated hair cells in the lateral compartment of neonatal mice are innervated, but they simultaneously express markers for both outer and inner hair cells, i.e., oncomodulin *(Ocm)* and vesicular glutamate transporter 3 (*VGlut3*), respectively. It is, therefore, possible that cochlear hair cells, regenerated postnatally, may suffer from a delay or inability to differentiate into OHCs due to the alteration of signaling gradients that normally instruct such fates during development. Finally, Rudolf et al. provide evidence suggesting that the reduced proliferative capacity in mammalian utricular supporting cells may relate to the fact that circumferential F-actin bands are thicker than in their avian counterparts where hair cell regeneration is well documented. Differences in the stiffness and contractility of cytoskeletal elements that reinforce junctions between neighboring supporting cells may impact epithelial repair by reducing mechanical forces that evoke proliferation. In contrast to mice, chicken utricles remain relatively compliant, facilitating the dynamic mechanical signals produced during hair cell loss, and promoting their regeneration.

The possibility of developing effective interventions to mitigate hearing loss is supported by work from Chen et al.. Transcriptome-wide gene networks are shown to reflect shared molecular circuits and regulators in mouse models of sensorineural hearing loss due to aging, noise exposure and ototoxic drugs. The potential to use a single therapeutic approach to minimize the hearing loss associated with various etiologies would be most welcome. Mechanisms underlying aminoglycoside ototoxicity are also reviewed (Fu et al.). In addition to mitochondrial DNA mutations that increase susceptibility, over expression of NMDA receptors and the formation of free radicals also play a role. Administration of aminoglycosides increases the entry of calcium ions via NMDA receptors, ultimately resulting in neuronal cell death. Hence, glutamate-like excitotoxicity can be induced by aminoglycosides. A better understanding of the underlying mechanisms will guide the development of interventions to reduce hearing loss due to ototoxic drugs, facilitating the transition from animal research to clinical practice. Lastly, given the current interest in synaptopathy, the development of more sophisticated diagnostic tools may help to categorize individuals with this malady and to better track their response to various therapeutics. Hence, the report by Bao et al. may provide a reliable metric for detecting synapse loss. Rather than measuring decreases in the Wave I ABR amplitude, they report greater reliability when quantifying curvature of the Wave I peak produced by clicks in mice pre- and post-noise exposure. If this approach can be validated in humans, it may provide an additional metric for clinical diagnoses.

Future studies are required to further elucidate the processes that guide hair cell differentiation, regeneration, and repair. The results of these endeavors will foster the development of new interventions that mitigate or prevent hearing loss and deafness.

Author contributions

All authors listed have made a substantial, direct, and intellectual contribution to the work and approved it for publication.

Conflict of interest

The authors declare that the research was conducted in the absence of any commercial or financial relationships that could be construed as a potential conflict of interest.

Publisher's note

References

International Human Genome Sequencing Consortium (2004). Finishing the euchromatic sequence of the human genome. *Nature* 431, 931–945. doi: 10.1038/nature03001

Kakegawa, W., Mitakidis, N., Miura, E., Abe, M., Matsuda, K., Takeo, Y. H., et al. (2015). Anterograde C1ql1 signaling is required in order to determine and maintain a single-winner climbing fiber in the mouse cerebellum. *Neuron* 85, 316–329. doi: 10.1016/j.neuron.2014.12.020

Li, Y., Liu, H., Giffen, K. P., Chen, L., Beisel, K. W., and He, D. Z. Z. (2018). Transcriptomes of cochlear inner and outer hair cells from adult mice. *Sci. Data* 5, 180199. doi: 10.1038/sdata.2018.199

Miller, A. D. (1992). Human gene therapy comes of age. *Nature* 357, 455–460. doi: 10.1038/357455a0

Nurk, S., Koren, S., Rhie, A., Rautiainen, M., Bzikadze, A. V., Mikheenko, A., et al. (2022). The complete sequence of a human genome. *Science* 376, 44–53. doi: 10.1101/2021.05.26.445798

Sigoillot, S. M., Iyer, K., Binda, F., González-Calvo, I., Talleur, M., Vodjdani, G., et al. (2015). The secreted protein C1QL1 and its receptor BAI3 control the synaptic connectivity of excitatory inputs converging on cerebellar purkinje cells. *Cell Rep*. 10, 820–832. doi: 10.1016/j.celrep.2015.01.034

frontiers
in Cellular Neuroscience

REVIEW
published: 15 June 2021
doi: 10.3389/fncel.2021.692762

Mechanism and Prevention of Ototoxicity Induced by Aminoglycosides

Xiaolong Fu[1†], *Peifeng Wan*[2†], *Peipei Li*[3†], *Jinpeng Wang*[4], *Siwei Guo*[2], *Yuan Zhang*[3], *Yachun An*[2], *Chao Ye*[2], *Ziyi Liu*[2], *Jiangang Gao*[2*], *Jianming Yang*[5*], *Jiangang Fan*[6*] and *Renjie Chai*[1,7,8,9*]

[1] State Key Laboratory of Bioelectronics, Jiangsu Province High-Tech Key Laboratory for Bio-Medical Research, School of Life Sciences and Technology, Southeast University, Nanjing, China, [2] School of Life Science, Shandong University, Qingdao, China, [3] Department of Otology, The First Affiliated Hospital of Zhengzhou University, Zhengzhou, China, [4] The Key Laboratory of Animal Resistant Biology of Shandong, College of Life Science, Shandong Normal University, Jinan, China, [5] Second Hospital of Anhui Medical University, Hefei, China, [6] Department of Otolaryngology Head and Neck Surgery, Sichuan Academy of Medical Science, Sichuan Provincial People's Hospital, Chengdu, China, [7] Co-Innovation Center of Neuroregeneration, Nantong University, Nantong, China, [8] Institute of Stem Cell and Regeneration, Chinese Academy of Sciences, Beijing, China, [9] Beijing Key Laboratory of Neural Regeneration and Repair, Capital Medical University, Beijing, China

Edited by:
David Z. He,
Creighton University, United States

Reviewed by:
Vikrant Borse,
Washington University in St. Louis,
United States
Leonard Rybak,
Southern Illinois University
Carbondale, United States

***Correspondence:**
Renjie Chai
renjiec@seu.edu.cn
Jiangang Fan
entscfjg@163.com
Jiangang Gao
jggao@sdu.edu.cn
Jianming Yang
jmyang88@163.com

†These authors have contributed equally to this work

Specialty section:
This article was submitted to
Non-Neuronal Cells,
a section of the journal
Frontiers in Cellular Neuroscience

Received: *09 April 2021*
Accepted: *20 May 2021*
Published: *15 June 2021*

Citation:
Fu X, Wan P, Li P, Wang J, Guo S, Zhang Y, An Y, Ye C, Liu Z, Gao J, Yang J, Fan J and Chai R (2021) Mechanism and Prevention of Ototoxicity Induced by Aminoglycosides. Front. Cell. Neurosci. 15:692762. doi: 10.3389/fncel.2021.692762

Aminoglycosides, a class of clinically important drugs, are widely used worldwide against gram-negative bacterial infections. However, there is growing evidence that aminoglycosides can cause hearing loss or balance problems. In this article, we mainly introduce the main mechanism of ototoxicity induced by aminoglycosides. Genetic analysis showed that the susceptibility of aminoglycosides was attributable to mutations in mtDNA, especially A1555G and C1494T mutations in 12S rRNA. In addition, the overexpression of NMDA receptors and the formation of free radicals also play an important role. Understanding the mechanism of ototoxicity induced by aminoglycosides is helpful to develop new therapeutic methods to protect hearing. In this article, the prevention methods of ototoxicity induced by aminoglycosides were introduced from the upstream and downstream aspects.

Keywords: ototoxicity, aminoglycosides, hearing loss, mechanism, prevention

INTRODUCTION

Hearing loss is the most common sensory disorder worldwide. The World Health Organization estimates that around 466 million people worldwide suffer from disabling hearing loss and that by 2050 more than 900 million people will have this condition. Disabled hearing loss is defined as a loss of more than 40 dB in the better-hearing ear of an adult and more than 30 dB in the better-hearing ear of a child. Hearing loss can affect an individual's quality of life, making it difficult to understand speech in life. And untreated hearing loss costs the world an additional $750 billion a year.

Hearing loss has both congenital and acquired caused. Congenital causes are caused by hereditary or non-hereditary factors. Acquired deafness can be caused by noise, ear infections, age, and medication. It is worth noting that ototoxic drugs are an important factor in the induction of hearing loss. Ototoxic drugs mainly affect hair cells, causing permanent damage to hearing. Because hair cells in mammals are terminally differentiated and do not have the ability to regenerate spontaneously if they die, ototoxic drugs can have serious effects on hearing (Forge et al., 1993). Ototoxic drugs mainly include aminoglycoside antibiotics, non-aminoglycoside antibiotics, antitumor drugs, and salicylate, etc. Aminoglycoside antibiotics are one of the early antibiotics used in the treatment of bacterial infections, and are widely used in the world, especially in developing countries. In this article, we introduce the mechanism of ototoxicity induced by aminoglycosides and propose some prevention strategies.

AMINOGLYCOSIDES

Some therapeutic drugs used to treat life-threatening conditions, such as aminoglycosides and antitumor drugs, can cause hearing loss and/or balance problems (Guo et al., 2019). Antibiotics are widely used in clinical practice, and more than 100 kinds of ototoxic drugs have been found. Aminoglycosides have been shown to be highly effective against gram-negative infections (Gao et al., 2017). Aminoglycosides are glycosides formed from amino sugars and aminocyclitol linked by an oxygen bridge. Aminoglycosides are bactericide that inhibit protein synthesis and have a wide antibacterial spectrum and strong antibacterial activity. They are commonly used in clinical practice. Although aminoglycosides are highly effective and relatively inexpensive, they are known to have ototoxicity and vestibular toxicity. Aminoglycosides can accumulate in the inner ear and are difficult to metabolize, leading to permanent hearing loss (Fischel-Ghodsian, 2005). The most common aminoglycoside drugs are streptomycin, gentamicin, neomycin, it's long-term use will lead to neurological tinnitus, neurological deafness, and even memory loss, hearing loss, dizziness and other conditions. The use of antibiotics (especially aminoglycoside antibiotics) has become the main cause of hearing loss in children in China, and both topical and systemic drugs can lead to hearing loss.

MECHANISM OF AMINOGLYCOSIDE OTOTOXICITY

Clinically, aminoglycoside drugs mainly enter the inner ear through systemic and topical pathways. In the systemic pathway, the drug passes through the blood-labyrinth barrier (BLB) and enters the inner ear through the stria vascularis. In topical administration, the drug can bypass the BLB into the middle ear and then through the round window into the inner ear. The drug is absorbed either by endocytosis on the apical surface (Hashino and Shero, 1995) or by transduction channels (Marcotti et al., 2005). Early genetic analysis showed that the susceptibility of aminoglycosides was related to mitochondrial DNA mutations, which inhibited the synthesis of mitochondrial proteins. However, evidence is accumulating to suggest that the overactivation of N-methyl-D-aspartate (NMDA) receptors and the production of free radicals are also important factors in the ototoxicity of aminoglycosides (Strupp and Arbusow, 2001). The mechanism of aminoglycosides-induced ototoxicity is very subtle. How does aminoglycoside cause hearing loss has been a hot research topic.

Associations Between Susceptibility to Aminoglycosides and Mitochondrial DNA Mutations

Mitochondria are energy providers and mediators of cell apoptosis, which play an important role in cell survival. Aminoglycoside susceptibility has been reported to be related to genetic background in many individuals. The mammalian mitochondria genome is maternally inherited. Interestingly, lineage analysis suggests that aminoglycosides-induced hearing loss is also maternally inherited (Prezant et al., 1993; Rydzanicz et al., 2010). It is suggested that aminoglycoside sensitivity is related to mitochondria. Mitochondria have their own genome, called mtDNA, which encodes 22 tRNAs, 13 mRNAs, and 2 rRNAs, which are important for the composition of the OXPHOS respiratory chain complex (Kokotas et al., 2007). Studies have found that when mitochondrial DNA (especially 12S rRNA) is mutated, it increases the binding to aminoglycosides, inhibits the synthesis of mitochondrial proteins and increases the formation of free radicals, which in turn affects hearing (Qian and Guan, 2009). This suggests that mitochondrial DNA mutations are associated with susceptibility to aminoglycosides.

Mitochondria

Mitochondria are closely related to cell survival. There areresponsible for the production of cellular adenosine triphosphate (ATP), which provides organisms with the energy necessary for survival, and for the regulation of important function, including apoptosis and the production of free radicals (Van Remmen and Jones, 2009). They have their own DNA called mtDNA, which codes for mitochondria proteins. MtDNA accounts for about 0.5% of the total DNA in a nucleated somatic cell (Kokotas et al., 2007). The mtDNA molecule is a double stranded, circular structure with a total length of 16,568 bp, encoding 22 tRNAs, 13mRNAs, 2rRNAs (Kokotas et al., 2007). The 13 mitochondrial proteins are involved in the formation of the OXPHOS respiratory chain complex. Once the translation defect or dysfunction of several components of OXPHOS occurs, it may affect the generation of energy, thus affecting the survival state of cells and causing a variety of diseases (Kawamata and Manfredi, 2017). Another important function of the mitochondria is to produce free radicals. Free radicals can be produced in a variety of ways, of which mitochondria are the main source. In normal metabolic processes, 1–4% of oxygen is incompletely reduced, resulting in the production of ROS (Zorov et al., 2014). In addition, the monoamine oxidase in the outer membrane of mitochondria and the α-ketoglutarate dehydrogenase complex in the matrix can also produce ROS (Starkov, 2013).

In eukaryotes, ribosomes have also been detected in mitochondria in addition to the cytoplasm. Interestingly, mammalian mitochondria ribosomes are more similar to prokaryotes 70S ribosomes (Collatz et al., 1976). According to the "endosymbiotic theory," mitochondria are derived from bacteria, that is, after bacteria are swallowed by eukaryotes, in the long-term symbiosis process, they form mitochondria through evolution (Martin et al., 2015). According to this theory, the ancestral mitochondria (a kind of gram-negative bacteria that can carry out the tricarboxylic acid cycle and electron transfer) were swallowed by the primitive eukaryotes and formed a symbiotic relationship with the host. The mammalian mitochondrial ribosome is a 55S protein complex composed of two subunits, 28S and 39S, which has the function of translating mitochondrial mRNA encoded by mtDNA (Collatz et al., 1976). What's more, the mtDNA encodes 12S ribosomal RNA. When mitochondrial ribosomes are damaged, it will lead to impaired synthesis of mitochondrial protein, affect the generation of cellular energy, and cause damage to the survival state of cells.

Aminoglycosides Destroy Bacteria

Aminoglycosides are widely used to fight gram-negative bacterial infections. Early studies have found that aminoglycosides act on the 30S subunits of bacterial ribosomes, causing bacterial code reading errors and eventually causing bacterial death. The prokaryotic ribosomes are composed of 30S and 50S subunits, while the eukaryotic ribosomes are composed of 40S and 60S subunits (Wimberly et al., 2000). Because of the structural difference between the 70S and 80S ribosomes of bacteria, aminoglycosides kill bacteria without destroying the infected cells (Gutell et al., 1994). In recent years, more in-depth studies have found that aminoglycosides directly bind to the A site of the 16S rRNA. Interestingly, in mammalian mitochondria, the A site on the aminoglycoside binding 16S rRNA is replaced by the G site (Huth et al., 2015). This may account for the difference between the effects of aminoglycosides on mammals and bacteria.

Associations Between Mitochondrial DNA Mutations and Aminoglycosides

Mitochondria have their own genomes, encoding mitochondrial proteins. Previous studies have found that mtDNA has a higher mutation rate than nuclear DNA and accumulates in cells with age, with a mutation at least 10-fold than in nuclear DNA (Wallace et al., 1987). Moreover, mitochondrial DNA has a poorer repair mechanism than nuclear DNA. Mitochondria play a very important role in the survival of cells. When mitochondrial function is abnormal, it will cause serious physiological dysfunction. MtDNA plays an important role in maintaining mitochondrial function. MtDNA mutations might lead to both multisystem disorders, such as Leber hereditary optic neuropathy (LHON); myoclonus epilepsy associated with ragged-red fibers (MERRF); or non-syndromic deafness (Kokotas et al., 2007). Mutations in some mtDNA that encode rRNA or tRNA have been found to cause non-syndromic hearing loss. It is mainly due to the mutation of mitochondrial ribosomal small subunits, especially A1555G and C1494T are primary genetic characteristics of the mutation, and susceptible to aminoglycoside-induced hearing loss (Zhao et al., 2004; Young et al., 2005; Bravo et al., 2006).

The A1555G mutation is the most common type of mitochondrial 12S rRNA mutation in aminoglycoside-induced hearing loss (Bravo et al., 2006). The A1555G alone is not sufficient to induce a clinical phenotype, and there may be other factors that co-regulate the effects of A1555G mutations on hearing. The A1555G mutation-associated deafness penetrance may be regulated by aminoglycosides, nuclear modifiers genes, or other mtDNA mutations (Guan et al., 1996, 2000). It was reported that the homoplasmic A1555G mutation at the A site of highly conserved 12S rRNA have been associated with aminoglycoside-induced non-syndromic hearing loss in many families worldwide (Li et al., 2004; Young et al., 2005; Yuan et al., 2005). When the 1555A is mutated to G, the secondary structure of 12S rRNA more closely resembles the corresponding region of 16S rRNA in bacteria. Thus, the A1555G mutation may alter the secondary structure of 12S rRNA, leading to increased susceptibility of aminoglycosides (Kokotas et al., 2007).

The second mutation, the C1494T mutation of the mitochondrial 12S rRNA gene. Sequence analysis of mitochondria DNA from a large Chinese family of aminoglycoside-induced hearing loss revealed the C1494T mutation in the 12S rRNA gene (Zhao et al., 2004). The site of 1,494 is the corresponding site of 1,555 located at 12S rRNA highly conserved A-site (Zhao et al., 2004).

Complete mitochondrial genome sequence analysis of individuals revealed that aminoglycoside drug sensitivity was associated with several other mitochondrial DNA mutations. Mitochondrial genome mutation analysis revealed the presence of homoplasmic 12S rRNA A827G mutation in the patient's mitochondria, which is associated with hearing loss (Chaig et al., 2008). The A827G mutation may lead to tertiary or quaternary structural changes in the 12S rRNA that affect mitochondrial function, thus playing an important role in aminoglycosides-induced hearing loss (Chaig et al., 2008). The study found that when individuals with the T1095C mutation were exposed to aminoglycoside antibiotics, the number of apoptotic cells in the mutant individuals were ten-fold higher than in the control group. These results indicate the pathogenicity of the T1095C mutation, which increases the susceptibility of aminoglycoside (Muyderman et al., 2012). Furthermore, mutations such as A745G, C792T, A801G, A856G, A1027G, C1192T, C1310T and A1331G may be related to the aminoglycoside ototoxicity (Lu et al., 2010). ADDIN EN.CITE (Hong et al., 2006).

NMDA Is Involved in Ototoxicity Induced by Aminoglycosides

The N-methyl-D-aspartate (NMDA) is a glutamate receptor, which exists at the synaptic site between cochlear hair cells and the radical dendrites of spiral ganglion afferents. Aminoglycosides may mimic the effects of polyamines on NMDA receptors (Puel, 1995). The association between aminoglycosides and polyamines may explain the glutamate-like excitotoxicity induced by aminoglycosides. The overstimulation of NMDA receptors (NMDARs) increases the formation of nitric oxide (NO), resulting in oxidative stress on hair cells. In addition, some studies have shown that gentamicin treatment can increase the expression of nNOS and iNOS to induce hair cell injury (Hong et al., 2006; Jia et al., 2018). More importantly, high doses of aminoglycosides may increase the entry of calcium ions through NMDA-related channels (Bienkowski et al., 2000). Increased influx of calcium ions is the basis for formation of excitotoxicity. Excitotoxicity can be produced by a two-step mechanism: The first is acute swelling, which accompanies the destruction of postsynaptic structure, followed by a cascade of calcium ions that leads to the death of neuron (Pavlidis et al., 2014). In the experiment, after intramuscular injection of amikacin, the amplitude of DPOAE was significantly different from that of the control group (Pavlidis et al., 2014). More importantly, NMDA receptors antagonists can prevent ototoxicity caused by aminoglycosides and treat hearing loss (Basile et al., 1996; Pavlidis et al., 2014). It is interesting to note the influx of calcium through NMDARs may induce immediate transcription of early genes through mitogen-activated protein kinases (MAPK)-dependent mechanisms (Xia et al., 1996). Substrates of ERK and JNK subfamilies of MAPK, c-Fos and c-Jun, form AP-1 transcription factor complexes (Xia et al., 1996). It can be seen from the above studies that NMDA plays an important role in the ototoxicity induce by aminoglycosides, which is worth further exploration.

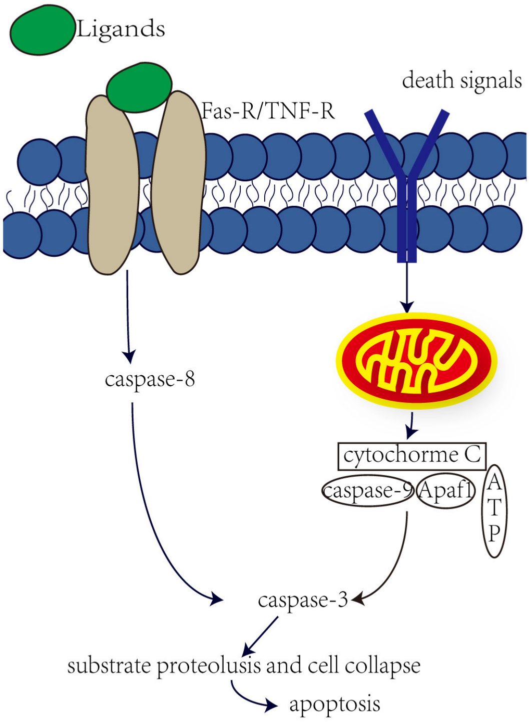

FIGURE 1 | Internal and external pathway that induce apoptosis. The external pathway, the ligand binds to the death receptor to active it, which in turn induces a cascade of caspase-8 and caspase-3, leading to apoptosis. The internal pathway, some death signals, such as stress, DNA damage and faulty cell signaling, can induce mitochondria to release cytochrome c, which may form apoptotic bodies, which in turn activate caspase-3 and lead to apoptosis.

ROS Is Involved in Ototoxicity Induced by Aminoglycosides

It is generally accepted that ROS is involved in ototoxicity induced by aminoglycosides, and antioxidants can mitigate the effects of ototoxicity (Xie et al., 2011). Aminoglycosides have also been reported to produce free radicals in the inner ear that subsequently cause damage to sensory cells and neurons, leading to hearing loss (Rybak and Kelly, 2003). ROS is a normal product in the metabolic of organisms. It plays a role in regulating messengers in various processes such as proliferation, survival, gene expression and apoptosis, and is also a signal molecule for homeostasis adaptation under stress conditions (Finkel, 2012). Under normal circumstances, ROS are easily cleared by antioxidants in the body, such as catalase, superoxide dismutase (SOD) and glutathione, to prevent ROS from escaping and entering cells, so as to maintain homeostasis in the inner ear (Kopke et al., 1999; Bared et al., 2010). However, aging, drugs, the environment and other factors can change this balance. ROS can be generated by, NADPH oxidase and mitochondrial, peroxisomal, or microsomal pathways (Bottger and Schacht, 2013). In addition, aminoglycosides can combine with transition metals such as iron and copper to form free radicals (Schacht, 1999; Dehne et al., 2002). It has been reported that Fe II-aminoglycoside complexes can combine with phosphatidylinositol and induce the release of arachidonic acid. At the same time, arachidonic acid can form ternary complexes with iron and aminoglycosides, leading to the formation of ROS (Lesniak et al., 2005). However, it is not clear which mechanism is the main source of ROS, and the formation mechanism of ROS remains to be solved.

Aminoglycosides have both been reported to induce cell necrosis and apoptosis, but seem to be the main cause of cell apoptosis. Apoptosis is mainly regulated by the activation of caspase through internal or external pathways (**Figure 1**). In the internal pathway, mitochondria release apoptogenic factors into the cytoplasm to active caspase, in the external pathway, caspase is activated by ligand binding to death receptors (Rybak and Kelly, 2003). Studies have shown that aminoglycosides induce apoptosis through internal rather than external pathways. Perhaps in response to the production of ROS by aminoglycosides, the expression of anti-apoptotic Bcl-2 was decreased, and the expression of pro-apoptotic Bcl-X_L was increased, and Bcl-X_L was transferred into the mitochondria. This in turn leads to increased mitochondrial permeability, the release of apoptotic factors, and the possible formation of "apoptotic bodies" with Apaf1 and caspase-9. Downstream caspases are activated, such as caspase-3 and caspase-7, leading to substrate proteolysis and cell collapse. In aminoglycoside toxicity, overexpression of Bcl-2 prevents hair death and activation of caspase-9 (Cunningham et al., 2004). Meanwhile, after aminoglycoside administration, an increase in JNK components was observed, and JNK plays important role in mitochondria-mediated apoptosis. JNK can promote the release of cytochrome c. However, recent studies have shown that O2● from liver tumor cells and directly cause the release of cytochrome c through a voltage-dependent anion transport channels without damaging the mitochondrial membrane (Madesh and Hajnoczky, 2001). Therefore, ROS plays an important role in aminoglycosides-induced hearing loss.

PREVENTION OF OTOTOXICITY INDUCED BY AMINOGLYCOSIDE

In the course of clinical treatment, alternative drugs should be used as far as possible or to reduce ototoxicity. Patients treated with ototoxic drugs should be monitored for the prevention of ototoxicity due to medication. At present, medical personnel consider three ways to reduce the problem of drug-induced ototoxicity: ① development of efficacious ototoxic protective drugs; ② reversing ototoxicity-induced symptoms using neurotrophic grow factor; ③ screening for genetic markers in patients at high risk of ototoxicity (for example, people who carry mutations in mtDNA such as A1555G or C1494T) (Ramma et al., 2019).

According to the mechanism of ototoxicity induced by aminoglycosides introduced previously, prevention of ototoxicity mainly includes two aspects: "upstream protection" and "downstream protection." "Upstream prevention" refers to blocking of ROS formation or ROS scavenging, inhibition of nitric oxide synthesis, use of NMDA receptors antagonists, and increase of endogenous antioxidant enzymes. "Downstream prevention" refers to the inhibition of the downstream caspase cascade induced by ROS, as well as the inhibition of JNK cascade.

Upstream Prevention

Studies have shown that inhibiting ROS formation and ROS scavenging can reduce aminoglycoside-induced ototoxicity. Because aminoglycosides can interact with iron to produce ROS (Lesniak et al., 2005), metal chelators may be used as protectors for ototoxic drugs. The study found that deferoxamine and the iron chelators 2.2′-dipyridyl had a protective effect against gentamicin-induced hearing loss (Dehne et al., 2002). This suggests that metal chelating agents can act as protective agents. Use of antioxidants can reduce ROS levels and effectively prevent aminoglycosides-induced ototoxicity. These include coenzyme Q10 (Fetoni et al., 2012), alpha-tocopherol (Fetoni et al., 2003), D-methionine (Campbell et al., 2016). ROS can be produced in a variety of ways, and mitochondria are the main source of ROS. What's more, ROS production can attack mitochondria. Intrinsic mitochondrial cell death pathway plays an important role in the process of hair cell death induced by aminoglycosides. Therefore, therapies that control mitochondrial homeostasis may be more effective in preventing aminoglycoside-induced hearing loss. Mitochondria-targeted antioxidants are superior in reducing mitochondrial oxidative damage (Dhanasekaran et al., 2004). Mitochondria-targeted antioxidants are expected to help prevent mitochondria-related diseases (Fujimoto and Yamasoba, 2019). Recent studies have shown that SS-31 peptides may be able to achieve mitochondria-targeted drug delivery to prevent aminoglycosides from damaging hair cells (Kuang et al., 2017). Therefore, the strategy of blocking the formation of ROS induced by aminoglycosides with metal chelators and eliminating ROS with mitochondrial targeted antioxidant drugs may effectively prevent the ototoxicity induced by aminoglycosides.

In addition, the nitric oxide (NO) synthesis inhibitor was found to have a protective effect against the ototoxicity of aminoglycoside. Dexamethasone acts mainly as a glucocorticoid, not a mineralocorticoid (Himeno et al., 2002). Dexamethasone can inhibit the increase of NO synthase mRNA, inhibit NO synthesis and free radical formation to protect OHC from the ototoxic effects of aminoglycosides (Himeno et al., 2002; Park et al., 2004).

Increasing evidence suggests that aminoglycosides may mimic the effects of polyamines on NMDA receptors (Puel, 1995). Aminoglycosides play a key role in ototoxicity by activating polyamine-like NMDARs. More importantly, overactivation of NMDARs produces NO, which induces oxidative stress on hair cells. Therefore, it has been suggested that NMDA receptors antagonists may prevent aminoglycoside-induced ototoxicity. Memantine is an NMDA receptors antagonist that reduces aminoglycoside induced hearing loss (Pavlidis et al., 2014). This suggests that NMDA receptors antagonists are a strategy for the induction of ototoxicity by aminoglycosides.

Under normal circumstances, ROS can be cleared by endogenous antioxidant enzymes (Kopke et al., 1999). Therefore, it has been proposed to increase the endogenous antioxidant enzyme pathway to prevent aminoglycoside-induced ototoxicity. A study showed that M40403, a superoxide dismutase mimetic, prevented gentamicin-induced ototoxicity (McFadden et al., 2003).

Downstream Protection

Recently, an increasing number of studies have shown that the administration of aminoglycosides leads to JNK activation and apoptosis of vestibular hair cells (**Figure 2**). The c-Jun N-terminal kinases (JNK) is a key member of the MAPK family and plays an important role in cell apoptosis. ROS may be upstream modulators of JNK activation, which may activate kinase cascades. Systemic administration of CEP-1347 (a JNK signal inhibitor) attenuates gentamicin-induced hearing loss and hair cell damage (Ylikoski et al., 2002). Another study showed that D-JNKI-1 (A synthetic inhibitor of JNK phosphorylation) protects against aminoglycoside-induced hair cell damage and hearing loss (Eshraghi et al., 2007). Therefore, blocking c-Jun N-terminal kinase can prevent the ototoxicity induced by aminoglycosides.

ROS induced by aminoglycosides can cause the release of cytochrome c in mitochondria and cascade activation of caspase, leading to substrate proteolysis and cell collapse. The release of cytochrome c is mediated by B-cell lymphoma-2 (Bcl-2) family. Studies have shown that overexpression of Bcl-2 in transgenic mice can reduce hair cell loss and prevent hearing loss after aminoglycosides administration (Cunningham et al., 2004). Caspase inhibitions (DEVE and ZVAD) attenuate the ototoxicity of gentamicin by blocking the activation of caspase-3 induced by gentamicin (Wei et al., 2005). What's more, minocycline attenuate ototoxicity better than the use of caspase inhibitors alone (Wei et al., 2005). In addition to inhibiting the activation of caspase-3, Minocycline may also inhibit phosphorylation of P38 MAPK and the release of cytochrome c (Wei et al., 2005). Therefore, it may be more effective to inhibit these ototoxic-inducing pathways together.

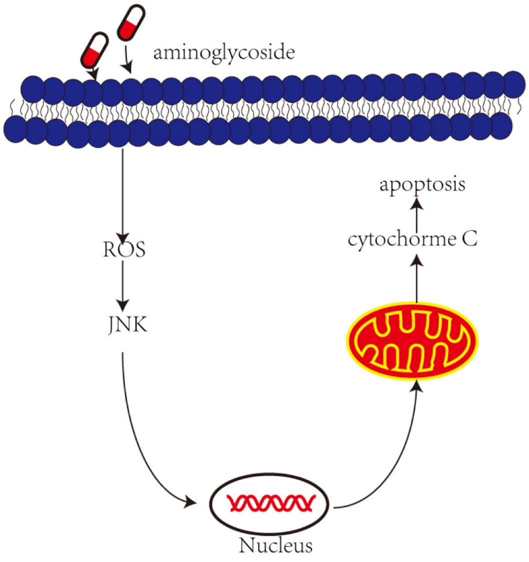

FIGURE 2 | Aminoglycoside induce activation of JNK and then induces apoptosis. Aminoglycosides enter the outer hair cells, induce the production of ROS. In response to ROS and then activate JNK, they are translocated into the nucleus and activate some genes, which in turn induce mitochondria to release cytochrome c and induce cell apoptosis.

DISCUSSION

The above protective agents are based on animal studies and have a preventive effect on ototoxicity. However, there are some limitations in animal research and there are some problems in the transition from animal research to human clinical research. On the one hand, we need to find suitable protective agents for clinical use, so that the protective agents will not affect the antimicrobial effect of aminoglycosides. Studies have shown that D-methionine does not interfere with antimicrobial effects of tobramycin (Fox et al., 2016), but it is not clear whether other protective agents have any effects on the antimicrobial activity of aminoglycosides. On the other hand, because of the obvious differences in pharmacokinetics and drug elimination between animals and humans, it is not effective to calculate drug dosage by body weight. In addition to the above protective agents, aminoglycosides with low ototoxicity such as etimicin can also be used, which can effectively reduce ototoxicity (Yao et al., 2020). At the same time, new alternative drugs can be developed to reduce ototoxicity. Recent studies have purified hospital gentamicin, and analyzed the ototoxicity and antimicrobial activity of individual C-subtypes and impurities, providing ideas for the design of future drugs (O'Sullivan et al., 2020).

CONCLUSION

Aminoglycosides, a class of clinically important drugs, are widely used worldwide against gram-negative bacterial infections. However, there is growing evidence that aminoglycosides can cause hearing loss or balance problems. In this article, we mainly introduce the main mechanism of ototoxicity induced by aminoglycosides. Genetic analysis showed that the susceptibility of aminoglycosides was attributable to mutations in mtDNA, especially A1555G and C1494T mutations in 12S rRNA. In addition, the overexpression of NMDA receptors and the formation of free radicals also play an important role. Understanding the mechanism of ototoxicity induced by aminoglycosides is helpful to develop new therapeutic methods to protect hearing. In this article, the prevention methods of ototoxicity induced by aminoglycosides were introduced from the upstream and downstream aspects. It has been shown that the use of some antioxidants and inhibitors of caspase can prevent cell apoptosis and effectively prevent aminoglycosides-induced hearing loss. In addition, the delivery of mitochondria-targeted drugs is of great significance for treatment. However, recent reports have found that autophagy may also play an important role in the induction of ototoxicity by aminoglycosides, and autophagy may be protective mechanism of hearing (He et al., 2017). Meanwhile, autophagy has been reported to play a role in hearing protection (He et al., 2020; Zhou et al., 2020; Liu et al., 2021). Autophagy may be another good way to prevent ototoxicity induced by aminoglycosides.

The mechanism of ototoxicity induced by aminoglycosides and prevention methods described above have been established from animal experiments and can be used as a potential means to prevent ototoxicity induced by aminoglycosides. We still have a lot of work to do in the transition from animal research to clinical use. The side effects brought by aminoglycosides to patients should not be ignored, and we should further develop new alternative or therapeutic drugs to treat hearing loss caused by ototoxic drugs.

AUTHOR CONTRIBUTIONS

XF, PW, and PL: writing-original draft, investigation, software, and writing-review and editing. JP, SG, YZ, YA, CY, and ZY: investigation. JG, JY, and JF: writing-review and editing, supervision, and administration. RC writing-review and editing, funding acquisition, and supervision. All authors contributed to the article and approved the submitted version.

FUNDING

This work was supported by grants from the National Basic Research Program of China (SQ2020YFA010013), Strategic Priority Research Program of the Chinese Academy of Science (XDA16010303), the National Science Foundation of China (Grant Nos. 82030029, 81970882, and 81900937), National Key R&D Program of China (No. 2017YFA0103903), Natural Science Foundation from Jiangsu Province (BE2019711), Shenzhen Fundamental Research Program (JCYJ20190814093401920), Open Research Fund of State Key Laboratory of Genetic Engineering, Fudan University (No. SKLGE1809).

REFERENCES

Bared, A., Ouyang, X., Angeli, S., Du, L. L., Hoang, K., Yan, D., et al. (2010). Antioxidant enzymes, presbycusis, ethnic variability. *Otolaryngol. Head Neck Surg.* 143, 263–268. doi: 10.1016/j.otohns.2010.03.024

Basile, A. S., Huang, J. M., Xie, C., Webster, D., Berlin, C., and Skolnick, P. (1996). N-methyl-D-aspartate antagonists limit aminoglycoside antibiotic-induced hearing loss. *Nat. Med.* 2, 1338–1343. doi: 10.1038/nm1296-1338

Bienkowski, P., Scinska, A., Kostowski, W., Koros, E., and Kukwa, A. (2000). Ototoxic mechanism of aminoglycoside antibiotics–role of glutaminergic NMDA receptors. *Pol. Merkur. Lekarski.* 9, 713–715.

Bottger, E. C., and Schacht, J. (2013). The mitochondrion: a perpetrator of acquired hearing loss. *Hear. Res.* 303, 12–19. doi: 10.1016/j.heares.2013.01.006

Bravo, O., Ballana, E., and Estivill, X. (2006). Cochlear alterations in deaf and unaffected subjects carrying the deafness-associated A1555G mutation in the mitochondrial 12S rRNA gene. *Biochem. Biophys. Res. Commun.* 344, 511–516. doi: 10.1016/j.bbrc.2006.03.143

Campbell, K. C., Martin, S. M., Meech, R. P., Hargrove, T. L., Verhulst, S. J., and Fox, D. J. (2016). D-methionine (D-met) significantly reduces kanamycin-induced ototoxicity in pigmented guinea pigs. *Int. J. Audiol.* 55, 273–278. doi: 10.3109/14992027.2016.1143980

Chaig, M. R., Zernotti, M. E., Soria, N. W., Romero, O. F., Romero, M. F., and Gerez, N. M. (2008). A mutation in mitochondrial 12S rRNA, A827G, in Argentinean family with hearing loss after aminoglycoside treatment. *Biochem. Biophys. Res. Commun.* 368, 631–636. doi: 10.1016/j.bbrc.2008.01.143

Collatz, E., Kuchler, E., Stoffler, G., and Czernilofsky, A. P. (1976). The site of reaction on ribosomal protein L27 with an affinity label derivative of tRNA Met f. *FEBS Lett.* 63, 283–286. doi: 10.1016/0014-5793(76)80112-3

Cunningham, L. L., Matsui, J. I., Warchol, M. E., and Rubel, E. W. (2004). Overexpression of Bcl-2 prevents neomycin-induced hair cell death and caspase-9 activation in the adult mouse utricle *in vitro*. *J. Neurobiol.* 60, 89–100. doi: 10.1002/neu.20006

Dehne, N., Rauen, U., de Groot, H., and Lautermann, J. (2002). Involvement of the mitochondrial permeability transition in gentamicin ototoxicity. *Hear. Res.* 169, 47–55. doi: 10.1016/S0378-5955(02)00338-6

Dhanasekaran, A., Kotamraju, S., Kalivendi, S. V., Matsunaga, T., Shang, T., Keszler, A., et al. (2004). Supplementation of endothelial cells with mitochondria-targeted antioxidants inhibit peroxide-induced mitochondrial iron uptake, oxidative damage, and apoptosis. *J. Biol. Chem.* 279, 37575–37587. doi: 10.1074/jbc.M404003200

Eshraghi, A. A., Wang, J., Adil, E., He, J., Zine, A., Bublik, M., et al. (2007). Blocking c-Jun-N-terminal kinase signaling can prevent hearing loss induced by both electrode insertion trauma and neomycin ototoxicity. *Hear. Res.* 226, 168–177. doi: 10.1016/j.heares.2006.09.008

Fetoni, A. R., Eramo, S. L., Rolesi, R., Troiani, D., and Paludetti, G. (2012). Antioxidant treatment with coenzyme Q-ter in prevention of gentamycin ototoxicity in an animal model. *Acta Otorhinolaryngol. Ital.* 32, 103–110.

Fetoni, A. R., Sergi, B., Scarano, E., Paludetti, G., Ferraresi, A., and Troiani, D. (2003). Protective effects of alpha-tocopherol against gentamicin-induced Oto-vestibulo toxicity: an experimental study. *Acta Otolaryngol.* 123, 192–197. doi: 10.1080/00016480310001484

Finkel, T. (2012). Signal transduction by mitochondrial oxidants. *J. Biol. Chem.* 287, 4434–4440. doi: 10.1074/jbc.R111.271999

Fischel-Ghodsian, N. (2005). Genetic factors in aminoglycoside toxicity. *Pharmacogenomics* 6, 27–36. doi: 10.1517/14622416.6.1.27

Forge, A., Li, L., Corwin, J. T., and Nevill, G. (1993). Ultrastructural evidence for hair cell regeneration in the mammalian inner ear. *Science* 259, 1616–1619. doi: 10.1126/science.8456284

Fox, D. J., Cooper, M. D., Speil, C. A., Roberts, M. H., Yanik, S. C., Meech, R. P., et al. (2016). d-Methionine reduces tobramycin-induced ototoxicity without antimicrobial interference in animal models. *J. Cyst. Fibros* 15, 518–530. doi: 10.1016/j.jcf.2015.06.005

Fujimoto, C., and Yamasoba, T. (2019). Mitochondria-targeted antioxidants for treatment of hearing loss: a systematic review. *Antioxidants* 8:109. doi: 10.3390/antiox8040109

Gao, Z., Chen, Y., and Guan, M. X. (2017). Mitochondrial DNA mutations associated with aminoglycoside induced ototoxicity. *J. Otol.* 12, 1–8. doi: 10.1016/j.joto.2017.02.001

Guan, M. X., Fischel-Ghodsian, N., and Attardi, G. (1996). Biochemical evidence for nuclear gene involvement in phenotype of non-syndromic deafness associated with mitochondrial 12S rRNA mutation. *Hum. Mol. Genet.* 5, 963–971. doi: 10.1093/hmg/5.7.963

Guan, M. X., Fischel-Ghodsian, N., and Attardi, G. (2000). A biochemical basis for the inherited susceptibility to aminoglycoside ototoxicity. *Hum. Mol. Genet.* 9, 1787–1793. doi: 10.1093/hmg/9.12.1787

Guo, J., Chai, R., Li, H., and Sun, S. (2019). Protection of hair cells from ototoxic drug-induced hearing loss. *Adv. Exp. Med. Biol.* 1130, 17–36. doi: 10.1007/978-981-13-6123-4_2

Gutell, R. R., Larsen, N., and Woese, C. R. (1994). Lessons from an evolving rRNA: 16S and 23S rRNA structures from a comparative perspective. *Microbiol. Rev.* 58, 10–26. doi: 10.1128/MR.58.1.10-26.1994

Hashino, E., and Shero, M. (1995). Endocytosis of aminoglycoside antibiotics in sensory hair cells. *Brain Res.* 704, 135–140. doi: 10.1016/0006-8993(95)01198-6

He, Z., Guo, L., Shu, Y., Fang, Q., Zhou, H., Liu, Y., et al. (2017). Autophagy protects auditory hair cells against neomycin-induced damage. *Autophagy* 13, 1884–1904. doi: 10.1080/15548627.2017.1359449

He, Z. H., Zou, S. Y., Li, M., Liao, F. L., Wu, X., Sun, H. Y., et al. (2020). The nuclear transcription factor FoxG1 affects the sensitivity of mimetic aging hair cells to inflammation by regulating autophagy pathways. *Redox Biol.* 28:101364. doi: 10.1016/j.redox.2019.101364

Himeno, C., Komeda, M., Izumikawa, M., Takemura, K., Yagi, M., Weiping, Y., et al. (2002). Intra-cochlear administration of dexamethasone attenuates aminoglycoside ototoxicity in the guinea pig. *Hear. Res.* 167, 61–70. doi: 10.1016/S0378-5955(02)00345-3

Hong, S. H., Park, S. K., Cho, Y. S., Lee, H. S., Kim, K. R., Kim, M. G., et al. (2006). Gentamicin induced nitric oxide-related oxidative damages on vestibular afferents in the guinea pig. *Hear. Res.* 211, 46–53. doi: 10.1016/j.heares.2005.08.009

Huth, M. E., Han, K. H., Sotoudeh, K., Hsieh, Y. J., Effertz, T., Vu, A. A., et al. (2015). Designer aminoglycosides prevent cochlear hair cell loss and hearing loss. *J. Clin. Invest.* 125, 583–592. doi: 10.1172/JCI77424

Jia, Z., He, Q., Shan, C., and Li, F. (2018). Tauroursodeoxycholic acid attenuates gentamicin-induced cochlear hair cell death *in vitro*. *Toxicol. Lett.* 294, 20–26. doi: 10.1016/j.toxlet.2018.05.007

Kawamata, H., and Manfredi, G. (2017). Proteinopathies and OXPHOS dysfunction in neurodegenerative diseases. *J. Cell. Biol.* 216, 3917–3929. doi: 10.1083/jcb.201709172

Kokotas, H., Petersen, M. B., and Willems, P. J. (2007). Mitochondrial deafness. *Clin. Genet.* 71, 379–391. doi: 10.1111/j.1399-0004.2007.00800.x

Kopke, R., Allen, K. A., Henderson, D., Hoffer, M., Frenz, D., and Van de Water, T. (1999). A radical demise. Toxins and trauma share common pathways in hair cell death. *Ann. N. Y. Acad. Sci.* 884, 171–191. doi: 10.1111/j.1749-6632.1999.tb08641.x

Kuang, X., Zhou, S., Guo, W., Wang, Z., Sun, Y., and Liu, H. (2017). SS-31 peptide enables mitochondrial targeting drug delivery: a promising therapeutic alteration to prevent hair cell damage from aminoglycosides. *Drug Deliv.* 24, 1750–1761. doi: 10.1080/10717544.2017.1402220

Lesniak, W., Pecoraro, V. L., and Schacht, J. (2005). Ternary complexes of gentamicin with iron and lipid catalyze formation of reactive oxygen species. *Chem. Res. Toxicol.* 18, 357–364. doi: 10.1021/tx0496946

Li, R., Xing, G., Yan, M., Cao, X., Liu, X. Z., X., et al. (2004). Cosegregation of C-insertion at position 961 with the A1555G mutation of the mitochondrial 12S rRNA gene in a large Chinese family with maternally inherited hearing loss. *Am. J. Med. Genet. A* 124A, 113–117. doi: 10.1002/ajmg.a.20305

Liu, W., Xu, L., Wang, X., Zhang, D., Sun, G., Wang, M., et al. (2021). PRDX1 activates autophagy via the PTEN-AKT signaling pathway to protect against cisplatin-induced spiral ganglion neuron damage. *Autophagy.* 1–23. doi: 10.1080/15548627.2021.1905466

Lu, J., Li, Z., Zhu, Y., Yang, A., Li, R., Zheng, J., et al. (2010). Mitochondrial 12S rRNA variants in 1642 Han Chinese pediatric subjects with aminoglycoside-induced and nonsyndromic hearing loss. *Mitochondrion* 10, 380–390. doi: 10.1016/j.mito.2010.01.007

Madesh, M., and Hajnoczky, G. (2001). VDAC-dependent permeabilization of the outer mitochondrial membrane by superoxide induces rapid and massive cytochrome c release. *J. Cell. Biol.* 155, 1003–1015. doi: 10.1083/jcb.200105057

Marcotti, W., van Netten, S. M., and Kros, C. J. (2005). The aminoglycoside antibiotic dihydrostreptomycin rapidly enters mouse outer hair cells through the mechano-electrical transducer channels. *J. Physiol.* 567, 505–521. doi: 10.1113/jphysiol.2005.085951

Martin, W. F., Garg, S., and Zimorski, V. (2015). Endosymbiotic theories for eukaryote origin. *Philos. Trans. R. Soc. Lond. B Biol. Sci.* 370:20140330. doi: 10.1098/rstb.2014.0330

McFadden, S. L., Ding, D., Salvemini, D., and Salvi, R. J. (2003). M40403, a superoxide dismutase mimetic, protects cochlear hair cells from gentamicin, but not cisplatin toxicity. *Toxicol. Appl. Pharmacol.* 186, 46–54. doi: 10.1016/S0041-008X(02)00017-0

Muyderman, H., Sims, N. R., Tanaka, M., Fuku, N., Raghupathi, R., and Thyagarajan, D. (2012). The mitochondrial T1095C mutation increases gentamicin-mediated apoptosis. *Mitochondrion* 12, 465–471. doi: 10.1016/j.mito.2012.06.006

O'Sullivan, M. E., Song, Y., Greenhouse, R., Lin, R., Perez, A., Atkinson, P. J., et al. (2020). Dissociating antibacterial from ototoxic effects of gentamicin C-subtypes. *Proc. Natl. Acad. Sci. U.S.A.* 117, 32423–32432. doi: 10.1073/pnas.2013065117

Park, S. K., Choi, D., Russell, P., John, E. O., and Jung, T. T. (2004). Protective effect of corticosteroid against the cytotoxicity of aminoglycoside otic drops on isolated cochlear outer hair cells. *Laryngoscope* 114, 768–771. doi: 10.1097/00005537-200404000-00033

Pavlidis, P., Maurer, J., Apostolidou, E., Kekes, G., and Kouvelas, D. (2014). Memantine's action against aminoglycoside-induced ototoxicity. *Eur. Arch. Otorhinolaryngol.* 271, 1491–1496. doi: 10.1007/s00405-013-2647-1

Prezant, T. R., Agapian, J. V., Bohlman, M. C., Bu, X., Oztas, S., Qiu, W. Q., et al. (1993). Mitochondrial ribosomal RNA mutation associated with both antibiotic-induced and non-syndromic deafness. *Nat. Genet.* 4, 289–294. doi: 10.1038/ng0793-289

Puel, J. L. (1995). Chemical synaptic transmission in the cochlea. *Prog. Neurobiol.* 47, 449–476. doi: 10.1016/0301-0082(95)00028-3

Qian, Y., and Guan, M. X. (2009). Interaction of aminoglycosides with human mitochondrial 12S rRNA carrying the deafness-associated mutation. *Antimicrob. Agents Chemother.* 53, 4612–4618. doi: 10.1128/AAC.00965-08

Ramma, L., Schellack, N., and Heinze, B. (2019). Prevention of treatment-induced ototoxicity: an update for clinicians. *SAMJ* 109, 145–149. doi: 10.7196/SAMJ.2019.v109i3.013903

Rybak, L. P., and Kelly, T. (2003). Ototoxicity: bioprotective mechanisms. *Curr. Opin. Otolaryngol. Head Neck Surg.* 11, 328–333. doi: 10.1097/00020840-200310000-00004

Rydzanicz, M., Wrobel, M., Pollak, A., Gawecki, W., Brauze, D., Kostrzewska-Poczekaj, M., et al. (2010). Mutation analysis of mitochondrial 12S rRNA gene in Polish patients with non-syndromic and aminoglycoside-induced hearing loss. *Biochem. Biophys. Res. Commun.* 395, 116–121. doi: 10.1016/j.bbrc.2010.03.149

Schacht, J. (1999). Antioxidant therapy attenuates aminoglycoside-induced hearing loss. *Ann. N. Y. Acad. Sci.* 884, 125–130.

Starkov, A. A. (2013). An update on the role of mitochondrial alpha-ketoglutarate dehydrogenase in oxidative stress. *Mol. Cell. Neurosci.* 55, 13–16. doi: 10.1016/j.mcn.2012.07.005

Strupp, M., and Arbusow, V. (2001). Acute vestibulopathy. *Curr. Opin. Neurol.* 14, 11–20. doi: 10.1097/00019052-200102000-00003

Van Remmen, H., and Jones, D. P. (2009). Current thoughts on the role of mitochondria and free radicals in the biology of aging. *J. Gerontol. A Biol. Sci. Med. Sci.* 64, 171–174. doi: 10.1093/gerona/gln058

Wallace, D. C., Ye, J. H., Neckelmann, S. N., Singh, G., Webster, K. A., and Greenberg, B. D. (1987). Sequence analysis of cDNAs for the human and bovine ATP synthase beta subunit: mitochondrial DNA genes sustain seventeen times more mutations. *Curr. Genet.* 12, 81–90. doi: 10.1007/BF00434661

Wei, X., Zhao, L., Liu, J., Dodel, R. C., Farlow, M. R., and Du, Y. (2005). Minocycline prevents gentamicin-induced ototoxicity by inhibiting p38 MAP kinase phosphorylation and caspase 3 activation. *Neuroscience* 131, 513–521. doi: 10.1016/j.neuroscience.2004.11.014

Wimberly, B. T., Brodersen, D. E., Clemons, W. M. Jr., Morgan-Warren, R. J., Carter, A. P., Vonrhein, C., et al. (2000). Structure of the 30S ribosomal subunit. *Nature* 407, 327–339. doi: 10.1038/35030006

Xia, Z., Dudek, H., Miranti, C. K., and Greenberg, M. E. (1996). Calcium influx via the NMDA receptor induces immediate early gene transcription by a MAP kinase/ERK-dependent mechanism. *J. Neurosci.* 16, 5425–5436. doi: 10.1523/JNEUROSCI.16-17-05425.1996

Xie, J., Talaska, A. E., and Schacht, J. (2011). New developments in aminoglycoside therapy and ototoxicity. *Hear. Res.* 281, 28–37. doi: 10.1016/j.heares.2011.05.008

Yao, L., Zhang, J. W., Chen, B., Cai, M. M., Feng, D., Wang, Q. Z., et al. (2020). Mechanisms and pharmacokinetic/pharmacodynamic profiles underlying the low nephrotoxicity and ototoxicity of etimicin. *Acta. Pharmacol. Sin.* 41, 866–878. doi: 10.1038/s41401-019-0342-5

Ylikoski, J., Xing-Qun, L., Virkkala, J., and Pirvola, U. (2002). Blockade of c-Jun N-terminal kinase pathway attenuates gentamicin-induced cochlear and vestibular hair cell death. *Hear. Res.* 163, 71–81. doi: 10.1016/S0378-5955(01)00380-X

Young, W. Y., Zhao, L., Qian, Y., Wang, Q., Li, N., Greinwald, J. H. Jr., et al. (2005). Extremely low penetrance of hearing loss in four Chinese families with the mitochondrial 12S rRNA A1555G mutation. *Biochem. Biophys. Res. Commun.* 328, 1244–1251. doi: 10.1016/j.bbrc.2005.01.085

Yuan, H., Qian, Y., Xu, Y., Cao, J., Bai, L., Shen, W., et al. (2005). Cosegregation of the G7444A mutation in the mitochondrial COI/tRNA[Ser(UCN)] genes with the 12S rRNA A1555G mutation in a Chinese family with aminoglycoside-induced and nonsyndromic hearing loss. *Am. J. Med. Genet. A* 138A, 133–140. doi: 10.1002/ajmg.a.30952

Zhao, H., Li, R., Wang, Q., Yan, Q., Deng, J. H., Han, D., et al. (2004). Maternally inherited aminoglycoside-induced and nonsyndromic deafness is associated with the novel C1494T mutation in the mitochondrial 12S rRNA gene in a large Chinese family. *Am. J. Hum. Genet.* 74, 139–152. doi: 10.1086/381133

Zhou, H., Qian, X., Xu, N., Zhang, S., Zhu, G., Zhang, Y., et al. (2020). Disruption of Atg7-dependent autophagy causes electromotility disturbances, outer hair cell loss, and deafness in mice. *Cell Death. Dis.* 11:913. doi: 10.1038/s41419-020-03110-8

Zorov, D. B., Juhaszova, M., and Sollott, S. J. (2014). Mitochondrial reactive oxygen species (ROS) and ROS-induced ROS release. *Physiol. Rev.* 94, 909–950. doi: 10.1152/physrev.00026.2013

Conflict of Interest: The authors declare that the research was conducted in the absence of any commercial or financial relationships that could be construed as a potential conflict of interest.

frontiers
in Cellular Neuroscience

ORIGINAL RESEARCH
published: 21 July 2021
doi: 10.3389/fncel.2021.714070

Murine GRXCR1 Has a Different Function Than GRXCR2 in the Morphogenesis of Stereocilia

*Chang Liu and Bo Zhao**

Department of Otolaryngology-Head and Neck Surgery, Indiana University School of Medicine, Indianapolis, IN, United States

Mutations in human glutaredoxin domain-containing cysteine-rich protein 1 (*GRXCR1*) and its paralog *GRXCR2* have been linked to hearing loss in humans. Although both GRXCR1 and GRXCR2 are required for the morphogenesis of stereocilia in cochlear hair cells, a fundamental question that remains unclear is whether GRXCR1 and GRXCR2 have similar functions in hair cells. Previously, we found that GRXCR2 is critical for the stereocilia morphogenesis by regulating taperin localization at the base of stereocilia. Reducing taperin expression level rescues the morphological defects of stereocilia and hearing loss in *Grxcr2*-deficient mice. So far, functions of GRXCR1 in mammalian hair cells are still unclear. *Grxcr1*-deficient hair cells have very thin stereocilia with less F-actin content inside, which is different from *Grxcr2*-deficient hair cells. In contrast to GRXCR2, which is concentrated at the base of stereocilia, GRXCR1 is diffusely distributed throughout the stereocilia. Notably, GRXCR1 interacts with GRXCR2. In *Grxcr1*-deficient hair cells, the expression level of GRXCR2 and taperin is reduced. Remarkably, different from that in *Grxcr2*-deficient mice, reducing taperin expression level does not rescue the morphological defects of stereocilia or hearing loss in *Grxcr1*-deficient mice. Thus, our findings suggest that GRXCR1 has different functions than GRXCR2 during the morphogenesis of stereocilia.

Keywords: hearing loss, hair cell, stereocilia, GRXCR1, GRXCR2

Edited by:
David Z. He,
Creighton University, United States

Reviewed by:
Hong-Bo Zhao,
University of Kentucky, United States
Sung-Ho Huh,
University of Nebraska Medical Center, United States

****Correspondence:***
Bo Zhao
zhaozb@iu.edu

Specialty section:
This article was submitted to Non-Neuronal Cells, a section of the journal Frontiers in Cellular Neuroscience

Received: *24 May 2021*
Accepted: *25 June 2021*
Published: *21 July 2021*

Citation:
Liu C and Zhao B (2021) Murine GRXCR1 Has a Different Function Than GRXCR2 in the Morphogenesis of Stereocilia. Front. Cell. Neurosci. 15:714070. doi: 10.3389/fncel.2021.714070

INTRODUCTION

As the fourth leading cause of disability, hearing loss is affecting over 5% of the population or 430 million people in the world, estimated by World Health Organization. Sensorineural hearing loss is the most common type of hearing loss, frequently caused by the damage of inner ear hair cells, which transform the mechanical sound stimuli into electrical signals (Gillespie and Muller, 2009; Pacentine et al., 2020). Many forms of hearing loss are due to genetic mutations. By 2011, 135 loci for the monogenic forms of human deafness had been reported (Richardson et al., 2011). So far, more than 60 of the affected genes have been identified, and many of those genes are specifically expressed in hair cells (Scheffer et al., 2015). Technological refinements in positional cloning and the sequencing of the human genome have dramatically accelerated the pace to identify deafness-related genes. However, the underlying mechanisms by which these genes affect auditory perceptions are only just beginning to be elucidated.

The glutaredoxin domain-containing cysteine-rich family of genes, *GRXCR1* and *GRXCR2*, have been identified as the mutated genes in nonsyndromic deafness DFNB25 and DFNB101, respectively (Odeh et al., 2010; Schraders et al., 2010; Imtiaz et al., 2014; Wonkam et al., 2021). Both GRXCR1 and GRXCR2 are specifically expressed in cochlear hair cells and essential for the morphogenesis of stereocilia, the mechanosensing subcellular organelles that protrude from the apical surface of hair cells (Beyer et al., 2000; Erven et al., 2002; Odeh et al., 2004, 2010; Avenarius et al., 2018; Liu et al., 2018). A previous study found that GRXCR2 is critical for the morphogenesis of stereocilia by regulating the localization of taperin at the base of stereocilia. Reducing taperin expression level rescues the morphological defects of stereocilia and partially restores the hearing in the *Grxcr2* mutant (Liu et al., 2018). Although the sequences of GRXCR1 and GRXCR2 are 32% identical, it is still unknown whether GRXCR1 and GRXCR2 have similar functions in hair cells.

The central region of GRXCR1 shows some similarity with glutaredoxin proteins, enzymes that reduce disulfide bonds or catalyze reversible protein glutathionylation or deglutathionylation. A previous study found that zebrafish GRXCR1 is essential for stereocilia morphogenesis through its glutaredoxin enzyme activity (Blanco-Sanchez et al., 2018). Interestingly, a significant amount of GRXCR1 is localized in the Golgi apparatus in zebrafish (Blanco-Sanchez et al., 2018), which is different from the localization of GRXCR1 in mouse hair cells (Odeh et al., 2010). Different localization indicates that GRXCR1 might have different functions in murine hair cells. The *bona fide* glutaredoxin enzyme activity of murine GRXCR1 needs experimental verification.

In this study, we analyzed the localization of GRXCR1 and GRXCR2 in hair cells. We reduced taperin expression level in *Grxcr1* mutant and characterized different mouse lines bearing *Grxcr1* and/or *taperin* mutations. In addition, we purified murine GRXCR1 protein and measured the glutaredoxin activity. Our results suggest that GRXCR1 has different functions than GRXCR2 during the morphogenesis of stereocilia.

MATERIALS AND METHODS

Animal Models and Animal Care

Grxcr2$^{-/-}$ mouse (previously named as *Grxcr2*$^{D46/D46}$ mouse) and *taperin*$^{-/-}$ mouse (previously named as *taperin*$^{in103/in103}$ mouse) have been described previously (Liu et al., 2018). *Grxcr1*$^{-/-}$ mouse (also named as *Grxcr1*$^{pi\text{-}2J}$ mouse) was purchased from Jackson Laboratories, Bar Harbor, ME, USA (Odeh et al., 2010). All animal experiments were approved by Institutional Animal Care and Use Committee of Indiana University School of Medicine. Both male and female mice were used in our experiment. We did not find any sex-based differences.

Scanning Electron Microscopy

The experiments were performed as described (Zhao et al., 2016; Liu et al., 2018). In brief, inner ears from P7 pups were dissected in a fixative containing 2.5% glutaraldehyde and 4% formaldehyde. Samples were then fixed for 1 h at RT and dissected to remove the stria vascularis, Reissner's membrane, and tectorial membrane. After being post-fixed in the same fixative overnight at 4°C, samples were fixed with 1% OsO_4 for 1 h at room temperature. Then samples were serially dehydrated in ethanol, dried in a critical point drier (Autosamdri-815A, Tousimis, Rockville, MD, USA), finely dissected, and mounted on aluminum stubs. Samples were then coated by gold. Images were captured using a JEOL 7800F scanning electron microscope (Jeol, Tokyo, Japan). At least three animals representative of each experimental paradigm were analyzed.

To measure the width of the tallest row of stereocilia in inner hair cells, single hair cells were imaged at high magnification (×∼20,000) using a JEOL 7800F scanning electron microscope. Then, the width of the tallest row of stereocilia at about 1/3 of the height from the top was measured using ImageJ (NIH, Bethesda, MD, USA).

Whole Mount Immunostaining

Whole mount staining was carried out as described (Zhao et al., 2016; Liu et al., 2018). In brief, organ of Corti tissue was dissected and fixed in a fixative containing 4% paraformaldehyde (PFA) for 20 min. Samples were blocked for 20 min at room temperature in a blocking buffer containing 5% bovine serum albumin (BSA), 1% goat serum, and 0.5% Triton X-100. Then, samples were incubated with primary antibodies overnight at 4°C. Samples were washed and incubated 2 h at room temperature with secondary antibodies. After mounting in ProLong® Antifade Reagents (Invitrogen, Waltham, MA, USA), stacked images were captured by deconvolution microscope (Leica) using a ×100 objective. Images were deconvoluted using blind deconvolution method.

To costain β-actin and γ-actin, cochlear whole mounts were fixed in 4% PFA for 20 min and then ice-cold methanol for 15 min. Then, samples were blocked for 20 min at room temperature in a blocking buffer containing 5% BSA, 1% goat serum, and 0.5% Triton X-100. Then, samples were incubated with a primary antibody against γ-actin (Abcam, Cambridge, UK) overnight at 4°C. Samples were then washed and incubated with secondary antibody for 2 h at room temperature. Then, samples were washed again and incubated with FITC-conjugated β-actin antibody (Abcam, Cambridge, UK) overnight at 4°C. After washing, samples were mounted and imaged.

To raise antibodies against GRXCR1, two peptides (NEQEKDQDNLLVLART and KFEEKNIALNGDYGKELDER) were covalently linked to KLH and immunized New Zealand rabbits (Thermo Fisher Scientific, Waltham, MA, USA). Affinity purification was then performed. Other primary antibodies used in this study were as follows: anti-GRXCR2 (Cat# HPA059421, Sigma, Saint Louis, MO, USA) and anti-taperin (Cat# HPA020899, Sigma, Saint Louis, MO, USA). Additional reagents were as follows: Alexa Fluor 488-phalloidin (Thermo Fisher Scientific, Waltham, MA, USA), Alexa Fluor 568-phalloidin (Thermo Fisher Scientific, Waltham, MA, USA), Alexa Fluor 647-phalloidin (Thermo Fisher Scientific, Waltham, MA, USA), Alexa Fluor 488 goat anti-rabbit (Thermo Fisher

Scientific, Waltham, MA, USA), Alexa Fluor 555 goat anti-mouse (Thermo Fisher Scientific, Waltham, MA, USA), and Alexa Fluor 546 goat anti-rabbit (Thermo Fisher Scientific, Waltham, MA, USA).

Auditory Brainstem Response Measurement

Auditory brainstem responses (ABRs) of mice were recorded as described (Zhao et al., 2016; Liu et al., 2018) using TDT Bioacoustic system 3 and BioSigRZ software. In brief, mice were anesthetized using a mixture of 100 mg/kg ketamine and 10 mg/kg xylazine. Electrodes were inserted under the skin at the vertex and ipsilateral ear, while a ground was inserted under the skin near the tail. The speaker was placed 5 cm away from the mouse ear, and tone stimulus is presented 21 times per second. Band pass filtered from 300–3,000 Hz and a total of 512 responses were averaged at each frequency and level combination. The intensity of sound stimulus was started at 90 dB sound pressure level (SPL) and decreased to 10 dB SPL stepwise to a sub-threshold level. ABR thresholds were analyzed for a range of frequencies (for pure tone, 4–28 kHz). If no ABR wave was detected at maximum intensity stimulation, a nominal threshold of 90 dB was assigned.

Cell Culture

HEK293 cell line was obtained from ATCC (Manassas, VA, USA). Cells were maintained in the DMEM medium (Thermo Fisher Scientific, Waltham, MA, USA) supplemented with 10% heat-inactivated fetal bovine serum (Thermo Fisher

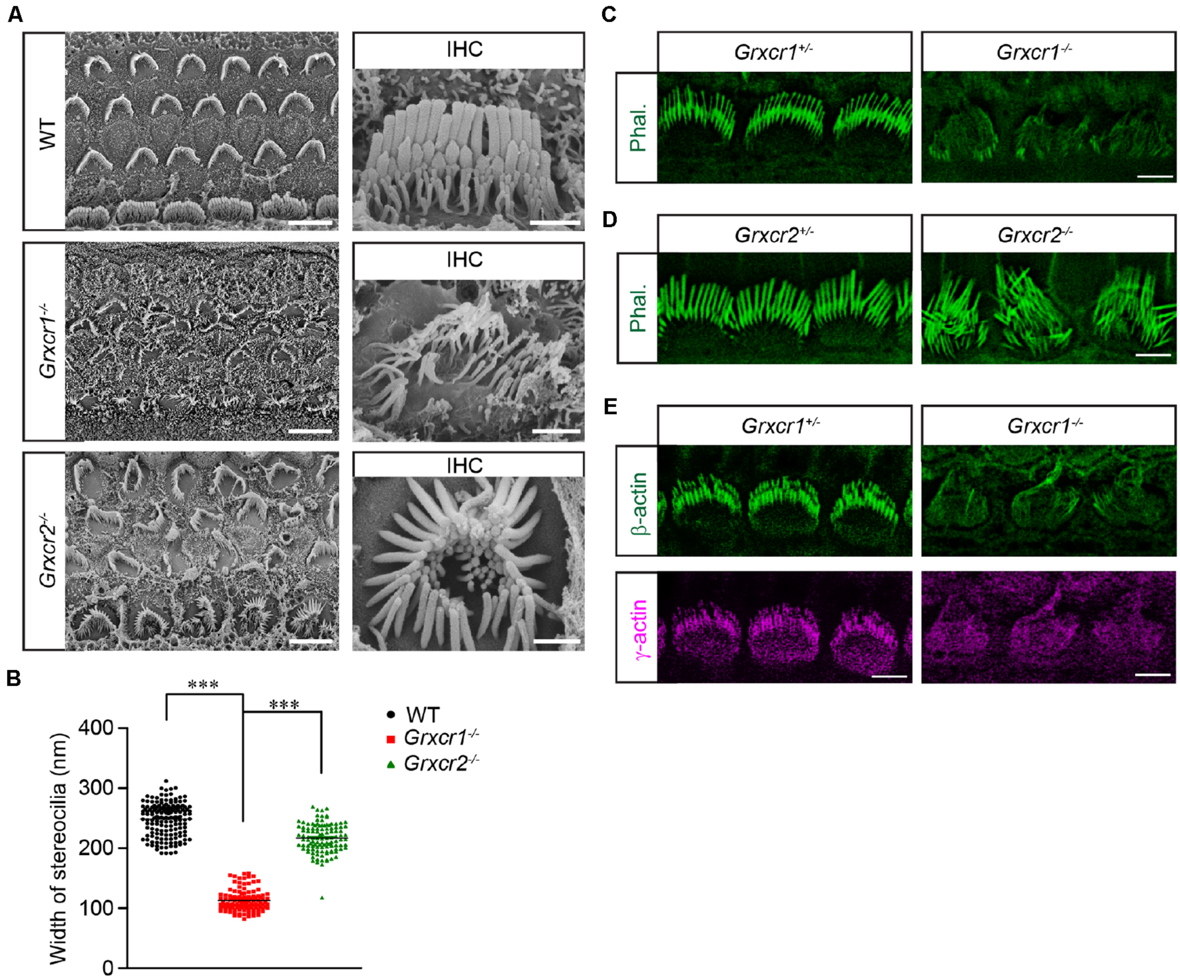

FIGURE 1 | Stereocilia morphology in *Grxcr1*-deficient hair cells. **(A)** Scanning electron microscope images showing auditory epithelia of wild-type, *Grxcr1*$^{-/-}$, and *Grxcr2*$^{-/-}$ mice at the age of P7. Stereocilia of inner hair cells (IHCs) and outer hair cells (OHCs) from *Grxcr1*$^{-/-}$ and *Grxcr2*$^{-/-}$ hair cells were disorganized. Note, stereocilia in *Grxcr1*$^{-/-}$ hair cells were extremely thin. Scale bars: left, 5 μm; right 1 μm. **(B)** Width of the tallest row of stereocilia of IHCs from wild-type, *Grxcr1*$^{-/-}$, and *Grxcr2*$^{-/-}$ mice at the age of P7. All values are represented as the mean ± SEM. ***$p < 0.001$ by Student's t test. **(C,D)** Cochlear whole mounts from *Grxcr1*$^{-/-}$ **(C)** and *Grxcr2*$^{-/-}$ **(D)** mice at P7 were stained for phalloidin to reveal stereocilia. Note the weak phalloidin staining signal in *Grxcr1*$^{-/-}$ IHCs. Scale bars: 5 μm. **(E)** Cochlear whole mounts from *Grxcr1*$^{-/-}$ mice at P7 were stained for β-actin and γ-actin. Scale bars: 5 μm.

Scientific, Waltham, MA, USA), 100 U/ml penicillin, and 100 μg/ml streptomycin (Thermo Fisher Scientific, Waltham, MA, USA). Cells were grown at 37°C in a 5% CO_2-humidified atmosphere.

cDNA Constructions, Immunoprecipitations, and Western Blots

The coding sequence of *Grxcr1* was amplified from mouse cochlear cDNA library. Expression of the constructs, immunoprecipitations, and western blots were carried out as described (Senften et al., 2006; Zhao et al., 2016; Liu et al., 2018). Immunoprecipitation experiments were carried out at least three times to verify the reproducibility of the data. The following antibodies were used for the experiments: anti-Myc (Cat# 2278S, Cell Signaling Technology, Danvers, MA, USA), anti-Myc (Cat# sc-40, Santa Cruz Biotechnology, Dallas, TX, USA), and anti-GFP (Cat# sc-9996, Santa Cruz Biotechnology, Dallas, TX, USA).

Purification of GRXCR1

Mouse *Grxcr1* cDNA fused with six XHis tag at C terminus was inserted into pMAL-c5x plasmid. *Escherichia coli* BL21 (DE3) cells were cultured in LB containing 100 μg/ml ampicillin at 37°C. The expression of fusion protein was induced overnight with 1 mM isopropylthio-β-galactoside at room temperature. Cells were harvested and resuspended in 25 mM Tris-base (pH 7.6) and 125 mM NaCl buffer. After sonication, the lysate was centrifuged at 15,000 rpm for 30 min. The supernatant was incubated with His-bind resin, and then, protein was eluted by an elution buffer containing 250 mM imidazole. To increase the purity, the eluted protein was then incubated with amylose resin and eluted by an elution buffer containing 10 mM maltose.

Glutaredoxin Activity Assay

Glutaredoxin activity assay was performed following the published protocol (Mieyal et al., 1991a,b). In brief, the 0.9 ml reaction mixture contained 0.2 mM NADPH, 0.5 mM GSH, 0.1 M potassium phosphate buffer (pH 7.4), 0.4 U of GSSG reductase, and an aliquot of purified GRXCR1 or glutaredoxin-2 (GLRX2; Thermo Fisher Scientific, Waltham, MA, USA). The mixture was preincubated for 5 min at 30°C. After adding 0.1 ml 20 mM hydroxyethyl disulfide (HEDS) to initiate the reaction, $A_{340\ \mathrm{nm}}$ was measured by Synergy H1 spectrophotometer (BioTek, Winooski, VT, USA) to determine the slope of the linear portion of the time course for absorption loss (subtracted blank control). One unit of glutaredoxin activity was defined as 1 μmol of NADPH oxidized per minute under these standard assay conditions.

Quantification and Statistical Analysis

All data are mean ± standard error of the mean (SEM). Student's two-tailed unpaired *t* test or two-way ANOVA were used to determine statistical significance ($*p < 0.05$, $**p < 0.01$, $***p < 0.001$).

RESULTS

GRXCR1 Is Essential for Stereocilia Morphogenesis

Both GRXCR1 and GRXCR2 are required for stereocilia morphogenesis and auditory perception. To investigate whether their detailed functions are similar in hair cells, we characterized the *Grxcr1* null mutant ($Grxcr1^{pi\text{-}2J}$, referred as $Grxcr1^{-/-}$ hereafter) and *Grxcr2* null mice that we previously generated ($Grxcr2^{D46/D46}$, referred as $Grxcr2^{-/-}$ hereafter). Both $Grxcr1^{-/-}$

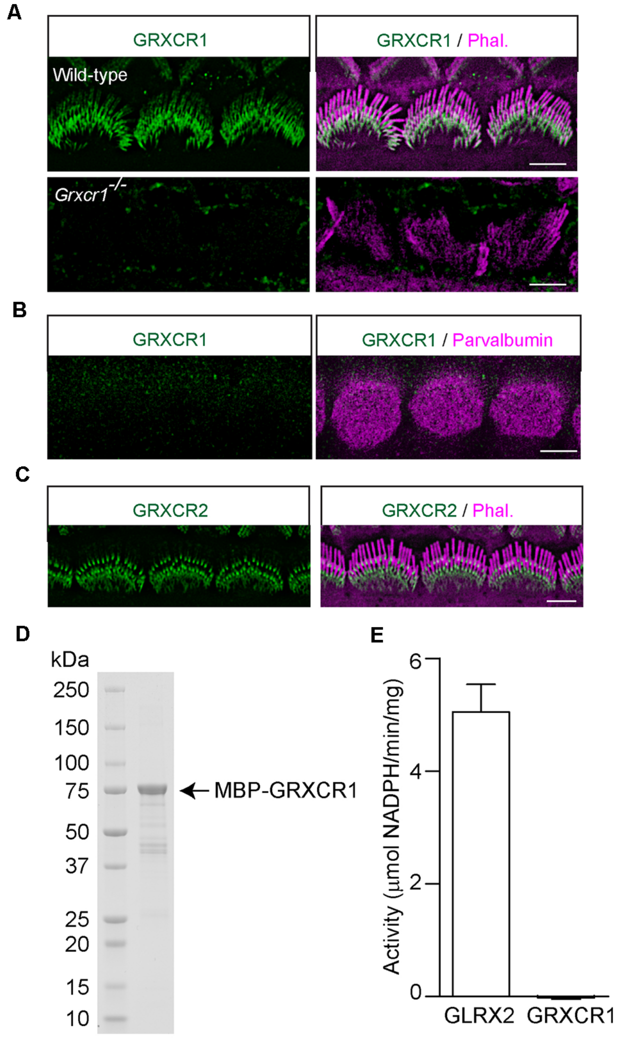

FIGURE 2 | Localization of GRXCR1 and GRXCR2 in hair cells. **(A)** Costaining of P7 cochlear whole mounts with GRXCR1-antibody (green) and phalloidin (magenta). Note the absence of a signal in $Grxcr1^{-/-}$ inner hair cells. **(B)** Costaining of P7 wild-type cochlear whole mounts with GRXCR1-antibody (green) and parvalbumin-antibody (magenta) to reveal cell body of inner hair cells. Note that there is no signal of GRXCR1 in the cell body. **(C)** Costaining of P7 wild-type cochlear whole mounts with GRXCR2-antibody and phalloidin. Note, GRXCR2 is concentrated at the base of stereocilia. **(D)** GRXCR1 was expressed and purified from *E. coli*. **(E)** Glutaredoxin activity of GLRX2 and GRXCR1 was measured. Note that there is no detectable enzyme activity of GRXCR1. Scale bars: 5 μm.

and *Grxcr2*$^{-/-}$ hair bundles are severely disorganized and have lost the typical staircase organization at postnatal day 7 (P7). Hair bundle fragmentation and misorientation are frequently observed in hair cells from both mutants. Remarkably, stereocilia in *Grxcr1*$^{-/-}$ hair cells are extremely thin compared with that in the wild-type hair cells or *Grxcr2*$^{-/-}$ hair cells (**Figures 1A,B**), which is consistent with the previous results (Beyer et al., 2000; Erven et al., 2002; Odeh et al., 2004). Stereocilia are filled with tightly cross-linked and uniformly oriented actin filaments that provide stiffness. The very strong phalloidin staining signal in the wild-type stereocilia suggests the abundance of actin filaments inside the stereocilia. Remarkably, very low phalloidin staining signal along the disorganized stereocilia was obtained from *Grxcr1*$^{-/-}$ mice, suggesting that the F-actin content is dramatically reduced in the *Grxcr1*$^{-/-}$ hair bundles (**Figure 1C**). Although stereocilia are also disorganized in the *Grxcr2*$^{-/-}$ mice, there is no detectable reduction of F-actin content inside the stereocilia, revealed by phalloidin staining (**Figure 1D**). To further confirm this result, the amount of β-actin and γ-actin, two major actin isoforms in the stereocilia, was evaluated in *Grxcr1*$^{-/-}$ hair cells by immunostaining. Both β-actin and γ-actin are reduced in the *Grxcr1*$^{-/-}$ hair cells (**Figure 1E**). These results suggest that the pathophysiological changes in hair cells associated with *Grxcr1* and *Grxcr2* mutations are different.

GRXCR1 Is Diffused Along the Stereocilia

Odeh et al. (2010) in Dr. David Kohrman's lab found that GRXCR1 is diffused along the stereocilia in murine hair cells. In zebrafish, a significant amount of GRXCR1 is also localized in the Golgi apparatus and endoplasmic reticulum—Golgi intermediate compartment (Odeh et al., 2010; Blanco-Sanchez et al., 2018). In our previous studies, we found that exogenously expressed GRXCR1 is localized along the stereocilia without any obvious immunostaining signals in ER or Golgi structures (Liu et al., 2018). To study the localization of endogenous GRXCR1 protein in murine hair cells, we generated an antibody against GRXCR1. Immunostaining was performed using cochlear whole mounts dissected from wild-type and *Grxcr1*$^{-/-}$ mice. The immunostaining signal outlined the shape of the stereociliary bundle in the wild-type cochlea, but not in the *Grxcr1*-deficient cochlea (**Figure 2A**), suggesting that the antibody specifically recognize GRXCR1 in murine hair cells. In agreement with the findings of Odeh et al. (2010), GRXCR1 was localized along the shaft of stereocilia in hair cells (**Figure 2A**). Interestingly, we also noticed a stronger immunostaining signal at the base of stereocilia especially in inner hair cells, suggesting that GRXCR1 is relatively concentrated at the base of stereocilia (**Figure 2A**). In addition, we did not see any immunostaining signal of GRXCR1 in the cell body (**Figure 2B**), which is different from that in zebrafish hair cells (Blanco-Sanchez et al., 2018). Different from GRXCR1, GRXCR2 is localized at the base of stereocilia (**Figure 2C**).

In zebrafish, GRXCR1 is essential for the morphogenesis of stereocilia through its glutaredoxin activity (Blanco-Sanchez et al., 2018). Although the central region of mammalian GRXCR1 shows some similarity with glutaredoxin proteins, it lacks the typical dual cysteines essential for enzyme activity, and the putative thioredoxin fold in mammalian GRXCR1 might just act as an interface mediating the protein–protein interaction (Odeh et al., 2010). To investigate whether murine GRXCR1 has

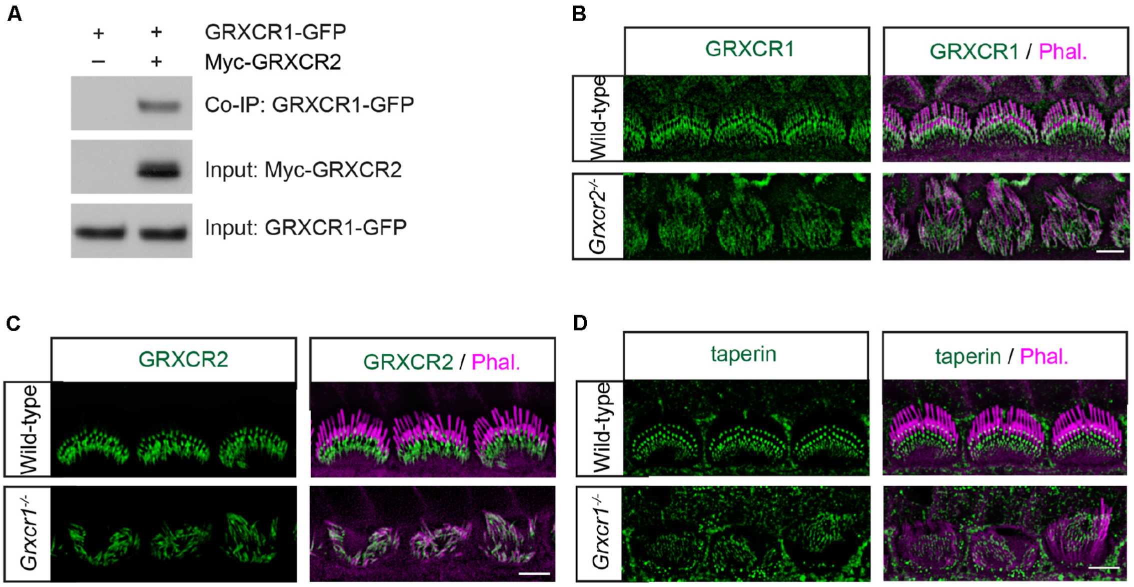

FIGURE 3 | Localization of taperin and GRXCR2 in *Grxcr1*-deficient hair cells. **(A)** HEK293 cells were transfected with GRXCR1-GFP and Myc-GRXCR2. Immunoprecipitation was carried out with Myc-antibody. The upper row shows co-IP result and the lower rows show input proteins. **(B)** Cochlear whole mounts from *Grxcr2*$^{-/-}$ mice at P7 was stained for GRXCR1. **(C,D)** Cochlear whole mounts from *Grxcr1*$^{-/-}$ mice at P7 were stained for GRXCR2 **(C)** and taperin **(D)**. Scale bars: 5 μm.

enzyme activity, GRXCR1 was expressed in *E. coli* and purified (**Figure 2D**). Catalytic properties of murine GRXCR1 were determined in parallel with and compared with human GLRX2. Consistent with previous studies, GLRX2 showed high glutaredoxin activity (Gladyshev et al., 2001); however, we did not detect any enzyme activity of murine GRXCR1 (**Figure 2E**), suggesting that in murine hair cells, GRXCR1 is essential for the morphogenesis of stereocilia probably *via* different mechanisms.

Localization of Taperin and GRXCR2 in *Grxcr1*-Deficient Hair Cells

A previous study found that GRXCR1 interacts with GRXCR2 when they are expressed in yeast (Avenarius, 2012). To investigate whether GRXCR1 interacts with GRXCR2 in mammalian cells, we carried out co-immunoprecipitation experiments with extracts from HEK293 cells that were transfected with Myc-tagged GRXCR2 and GFP-tagged GRXCR1. Indeed, GRXCR1-GFP was co-immunoprecipitated with Myc-GRXCR2 (**Figure 3A**), suggesting a heterodimeric interaction between GRXCR1 and GRXCR2.

To investigate the extent to which the interaction between GRXCR1 and GRXCR2 is required for their proper localization in the stereocilia, immunohistochemistry experiments were performed. In the *Grxcr2*$^{-/-}$ hair cells, GRXCR1 was a little bit more diffusely distributed along the stereocilia (**Figure 3B**). In the *Grxcr1*$^{-/-}$ hair cells, GRXCR2 was diffused along the stereocilia and the intensity of immunostaining signal was reduced (**Figure 3C**). The intensity of taperin immunostaining signal was also reduced, and no diffusion of taperin along the stereocilia was observed in P7 *Grxcr1*$^{-/-}$ hair cells (**Figure 3D**). As the stereocilia in *taperin*$^{-/-}$ hair cells are fairly normal at P7 (Liu et al., 2018), the extremely thin stereocilia in *Grxcr1*$^{-/-}$ hair cells are likely not mainly caused by the reduction of taperin. Since the stereocilia are extremely thin in *Grxcr1*$^{-/-}$ hair cells, it is possible that the reduction of taperin and GRXCR2 might be secondary to the stereociliary morphogenesis defects.

Reducing Taperin Expression Could Not Rescue the Morphological Defects of Stereocilia in *Grxcr1*-Deficient Mice

The morphological defects of stereocilia in *Grxcr2*$^{-/-}$ mice is caused by the mislocalization of taperin, as reducing taperin expression level rescues the stereocilia morphology in *Grxcr2*$^{-/-}$-deficient hair cells (Liu et al., 2018). The pathophysiological changes in hair cells associated with *Grxcr1* and *Grxcr2* mutations are different, suggesting that *Grxcr1* deficiency induced the stereocilia disorganization might be through a different mechanism. GRXCR1 interacts with GRXCR2. Lack of GRXCR1 affects the localization and expression of GRXCR2 and taperin in stereocilia. To investigate whether the morphological defects in *Grxcr1*$^{-/-}$ hair cells is caused or partially caused by taperin, we crossed *Grxcr1*$^{-/-}$ mice with *taperin* null mice that we previously generated (*taperin*$^{in103/in103}$, referred as *taperin*$^{-/-}$ hereafter) and then immunostaining was performed. Similar to *Grxcr1*$^{-/-}$ hair cells, *Grxcr1*$^{-/-}$*taperin*$^{+/-}$ and *Grxcr1*$^{-/-}$*taperin*$^{-/-}$ hair cells have disorganized stereocilia with less F-actin content inside (**Figure 4A**). In contrast, reducing taperin expression level rescued the morphological defects of stereocilia in *Grxcr2*$^{-/-}$ hair cells (**Figure 4B**).

To analyze the stereocilia morphology in more detail, we carried out additional scanning electron microscopy analyses with hair cells at P7. Similar to that in *Grxcr1*$^{-/-}$ hair cells, stereocilia in *Grxcr1*$^{-/-}$*taperin*$^{+/-}$ and *Grxcr1*$^{-/-}$*taperin*$^{-/-}$ hair cells are very thin and disorganized (**Figure 5**). These results suggest that reducing taperin expression level could not restore the morphological defects in *Grxcr1*$^{-/-}$ hair cells.

Reducing Taperin Expression Could Not Restore the Hearing in *Grxcr1*-Deficient Mice

To investigate whether reducing taperin expression could restore the hearing in *Grxcr1*$^{-/-}$ mice, we measured auditory perceptions of 6-week-old *Grxcr1*$^{-/-}$*taperin*$^{+/-}$ and *Grxcr1*$^{-/-}$*taperin*$^{-/-}$ mice. Similar to the *Grxcr1*$^{-/-}$ mice,

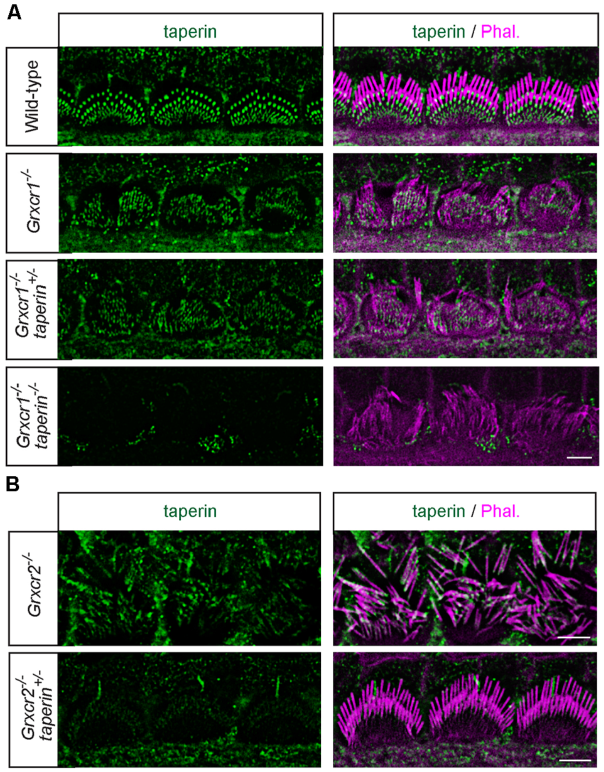

FIGURE 4 | Analysis of stereocilia morphology by immunostaining. **(A)** Whole mounts from the middle region of the cochlea from wild-type, *Grxcr1*$^{-/-}$, *Grxcr1*$^{-/-}$*taperin*$^{+/-}$, and *Grxcr1*$^{-/-}$*taperin*$^{-/-}$ mice at the age of P7 were stained with taperin-antibody (green) and phalloidin (magenta). Note the disorganized stereocilia in *Grxcr1*$^{-/-}$, *Grxcr1*$^{-/-}$*taperin*$^{+/-}$, and *Grxcr1*$^{-/-}$*taperin*$^{-/-}$ mice. **(B)** Whole mounts from the middle region of cochlea from *Grxcr2*$^{-/-}$ and *Grxcr2*$^{-/-}$*taperin*$^{+/-}$ mice at the age of P7 were stained with taperin-antibody and phalloidin. Note the disorganized stereocilia in *Grxcr2*$^{-/-}$ mice and well-maintained stereocilia in *Grxcr2*$^{-/-}$*taperin*$^{+/-}$ mice. Scale bars: 5 μm.

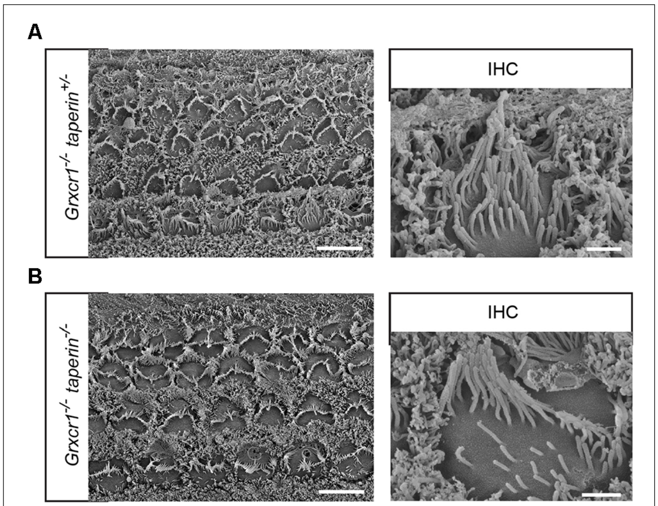

FIGURE 5 | Analysis of stereocilia morphology by scanning electron microscopy. **(A,B)** Whole mounts from the middle region of the cochlea from *Grxcr1*$^{-/-}$*taperin*$^{+/-}$ **(A)** and *Grxcr1*$^{-/-}$*taperin*$^{-/-}$ **(B)** mice at the age of P7 were analyzed by scanning electron microscopy. Note, stereocilia in *Grxcr1*$^{-/-}$, *Grxcr1*$^{-/-}$*taperin*$^{+/-}$, and *Grxcr1*$^{-/-}$*taperin*$^{-/-}$ mice were extremely thin and disorganized. Scale bars: left, 5 μm; right, 1 μm.

Grxcr1$^{-/-}$*taperin*$^{+/-}$ and *Grxcr1*$^{-/-}$*taperin*$^{-/-}$ could not respond to the 90-dB sound stimuli, suggesting that they were profoundly deaf (**Figure 6A**). Recording ABRs in response to pure tones revealed that all these mice had profound hearing loss across the entire analyzed frequency spectrum (**Figure 6B**). These results suggest that reducing taperin expression level could not restore the hearing in the *Grxcr1*$^{-/-}$ mice. Thus, our results suggest that GRXCR1 has different functions than GRXCR2 during the morphogenesis of stereocilia.

DISCUSSION

GRXCR1 and GRXCR2 have more than 30% amino acid identity. Both of them are essential for the morphogenesis of stereocilia and auditory perception. However, several lines of evidence in this study suggest that they have different functions in hair cells. First, the pathophysiological changes of stereocilia associated with *Grxcr1* and *Grxcr2* mutations are very different. Second, although both of them are localized at the stereocilia, GRXCR1 is diffusely distributed throughout the stereocilia. Third, although we could alleviate of the auditory defects in *Grxcr2*$^{-/-}$ mice by reducing taperin expression level, using a similar strategy, we could not rescue the morphological defects of stereocilia or restore the hearing in *Grxcr1*$^{-/-}$ mice.

GRXCR1 shows some similarity with glutaredoxin proteins. In zebrafish, the glutaredoxin activity of GRXCR1 is crucial for regulating the physical interaction between Harmonin and Sans (Blanco-Sanchez et al., 2018). Consistently, *Grxcr1*, *harmonin*, and *sans* zebrafish mutants have very similar phenotypes with significantly thinner, fewer hair bundles and splayed stereocilia (Blanco-Sanchez et al., 2018). However, in mouse, the phenotypes of *Grxcr1*, *harmonin*, and *sans*-mutant hair cells are different. *Grxcr1* mutant hair cells have very thin and short stereocilia, while the length and width of the tallest row of stereocilia in *harmonin* and *sans* mutant hair cells are similar to the wild-type hair cells (Lefevre et al., 2008; Corns et al., 2018), suggesting that GRXCR1 probably has different functions in mouse hair cells. In our study, we purified mouse GRXCR1 and measured its glutaredoxin activity. We did not detect any

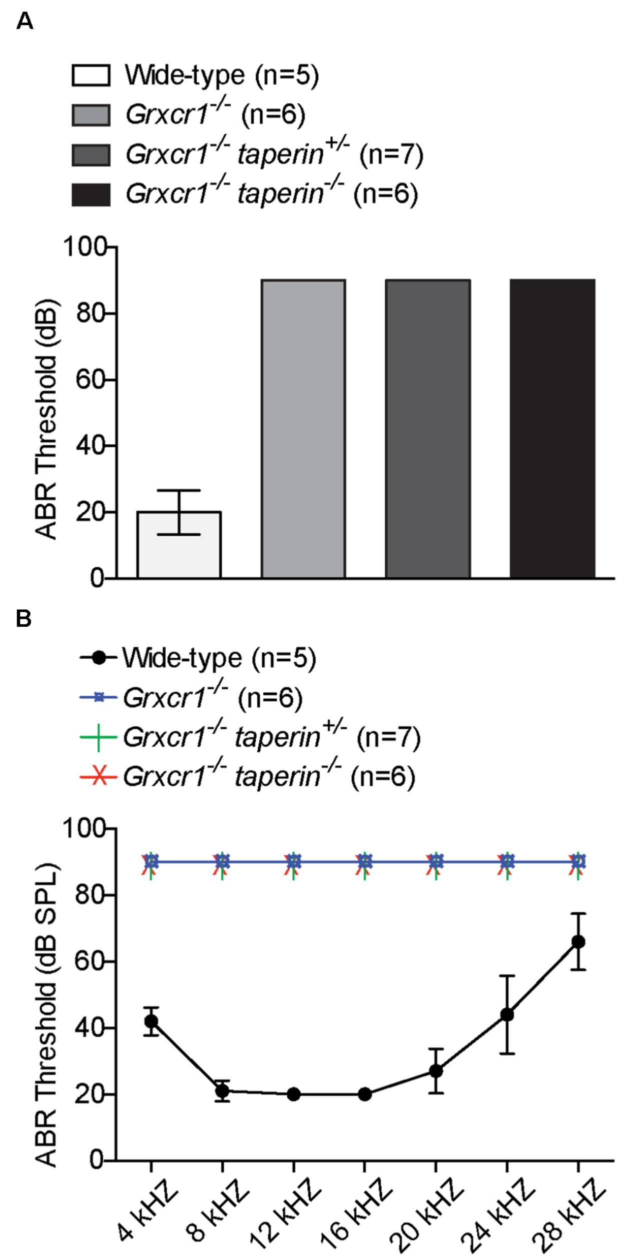

FIGURE 6 | Analysis of hearing function by ABR. **(A,B)** ABR thresholds for click stimuli **(A)** and pure tones **(B)** at the age of 6 weeks. Note the profound hearing loss in *Grxcr1*$^{-/-}$, *Grxcr1*$^{-/-}$*taperin*$^{+/-}$, and *Grxcr1*$^{-/-}$*taperin*$^{-/-}$ mice across the entire frequency spectrum analyzed. $p < 0.001$ between wild-type and *Grxcr1*$^{-/-}$, *Grxcr1*$^{-/-}$*taperin*$^{+/-}$, and *Grxcr1*$^{-/-}$*taperin*$^{-/-}$ mice (two-way ANOVA).

enzyme activity using purified murine GRXCR1. There is a possibility that GRXCR1 purified from bacteria might not fold properly. Thus, the *bona fide* glutaredoxin activity of murine GRXCR1 needs to be further verified using other experimental approaches in future. GRXCR1 also shows some similarity with THRUMIN1 from *Arabidopsis thaliana* (Avenarius, 2012). An *in vitro* study shows that THRUMIN1 binds to and bundles F-actin (Whippo et al., 2011). Interestingly, in the *Grxcr1*$^{-/-}$ hair cells, the stereocilia are extremely thin and F-actin content is reduced. The question arose whether GRXCR1 is essential for the morphogenesis of stereocilia by directly or indirectly regulating actin cytoskeleton inside the stereocilia. To test this hypothesis, further studies to investigate whether purified GRXCR1 could bind to actin and regulate actin dynamics *in vitro* would be informative.

Although GRXCR1 and GRXCR2 have similar amino acid sequences, only GRXCR2 binds to taperin (Liu et al., 2018). In addition, different localization patterns of these two proteins in stereocilia also suggest that they probably have different binding partners in hair cells. To extensively illustrate the functions of GRXCR1 and mechanisms of *Grxcr1* deficiency-induced hearing loss, it will be of interest to screen interacting proteins of GRXCR1 and investigate the extent to which those binding partners are required for GRXCR1 functions and stereocilia morphogenesis in hair cells.

DATA AVAILABILITY STATEMENT

The original contributions presented in the study are included in the article, further inquiries can be directed to the corresponding author.

ETHICS STATEMENT

The animal study was reviewed and approved by Institutional Animal Care and Use Committee of Indiana University School of Medicine.

AUTHOR CONTRIBUTIONS

CL and BZ made significant contributions in the methodology, investigation, and writing. BZ made significant contributions in the conceptualization and supervision of the study. All authors contributed to the article and approved the submitted version.

FUNDING

This work was supported by the National Institute on Deafness and Other Communication Disorders (NIDCD) grant DC017147 (BZ) and the Indiana University School of Medicine startup funding (BZ).

REFERENCES

Avenarius, M. (2012). The glutaredoxin-like cysteine-rich family of genes, Grxcr1 and Grxcr2, in stereocilia development and function. PhD Thesis. Ann Arbor, MI: University of Michigan.

Avenarius, M. R., Jung, J. Y., Askew, C., Jones, S. M., Hunker, K. L., Azaiez, H., et al. (2018). Grxcr2 is required for stereocilia morphogenesis in the cochlea. *PLoS One* 13:e0201713. doi: 10.1371/journal.pone.0201713

Beyer, L. A., Odeh, H., Probst, F. J., Lambert, E. H., Dolan, D. F., Camper, S. A., et al. (2000). Hair cells in the inner ear of the pirouette and shaker 2 mutant mice. *J. Neurocytol.* 29, 227–240. doi: 10.1023/a:1026515619443

Blanco-Sanchez, B., Clement, A., Fierro, J. Jr., Stednitz, S., Phillips, J. B., Wegner, J., et al. (2018). Grxcr1 promotes hair bundle development by destabilizing the physical interaction between harmonin and sans usher syndrome proteins. *Cell Rep.* 25, 1281–1291.e4. doi: 10.1016/j.celrep.2018.10.005

Corns, L. F., Johnson, S. L., Roberts, T., Ranatunga, K. M., Hendry, A., Ceriani, F., et al. (2018). Mechanotransduction is required for establishing and maintaining mature inner hair cells and regulating efferent innervation. *Nat. Commun.* 9:4015. doi: 10.1038/s41467-018-06307-w

Erven, A., Skynner, M. J., Okumura, K., Takebayashi, S., Brown, S. D., Steel, K. P., et al. (2002). A novel stereocilia defect in sensory hair cells of the deaf mouse mutant Tasmanian devil. *Eur. J. Neurosci.* 16, 1433–1441. doi: 10.1046/j.1460-9568.2002.02213.x

Gillespie, P. G., and Muller, U. (2009). Mechanotransduction by hair cells: models, molecules and mechanisms. *Cell* 139, 33–44. doi: 10.1016/j.cell.2009.09.010

Gladyshev, V. N., Liu, A., Novoselov, S. V., Krysan, K., Sun, Q. A., Kryukov, V. M., et al. (2001). Identification and characterization of a new mammalian glutaredoxin (thioltransferase), Grx2. *J. Biol. Chem.* 276, 30374–30380. doi: 10.1074/jbc.M100020200

Imtiaz, A., Kohrman, D. C., and Naz, S. (2014). A frameshift mutation in GRXCR2 causes recessively inherited hearing loss. *Hum. Mutat.* 35, 618–624. doi: 10.1002/humu.22545

Lefevre, G., Michel, V., Weil, D., Lepelletier, L., Bizard, E., Wolfrum, U., et al. (2008). A core cochlear phenotype in USH1 mouse mutants implicates fibrous links of the hair bundle in its cohesion, orientation and differential growth. *Development* 135, 1427–1437. doi: 10.1242/dev.012922

Liu, C., Luo, N., Tung, C. Y., Perrin, B. J., and Zhao, B. (2018). GRXCR2 regulates taperin localization critical for stereocilia morphology and hearing. *Cell Rep.* 25, 1268–1280.e4. doi: 10.1016/j.celrep.2018.09.063

Mieyal, J. J., Starke, D. W., Gravina, S. A., Dothey, C., and Chung, J. S. (1991a). Thioltransferase in human red blood cells: purification and properties. *Biochemistry* 30, 6088–6097. doi: 10.1021/bi00239a002

Mieyal, J. J., Starke, D. W., Gravina, S. A., and Hocevar, B. A. (1991b). Thioltransferase in human red blood cells: kinetics and equilibrium. *Biochemistry* 30, 8883–8891. doi: 10.1021/bi00100a023

Odeh, H., Hagiwara, N., Skynner, M., Mitchem, K. L., Beyer, L. A., Allen, N. D., et al. (2004). Characterization of two transgene insertional mutations at pirouette, a mouse deafness locus. *Audiol. Neurootol.* 9, 303–314. doi: 10.1159/000080701

Odeh, H., Hunker, K. L., Belyantseva, I. A., Azaiez, H., Avenarius, M. R., Zheng, L., et al. (2010). Mutations in Grxcr1 are the basis for inner ear dysfunction in the pirouette mouse. *Am. J. Hum. Genet.* 86, 148–160. doi: 10.1016/j.ajhg.2010.01.016

Pacentine, I., Chatterjee, P., and Barr-Gillespie, P. G. (2020). Stereocilia rootlets: actin-based structures that are essential for structural stability of the hair bundle. *Int. J. Mol. Sci.* 21:324. doi: 10.3390/ijms21010324

Richardson, G. P., De Monvel, J. B., and Petit, C. (2011). How the genetics of deafness illuminates auditory physiology. *Annu. Rev. Physiol.* 73, 311–334. doi: 10.1146/annurev-physiol-012110-142228

Scheffer, D. I., Shen, J., Corey, D. P., and Chen, Z. Y. (2015). Gene expression by mouse inner ear hair cells during development. *J. Neurosci.* 35, 6366–6380. doi: 10.1523/JNEUROSCI.5126-14.2015

Schraders, M., Lee, K., Oostrik, J., Huygen, P. L., Ali, G., Hoefsloot, L. H., et al. (2010). Homozygosity mapping reveals mutations of GRXCR1 as a cause of autosomal-recessive nonsyndromic hearing impairment. *Am. J. Hum. Genet.* 86, 138–147. doi: 10.1016/j.ajhg.2009.12.017

Senften, M., Schwander, M., Kazmierczak, P., Lillo, C., Shin, J. B., Hasson, T., et al. (2006). Physical and functional interaction between protocadherin 15 and myosin VIIa in mechanosensory hair cells. *J. Neurosci.* 26, 2060–2071. doi: 10.1523/JNEUROSCI.4251-05.2006

Whippo, C. W., Khurana, P., Davis, P. A., Deblasio, S. L., Desloover, D., Staiger, C. J., et al. (2011). THRUMIN1 is a light-regulated actin-bundling protein involved in chloroplast motility. *Curr. Biol.* 21, 59–64. doi: 10.1016/j.cub.2010.11.059

Wonkam, A., Lebeko, K., Mowla, S., Noubiap, J. J., Chong, M., Pare, G., et al. (2021). Whole exome sequencing reveals a biallelic frameshift mutation in GRXCR2 in hearing impairment in Cameroon. *Mol. Genet. Genomic Med.* 9:e1609. doi: 10.1002/mgg3.1609

Zhao, B., Wu, Z., and Muller, U. (2016). Murine Fam65b forms ring-like structures at the base of stereocilia critical for mechanosensory hair cell function. *eLife* 5:e14222. doi: 10.7554/eLife.14222

Conflict of Interest: The authors declare that the research was conducted in the absence of any commercial or financial relationships that could be construed as a potential conflict of interest.

frontiers
in Cellular Neuroscience

ORIGINAL RESEARCH
published: 19 August 2021
doi: 10.3389/fncel.2021.721950

Vestibular and Auditory Hair Cell Regeneration Following Targeted Ablation of Hair Cells With Diphtheria Toxin in Zebrafish

*Erin Jimenez, Claire C. Slevin, Luis Colón-Cruz and Shawn M. Burgess**

Translational and Functional Genomics Branch, National Human Genome Research Institute, National Institutes of Health, Bethesda, MD, United States

Millions of Americans experience hearing or balance disorders due to loss of hair cells in the inner ear. The hair cells are mechanosensory receptors used in the auditory and vestibular organs of all vertebrates as well as the lateral line systems of aquatic vertebrates. In zebrafish and other non-mammalian vertebrates, hair cells turnover during homeostasis and regenerate completely after being destroyed or damaged by acoustic or chemical exposure. However, in mammals, destroying or damaging hair cells results in permanent impairments to hearing or balance. We sought an improved method for studying hair cell damage and regeneration in adult aquatic vertebrates by generating a transgenic zebrafish with the capacity for targeted and inducible hair cell ablation *in vivo*. This model expresses the human diphtheria toxin receptor (hDTR) gene under the control of the *myo6b* promoter, resulting in hDTR expressed only in hair cells. Cell ablation is achieved by an intraperitoneal injection of diphtheria toxin (DT) in adult zebrafish or DT dissolved in the water for larvae. In the lateral line of 5 days post fertilization (dpf) zebrafish, ablation of hair cells by DT treatment occurred within 2 days in a dose-dependent manner. Similarly, in adult utricles and saccules, a single intraperitoneal injection of 0.05 ng DT caused complete loss of hair cells in the utricle and saccule by 5 days post-injection. Full hair cell regeneration was observed for the lateral line and the inner ear tissues. This study introduces a new method for efficient conditional hair cell ablation in adult zebrafish inner ear sensory epithelia (utricles and saccules) and demonstrates that zebrafish hair cells will regenerate *in vivo* after this treatment.

Keywords: cell ablation, hair cell regeneration, zebrafish, diphtheria toxin, inner ear, hearing, hair cell loss

Edited by:
Bernd Fritzsch,
The University of Iowa, United States

Reviewed by:
Daniela Vallone,
Karlsruhe Institute of Technology (KIT), Germany
Walace Gomes-Leal,
Federal University of Western Pará, Brazil

***Correspondence:**
Shawn M. Burgess
burgess@mail.nih.gov

Specialty section:
This article was submitted to Non-Neuronal Cells, a section of the journal Frontiers in Cellular Neuroscience

Received: 07 June 2021
Accepted: 30 July 2021
Published: 19 August 2021

Citation:
Jimenez E, Slevin CC, Colón-Cruz L and Burgess SM (2021) Vestibular and Auditory Hair Cell Regeneration Following Targeted Ablation of Hair Cells With Diphtheria Toxin in Zebrafish. Front. Cell. Neurosci. 15:721950. doi: 10.3389/fncel.2021.721950

INTRODUCTION

Loss of hearing or balance can be debilitating and imposes a significant personal, societal, and economic burden upon individuals, their families, and communities. Approximately 37.5 million Americans report some degree of hearing loss with incidences increasing with age. About 33.4 million adults reported a problem during the past 12 months with balance, unsteadiness, or blurred vision after moving their head. Hearing and balance disorders are most often attributed to loss or damage to the sensory hair cells of the auditory and vestibular organs. The hair cells are mechanosensory receptors that receive signals from our environment and transmit them to the brain. These hair cells reside in the sensory epithelia of auditory and vestibular organs in all vertebrates as well as in the lateral line systems of aquatic vertebrates (Popper and Fay, 1993; Bever and Fekete, 2002; Nicolson, 2005). In zebrafish and non-mammalian vertebrates, hair cells turnover during homeostasis and regenerate completely after being damaged or destroyed by acoustic or chemical exposure, while in mammals, destroying or damaging hair cells results in permanent impairments to hearing and balance. Mammalian hair cell regeneration has been observed but in a very limited fashion in the auditory and vestibular organs of embryonic and newborn mice and mature adults (Burns et al., 2012; Golub et al., 2012; Bucks et al., 2017). Since the majority of hearing and balance disorders in humans are due to the loss or damage of hair cells, understanding how to stimulate the hair cell regeneration process in the mammalian inner ear represents a direct solution to hearing loss or vestibular problems. The zebrafish is an excellent genetic model to understand hair cell regeneration and inner ear function. Yet, the majority of zebrafish hair cell regeneration and inner ear research to date has focused on the larval lateral line due to its relatively simple structure and accessibility. Lateral line regeneration occurs through support cell proliferation and differentiation. Lateral line hair cells frequently undergo apoptosis, constant turnover, and are renewed by peripheral supporting cell division. Research on the zebrafish lateral line has identified candidate genes, pathways, and cell populations involved in hair cell regeneration at single-cell resolution (Baek et al., 2021). Less is known about the mechanisms underlying hair cell regeneration within the inner ear sensory epithelium of zebrafish. The inner ear sensory epithelium is composed of sensory hair cells organized into "orientation groups" that are surrounded by supporting cells and are innervated by fibers from the eighth cranial nerve (Popper, 2020; Popper and Hawkins, 2021). In the adult inner ear, the sensory epithelium continues to expand for the first 10 months of life and subsequently have a low but measurable turnover of hair cells (Lombarte and Popper, 1994; Higgs et al., 2002).

To uncover detailed mechanisms of hair cell regeneration in animals that possess the capacity to regenerate hearing, frequently used models for experimental hair cell destruction in adult fish include acoustic overstimulation/sound exposure (Smith et al., 2004; Schuck and Smith, 2009; Liang et al., 2012), blast wave exposure (Wang et al., 2019), and aminoglycoside antibiotics (Song et al., 1995; Uribe et al., 2013). However, sound exposure experiments achieved $\leq$75% hair cell ablation and only in the auditory organs while blast wave exposure elicited more serious hearing loss phenotypes, but also caused brain injury with increased cell apoptosis and decreased neurogenesis. Aminoglycoside administration using a high dose of gentamicin induced only a 15% reduction in sensory hair cell loss across the entire saccule and utricle. Adult zebrafish experiments that use aminoglycosides, laser ablation, or sound exposure to induce hair cell death show that supporting cells repopulate the inner ear within 1–7 days post hair cell death (Schuck and Smith, 2009; Liang et al., 2012; Uribe et al., 2013). Despite similarities between the lateral line and inner ear sensory epithelium, such as the shared type I- and type II-like hair cell types (Song et al., 1995), it is unclear whether the adult inner ear regeneration pathways are distinct in some way from the lateral line.

In order to investigate the mechanism of hair cell regeneration in adult auditory and vestibular organs, we sought to establish a robust new model for hearing loss and regeneration research by generating a transgenic zebrafish with the capacity for targeted and inducible hair cell ablation *in vivo*. The gene encoding the human diphtheria toxin receptor (hDTR) was placed downstream of the zebrafish *myo6b* promoter whose expression is limited to differentiated hair cells in zebrafish. Since the orthologous zebrafish receptor has a significantly lower affinity to diphtheria toxin (DT) than the human one, treatment with DT resulted in hair cell specific ablation with minimal systemic side effects. Here we show that a single, low concentration, intraperitoneal injection of DT in the Tg(*myo6b*:hDTR) transgenic background caused complete loss of hair cells in the adult zebrafish utricle and saccule and that over time the hair cells regenerated. We also show that DT exposure ablated larval lateral line hair cells in a dose-dependent manner. This ablation approach could also be used in other tissues where cell-specific ablation is desirable in zebrafish.

MATERIALS AND METHODS

Experimental Animals

TAB5 wild-type (WT) zebrafish were used in this study. Fish were randomly selected and represented roughly equal numbers of males and females. All animal experiments were performed under an approved Animal Study Protocol (G-01-3) and animals were handled in compliance with the NHGRI Animal Care and Use Committee's written guidance and the Shared Zebrafish Facility User Standards and Operating Procedures.

Generation of *myo6b*-DTR Zebrafish

We targeted expression of the hDTR (heparin-binding epidermal growth factor precursor; proHB-EGF) to zebrafish hair cells by using the hair cell-specific *myo6b* promoter (Kindt et al., 2012). We generated the Tg(*myo6b*:hDTR) construct as follows. The full coding region of the hDTR gene (Genscript Clone ID OHu26607D) was PCR amplified with the following 5′ adaptor (attB) sequences to increase the specificity of cloning orientation (Forward primer adds attB1 site 5′-GGGGACAAGTTTGTACAAAAAAGCAGGCTTAACCCACTGCTTACTGGCTTA-3′ and Reverse Primer adds attB2 site and a stop codon 5′ - GGGGACCACTTTGTACAAGAAAGCTGGGTACTAACTAGAAGGCACAGTCGAGG-3′. A middle entry clone was generated by performing a BP recombination between the attB hDTR PCR product with the pDONR 221 clone. The hDTR-pDONR221 middle entry clone was verified by restriction digest and sequencing. To create a Gateway expression clone, an LR reaction was performed using a 5′ Entry *myo6b* clone (gift from Dr. Katie Kindt), hDTR middle entry clone, 3′ Entry PolyA clone, and destination vector pDestTol2CG2. The *myo6b*:hDTR construct was verified by sequencing and injected into TAB5

1-cell stage embryos with mRNA encoding the Tol2 transposase (Kawakami et al., 2000). All experimental zebrafish used in this study were heterozygous, Tg(*myo6b*:hDTR).

In situ Hybridization Chain Reaction

Three dpf embryos were fixed in a 4% formaldehyde solution and stored overnight in 100% methanol. Embryos were rehydrated with a series of graded 1 mL methanol/PBST washes (75, 50, and 25% methanol) for 5 min and then rinsed five times in PBST (0.1% Tween-20) for 5 min. Embryos were treated with 1 mL of proteinase K (2 mg/mL) for 10 min at room temperature followed by two washes with PBST without incubation. Embryos were then postfixed with a 4% formaldehyde solution for 20 min at room temperature. Following fixation, embryos were washed five times for 5 min with PBST. Embryos were hybridized with *in situ* hybridization chain reaction (HCR) probes that were purchased commercially (Molecular Instruments, Inc.) and targeted hDTR (HBEGF, NM_001945.3) and *myo6b* (NM_001004110.1). Detection and amplification was performed in accordance with the HCR v3.0 protocol for whole-mount zebrafish embryos and larvae (Choi et al., 2016). Embryos were mounted in 0.8% low melting agarose and imaged on a Zeiss LSM 880 confocal microscope. Maximum intensity projections of z-stacks were generated in Image J/Fiji software (Schindelin et al., 2012).

RNA Isolation From Adult Inner Ear Tissues

Saccules and utricles were dissected from adult WT and Tg(*myo6b*:hDTR) zebrafish and homogenized in 0.7 mL TRIzol Reagent (Thermo Fisher Scientific, United States) with a power homogenizer. RNA was isolated from aqueous phase after TRIzol/chloroform extraction and treated with DNase I. RNA was purified using the RNA Clean & Concentrator-5 (Zymo Research) and measured (Nanodrop One).

Quantitative Real-Time PCR Analysis on Adult Inner Ear Tissues

RNA was transcribed into cDNA according to manufacturer's instructions (SuperScript III RT, Thermo Fisher Scientific, United States). Quantitative Real-Time PCR Analysis (RT-qPCR) was performed in technical replicates using 1:1 cDNA in each reaction and a primer concentration of 0.5 μM. PowerUp SYBR Green Master Mix (Thermo Fisher Scientific Cat, #4344463, United States) and self-designed primers were used (Eurofins, Luxembourg). Primers were designed by using Primer3 followed by a UCSC *in silico* PCR to search the zebrafish sequence database. hDTR was amplified using the forward primer 5′-GACCCTCCCACTGTATCCAC-3′ and the reverse primer 5′-GCTCCTCCTTGTTTGGTGTG-3′. *myo6b* was amplified using the forward primer 5′-ATTAAGAGCTATCAGGGACGC-3′ and the reverse primer 5′-GCTCATCTTCAGAACCCTCAT-3′. ef1alpha was used as a housekeeping gene and was amplified using the forward primer 5′-CGACAAGAGAACCATCGAGAAGTT-3′ and the reverse primer 5′-CCAGGCGTACTTGAAGGA-3′.

Larval Zebrafish Diphtheria Toxin Treatments

Diphtheria toxin was purchased from Sigma-Aldrich (D0564). Five dpf transgenic larvae were exposed for 3–12 h in various concentrations of DT dissolved in 1X Holtfreter's medium, washed and then maintained in 1X Holtfreter's for up to 3 days. Eight dpf zebrafish were treated with 8 μM YO-PRO-1 dye (Y3603, Molecular Probes, OR, United States) dissolved in 1X Holtfreter's medium for 1 h at 28.5°C. After washing, fish were lightly anesthetized with 0.01% tricaine and placed in 96-well, glass bottomed plates for observation. Stained neuromasts in the lateral trunk region were visualized and quantified with an inverted Leica stereomicroscope using a 10X objective. For time-course experiments, larvae were returned to 1X Holtfreter's medium for recovery.

Adult Zebrafish Diphtheria Toxin Administration

Diphtheria toxin was dissolved in 1XPBS. Six to ten month-old WT (TAB5) and transgenic adult zebrafish of mixed sex were injected one time with DT into the abdominal cavity, posterior to the pelvic girdle, using a microsyringe for nanoliter injection with a 35G beveled needle. Concentration ranges from 0.01 to 50 ng per fish were tested. Before intraperitoneal injection, fish were fasted for 24 h and then lightly anesthetized with buffered MS-222. Immediately after injection, fish recovered in fresh system water and maintained off system for up to 14 days. Tank density was limited to 25 adult zebrafish in a 6 L tank. Fish were fed and water changed once daily. Health and water quality inspections were completed twice daily. Injection experiments required approximately 150 adult zebrafish total per genotype.

Histological Methods

Adult zebrafish were euthanized using buffered MS-222. The heads were dissected and fixed in 4% formaldehyde overnight at 4°C. Inner ears were dissected as previously described in Liang and Burgess (2009).

Hair Cell Labeling

Alexa Fluor 488 phalloidin was used to visualize and quantify F-actin in stereocilia of zebrafish. Utricles and saccules were dissected and stained using Alexa Fluor 488 phalloidin as previously described in Liang and Burgess (2009)Liang and Burgess (2012). Proteins were detected in whole-mount utricles and saccules using standard immunofluorescence labeling methods.

Following overnight fixation, inner ear sensory epithelia were rinsed several times in PBTX (PBS plus 0.1% Triton X-100) and blocked for 1 h in BBTX at room temperature (PBS plus 0.5% BSA, 2% NGS, and 0.1% Triton X-100). Inner ear sensory epithelia were incubated overnight at 4°C with primary antibodies. Inner ears were washed three times for 10 min in PBTX and then incubated overnight at 4°C with secondary antibodies in BBTX. After washing three times for 10 min in PBTX, inner ear sensory epithelia were incubated for 45 min at room temperature with Alexa Flour 488 phalloidin in PBS (Thermo Fisher Scientific, #A12379, United States, 1:1,000-dilution). Following three washes in PBS for 10 min, saccules (with or without lagena) and utricles were mounted in Vectashield with DAPI. Primary and secondary antibodies used include the rabbit myosin VI and myosin VIIa antibodies (Proteus Biosciences 25-6790 and 25-6791, 1:300-dilution), rabbit cleaved Caspase-3 (Cell Signaling #9661, 1:300-dilution), Alexa Fluor 568 goat anti-rabbit IgG (1:1,000-dilution).

Cellular Imaging and Analysis

Confocal images were acquired with a Zeiss LSM 880 confocal microscope. Confocal Z stacks of the entire saccule and utricle were projected into a single image to capture all phalloidin positive cells from different planes of focus for hair cell counting. Counts of phalloidin labeled hair cell bundles were obtained from preselected 50 μm × 50 μm digital boxes along the rostral-caudal axis of the saccule or the medial-striola planes of the utricle. Normal hair cells were quantified as hair cell bundles with intact stereocilia using Image J/Fiji software (Schindelin et al., 2012). Cleaved caspase-3 positive cells were counted with Image J/Fiji software from the entire saccule and utricle whole mount.

RESULTS

Generation of *myo6b*:hDTR Zebrafish

To create a model that would allow for hair cell specific ablation, we utilized the human DTR gene, which has previously been used to effectively ablate hair cells in the mouse utricle (Golub et al., 2012). In order to drive expression of hDTR only in hair cells, we use the zebrafish hair cell specific promoter *myo6b* which is expressed in auditory, vestibular, and lateral line hair cells in zebrafish (**Figure 1A**; Obholzer et al., 2008; Matern et al., 2018). The construct was cloned using the Gateway System into a Tol2 transposon vector and was injected with Tol2 transposase mRNA (Kawakami et al., 2000) into zebrafish embryos at the one-cell stage to create a stable transgenic line. Single-copy F_1 fish were identified by PCR. hDTR expression was verified by qRT-PCR in adult zebrafish inner ear auditory (saccule) and vestibular (utricle) sensory epithelia of stable transgenic lines carrying a single Tg(*myo6b*:hDTR) transgene (**Figure 1B**). Considering hDTR mRNA levels were robustly expressed in adult inner ear sensory epithelia heterozygous for the Tg(*myo6b*:hDTR) allele, we reasoned that heterozygous expression of the transgene would suffice for the hair cell ablation response to DT. Therefore, all hair cell ablation experiments were performed on animals carrying a single Tg(*myo6b*:hDTR) transgene in larvae and adult zebrafish. To confirm Tg(*myo6b*:hDTR) was expressed in hair cells, we performed HCR on WT and Tg(*myo6b*:hDTR) 3 dpf embryos using a probe targeting the hDTR. As expected, the hDTR fluorescent signal was present in lateral line hair cells and in the anterior macula of Tg(*myo6b*:hDTR) fish, but absent in WT controls. As a control, we simultaneously hybridized and detected a probe for *myo6b* in lateral line hair cells and in the anterior macula of the inner ear of Tg(*myo6b*:hDTR) and WT fish (**Figures 1C, D**). All hair cells can be seen expressing both genes simultaneously.

Diphtheria Toxin Induced Hair Cell Death and Regeneration in the Larval Lateral Line

Figure 2A shows the experimental regimen for the larval neuromast hair cell ablation studies. To determine whether DT was able to ablate hair cells of the lateral line of zebrafish expressing hDTR in hair cells, we performed a dose-response assay using 5 dpf larvae that were WT or heterozygous for the Tg(*myo6b*:hDTR) allele. We treated 5 dpf larvae with concentrations of dissolved DT ranging from 0.5 to 1.5 μg/mL and continuous exposure times ranging from 3 to 12 h. After rinsing the larvae three times in fresh medium, the number of YO-PRO-1 labeled cells in each of the four identified neuromasts (P1, P2, P3, and P4) was determined for the different exposure concentrations and timepoints following DT treatment. YO-PRO-1 labeled hair cell loss and recovery was analyzed at 0, 24, 48, and 72 h post-DT treatment. Hair cells were assessed by fluorescence microscopy and counted for approximately eight fish per group.

Diphtheria toxin had no effect on YO-PRO-1 staining in WT 5 dpf zebrafish at all concentrations and durations examined (**Figure 2B**). However, DT reduced the number of YO-PRO-1 labeled neuromast hair cells in 5 dpf Tg(*myo6b*:hDTR) fish in a dose-dependent manner with no general toxicity or mortality to the larvae at any of the doses or exposure times. At the higher exposure concentrations and longer exposure times, the YO-PRO-1 staining in the neuromasts was absent (**Figure 2B**). We observe a delayed onset of death and cumulative effect of DT on hair cells which is likely a result of diphtheria toxin's mechanism of action. The dose and time of exposure influenced the amount of hair cell ablation, but synchronous hair cell loss in Tg(*myo6b*:hDTR) continued even after withdrawal of DT. Lower doses and longer exposure times were as effective at ablating hair cells as high doses for shorter times. For example, at 3 h incubation with 1.5 μg/mL of DT (the highest concentration of toxin tested on larvae), hair cells are progressively lost until 24 h post treatment, but no significant hair cell loss is observed immediately after treatment at 0 h (**Figure 2B**). These data show a relationship between DT concentration, exposure time, and hair cell death.

Lateral line hair cells regenerate following acute chemical injury. In Tg(*myo6b*:hDTR) larvae, hair cell regeneration (defined as recovery in YO-PRO-1 labeling) was evident within 2 days post DT exposure for all concentrations and exposure durations tested (**Figure 2B**). At 72 h following DT exposure, the mean number of hair cells per neuromast was not significantly different from the unexposed larvae, indicating that recovery was complete at intermediate concentrations (0.5 and 1 μg/mL). Larvae exposed to DT at the highest (1.5 μg/mL) and longest duration (12 h) showed only partial hair cell regeneration by 72 h post-DT.

Figure 2C shows a representative WT zebrafish neuromast 24 h post exposure to 1 μg/mL of DT for 6 h and demonstrates individual hair cells in each of the four neuromasts (P1, P2,

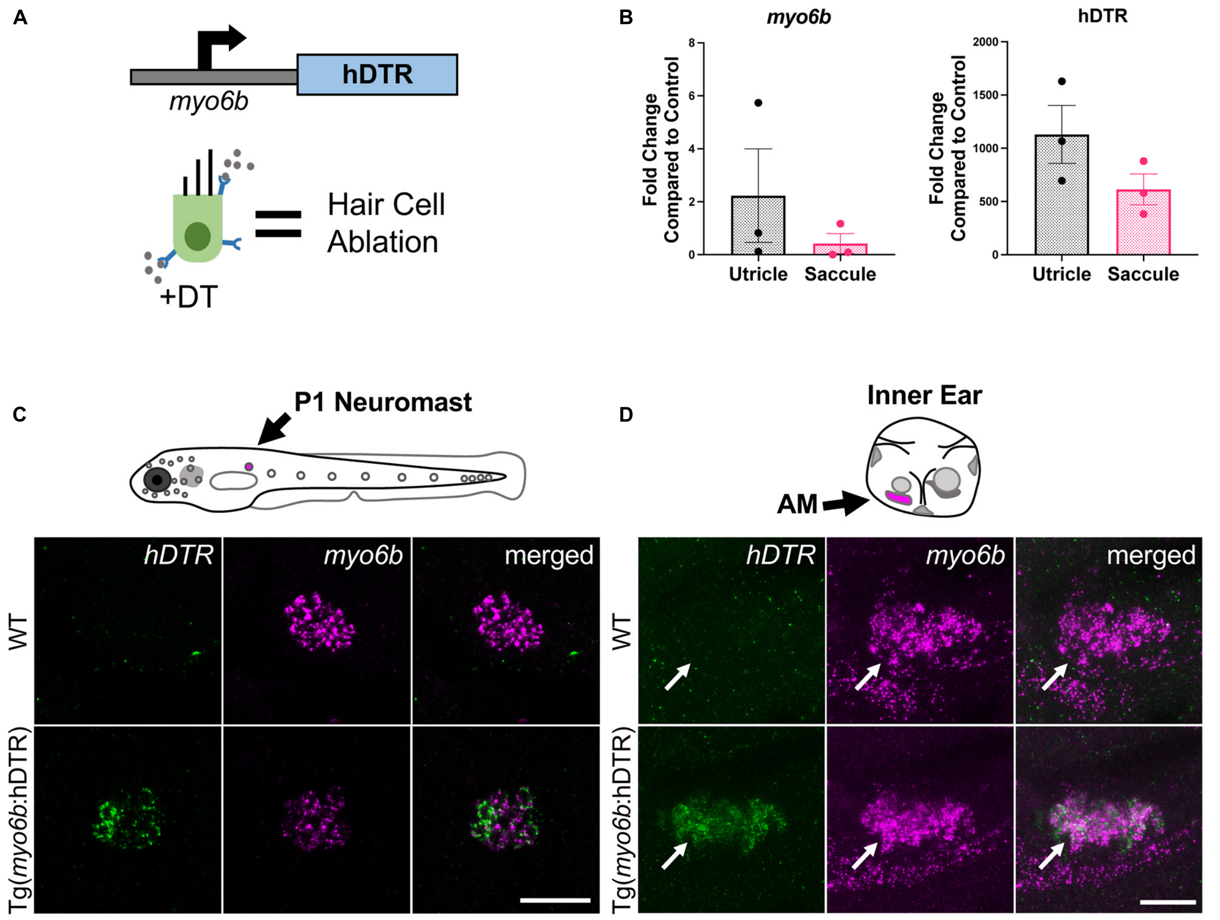

FIGURE 1 | The Tg(*myo6b*:hDTR) zebrafish. **(A)** Schematic representation of the human diphtheria toxin receptor (hDTR) construct driven by the hair cell-specific *myo6b* promoter and representation of the hair cell-specific ablation approach. Diphtheria toxin (DT) is internalized in cells specifically expressing the human version of the DT receptor, triggering cell death. **(B)** qRT-PCR analysis on untreated Tg(*myo6b*:hDTR) zebrafish saccule and utricle showing expression of *hDTR* and *myo6b* relative to wild-type (WT) animals. The values are represented as the mean ± SEM from three independent samples. **(C)** Schematic depicts a lateral view of a whole zebrafish larva with neuromasts (gray circles). The P1 neuromast examined for imaging is indicated by magenta fill. *In situ* HCR using probes targeting *hDTR* and *myo6b* in hair cells of a single P1 neuromast of 3 dpf WT and Tg(*myo6b*:hDTR) embryos is shown. Brightness and contrast adjusted 50 and 25%, respectively. Scale bar 20 μm. **(D)** Schematic depicts the left ear of a larval zebrafish with anterior macula indicated by magenta fill. Lateral views of inner ears are shown following HCR *in situ* with probes targeting *hDTR* and *myo6b* in 3 dpf WT and Tg(*myo6b*:hDTR) embryos. Brightness and contrast adjusted 65 and 35%, respectively. Scale bar 20 μm.

P3, and P4) brightly stained with YO-PRO-1. By comparison, Tg(*myo6b*:hDTR) larvae exposed to 1 μg/mL of DT for 6 h showed a clear reduction in the number of YO-PRO-1 labeled hair cells in all four neuromasts 24 h post exposure. **Supplementary Figure 1** shows the progression of cell death from 0 to 24 h post DT treatment (A, B) and the subsequent hair cell regeneration (C).

Diphtheria Toxin Induced Hair Cell Death and Regeneration in the Adult Inner Ear

Using fluorescently-tagged phalloidin to visualize adult inner ear hair cell bundles and myosin VI/VIIa antibodies for hair cell bodies, we assessed auditory (saccule) and vestibular (utricle) hair cells in untreated adult zebrafish that were WT or heterozygous for the Tg(*myo6b*:hDTR) allele (**Supplementary Figure 2**). Fluorescent phalloidin, a highly specific F-actin stain, was used to visualize hair cells (**Supplementary Figure 2**, green channel). Hair cell bodies were labeled with myosin VI/VIIa (**Supplementary Figure 2**, red channel), which labels the cytoplasm of hair cells to confirm cell death (as opposed to hair cell bundle damage). **Figure 3** illustrates the overall appearance of a phalloidin stained utricle and saccule (**Figure 3B**). The average hair cell densities of the untreated Tg(*myo6b*:hDTR) utricle and saccule macule are 85 and 161 per 2.5 mm^2 area, respectively. Myosin VI/VIIa was present in the cytoplasm of all hair cells examined in untreated WT, DT treated WT, and untreated DTR fish (**Supplementary Figure 2**, red channel). The pattern of phalloidin and myosin VI/VIIa labeling in the adult inner ear was consistent in treated and untreated WT controls and untreated Tg(*myo6b*:hDTR) sensory epithelia, although there was some variability in fluorescence intensity

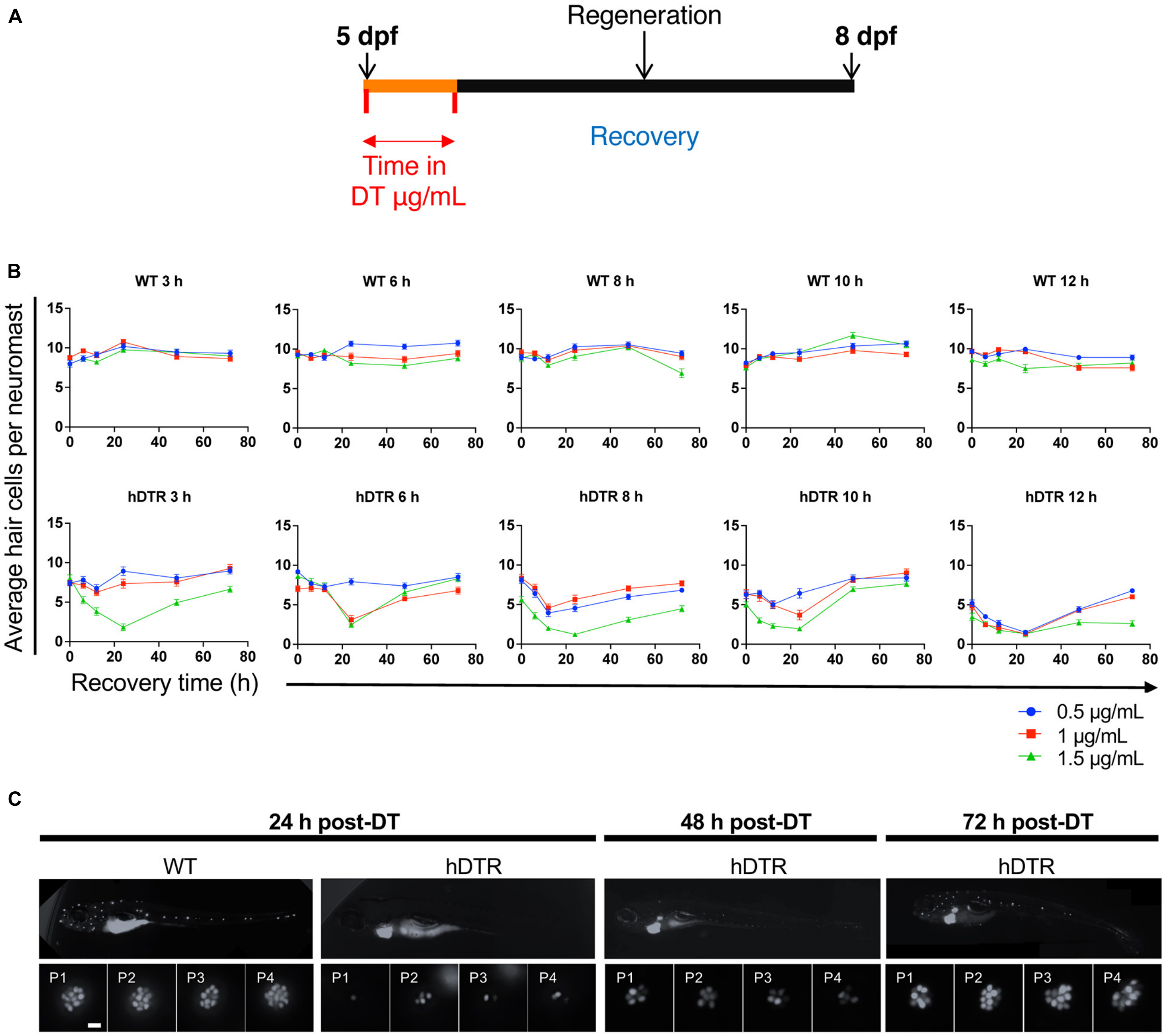

FIGURE 2 | Tg(*myo6b*:hDTR) larval zebrafish show hair cell loss and regeneration in lateral line neuromasts after *in vivo* DT treatment. **(A)** Schematic representation of the larval DT exposure treatment. **(B)** Wild-type (WT) and Tg(*myo6b*:hDTR) (hDTR) larvae were exposed to three concentrations of DT (0.5, 1, and 1.5 µg/mL) for various durations (3, 6, 8, 10, and 12 h). Neuromast viability was monitored daily by YO-PRO-1 labeling 0 to 72 h post-incubation. Shown is the quantification of YO-PRO-1 labeled hair cells. The values are represented as the mean ± SEM from eight fish. **(C)** Regeneration time-course showing P1–P4 over three days of recovery. Larvae were exposed to 1 µg/mL of DT for 6 h. Scale bar 100 µm.

that was not quantified (**Figure 4** red channel; **Supplementary Figure 2**; Coffin et al., 2007). The number of hair cells per utricle and saccule did not differ significantly between these two groups and no differences were observed with respect to hair cell appearance. These observations suggested that inner ear hair cell development and maintenance were not affected in adult Tg(*myo6b*:hDTR) zebrafish.

In order to determine an appropriate dose of DT to use for downstream ablation experiments in adult zebrafish, we evaluated the effect of various concentrations of injected DT (ranging from 0.01 to 10 ng per fish) on adult fish that were WT or heterozygous for the Tg(*myo6b*:hDTR) allele. No to minimal defects in swimming behaviors were observed in Tg(*myo6b*:hDTR) fish injected with 0.01–0.05 ng of DT. At concentrations above 1 ng per fish (such as 10 ng), Tg(*myo6b*:hDTR) fish exhibited consistent swimming defects that come out most strongly when the water was agitated (**Supplementary Video 1**). The behavior of injected Tg(*myo6b*:hDTR) fish with 10 ng of DT consisted of somersaulting and random lateral looping (**Figure 3A**). Tg(*myo6b*:hDTR) injected fish mimic the swimming behavior of fish under microgravity conditions (Von Baumgarten et al., 1975), fish that have undergone laceration or removal of the utricle (Pfeiffer, 1964), and the

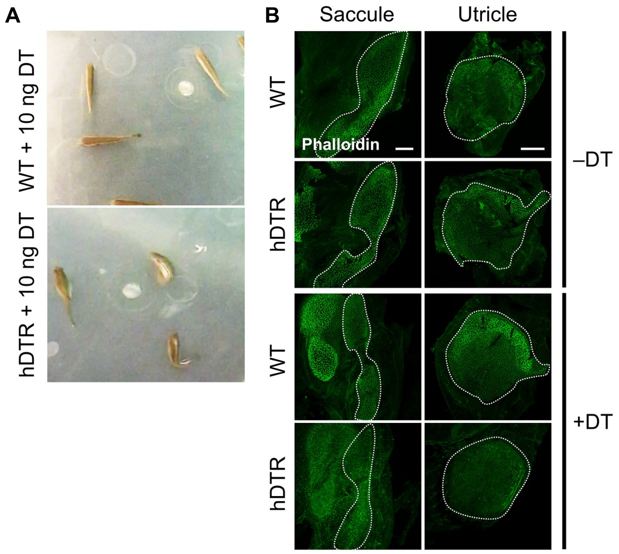

FIGURE 3 | Adult Tg(*myo6b*:hDTR) injected fish exhibit spatial disorientation and impaired balance. **(A)** Injected WT fish (WT), **(top)** and Tg(*myo6b*:hDTR) (hDTR), **(bottom)** with 10 ng of DT 3 days-post injection. **(B)** Saccule and utricle from untreated (–DT) or treated (+DT) WT and Tg(*myo6b*:hDTR) fish. Saccule and utricle from treated (+DT) WT and Tg(*myo6b*:hDTR) fish were isolated 3 days post-DT. Scale bar 100 μm.

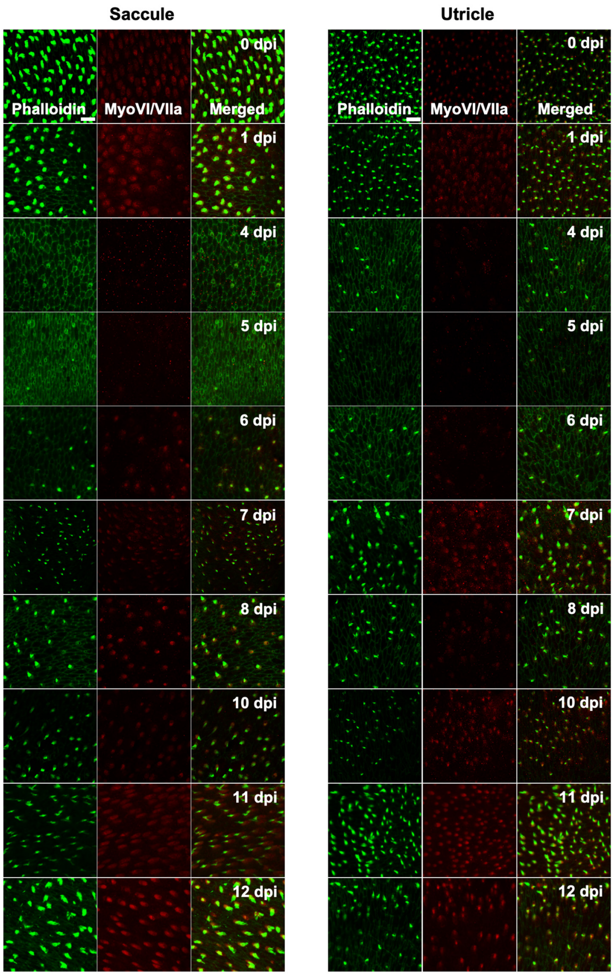

FIGURE 4 | Tg(*myo6b*:hDTR) adult zebrafish hair cell loss and regeneration in the inner ear after DT treatment. Saccule and utricle were isolated at specified timepoints following DT administration in Tg(*myo6b*:hDTR) fish. Close examination of hair cells with phalloidin (green channel) and hair cell bodies with anti-myosin VI/VIIa (red channel). Scale bar 100 μm. For qualitative purposes, brightness was increased 10% and contrast by 20% across all images.

sputnik and *orbiter* adult circler mutants with mutations affecting vestibular function (Nicolson et al., 1998). The onset of swimming defects correlated to when the hair cells in the inner ear were maximally ablated (**Figure 3**). Similarly, recovery in swimming behavior correlated to when the hair cells in the inner ear regenerated.

We characterized the time-course of hair cell loss and the minimum dose capable of completely ablating hair cells to help maximize animal viability and reduce excess stress. Similar to our observations in larval zebrafish treated with DT, we observed a delay and cumulative effect of DT on hair cell death in adult zebrafish. The dose of exposure influenced when hair cell loss was first observed and the time it took for hair cells to return. We determined a low DT dose of 0.05 ng per fish was sufficient for nearly complete hair cell ablation throughout the utricle, saccule and even lagena followed by hair cell recovery within a 13-day window, although we were only able to detect very subtle behavioral phenotypes at this concentration, suggesting looping behaviors may require complete loss of hair cell function to be observed.

Adult fish received a single intraperitoneal injection of 1 μL of 0.05 ng DT. Immediately following injection, fish were allowed to recover for up to 14 days in static tanks. Adult inner ears (utricle and saccule) were harvested following timepoints ranging from 0 to 13 days post injection. DT did not affect hair cells in injected WT zebrafish at any time point examined. In contrast, significant hair cell loss was observed between 4 and 5 days after DT treatment in adult Tg(*myo6b*:hDTR) zebrafish (**Figure 4**). We confirmed elimination of hair cells (as opposed to hair cell bundle damage) by co-labeling sensory epithelia with phalloidin and myosin VI/VIIa antibodies. Phalloidin staining revealed structural changes that occurred at the epithelial surface 4 and 5 days after DT treatment such as putative lesions and bundle-less cuticular plates in the region of stereociliary loss over the time course of hair cell death. The lack of phalloidin in stereocilia and bundle-less cuticular plates correlated with the absence of myosin VI/VIIa labeling (**Figure 4**). We conclude that complete hair cell loss is achieved 5 days post-DT treatment in adult Tg(*myo6b*:hDTR) zebrafish.

Hair cells re-emerged as indicated by the appearance of short phalloidin positive hair cell bundles and myosin VI/VIIa positive cell bodies by day 6 post-DT treatment. On day 7 post-DT, saccules and utricles exhibited an increase in short, immature-like bundles, and an increase in hair cell bundle density. The increase in phalloidin labeled stereocilia corresponded to an increase in myosin VI/VIIa positive cell bodies (**Figure 4**). The pattern of hair cell bundle density and intensity using phalloidin labeling remained consistent after day 8 in the saccule and utricle, although there was some variability in fluorescence intensity using myosin VI/VIIa labeling. Quantifying the hair cell density of randomly selected regions of the utricle and saccule, we could see that the hair cells return to control levels by 13 days post-DT (**Figure 5**).

Hair Cell Apoptosis Is Triggered by DT Treatment in hDTR Transgenic Fish

Apoptosis results in cleavage of caspase-3. Therefore, to test whether hair cells in treated Tg(*myo6b*:hDTR) fish were undergoing apoptosis, we stained for cleaved caspase-3 on DT treated fish. In the utricle and saccule of DT treated Tg(*myo6b*:hDTR) fish, we observed cleaved caspase-3-positive cells 1 day post-DT and the number of cleaved caspase-3 positive cells significantly increased by day 2 post-DT (**Figure 6**). The number of cleaved caspase-3 positive cells declined on day 3 post-DT and each day thereafter examined (**Figure 6B**). The number of caspase positive cells did appear to be lower than the number of hair cells ablated so we conclude that at least some but maybe not all of the hair cell death is due to apoptosis and cell death is initiated as early as 24 h post DT treatment.

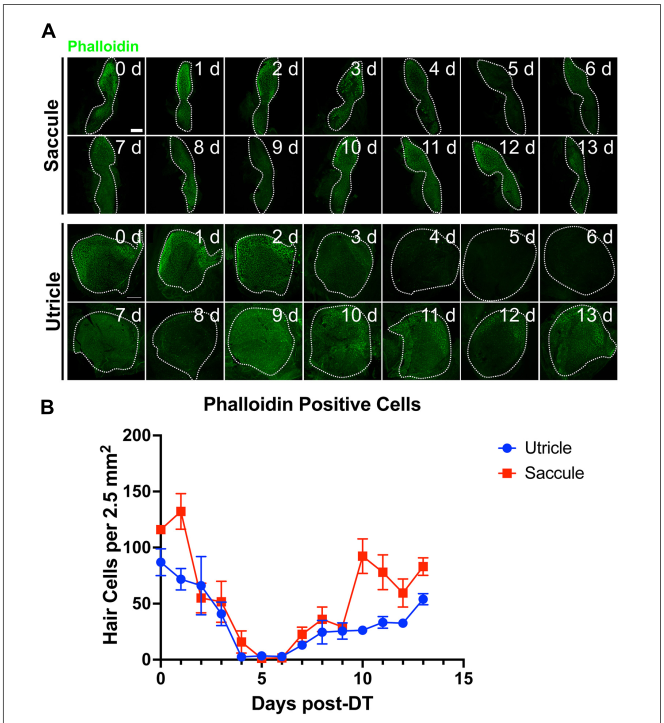

FIGURE 5 | Tg(*myo6b*:hDTR) adult zebrafish hair cell loss and regeneration in the inner ear after DT treatment. **(A)** Tg(*myo6b*:hDTR) saccule and utricle used for quantification were isolated at specified timepoints following DT administration and hair cells were labeled with phalloidin (green channel). Scale bar 100 μm. **(B)** Quantification of phalloidin positive hair cell number after DT injection. Error bars demonstrate the mean ± SEM.

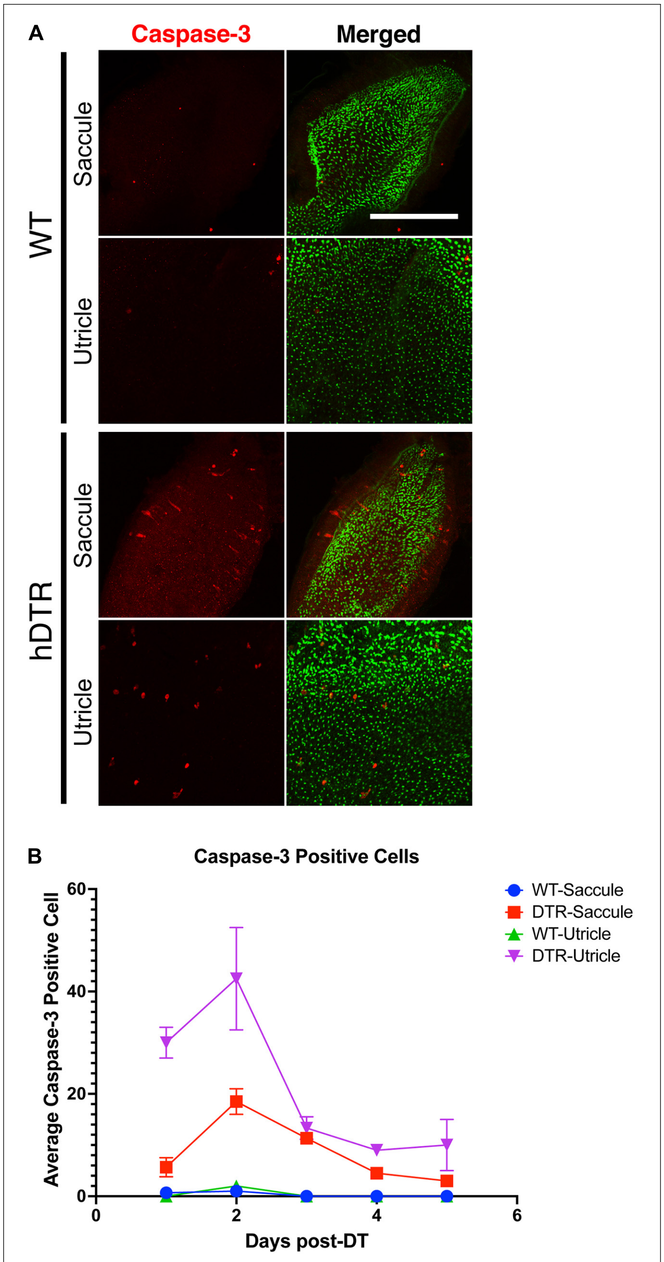

FIGURE 6 | Diphtheria toxin induced hair cell death is primarily due to apoptosis. **(A)** Saccule and utricle from WT and Tg(*myo6b*:hDTR) (hDTR) inner ear tissues 2 days post-DT. Hair cells are labeled with phalloidin (green channel) and cleaved caspase-3 (red channel) positive cells were detected 2 days post-DT. **(B)** Quantification of cleaved caspase-3 positive cells in saccule and utricle dissected on days 1–5 following DT injection. Scale bar 100 μm. For qualitative purposes, brightness and contrast increased by 20%.

DISCUSSION

Hair Cell Regeneration

Efforts have been made to manipulate a small number of factors in the mammalian inner ear to reactivate hair cell regeneration. There has been some limited success inducing hair cell differentiation in a mature mammalian auditory organ by overexpressing the Atoh1 transcription factor an inducer of hair cell fate in all vertebrates (Groves et al., 2013). However, more work is required to identify if there are other factors involved in hair cell regeneration. Our understanding and potentially rescuing hair cell regeneration in mammals requires a comprehensive investigation of how regeneration successfully occurs in other vertebrates, such as the zebrafish. A long term motivation is to investigate the transcriptomic and epigenomic regulation of zebrafish inner ear hair cell regeneration with spatio-temporal resolution. Results from these studies could shed light on the gene regulatory responses that occur as a consequence of hair cell regeneration and provide insight on how supporting cells contribute new hair cells in an adult vertebrate inner ear.

A New Model of Hair Cell Loss

We show that a stable zebrafish line expressing the hDTR in a tissue-specific fashion, can be successfully applied to the analysis of hair cell regeneration in the zebrafish adult inner ear and larval lateral line systems. Environmental exposure of larvae to DT or adult injection of DT was utilized to achieve hair cell specific ablation in zebrafish expressing hDTR under the control of the *myo6b* promoter. With this technique, we observed extensive, targeted cell death after a delay, which was likely due to the mechanism of action for DT. DT binds to the toxin receptor, it internalizes, and the catalytic A subunit acts as an inhibitor of protein synthesis and arrests RNA synthesis, which ultimately leads to apoptosis or cell death (Collier, 1975). A potential drawback of the system is the extreme potency of the toxin which could cause "off-site injuries" by binding to the lower affinity endogenous receptors. Studies which express diphtheria toxin A fragment (DTA) in zebrafish embryos in the retina (Kurita et al., 2003) or in the germline (Slanchev et al., 2005) resulted in undesired ablation of other cells and even death of the organism due to DT toxicity. However, we find that cell specific expression of the hDTR in hair cells using the *myo6b* promoter causes no morphological defects in comparison to WT fish. Moreover, DT can be administered at low enough doses to cause cell specific ablation with limited to no toxicity in other cells and no noticeable toxicity to the animal.

Comparison With Other Adult Zebrafish Models for Hair Cell Ablation

At least three additional zebrafish models have been used to ablate hair cells in the adult inner ear. Immediately following cessation of sound exposure (to 100 Hz pure tone at 179 dB re 1 μPa RMS) for 36 h results in a 75% reduction in stereocilia density of the auditory hair cells in saccules. These sound exposure experiments significantly decrease hair cells to 43% in the caudal region and 75% of the total distance from the rostral tip. Specifically, sound exposure produces hair bundle loss only in the caudal region of the saccule and then 2 days later noticeable bundle loss is seen in the central portion of the rostral region (25%) 0 and 2 days post sound exposure (Schuck and Smith, 2009). Similar to our observations using DTR-fish treated with DT, auditory hair cell regeneration was observed 2 days post sound exposure. Aminoglycoside administration using a single intraperitoneal injection of a high dose of gentamicin induced a noticeable but limited reduction in sensory hair cell loss across the entire saccule and utricle, accompanied by shifts in auditory thresholds (Uribe et al., 2013). It was not shown whether hair cells replenished following gentamicin exposure. In contrast to both acoustic and ototoxic exposure, we observed near complete hair cell loss throughout the auditory and vestibular sensory epithelia followed by regeneration of hair cells. The Tg(*myo6b*:hDTR) zebrafish and DT system represents an ideal method for hair cell ablation in a regeneration study as the method induces synchronous destruction of all hair cells with negligible effects on neighboring inner ear cells. Moreover, this system is mild enough to allow subsequent hair cell regeneration. It was interesting to note that while 0.05 ng DT injections ablated essentially all but a few residual hair cells, we typically did not observe significant circling behavior in those fish. It suggests to us that overt vestibular behaviors are perhaps only observable in the most severe cases of functional hair cell deficiency in zebrafish.

Most hair cell regeneration studies have been implemented using the larval lateral line systems. However, the larval lateral line system and inner ear hair cells are not identical and examination of adult inner ears could have significant differences relevant to potential therapeutic treatments. The Tg(*myo6b*:hDTR) fish will enable examination of adult behaviors associated with auditory dysfunction and equilibrium orientation defects. DT treated Tg(*myo6b*:hDTR) adult zebrafish have defects similar to those seen in human hereditary and environmentally induced forms of deafness which may serve as a model for such disorders since zebrafish are accessible to a wide range of analyses. This method could facilitate uncovering roles of specific tissues during development, homeostasis, and aging of the ear. Analysis of the recovery after cell ablation may also reveal novel cellular and molecular mechanisms underlying the regenerative processes, thus bringing insights to the field of regenerative medicine.

DATA AVAILABILITY STATEMENT

The original contributions presented in the study are included in the article/**Supplementary Material**, further inquiries can be directed to the corresponding author.

ETHICS STATEMENT

The animal study was reviewed and approved by the National Human Genome Research Animal Care and Use Committee.

AUTHOR CONTRIBUTIONS

EJ and SB designed the experiments and wrote the manuscript. EJ, CS, and LC-C performed the experiments. All authors contributed to the article and approved the submitted version.

FUNDING

This research was supported by the Intramural Research Program of the National Human Genome Research Institute (ZIAHG200386-06).

ACKNOWLEDGMENTS

We thank Katie Kindt for generously donating the 5′ entry *myo6b* clone; Blake Carrington and Raman Sood for assistance with cell injections; Stephen Frederickson and Tannia Clark, and Charles River for zebrafish care; and the members of the Burgess laboratory for helpful discussion.

SUPPLEMENTARY MATERIAL

The Supplementary Material for this article can be found online at: https://www.frontiersin.org/articles/10.3389/fncel.2021.721950/full#supplementary-material

REFERENCES

Baek, S., Tran, N. T. T., Diaz, D. C., Tsai, Y.-Y., Acedo, J. N., Lush, M. E., et al. (2021). High-resolution single cell transcriptome analysis of zebrafish sensory hair cell regeneration. *bioRxiv* [Preprint]. doi: 10.1101/2021.07.15.452338

Bever, M. M., and Fekete, D. M. (2002). Atlas of the developing inner ear in zebrafish. *Dev. Dyn.* 223, 536–543. doi: 10.1002/dvdy.10062

Bucks, S. A., Cox, B. C., Vlosich, B. A., Manning, J. P., Nguyen, T. B., and Stone, J. S. (2017). Supporting cells remove and replace sensory receptor hair cells in a balance organ of adult mice. *Elife* 6:e18128. doi: 10.7554/eLife.18128

Burns, J. C., Cox, B. C., Thiede, B. R., Zuo, J., and Corwin, J. T. (2012). In vivo proliferative regeneration of balance hair cells in newborn mice. *J. Neurosci.* 32, 6570–6577. doi: 10.1523/JNEUROSCI.6274-11.2012

Choi, H. M., Calvert, C. R., Husain, N., Huss, D., Barsi, J. C., Deverman, B. E., et al. (2016). Mapping a multiplexed zoo of mRNA expression. *Development* 143, 3632–3637. doi: 10.1242/dev.140137

Coffin, A. B., Dabdoub, A., Kelley, M. W., and Popper, A. N. (2007). Myosin VI and VIIa distribution among inner ear epithelia in diverse fishes. *Hear. Res.* 224, 15–26. doi: 10.1016/j.heares.2006.11.004

Collier, R. J. (1975). Diphtheria toxin: mode of action and structure. *Bacteriol. Rev.* 39, 54–85. doi: 10.1128/br.39.1.54-85.1975

Golub, J. S., Tong, L., Ngyuen, T. B., Hume, C. R., Palmiter, R. D., Rubel, E. W., et al. (2012). Hair cell replacement in adult mouse utricles after targeted ablation of hair cells with diphtheria toxin. *J. Neurosci.* 32, 15093–15105. doi: 10.1523/JNEUROSCI.1709-12.2012

Groves, A. K., Zhang, K. D., and Fekete, D. M. (2013). The genetics of hair cell development and regeneration. *Annu. Rev. Neurosci.* 8, 361–381. doi: 10.1146/annurev-neuro-062012-170309

Higgs, D. M., Souza, M. J., Wilkins, H. R., Presson, J. C., and Popper, A. N. (2002). Age- and size-related changes in the inner ear and hearing ability of the adult zebrafish (Danio rerio). *J. Assoc. Res. Otolaryngol.* 3, 174–184. doi: 10.1007/s101620020035

Kawakami, K., Shima, A., and Kawakami, N. (2000). Identification of a functional transposase of the Tol2 element, an Ac-like element from the Japanese medaka fish, and its transposition in the zebrafish germ lineage. *Proc. Natl. Acad. Sci. U.S.A.* 97, 11403–11408. doi: 10.1073/pnas.97.21.11403

Kindt, K. S., Finch, G., and Nicolson, T. (2012). Kinocilia mediate mechanosensitivity in developing zebrafish hair cells. *Dev. Cell* 23, 329–341. doi: 10.1016/j.devcel.2012.05.022

Kurita, R., Sagara, H., Aoki, Y., Link, B. A., Arai, K., and Watanabe, S. (2003). Suppression of lens growth by alphaA-crystallin promoter-driven expression of diphtheria toxin results in disruption of retinal cell organization in zebrafish. *Dev. Biol.* 255, 113–127. doi: 10.1016/s0012-1606(02)00079-9

Liang, J., and Burgess, S. M. (2009). Gross and fine dissection of inner ear sensory epithelia in adult zebrafish (Danio rerio). *J. Vis. Exp.* 27:1211. doi: 10.3791/1211

Liang, J., Wang, D., Renaud, G., Wolfsberg, T. G., Wilson, A. F., and Burgess, S. M. (2012). The stat3/socs3a pathway is a key regulator of hair cell regeneration in zebrafish. [corrected]. *J. Neurosci.* 32, 10662–10673. doi: 10.1523/JNEUROSCI.5785-10.2012

Lombarte, A., and Popper, A. N. (1994). Quantitative analyses of postembryonic hair cell addition in the otolithic endorgans of the inner ear of the European hake, *Merluccius merluccius* (Gadiformes, Teleostei). *J. Comp. Neurol.* 345, 419–428. doi: 10.1002/cne.903450308

Matern, M. S., Beirl, A., Ogawa, Y., Song, Y., Paladugu, N., Kindt, K. S., et al. (2018). Transcriptomic profiling of zebrafish hair cells using ribotag. *Front. Cell Dev. Biol.* 6:47. doi: 10.3389/fcell.2018.00047

Nicolson, T. (2005). The genetics of hearing and balance in zebrafish. *Annu. Rev. Genet.* 39, 9–22. doi: 10.1146/annurev.genet.39.073003.105049

Nicolson, T., Rusch, A., Friedrich, R. W., Granato, M., Ruppersberg, J. P., and Nusslein-Volhard, C. (1998). Genetic analysis of vertebrate sensory hair cell mechanosensation: the zebrafish circler mutants. *Neuron* 20, 271–283. doi: 10.1016/s0896-6273(00)80455-9

Obholzer, N., Wolfson, S., Trapani, J. G., Mo, W., Nechiporuk, A., Busch-Nentwich, E., et al. (2008). Vesicular glutamate transporter 3 is required for synaptic transmission in zebrafish hair cells. *J. Neurosci.* 28, 2110–2118. doi: 10.1523/JNEUROSCI.5230-07.2008

Pfeiffer, W. (1964). "Equilibrium orientation in fish1 1in memoriam Prof. Dr. Erich von Hoist," in *International Review of General and Experimental Zoology*, Vol. 1, eds W. J. L. Felts and R. J. Harrison (Amsterdam: Elsevier), 77–111. doi: 10.1016/B978-1-4831-9977-1.50008-0

Popper, A. N. (2020). Colleagues as friends. *ICES J. Mar. Sci.* 77, 2033–2042. doi: 10.1093/icesjms/fsaa097

Popper, A. N., and Fay, R. R. (1993). Sound detection and processing by fish: critical review and major research questions. *Brain Behav. Evol.* 41, 14–38. doi: 10.1159/000113821

Popper, A. N., and Hawkins, A. D. (2021). "Hearing," in *The Physiology of Fishes*, 5th Edn, eds S. Currie and D. H. Evans (Boca Raton, FL: CRC Press), 143–157. doi: 10.1201/9781003036401

Schindelin, J., Arganda-Carreras, I., Frise, E., Kaynig, V., Longair, M., Pietzsch, T., et al. (2012). Fiji: an open-source platform for biological-image analysis. *Nat. Methods* 9, 676–682. doi: 10.1038/nmeth.2019

Schuck, J. B., and Smith, M. E. (2009). Cell proliferation follows acoustically-induced hair cell bundle loss in the zebrafish saccule. *Hear. Res.* 253, 67–76. doi: 10.1016/j.heares.2009.03.008

Slanchev, K., Stebler, J., de la Cueva-Mendez, G., and Raz, E. (2005). Development without germ cells: the role of the germ line in zebrafish sex differentiation. *Proc. Natl. Acad. Sci. U.S.A.* 102, 4074–4079. doi: 10.1073/pnas.0407475102

Smith, M. E., Kane, A. S., and Popper, A. N. (2004). Noise-induced stress response and hearing loss in goldfish (*Carassius auratus*). *J. Exp. Biol.* 207(Pt 3), 427–435. doi: 10.1242/jeb.00755

Song, J., Yan, H. Y., and Popper, A. N. (1995). Damage and recovery of hair cells in fish canal (but not superficial) neuromasts after gentamicin exposure. *Hear. Res.* 91, 63–71. doi: 10.1016/0378-5955(95)00170-0

Uribe, P. M., Sun, H., Wang, K., Asuncion, J. D., Wang, Q., Chen, C. W., et al. (2013). Aminoglycoside-induced hair cell death of inner ear organs causes functional deficits in adult zebrafish (*Danio rerio*). *PLoS One* 8:e58755. doi: 10.1371/journal.pone.0058755

Von Baumgarten, R. J., Baldrighi, G., Shillinger, G. L. Jr., Harth, O., and Thuemler, R. (1975). Vestibular function in the space environment. *Acta Astronaut.* 2, 49–58. doi: 10.1016/0094-5765(75)90042-9

Wang, J., Yan, Z., Xing, Y., Lai, K., Wang, J., Yu, D., et al. (2019). A zebrafish model for hearing loss and regeneration induced by blast wave. *J. BioX Res.* 2, 87–97. doi: 10.1097/jbr.0000000000000033

Conflict of Interest: The authors declare that the research was conducted in the absence of any commercial or financial relationships that could be construed as a potential conflict of interest.

frontiers
in Cellular Neuroscience

ORIGINAL RESEARCH
published: 25 August 2021
doi: 10.3389/fncel.2021.713651

Deletion of *C1ql1* Causes Hearing Loss and Abnormal Auditory Nerve Fibers in the Mouse Cochlea

Yue Qi[1], Wei Xiong[1], Shukui Yu[1], Zhengde Du[1], Tengfei Qu[1], Lu He[1], Wei Wei[2], Lingjun Zhang[1], Ke Liu[1], Yi Li[3], David Z. He[4]* and Shusheng Gong[1]*

[1] Department of Otolaryngology Head and Neck Surgery, Beijing Friendship Hospital, Capital Medical University, Beijing, China, [2] Department of Otology, Sheng Jing Hospital, China Medical University, Shenyang, China, [3] Department of Otolaryngology Head and Neck Surgery, Beijing Tongren Hospital, Capital Medical University, Beijing, China, [4] Department of Biomedical Sciences, Creighton University, Omaha, NE, United States

Edited by:
Arturo Ortega,
Departamento de Toxicologia, Centro de Investigación y de Estudios Avanzados del Instituto Politécnico Nacional, Mexico

Reviewed by:
Hong-Bo Zhao,
University of Kentucky, United States
Rosario Vega,
Meritorious Autonomous University of Puebla, Mexico

***Correspondence:**
David Z. He
hed@creighton.edu
Shusheng Gong
gongss1962@163.com

Specialty section:
This article was submitted to Non-Neuronal Cells, a section of the journal Frontiers in Cellular Neuroscience

Received: 23 May 2021
Accepted: 21 July 2021
Published: 25 August 2021

Citation:
Qi Y, Xiong W, Yu S, Du Z, Qu T, He L, Wei W, Zhang L, Liu K, Li Y, He DZ and Gong S (2021) Deletion of C1ql1 Causes Hearing Loss and Abnormal Auditory Nerve Fibers in the Mouse Cochlea. Front. Cell. Neurosci. 15:713651. doi: 10.3389/fncel.2021.713651

Complement C1q Like 1 (C1QL1), a secreted component of C1Q-related protein, is known to play an important role in synaptic maturation, regulation, and maintenance in the central nervous system. *C1ql1* is expressed in adult cochlear inner and outer hair cells (IHCs and OHCs) with preferential expression in OHCs. We generated *C1ql1* null mice to examine the role of C1QL1 in the auditory periphery. *C1ql1*-null mice exhibited progressive hearing loss with elevated thresholds of auditory brainstem response and distortion product otoacoustic emission. Confocal microscopy showed that the number of nerve fibers innervating both IHCs and OHCs was significantly reduced. However, spiral ganglion neurons appeared to be normal under electron microscopy. IHC development and survival were not affected by deletion of *C1ql1.* Voltage-clamp recording and immunocytochmistry combined with confocal microscopy showed *C1ql1*-null IHCs showed no significant reduction of pre-synaptic proteins and synaptic vesicle release. This is in contrast to significant OHC loss in the KO mice. Our study suggests that *C1ql1* is essential for development of hair cell innervation and OHC survival. But maturation of presynaptic machinery in IHCs does not depend on C1QL1.

Keywords: C1QL1, hair cells, innervation, hearing loss, mice

SIGNIFICANCE STATEMENT

- We generated a *C1ql1* null mouse model and examined the role of C1QL1 in cochlear hair cells. The *C1ql1*-null mice had progressive loss of outer hair cells and hearing.
- We showed that the number of nerve fibers innervating both inner and outer hair cells was significantly reduced in *C1ql1*-null mice.
- We showed that *C1ql1* is essential for development of hair cell innervation and outer hair cells survival.
- Our study suggests *C1ql1* might be a deafness-related gene.

INTRODUCTION

Hair cells of all vertebrates are polarized neuroepithelial cells that serve as the sensory receptors for the acoustical, vestibular, and lateral-line organs (Beurg et al., 2006; Salvi et al., 2016). Hair cells transduce mechanical stimuli into electrical activity (Hudspeth and Corey, 1977; Marcotti et al., 2014). Inner hair cells (IHCs) and outer hair cells (OHCs) are the two types of sensory receptor cells critical for hearing in the mammalian cochlea. IHCs and OHCs are different in morphology and function (Dallos, 1992; Li et al., 2019). IHCs, innervated by type I nerve fibers, are considered to be the true sensory receptor and transmit information to the brain. OHCs, innervated by type II fibers and predominantly by efferent fibers (Thiers et al., 2008; Huang et al., 2012), serve as the effector cell that boosts input to IHCs by a receptor potential-driven somatic motility (Brownell et al., 1985; Zheng et al., 2000; Liberman et al., 2002).

Several previous studies examined cell-specific transcriptomes of adult IHCs and OHCs to identify genes that are preferentially expressed since these genes are likely involved in defining unique morphology or function of the two cell types (Liu et al., 2014; Li et al., 2018; Ranum et al., 2019). Among many genes that are preferentially expressed, *C1ql1* is one of the top 10 most differentially expressed genes with 7.7 Log2 fold difference favoring OHCs (Liu et al., 2014; Li et al., 2018). C1q-like family members (*C1ql1*–*C1ql4*), all containing a specific gC1q domain and widely expressed in the brain (Iijima et al., 2010; Shimono et al., 2010), are implicated in synapse formation or elimination in the central nervous system (CNS) (Bolliger et al., 2011; Kakegawa et al., 2015; Sigoillot et al., 2015). C1QL1 can select and maintain dominant nerve fibers, induce pruning to eliminate excess nerve fibers, and this selective and pruning effect is present in both developing and adult animals (Kakegawa et al., 2015), especially in the motor neurons in cerebellum. Since *C1ql1* is highly expressed in OHCs, which serve as a motor element for cochlear amplification, we speculate that C1QL1 gene may play a key role in OHC function and survival as well as establishing and maintaining innervations in hair cells.

We generated *C1ql1* null mice to examine the role of C1QL1 in cochlear hair cells. We showed that *C1ql1*-null mice had progressive loss of OHCs and hearing. Confocal microscopy showed that the number of nerve fibers innervating both IHCs and OHCs was significantly reduced. Interestingly, no significant IHC and spiral ganglion neuron loss was observed. Voltage-clamp recording and immunocytochmistry combined with confocal microscopy showed *C1ql1*-null IHCs showed no significant reduction of pre-synaptic proteins and synaptic vesicle release. In contrast, significant OHC loss was observed in the KO mice. Our study suggests that *C1ql1* is essential for development of hair cell innervation and OHC survival. But maturation of presynaptic machinery in IHCs does not depend on C1QL1.

MATERIALS AND METHODS

Ethics Statement

All animal experiments were performed with approval of Animal Care Committee of the Capital Medical University. All efforts were made to minimize animal suffering and the number of animals used.

Generation of *C1ql1* Knockout Mice

Knockout (*C1ql1* KO) mice were generated on Kunming(KM)background mice. Mouse model with *C1ql1* KO was generated by CRISPR/Cas9 technique. The null mutation of mouse *C1ql1* was created by homologous recombination. To determine the nucleotide sequence of mutated alleles, mouse genomic DNA was tested by the following primers: *C1ql1* forward, 5′-CAGTGGCCCCAGCCAGGGAAGG-3′ and *C1ql1* reverse, 5′-AGGCGCACCGCTCTGCTCGCTC-3′. Newborn mice were examined by Sanger sequencing and the sequencing sample were taken from mice tail tip tissue. Mice of both sexes aged from postnatal day 0 to 6 months were used for the study.

Auditory Brainstem Response (ABR) Measurements

Mice were tested under intraperitoneal anesthesia with ketamine (100mg/kg, Gutian Pharmaceutical Co., Ltd., Fujian, China) and xylazine (10mg/kg, Sigma-Aldrich Co. Llc., United States). An isothermal pad was used to keep body temperature of mice during audiometric testing. Needle electrodes and ground electrode were inserted subcutaneously beneath the pinna of the test ear, at the vertex and the contralateral ear, respectively. Auditory brainstem response (ABR) was recorded by Tucker-Davis Technologies (TDT) System III (Alachua, FL, United States). Both click (100 μs) and tone pips (4, 8, 12, 16, 32, and 40 kHz) were used for sound stimuli. 1024 responses were sampled and averaged at each sound level. Amplitude and latency of ABR wave I, and I–V wave interval was assessed at 90 dB SPL for each stimulus frequency. The lowest stimulus intensity that elicited a response was identified as ABR threshold, which was obtained by reducing the stimulus intensity in 10 dB SPL steps and then 5 dB steps. ABR threshold was determined by two trials to show repeatability.

Distortion Product Otoacoustic Emission (DPOAE) Measurements

Distortion product otoacoustic emission responses were recorded by TDT System III. Mice were anesthetized as mentioned above and their external auditory canals were cleaned before DPOAE test. Two primary tones (f1 and f2) were presented with an f2/f1 ratio of 1.2. The emitted acoustic signal was set at 65 dB SPL ranging from 1k to 20 kHz. Input/output functions of DPOAE were calculated for each tested frequency. The threshold of DPOAE was defined as 6 dB SPL above the noise floor.

Immunofluorescence

Mice were sacrificed by cervical dislocation and decapitated under anesthesia. Cochleae were removed and soaked in 0.01M phosphate-buffered saline (PBS) containing 4% paraformaldehyde (4% PFA/PBS) overnight at 4°C. Specimens were washed three times in PBS and subsequently treated with 10% EDTA decalcifying solution (PH = 7.2) for 12 h at room temperature (20–30°C). Then the cochlear tissues were carefully dissected under stereoscopic microscope (Nikon smz1000, Japan). Specimens were subsequently permeabilized by 0.3% Triton X-100 in 0.2 M PBS with 10% normal goat serum (ZSGB-BIO) for 2 h. Immunological histological chemistry (IHC) staining was performed using primary antibodies overnight at 4°C, followed by incubation with species-specific secondary antibodies for an additional 120 min at room temperature. Primary antibodies used were as follows: rabbit anti-C1QL1 polyclonal antibody (1:200, Bioss antibodies, bs-11045R), rabbit anti-myosin VIIa antibody (1:300, Proteus Biosciences, 25-6790), chicken anti-neurofilament 200 antibody (1:200, Chemicon, AB5539), and rat anti-myelin basic protein antibody (1:200, Millipore, MAB386). Fluorescent dye-conjugate secondary antibodies were conjugated to Alexa Fluor^{TM} 488, 568, or 647 (1:300, Invitrogen/Molecular Probes, Carlsbad, CA, catalog number: A11008, A21245, A11036, A11006, A21131, A21124, A11039, and A11041). Hair cell stereocilia were labeled with Alexa Fluor^{TM} 488 Phalloidin (Invitrogen/Molecular Probes, Carlsbad, CA, A12379). Prepared specimens were mounted on cover lip with antiblech mounting medium with DAPI (ZSGB-BIO, ZLI-9557).

Laser Confocal Microscopy

Cochlea were imaged by a high-resolution confocal microscope (TCS SP8 II; Leica Microsystems, Wetzlar, Germany) with a 63 × oil-immersion lens. Optimal excitation wavelengths were 488 nm (green), 568 nm (red), or 647 nm (far-red). DAPI was observed under an excitation wavelength of 358 nm (blue). Sequence scanning in z-axis was performed with an interval of 0.5 μm/layer from top to bottom, and the images were then superimposed.

Transmission Electron Microscopy (TEM)

For transmission electron microscopy (TEM),mice were sacrificed after anesthetized as mentioned above. The cochlear samples were removed and fixed overnight in 2.5% glutaraldehyde at 4°C. Specimens were rinsed with PBS in the next day, incubated in 1% osmium tetroxide for 2h at room temperature (20–30°C). Then specimens were dehydrated with graded acetone concentrations. Specimens were incubated in acetone mixed with Epon 812. Sections were cut at a 50nm thickness, located on copper grids, stained with uranyl acetate and lead citrate. Finally, the cochlear sections were examined in a transmission electron microscope (JEM-1400plus, JEOL, Japan). Images were captured with digital camera.

Electrophysiological Experiments

Freshly dissected organ of Corti from the apical turn of *C1ql1* knockout and wildtype mice at postnatal days 15 to 30 were used for real time capacitance measurement under the voltage-clamp condition. The extracellular solution contained (in mM): NaCl 135; KCl 1.3; CaCl2 1.3; MgCl2 0.9; NaH2PO4 0.7; Glucose 5.6; Na pyruvate 2; HEPES 10, pH 7.4, 305 mOsm. An EPC10 triple amplifier controlled by pulse software Patchmaster (HEKA Elektronik, Germany) was used for recording. Patch pipettes were pulled with a micropipette Puller P-97 Flaming/Brown (Sutter Instrument, Novato, CA, United States) and coated with dental wax to minimize pipette capacitance. The resistance range of the electrode was between 4 and 5 MΩ. Patch pipettes were filled with an intracellular cesium-based solution containing (in mM): Cesium methanesulfonate 118;CsCl 10; HEPES 10; EGTA 1;TEA-Cl 10; MgATP 3 and NaGTP 0.5; pH 7.2, 310 mOsm.

Real-time capacitance measurements (Cm) were performed using the Lock-in amplifier Patchmaster software (HEKA) by applying a 1 kHz command sine wave (amplitude 20 mV) at holding potential (−80 mV) before and after the pulse experiment, Cells with a holding current exceeding 50 pA at −80 mV were excluded from analysis. The time interval between each depolarization was set at 20 seconds to allow full replenishment of the RRP. ΔCm was estimated as the difference of the mean Cm over 300 ms after the end of the depolarization (the initial 50 ms were skipped) and the mean prepulse capacitance (300 ms) dates were analyzed using IGOR Software.

Statistical Analysis

Statistical analyses were performed using GraphPad Prism 7 software (GraphPad Software Inc, La Jolla, CA, United States) and IBM SPSS Statistics software. Means ± SEM (standard error of the mean) were calculated. Student's t test was utilized to compare variables in two groups and one-way analysis of variance (ANOVA) was utilized to compare variables in multiple groups. Significant statistical differences were defined as $^{*}P < 0.05$, $^{**}P < 0.01$, and $^{***}P < 0.001$.

RESULTS

Expression of *C1ql1* in the Adult Cochlea and Loss of C1QL1 in Knockout Mice

C1ql1 was expressed in adult IHCs and OHCs based on RNA-seq and microarray analyses (Liu et al., 2014; Li et al., 2018). We used immunofluorescence staining to show where *C1ql1* is expressed in the organ of Corti in adult wild-type mice. As shown in **Figures 1F,G**, positive staining is seen in the cell bodies of both hair cells (HC) and spiral ganglion cells (SGC).

C1ql1 belongs to C1q family with four known members (*C1ql1*, *C1ql2*, *C1ql3* and *C1ql4*). These members are highly homologous and all have a signature C1Q domain (Kishore and Reid, 2000). Mouse *C1ql1* gene in Chr17 contains two exons encoding 258 amino acids. We generated *C1ql1* KO mice by CRISPR/Cas9 genome editing technique. DNA sequencing in *C1ql1* KO mice revealed that a 4 base-pair (bp) fragment was deleted at nucleotide 34 (c.34_37delCTGG) of *C1ql1* gene, which caused a frameshift mutation and a premature appearance of termination codon (p. Leu12fsX1) in exon 1 (**Figures 1A–C**). This mutation was located in the conserved region between species (**Figure 1D**), and it was predicted that the mutation could lead to truncation of the C1QL1 protein and loss of the critical C1q domain (**Figure 1E**). We used immunofluorescence staining to confirm that C1QL1 was deleted by using an anti-C1QL1 polyclonal antibody. As shown in **Figures 1F,G**, the expression of C1QL1 is no longer detectable in *C1ql1* KO mice. This again confirms that *C1ql1* was successfully deleted.

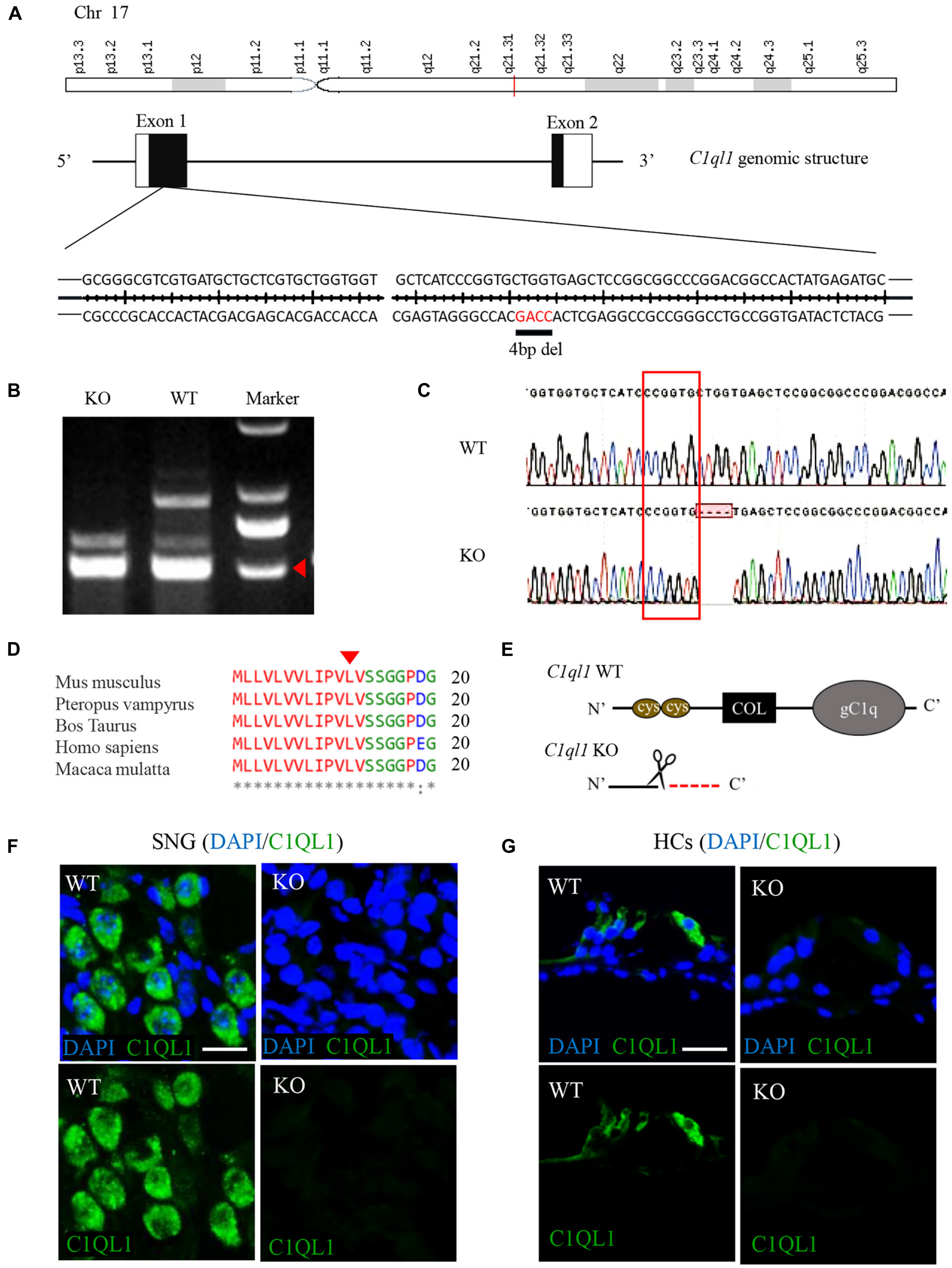

FIGURE 1 | Construction of *C1ql1* knockout mice. **(A)** Mouse *C1ql1* gene located in Chr17 contains two exons, and a 4 base-pair (bp) deleted at nucleotide 34 (c.34_37delCTGG) in the exon 1 revealed *C1ql1* KO mice. **(B)** The different bands of *C1ql1* gene sequencing between *C1ql1* gene WT mice and *C1ql1* gene KO mice. **(C)** The DNA sequencing of *C1ql1* showed the c.34_37delCTGG mutation in *C1ql1* KO mice. **(D)** The c.34_37delCTGG mutation was located in the height region between species. **(E)** The critical domains of C1QL1, and c.34_37delCTGG mutation resulted in domain deletions. **(F)** C1QL1 labeled by anti-C1QL1 (green) were detected in spiral ganglion cell of *C1ql1* WT mice but not in *C1ql1* KO mice. Scale bar = 10 μm. **(G)** C1QL1 labeled by anti-C1QL1 (green) were also detected in hair cells of *C1ql1* WT mice but is missing in *C1ql1* KO mice. Scale bar = 10 μm. Nucleus of cells were marked with DAPI (blue) in **(F,G)**.

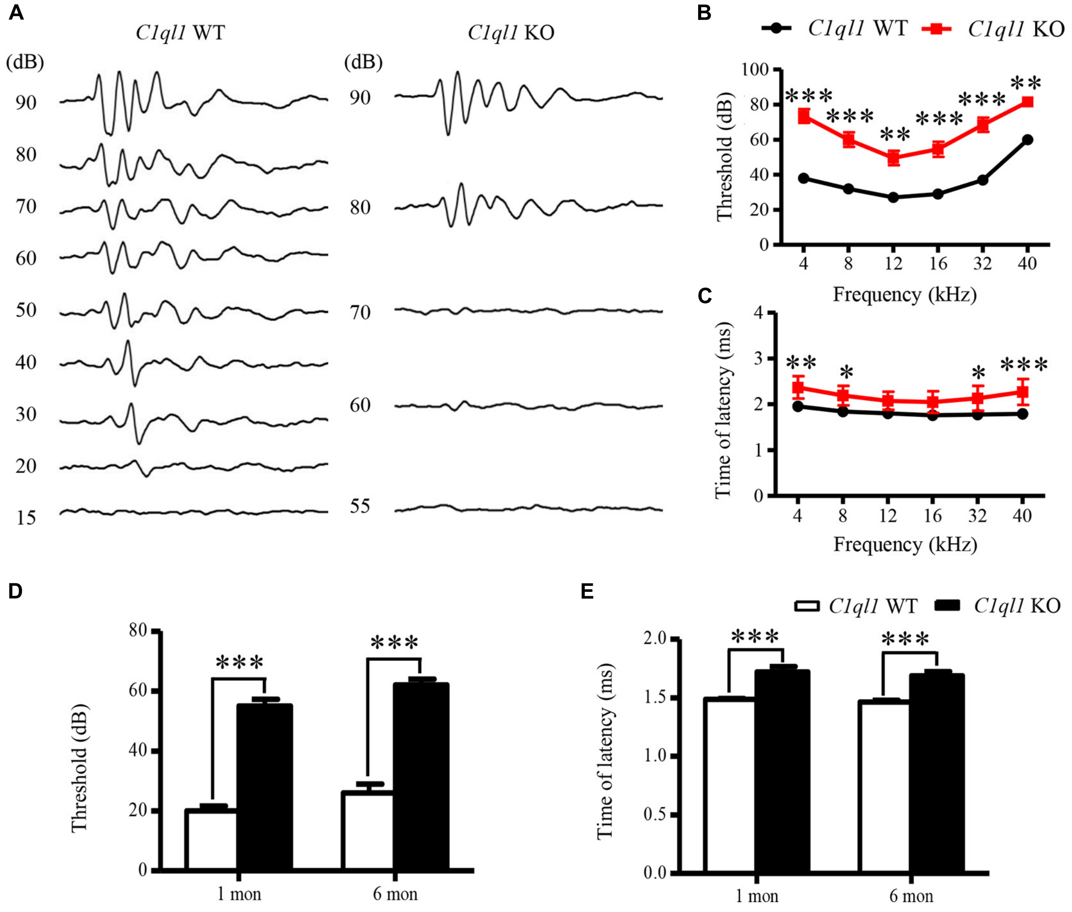

FIGURE 2 | Changes of ABR in *C1ql1* KO mice. **(A)** Representative waves of click ABR in *C1ql1* WT mice and *C1ql1* KO mice. **(B)** Changes in threshold of ABR between *C1ql1* KO mice and *C1ql1* WT mice ($n = 5$). **(C)** Changes in latency of ABR wave I between *C1ql1* KO mice and *C1ql1* WT mice. **(D)** Statistical differences in click ABR thresholds between *C1ql1* KO mice and *C1ql1* WT mice in postnatal 1 and 6 months ($n = 5$). **(E)** Statistical differences in latency of click ABR wave I between *C1ql1* KO mice and *C1ql1* WT mice in postnatal 1 and 6 months ($n = 5$). $^{*}P < 0.05$, $^{**}P < 0.01$, and $^{***}P < 0.001$.

Mice With Defective *C1ql1* Gene Have a Significant Hearing Impairment

Auditory function was evaluated by measuring ABR in *C1ql1* KO mice. Age-matched wild-type littermates were used for comparison. A 20 to 40 dB elevation of ABR threshold was observed in all frequencies (4, 8, 12, 16, 32, and 40 kHz) tested in the *C1ql1* KO mice in comparison to their wildtype littermates at 6 months (**Figures 2A,B**). The elevation in ABR thresholds of *C1ql1* KO ($n = 5$) and wild-type mice ($n = 5$) were statistically significant at all frequencies tested. Thresholds were also elevated when click-evoked ABR was used for measurements (**Figure 2A**).

We assessed the latency of wave I in the ABR waveforms. The latency is often used to evaluate the function of auditory nerve fibers. In *C1ql1* KO mice, the latency of wave I showed significant delays compared to those of the WT mice at 6 months (**Figure 2C**). Our data suggest that deletion of *C1ql1* led to deterioration of auditory function, in part by the abnormal signal transmission starting from cochlea. The differences in ABR threshold and latencies of wave I were detected from 1 month and to 6 months (**Figures 2D,E**).

We also examined outer hair cell (OHCs) function and status in the *C1ql1* KO mice. Unlike IHCs, we found significantly abnormal morphology and function of OHCs in the knockout mice. We measured the magnitude of distortion product evoked otoacoustic emissions (DPOAE) to assess function of OHCs. In the wild type mice, the amplitude of DPOAE did not change before 6 months (**Figure 3A**). In the *C1ql1* KO mice, the DPOAE magnitude was not significantly different from the wild type mice at 1 month ($n = 4$, $t = 0.4257$, $p > 0.05$). However, a progressive reduction of DPOAE amplitudes was observed in *C1ql1* KO mice after 2 months ($n = 4$, $t = 3.823$, $p < 0.01$) (**Figure 3B**). The reduction of DPOAE magnitude was significant between the *C1ql1* KO mice and wild types ($n = 4$, $t = 4.782$, $p < 0.001$) (**Figure 3C**).

Absence of C1QL1 Caused Abnormal Auditory Nerve Fibers

We investigated auditory nerve fibers and spiral ganglion cells (SGCs) in the *C1ql1* KO mice using immunofluorescence staining. Deletion of *C1ql1* affected the morphology of both type

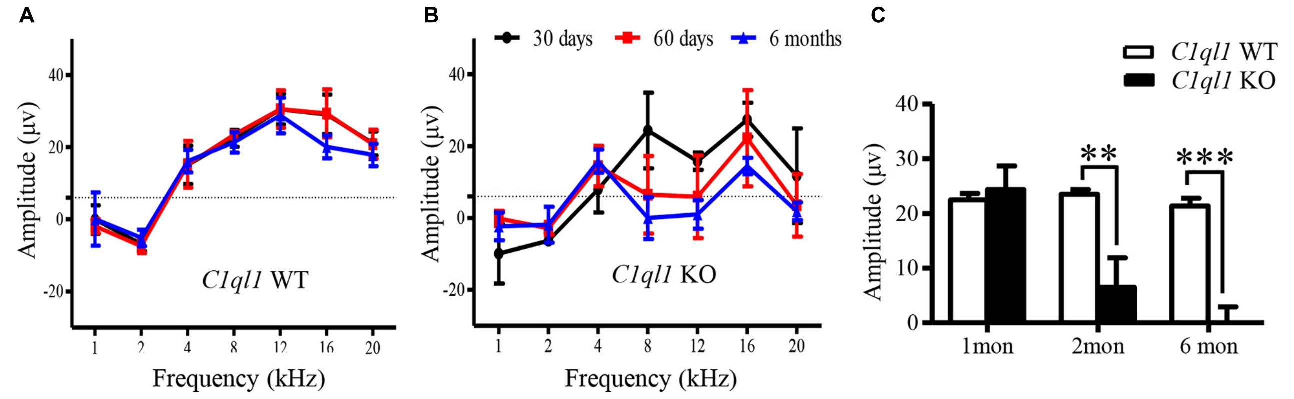

FIGURE 3 | Changes of DPOAE in *C1ql1* KO mice. **(A,B)** DPOAE in *C1ql1* WT mice and *C1ql1* KO mice. **(C)** Statistical differences in DPOAE between *C1ql1* KO mice and *C1ql1* WT mice in postnatal 1, 2, and 6 months at 12 kHz ($n = 4$). Statistical significance was defined as $^*P < 0.05$, $^{**}P < 0.01$, and $^{***}P < 0.001$.

I, type II nerve fibers and efferent fibers (**Figures 4A–D**). We measured the diameter and number of auditory nerve fibers between WT mice and *C1ql1* KO mice when the fibers were stained with anti-NF200 antibodies. A 50 × 50 μm area was used for measuring diameter and number of type I auditory nerve fibers, type II auditory nerve fibers and efferent fibers. **Figure 4** shows that the diameter of type ($P = 0.0018$), type II auditory nerve fibers and efferent fibers ($P < 0.001$) in *C1ql1* KO mice ($n = 10$) were significantly lower than those in WT littermate ($n = 10$) (**Figures 4E,F**). We measured the number of Type I nerve fibers and the nerve fibers passing through the tunnel which include both Type II and efferent fibers to OHCs. Type I auditory nerve fibers were counted in osseous spiral lamina regions on cochlear horizontal sections. Measurements were made in the area between habenular opening and spiral ganglia. The area measured was about 20–30 mm from the habenular opening in mice (Xing et al., 2012). As shown in **Figure 4J**, the number of type I auditory nerve fibers in the *C1ql1* KO mice ($n = 5$) is significantly lower than that of the WT mice ($P = 0.0353$, $n = 5$). The number of nerve fibers in the tunnel was also significantly reduced in adult *C1ql1* KO mice (15.20 ± 0.6464, $n = 10$) compared to that of the WT mice (8.400 ± 0.4761, $n = 10$). The number was counted in an area of 50 × 50 μm (**Figure 4G**). Our results indicate that deletion of *C1ql1* reduces both the type I auditory nerve fibers, type II auditory nerve fibers and efferent fibers innervating hair cells.

Deletion of C1ql1 Did Not Affect Morphology of Myelin Basic Protein (MBP) and SGC

Further, we explored whether deficiency of C1QL1 protein affected spiral ganglion and auditory nerve myelin. To answer this question, we performed immunofluorescence staining and transmission electron microscopy. The ultrastructure of the SGCs of *C1ql1* KO mice looked similar to those of the wild type mice (**Figures 5A–F**). The number of SGNs of *C1ql1* KO mice was also not statically different from that of the wild-type mice (**Figure 5G**). We measured the thickness of the myelin sheath of the auditory nerve from the electron micrograph. The mean thickness of myelin sheath was 0.426 ± 0.060 μm in WT mice and 0.459 ± 0.056 μm in KO mice (**Figures 5H,I**). No significant difference was seen between the WT ($n = 10$) and KO mice ($P = 0.22$, $n = 10$). Our result suggests that loss of C1QL1 did not affect morphology of spiral ganglion and nerve myelin.

Loss of C1QL1 Did Not Affect Morphology, Number, and Function of Cochlear Inner Hair Cells

To determine if loss of C1QL1 affect inner hair cell (IHC) morphology, survival and function, immunofluorescence, transmission electron microscopy, and patch clamp techniques were used. The IHCs of the *C1ql1* KO mice have normal gross morphology, such as complete cell body and normal-looking stereocilia bundles (**Figure 6**). We counted the number of IHCs in the wild type and *C1ql1* KO mice in cochlea. No significant IHC loss was seen in the KO mice ($P = 0.27$, $n = 5$). To determine if C1QL1 is necessary for the formation of ribbon synapses and neurotransmitter release, voltage-dependent Ca^{++} current and change in membrane capacitance associated with release of neurotransmitter (endocytosis) were measured. The magnitude of voltage-dependent Ca^{++} current and membrane capacitance change were similar to those seem in wildtype IHCs ($n = 3$, $p > 0.05$) (**Figure 7**). Our results suggest the deficiency of C1QL1 did not affect the morphology, survival and synaptic transmission of IHCs.

Loss of C1QL1 Leads to Progressive Loss of Outer Hair Cells

We examined the morphology of OHCs by immunostaining and by transmission electron microscopy. Consistent with the results of DPOAE test, we found loss of OHCs in *C1ql1* KO mice after 2 months (**Figures 8A′–C′**). More OHC loss was observed at 6 months (**Figures 8A″–C″**). In contrast, no obvious loss of OHCs was seen in wild-type mice at the same age (**Figures 8A‴–C‴**).

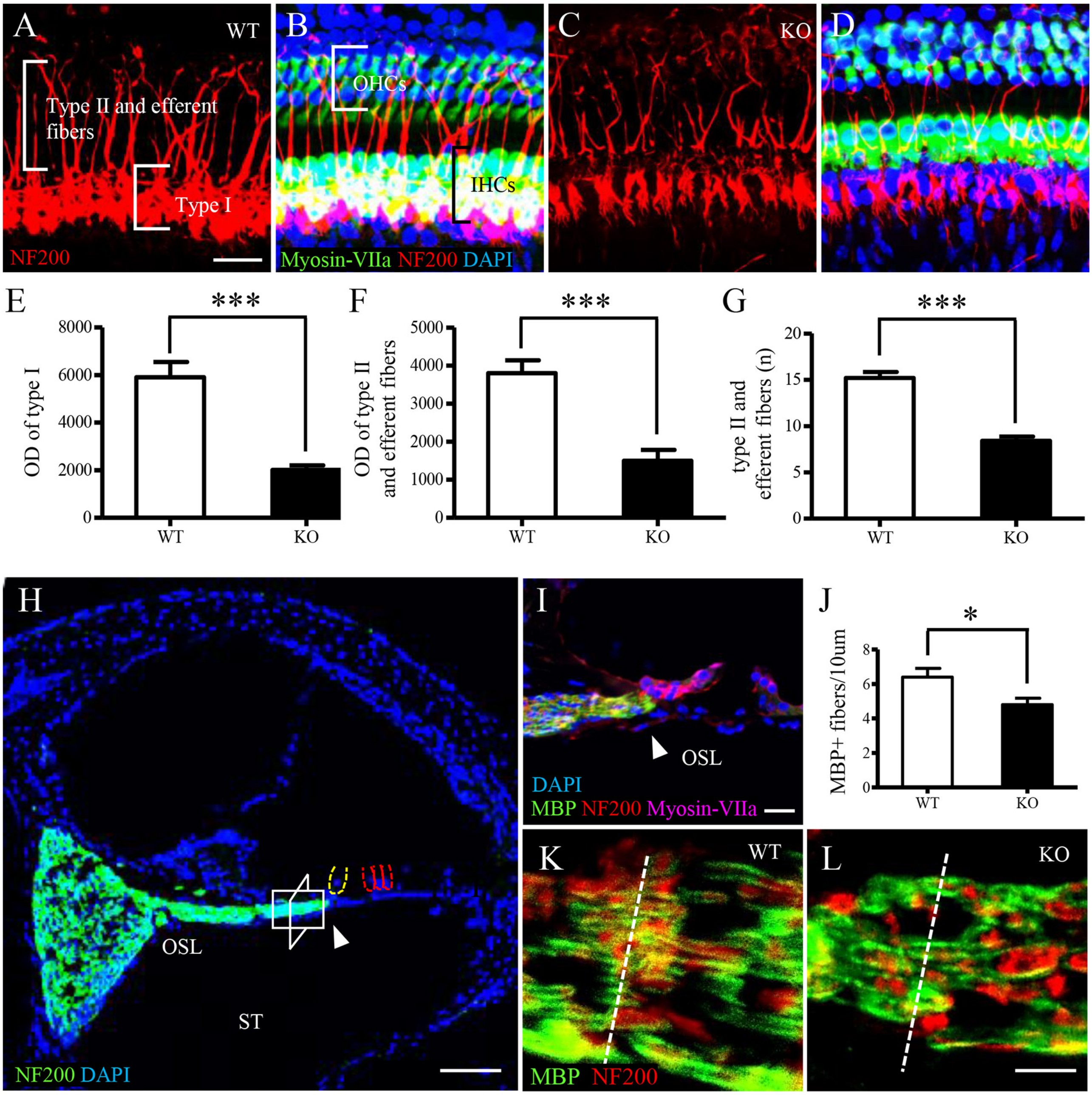

FIGURE 4 | Auditory nerve fibers in *C1ql1* WT and *C1ql1* KO mice. **(A,C)** Type I, type II auditory nerve fibers and efferent fibers (red, labeled by anti-NF200) in *C1ql1* WT mice **(A)** and in *C1ql1* KO mice (C). Scale bar = 10 µm. **(B,D)** Morphology of cochlea under basilar membrane stretched preparation technique. **(B)** Cochlear basilar membrane in *C1ql1* WT mice. **(D)** Cochlear basilar membrane in *C1ql1* WT mice. Cytoplasm of hair cells was marked with anti-myosin VIIa antibody (green), nucleus of cells with DAPI (blue), and auditory nerve fibers and efferent fibers with anti-NF200 (red). Scale bar = 10 µm. **(E)** is the statistical difference in optical density (OD) value of Type I auditory nerve fibers and **(F)** is the statistical difference in OD value of Type II auditory nerve fibers and efferent fibers between *C1ql1* KO mice and *C1ql1* WT mice. **(G)** Is the statistical difference in number of Type II auditory nerve fibers and efferent fibers between *C1ql1* KO mice and *C1ql1* WT mice. **(H)** Morphology of cochlea under cochlear horizontal sections. Scale bar = 25 µm. **(I)** Amplification of osseous spiral lamina (OSL) regions in cochlea. Scale bar = 10 µm. The arrow points to habenular opening in **(H,I)**. **(J)** Statistical difference in number of Type I auditory nerve fibers between *C1ql1* KO mice and *C1ql1* WT mice. Measurements were made in the area about 20–30 mm from the habenular opening. The measured areas in *C1ql1* WT mice and *C1ql1* KO mice were showed in **(K,L)**, respectively. Scale bar = 5 µm. $*P < 0.001$ and $***P < 0.001$.

Interestingly, although remaining OHCs appeared to be normal with normal looking stereocilia bundles under light microscope, scanning electron microscopy showed more phagosomes in the cytoplasm of OHCs in *C1ql1* KO mice than in WT mice (**Figures 8D–F**). Besides, many mitochondria showed some signs of swallowing (**Figures 8G,H**).

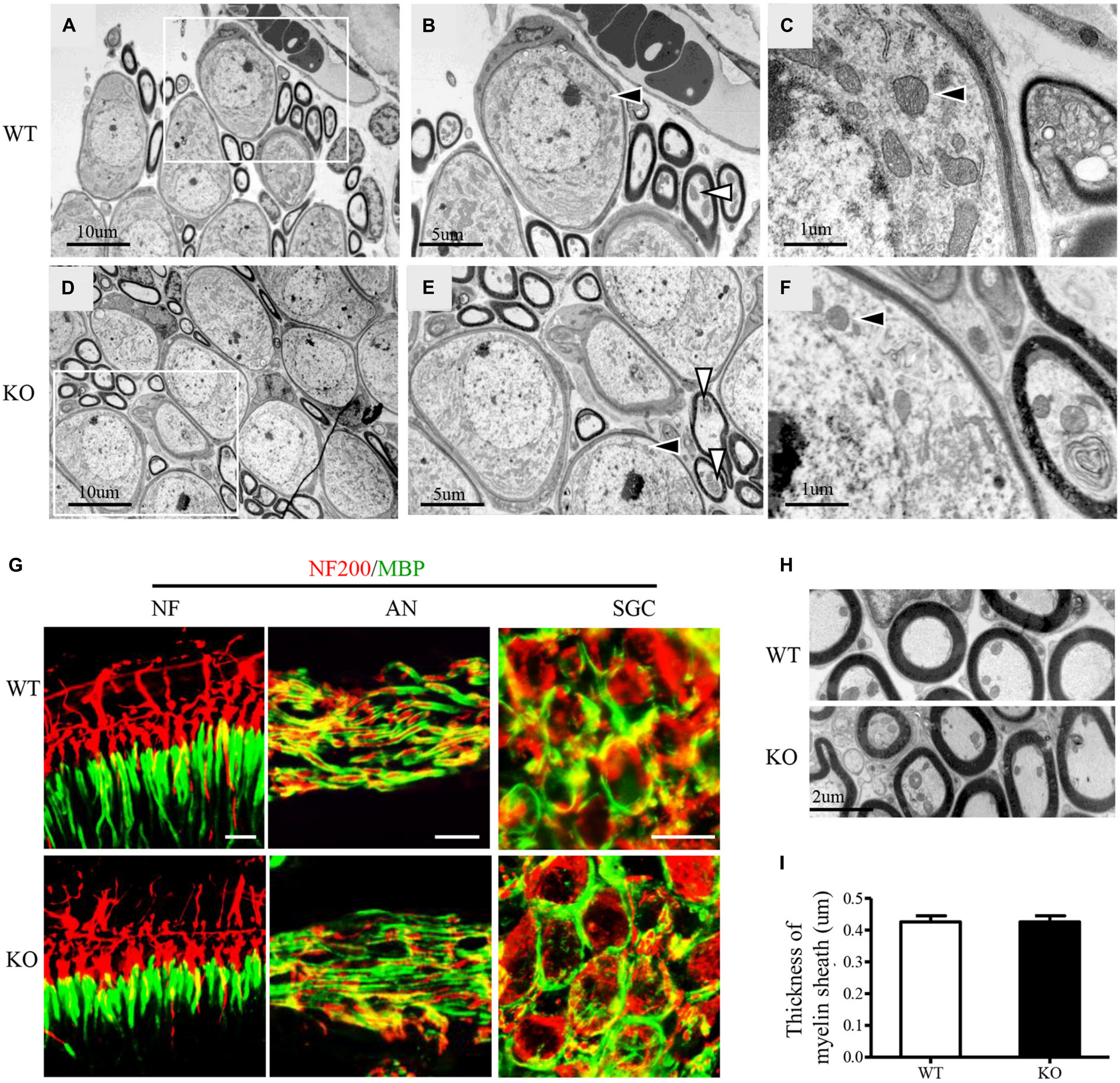

FIGURE 5 | Subcellular structures of auditory nerve and SGCs in *C1ql1* WT and *C1ql1* KO mice. **(A–C)** The subcellular structures of auditory nerve and SGCs in *C1ql1* WT mice. **(B)** Inside the white box in **(A)** are auditory nerve (white arrow) and SGCs (black arrow), which are shown magnified. **(C)** Is a further magnification and mitochondria with normal morphology (black arrow) in SGC. **(D–F)** The subcellular structures of auditory nerve and SGCs in *C1ql1* KO mice. **(E)** Inside the white box in **(D)** are auditory nerve (white arrow) and SGCs (black arrow), which are shown magnified. **(F)** is a further magnification and mitochondria with normal morphology (black arrow) in SGC. **(G)** Immunofluorescence staining shows normal myelin sheath in the ending of auditory nerve fibers (left), in the middle part of auditory nerve fibers (middle), and in SGSs (right) of *C1ql1* WT mice and *C1ql1* KO mice, respectively. Myelin sheath was marked with anti-MBP antibody (green) and auditory nerve fibers with anti-NF200 (red). Scale bar = 10 μm. **(H)** Transmission electron microscopy shows myelin sheath of auditory nerve fibers in *C1ql1* WT mice and *C1ql1* KO mice. **(I)** Measured on electron micrographs, no significant difference was seen between the *C1ql1* WT mice group ($n = 10$) and *C1ql1* KO mice group ($n = 10$). Unpaired *t*-test, $P = 0.22$.

DISCUSSION

C1ql1, widely expressed in brain, is an important gene associated with maturation, regulation and maintenance of synapses in nervous system (Bérubé et al., 1999; Hunsberger et al., 2005; Glanzer et al., 2007; Iijima et al., 2010). *C1ql1* is expressed in the central auditory pathways such as the ventral cochlear nucleus, lateral thalamus and trapezoid nuclei (Iijima et al., 2010). In the adult mouse cochlea, cell type-specific transcriptome analysis showed that *C1ql1* is expressed in IHCs, OHCs, pillar cells, and Deiters' cells with differential expression in OHCs (Liu et al., 2018). But its function in hair cells remained unclear.

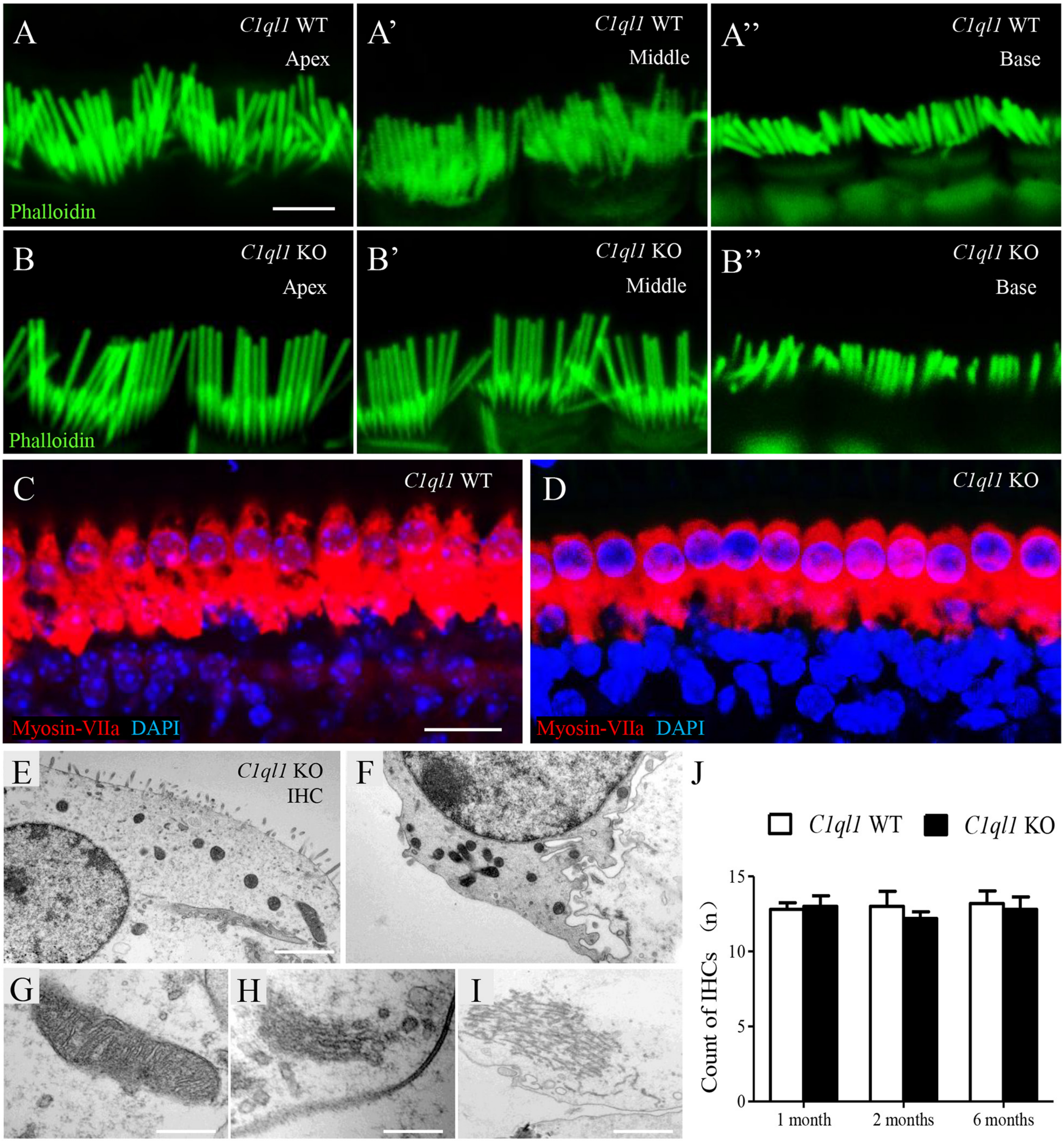

FIGURE 6 | Morphology of cochlear inner hair cells in *C1ql1* WT mice and *C1ql1* KO mice. **(A,B)** The stereocilia in apex turn, middle turn and base turn of inner hair cells (green, labeled by phalloidin) in *C1ql1* WT mice and *C1ql1* KO mice. Scale bar = 2.5 µm. **(C)** The normal gross morphology of IHCs in *C1ql1* WT mice. **(D)** The gross morphology of IHCs in *C1ql1* KO mice. Cytoplasm of inner hair cells was marked with anti-myosin VIIa antibody (red) and nucleus of cells with DAPI (blue). Scale bar = 10 µm. **(E–I)** Subcellular structures of inner hair cells in *C1ql1* KO mice, normal mitochondria, Golgi apparatus, and endoplasmic reticulum were showed, respectively. Scale bar = 2.5 µm **(E)**. **(J)** Count of OHCs in *C1ql1* WT mice and *C1ql1* KO mice in postnatal 1 and 6 months.

Using loss of function approach in the mouse model, we showed that *C1ql1* was necessary for development and maintenance of innervations in IHCs and OHCs. Loss of C1QL1 also led to accelerated OHC loss. Taken together, our study suggests that *C1ql1* is indispensable to maintain normal auditory function.

We first used immunostaining to show that C1QL1 was expressed in hair cells. The protein expression is consistent with *C1ql1* expression detected in RNA-seq analysis (Liu et al., 2014; Li et al., 2018). Furthermore, we also detected its expression in the cytoplasm of spiral ganglion cells. This is also consistent

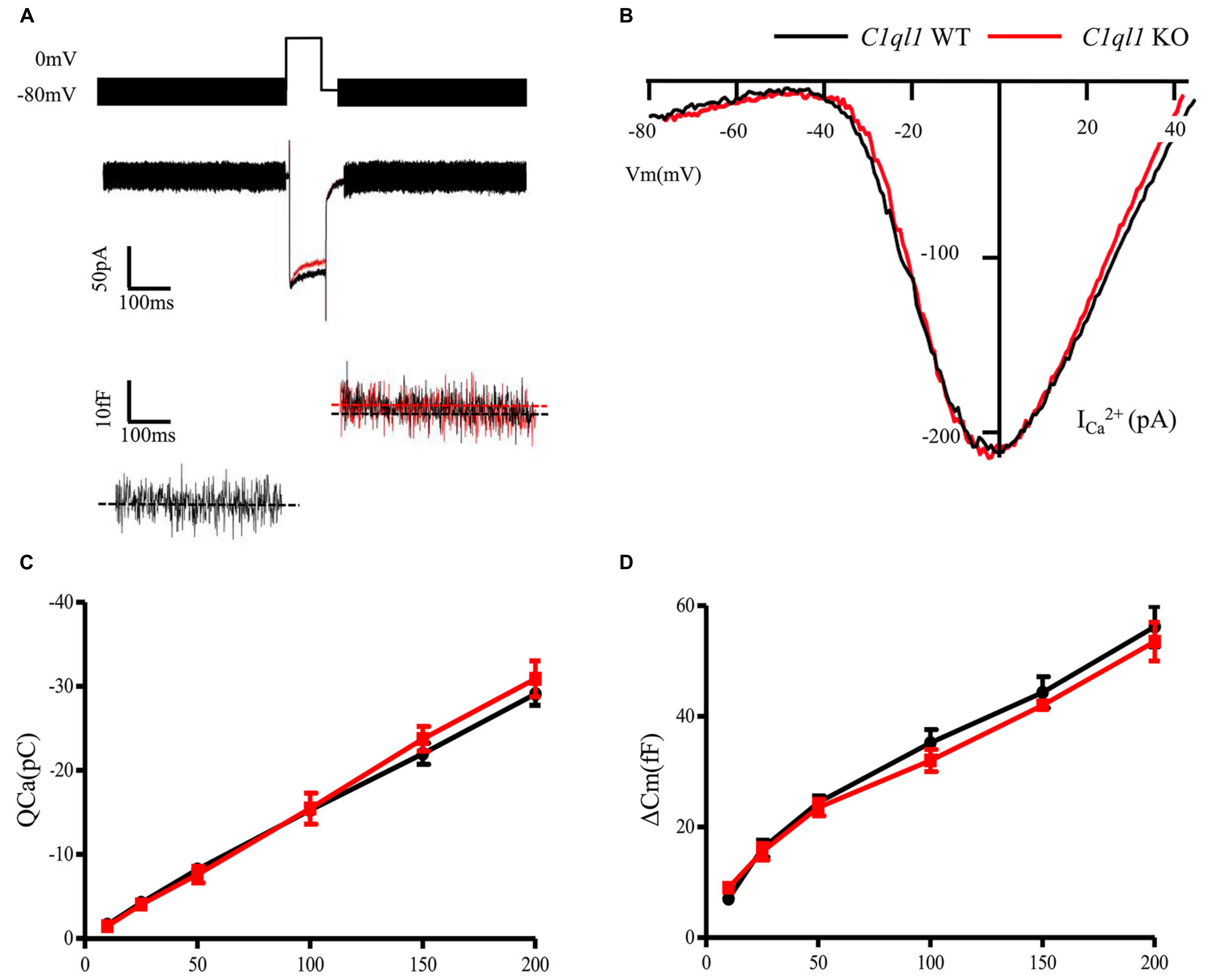

FIGURE 7 | Function of cochlear inner hair cells in *C1ql1* WT mice and *C1ql1* KO mice. **(A)** The wave of potential changes in IHCs of *C1ql1* WT mice and *C1ql1* KO mice. **(B)** The IHCs in *C1ql1* KO mice also had normal biophysical properties. Ca++ current of IHCs seemed to be quite normal in *C1ql1* KO mice compare to WT mice. **(C)** Integral Ca++ current as a function of depolarization duration (in milliseconds). **(D)** Change in membrane capacitance as a function of depolarization duration (in milliseconds).

with a previous study which showed that *C1ql1* is expressed in the mouse cochlear spiral ganglion neurons (Lu et al., 2011). We observed progressive hearing loss in *C1ql1* null mice. The hearing loss is likely caused by reduction of afferent innervation to IHCs and loss of OHCs. This was reflected by the elevation of ABR threshold, increased latency of ABR wave I, elevation of DPOAE threshold and loss of OHCs. Interestingly, loss of function of C1QL1 apparently did not impact the development and survival of IHCs as IHCs appeared to be normal with no obvious loss at 1 and 6 months. Apparently, C1QL1 is also not essential for the development of ribbon synapses as calcium current and neurotransmitter release recorded from *C1ql1*-null IHCs were not different from those of wildtype IHCs. It is interesting that reduction in afferent innervation to IHCs did not affect formation of presynaptic structure despite of the fact that the number of afferent fibers were reduced. The fact that IHCs and presynaptic structures develop normally suggest that that functional development of IHCs does not depend on influence of innervation or C1QL1. This is consistent with some previous studies which showed that morphological and physiological development of hair cells is autonomous (He, 1997; He et al., 2001).

Although *C1ql1*-null mice displayed loss of innervation in both IHCs and OHCs, it is unclear why C1QL1 is necessary and how it interacts with nerve terminals for synaptogenesis. Since presynaptic structures in hair cells remained normal, it is likely that C1QL1 may guide outgrowth of afferent and efferent fibers to hair cells. Previous studies have shown that the signaling pathway formed by the secreted protein C1QL1 and the adhesion-GPCR BAI3 (brain angiogenesis inhibitor 3) regulates the development of proper excitatory connectivity on cerebellar Purkinje cells (Sigoillot et al., 2015). C1QL1 controls climbing

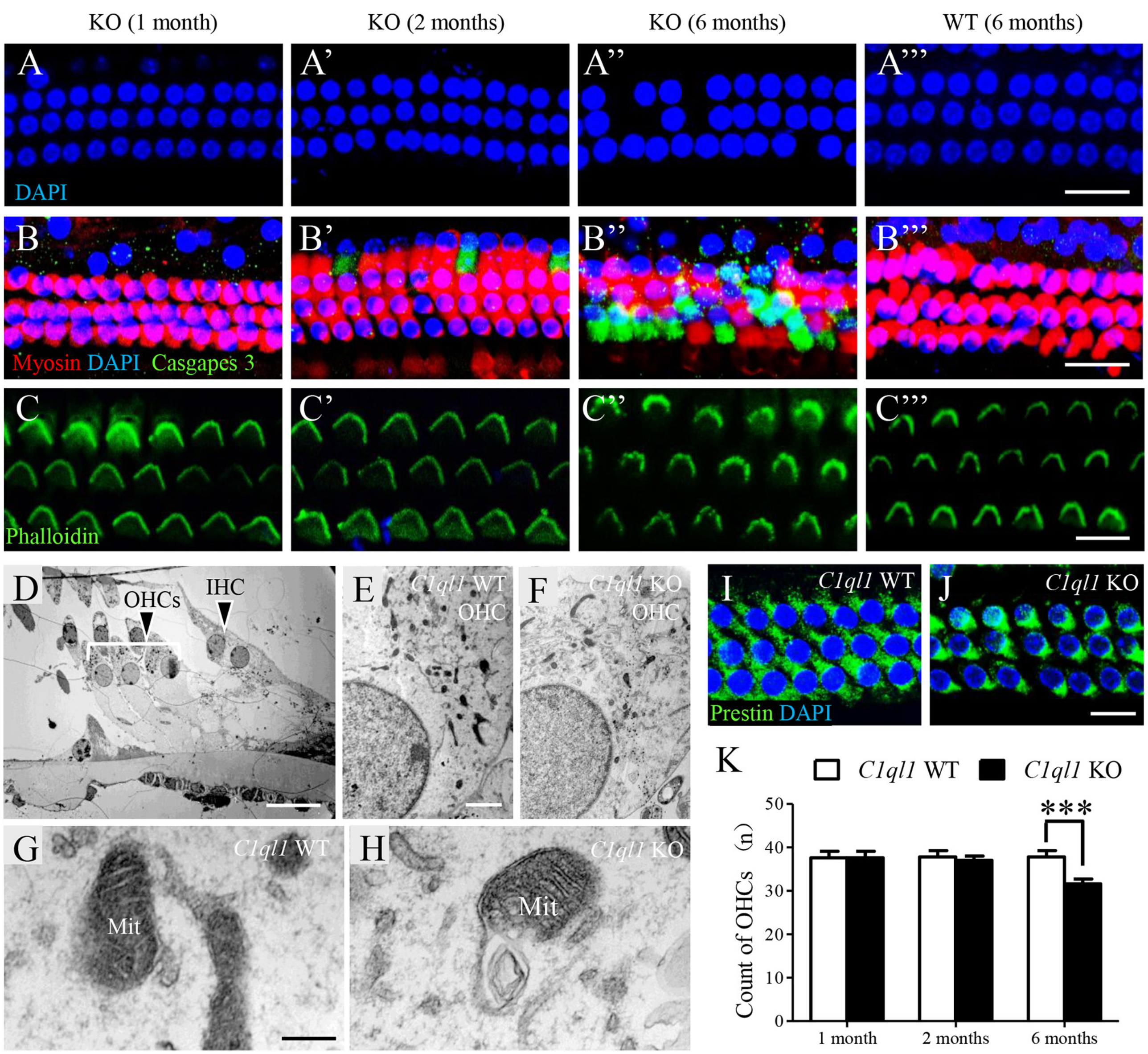

FIGURE 8 | Morphology of cochlear outer hair cells in *C1ql1* WT mice and *C1ql1* KO mice. **(A–C)** Outer hair cells showed by immunofluorescence staining in *C1ql1* KO mice (postnatal 30 and 60 days, and 6 months, respectively) and in *C1ql1* WT mice (postnatal 6 months, as control group). Scale bar = 10 μm. **(A–A‴)** The nucleus (blue, labeled by DAPI) of outer hair cells in groups aforementioned. **(B–B‴)** The apoptotic signal (green, labeled by caspase 9) of outer hair cells in groups aforementioned. **(C–C‴)** The stereocilia of outer hair cells (green, labeled by phalloidin) in groups aforementioned. **(D)** Subcellular structures of outer hair cells in mice. Scale bar = 5 μm. **(E,F)** Much more mitochondria have been observed being swallowed by phagosomes in *C1ql1* KO mice than *C1ql1* WT mice. **(G,H)** Mitochondria in *C1ql1* WT mice and *C1ql1* KO mice. **(I,J)** Prestin in *C1ql1* WT mice and *C1ql1* KO mice. Scale bar = 10 μm. **(K)** Count of OHCs in *C1ql1* WT mice and *C1ql1* KO mice in postnatal 1 and 6 months. $^{***}P < 0.001$.

fiber synaptogenesis and territory on Purkinje cells and C1QL1's modulation of Purkinje cell spinogenesis is BAI3-dependent. RNA-seq analysis shows that *Bai3* (*Baiap3*) is expressed in both IHCs and OHCs (Li et al., 2018) as well as in spiral ganglion neurons (Lu et al., 2011).

We observed reduction of fibers innervating OHCs in *C1ql1* KO mice. It is not clear if the reduction was only limited to type II fibers or if type II and efferent fibers to OHCs were both affected. Most nerve fibers crossing the tunnel are efferent fibers from MOC (Maison et al., 2016; Webber et al., 2021). We did not label these fibers using specific markers. However, a recent study showed that conditional deletion of *C1ql*1 only in OHCs reduced OHC afferent synapse maintenance (Biswas et al., 2021). We evaluated OHC function in *C1ql1* KO mice by measuring DPOAE. We observed a gradual decrease of DPOAE magnitude starting from 8 weeks after birth, which was correlated with the beginning of loss/degeneration of OHCs. Thus, our study suggests that long-term survival of OHCs depends on C1QL1 function. This is consistent with the fact that *C1ql1* is highly expressed in adult OHCs (Liu et al., 2014; Li et al., 2018). The cause of OHC loss is unknown. But it is unlikely due to reduction of afferent and/or efferent innervation as previous studies showed that denervation of efferent innervation did not impact hair cell survival. We note that a recent study showed that OHC-specific deletion of *C1ql1* did not reveal a compelling auditory phenotype (Biswas et al., 2021). We would like to point out that this is different from our study where *C1ql1* was unquietly deleted in hair cells and neurons. The auditory phenotype we observed was due to loss of innervations in IHCs and OHCs as well as loss of OHCs.

Loss of function due to mutations or deletion of many genes can lead to hearing loss with different auditory phenotypes. For example, mutations of *Tmc1* can lead to profound hearing loss due to loss of mechanotranduction in both IHCs and OHCs (Marcotti et al., 2006). Loss of *Slc26a5* can lead to loss of OHC motility and cochlear amplification (Liberman et al., 2002; Dallos et al., 2008). Loss of genes related to hair cell development can lead abnormal development of hair cells, resulting in hearing loss. Unless loss of function only affects IHC or neurons which is often manifested as auditory neuropath, the phenotype observed in loss of function of most genes is often mixed, as both IHCs and OHCs are affected. Deletion of *Slc26a5* also leads to unexpected IHC loss (Liberman et al., 2002; Dallos et al., 2008). The phenotype observed in *C1ql1* KO mice is due to loss of neuronal transmission (reflected by reduction in ABR threshold and increased latency in ABR wave I) and loss of OHC function (reflected by reduction in DPOAE magnitude).

Mutations or deficiencies affecting approximately 123 genes have been linked to inherited non-syndromic hearing loss in humans. There have been no reports of hearing loss due to mutations of *C1ql1*. It remains to be determined if *C1ql1* is a deafness-related gene. Since deletion of this gene can cause hearing loss, *C1ql1* mutations perhaps should be considered and screened in future genetic testing.

DATA AVAILABILITY STATEMENT

The original contributions presented in the study are included in the article/supplementary material, further inquiries can be directed to the corresponding author/s.

ETHICS STATEMENT

The animal study was reviewed and approved by Animal Care Committee of the Capital Medical University.

AUTHOR CONTRIBUTIONS

YQ, WX, SY, ZD, TQ, LH, WW, and LZ were responsible for the experiment design. YQ, KL, and YL were responsible for data analysis. DH and SG were responsible for providing overall ideas. All authors contributed to the article and approved the submitted version.

FUNDING

This work was supported by the National Natural Science Foundation of China (grant numbers 81771016, 81770997, and 81830030), Scientific Research and Cultivation Fund of Capital Medical University (grant number PYZ20152), and Beijing Natural Science Foundation (grant number 7174291).

ACKNOWLEDGMENTS

We wish to thank Jin Liangyun for technical assistance with electron microscopy, and Deng Jun for assistance with confocal microscopy. The *C1ql1* gene knockout mice were obtained from Chongqing Academy of Animal Sciences (Chongqing, China).

REFERENCES

Bérubé, N. G., Swanson, X. H., Bertram, M. J., Kittle, J. D., Didenko, V., Baskin, D. S., et al. (1999). Cloning and characterization of CRF, a novel C1q-related factor, expressed in areas of the brain involved in motor function. *Brain Res. Mol. Brain Res.* 63, 233–240. doi: 10.1016/s0169-328x(98)00278-2

Beurg, M., Evans, M. G., Hackney, C. M., and Fettiplace, R. (2006). A large-conductance calcium-selective mechanotransducer channel in mammalian cochlear hair cells. *J. Neurosci.* 26, 10992–11000. doi: 10.1523/jneurosci.2188-06.2006

Biswas, J., Pijewski, R. S., Makol, R., Miramontes, T. G., Thompson, B. L., Kresic, L. C., et al. (2021). C1ql1 is expressed in adult outer hair cells of the cochlea in a tonotopic gradient. *PLoS One* 16:e0251412. doi: 10.1371/journal.pone.0251412

Bolliger, M. F., Martinelli, D. C., and Südhof, T. C. (2011). The cell-adhesion G protein-coupled receptor BAI3 is a high-affinity receptor for C1q-like proteins. *Proc. Natl. Acad. Sci. U. S. A.* 108, 2534–2539. doi: 10.1073/pnas.1019577108

Brownell, W. E., Bader, C. R., Bertrand, D., and de Ribaupierre, Y. (1985). Evoked mechanical responses of isolated cochlear outer hair cells. *Science* 227, 194–196. doi: 10.1126/science.3966153

Dallos, P. (1992). The active cochlea. *J. Neurosci.* 12, 4575–4585.

Dallos, P., Wu, X., Cheatham, M. A., Gao, J., Zheng, J., Anderson, C. T., et al. (2008). Prestin-based outer hair cell motility is necessary for mammalian cochlear amplification. *Neuron* 58, 333–339. doi: 10.1016/j.neuron.2008.02.028

Glanzer, J. G., Enose, Y., Wang, T., Kadiu, I., Gong, N., Rozek, W., et al. (2007). Genomic and proteomic microglial profiling: pathways for neuroprotective inflammatory responses following nerve fragment clearance and activation. *J. Neurochem.* 102, 627–645. doi: 10.1111/j.1471-4159.2007.04568.x

He, D. Z. (1997). Relationship between the development of outer hair cell electromotility and efferent innervation: a study in cultured organ of corti of neonatal gerbils. *J. Neurosci.* 17, 3634–3643. doi: 10.1523/jneurosci.17-10-03634.1997

He, D. Z., Zheng, J., and Dallos, P. (2001). Development of acetylcholine receptors in cultured outer hair cells. *Hear. Res.* 162, 113–125. doi: 10.1016/s0378-5955(01)00376-8

Huang, L. C., Barclay, M., Lee, K., Peter, S., Housley, G. D., Thorne, P. R., et al. (2012). Synaptic profiles during neurite extension, refinement and retraction in the developing cochlea. *Neural Dev.* 7:38. doi: 10.1186/1749-8104-7-38

Hudspeth, A. J., and Corey, D. P. (1977). Sensitivity, polarity, and conductance change in the response of vertebrate hair cells to controlled mechanical stimuli. *Proc. Natl. Acad. Sci. U. S. A.* 74, 2407–2411. doi: 10.1073/pnas.74.6.2407

Hunsberger, J. G., Bennett, A. H., Selvanayagam, E., Duman, R. S., and Newton, S. S. (2005). Gene profiling the response to kainic acid induced seizures. *Brain Res. Mol. Brain Res.* 141, 95–112. doi: 10.1016/j.molbrainres.2005.08.005

Iijima, T., Miura, E., Watanabe, M., and Yuzaki, M. (2010). Distinct expression of C1q-like family mRNAs in mouse brain and biochemical characterization of their encoded proteins. *Eur. J. Neurosci.* 31, 1606–1615.

Kakegawa, W., Mitakidis, N., Miura, E., Abe, M., Matsuda, K., Takeo, Y. H., et al. (2015). Anterograde C1ql1 signaling is required in order to determine and maintain a single-winner climbing fiber in the mouse cerebellum. *Neuron* 85, 316–329. doi: 10.1016/j.neuron.2014.12.020

Kishore, U., and Reid, K. B. (2000). C1q: structure, function, and receptors. *Immunopharmacology* 49, 159–170. doi: 10.1016/s0162-3109(00)80301-x

Li, S., Yu, S., Ding, T., Yan, A., Qi, Y., Gong, S., et al. (2019). Different patterns of endocytosis in cochlear inner and outer hair cells of mice. *Physiol. Res.* 68, 659–665. doi: 10.33549/physiolres.934009

Li, Y., Liu, H., Giffen, K. P., Chen, L., Beisel, K. W., and He, D. (2018). Transcriptomes of cochlear inner and outer hair cells from adult mice. *Sci. Data* 5:180199.

Liberman, M. C., Gao, J., He, D. Z., Wu, X., Jia, S., and Zuo, J. (2002). Prestin is required for electromotility of the outer hair cell and for the cochlear amplifier. *Nature* 419, 300–304. doi: 10.1038/nature01059

Liu, H., Chen, L., Giffen, K. P., Stringham, S. T., Li, Y., Judge, P. D., et al. (2018). Cell-specific transcriptome analysis shows that adult pillar and Deiters' cells express genes encoding machinery for specializations of cochlear hair cells. *Front. Mol. Neurosci.* 11:356. doi: 10.3389/fnmol.2018.00356

Liu, H., Pecka, J. L., Zhang, Q., Soukup, G. A., Beisel, K. W., and He, D. Z. (2014). Characterization of transcriptomes of cochlear inner and outer hair cells. *J. Neurosci.* 34, 11085–11095. doi: 10.1523/jneurosci.1690-14.2014

Lu, C. C., Appler, J. M., Houseman, E. A., and Goodrich, L. V. (2011). Developmental profiling of spiral ganglion neurons reveals insights into auditory circuit assembly. *J. Neurosci.* 31, 10903–10918. doi: 10.1523/jneurosci.2358-11.2011

Maison, S., Liberman, L. D., and Liberman, M. C. (2016). Type II Cochlear Ganglion Neurons Do Not Drive the Olivocochlear Reflex: re-Examination of the Cochlear Phenotype in Peripherin Knock-Out Mice. *eNeuro* 3:e0207.

Marcotti, W., Corns, L. F., Desmonds, T., Kirkwood, N. K., Richardson, G. P., and Kros, C. J. (2014). Transduction without tip links in cochlear hair cells is mediated by ion channels with permeation properties distinct from those of the mechano-electrical transducer channel. *J. Neurosci.* 34, 5505–5514. doi: 10.1523/jneurosci.4086-13.2014

Marcotti, W., Erven, A., Johnson, S. L., Steel, K. P., and Kros, C. J. (2006). Tmc1 is necessary for normal functional maturation and survival of inner and outer hair cells in the mouse cochlea. *J. Physiol.* 574, 677–698. doi: 10.1113/jphysiol.2005.095661

Ranum, P. T., Goodwin, A. T., Yoshimura, H., Kolbe, D. L., Walls, W. D., Koh, J. Y., et al. (2019). Insights into the biology of hearing and deafness revealed by single-cell RNA sequencing. *Cell Rep.* 26, 3160–3171.e3.

Salvi, J. D., Ó Maoiléidigh, D., and Hudspeth, A. J. (2016). Identification of bifurcations from observations of noisy biological oscillators. *Biophys. J.* 111, 798–812. doi: 10.1016/j.bpj.2016.07.027

Shimono, C., Manabe, R., Yamada, T., Fukuda, S., Kawai, J., Furutani, Y., et al. (2010). Identification and characterization of nCLP2, a novel C1q family protein expressed in the central nervous system. *J. Biochem.* 147, 565–579. doi: 10.1093/jb/mvp203

Sigoillot, S. M., Iyer, K., Binda, F., González-Calvo, I., Talleur, M., Vodjdani, G., et al. (2015). The secreted protein C1QL1 and its receptor BAI3 control the synaptic connectivity of excitatory inputs converging on cerebellar purkinje cells. *Cell Rep.* 10, 820–832. doi: 10.1016/j.celrep.2015.01.034

Thiers, F. A., Nadol, J. B. Jr., and Liberman, M. C. (2008). Reciprocal synapses between outer hair cells and their afferent terminals: evidence for a local neural network in the mammalian cochlea. *J. Assoc. Res. Otolaryngol.* 9, 477–489. doi: 10.1007/s10162-008-0135-x

Webber, J. L., Clancy, J. C., Zhou, Y., Yraola, N., Homma, K., and García-Añoveros, J. (2021). Axodendritic versus axosomatic cochlear efferent termination is determined by afferent type in a hierarchical logic of circuit formation. *Sci. Adv.* 7:eabd8637. doi: 10.1126/sciadv.abd8637

Xing, Y., Samuvel, D. J., Stevens, S. M., Dubno, J. R., Schulte, B. A., and Lang, H. (2012). Age-related changes of myelin basic protein in mouse and human auditory nerve. *PLoS One* 7:e34500. doi: 10.1371/journal.pone.0034500

Zheng, J. L., Shou, J., Guillemot, F., Kageyama, R., and Gao, W. Q. (2000). Hes1 is a negative regulator of inner ear hair cell differentiation. *Development* 127, 4551–4560. doi: 10.1242/dev.127.21.4551

Conflict of Interest: The authors declare that the research was conducted in the absence of any commercial or financial relationships that could be construed as a potential conflict of interest.

frontiers
in Cellular Neuroscience

ORIGINAL RESEARCH
published: 09 March 2022
doi: 10.3389/fncel.2022.851500

Detecting Cochlear Synaptopathy Through Curvature Quantification of the Auditory Brainstem Response

Jianxin Bao[1,2]†, Segun Light Jegede[3]†, John W. Hawks[2], Bethany Dade[2], Qiang Guan[4], Samantha Middaugh[1], Ziyu Qiu[2], Anna Levina[3] and Tsung-Heng Tsai[3]*

[1] Department of Anatomy and Neurobiology, Northeast Ohio Medical University, Rootstown, OH, United States, [2] Department of Research and Development, Gateway Biotechnology Inc., Rootstown, OH, United States, [3] Department of Mathematical Sciences, Kent State University, Kent, OH, United States, [4] Department of Computer Science, Kent State University, Kent, OH, United States

Edited by:
David Z. He,
Creighton University, United States

Reviewed by:
Chris Spankovich,
University of Mississippi Medical Center, United States
Debashree Mukherjea,
Southern Illinois University Carbondale, United States

***Correspondence:**
Jianxin Bao
jbao@neomed.edu

†*These authors have contributed equally to this work*

Specialty section:
This article was submitted to Non-Neuronal Cells, a section of the journal Frontiers in Cellular Neuroscience

Received: *10 January 2022*
Accepted: *14 February 2022*
Published: *09 March 2022*

Citation:
Bao J, Jegede SL, Hawks JW, Dade B, Guan Q, Middaugh S, Qiu Z, Levina A and Tsai T-H (2022) Detecting Cochlear Synaptopathy Through Curvature Quantification of the Auditory Brainstem Response. Front. Cell. Neurosci. 16:851500. doi: 10.3389/fncel.2022.851500

The sound-evoked electrical compound potential known as auditory brainstem response (ABR) represents the firing of a heterogenous population of auditory neurons in response to sound stimuli, and is often used for clinical diagnosis based on wave amplitude and latency. However, recent ABR applications to detect human cochlear synaptopathy have led to inconsistent results, mainly due to the high variability of ABR wave-1 amplitude. Here, rather than focusing on the amplitude of ABR wave 1, we evaluated the use of ABR wave curvature to detect cochlear synaptic loss. We first compared four curvature quantification methods using simulated ABR waves, and identified that the cubic spline method using five data points produced the most accurate quantification. We next evaluated this quantification method with ABR data from an established mouse model with cochlear synaptopathy. The data clearly demonstrated that curvature measurement is more sensitive and consistent in identifying cochlear synaptic loss in mice compared to the amplitude and latency measurements. We further tested this curvature method in a different mouse model presenting with otitis media. The change in curvature profile due to middle ear infection in otitis media is different from the profile of mice with cochlear synaptopathy. Thus, our study suggests that curvature quantification can be used to address the current ABR variability issue, and may lead to additional applications in the clinic diagnosis of hearing disorders.

Keywords: cochlear synaptopathy, hidden hearing loss, noise-induced hearing loss, otitis media, Down syndrome

HIGHLIGHTS

- We developed a new method to detect cochlear synaptopathy using curvature quantification.
- We identified that the cubic spline method applied to five data points produces the most accurate curvature quantification of ABR waves.
- We demonstrated better detection ability using this curvature method than the currently accepted amplitude method.

INTRODUCTION

In neurodegenerative diseases, synaptic loss often occurs before obvious functional changes. Loss of synapses in Alzheimer's disease starts years before symptoms appear, which contributes to mild cognitive impairment (John and Reddy, 2021). A similar early synaptic loss occurs in both the peripheral and central auditory systems (for recent reviews, Bharadwaj et al., 2019; Ibrahim and Llano, 2019; Kujawa and Liberman, 2019). If synaptic loss could be diagnosed by non-invasive detection tools, risk factors favoring degenerative mechanisms could be identified in earlier stages, and the loss of the ability to manage daily living activities could be delayed (for reviews, Mukherjea et al., 2011; Henstridge et al., 2016; Spankovich and Yerraguntla, 2019). The seminal discovery of cochlear synaptopathy was initially made in CBA/CaJ mice following moderate noise exposure (Kujawa and Liberman, 2009). They showed, using a precise quantification of synaptic loss by means of immunocytochemistry, the loss of up to half of the synapses between inner hair cells (IHCs) and spiral ganglion neurons (SGNs), despite full recovery of hearing thresholds as measured by auditory brainstem response (ABR). Subsequent detailed analyses identified noise conditions that led to a significant permanent decrease in the supra-threshold growth of ABR wave I amplitude, despite a full recovery of distortion product otoacoustic emission (DPOAE) amplitudes (Furman et al., 2013; Fernandez et al., 2020). The DPOAE measurement is important because it eliminates possible confounding effects on the ABR wave I from damage to outer hair cells (OHCs).

Currently, there are no validated non-invasive clinical tools or battery of test to detect cochlear synaptopathy in humans (Bramhall et al., 2019). Pure-tone audiometry is still the primary tool for detecting hearing loss. However, clinicians often find that patients within normal audiometric thresholds complain of difficulty hearing in noise and other auditory perceptual anomalies (Plack et al., 2016). Hidden hearing loss (HHL) is used to describe this condition (Schaette and McAlpine, 2011). Although behavioral tests may be possible to detect cochlear deafferentation (e.g., Lobarinas et al., 2020), an ABR based detection method could be ideal for detecting auditory dysfunction because it is already used in clinical settings and a decreased ABR wave-I amplitude is associated with cochlear synaptopathy in animal studies (Kobel et al., 2017). In humans there are five prominent ABR waves that are labeled wave I, II, III, IV, and V, with the wave I and II have been correlated with auditory nerve function of the distal and more proximal portions, respectively (for review, Hall and Rupp, 1997). Five similar waves can be observed in animal models (Waves 1–5). Based on previous animal studies, HHL could be due to cochlear synaptopathy of SGNs with predominantly low spontaneous rate (SR) and high thresholds, which likely leads to no detectable changes in audiometric thresholds (Furman et al., 2013). Recent data from CBA/CaJ mice further confirmed this noise-induced synaptic loss, but demonstrated a synaptic loss of both low- and high-SR SGNs (Suthakar and Liberman, 2021). In spite of this emerging evidence of cochlear synaptopathy in rodents, primates (Valero et al., 2017) and post-mortem human tissues (Wu et al., 2019), functional determination of this synaptic loss in humans is not conclusive (e.g., Fulbright et al., 2017; Grinn et al., 2017; Prendergast et al., 2019). By comparing participant groups exposed to either low or high amounts of noise, a correlation between ABR or electrocochleography (ECochG) wave I amplitude and estimated noise exposure has been found in some studies but not in others (Stamper and Johnson, 2015a; Liberman et al., 2016; Bramhall et al., 2017; Guest et al., 2018). Most importantly, even if there is a consistent correlation from the population data, for clinical use, we still need a sensitive detection method for individual diagnosis. Failure of consistent detection with these methods is mainly due to high variability in wave-I amplitude. The high variability in human ABR/ECochG wave I in population studies is due to a number of factors, such as head size, sex, and genetic heterogeneity (Stamper and Johnson, 2015b; Bharadwaj et al., 2019). This variability can be reduced by using longitudinal studies of individual subjects, similar to preclinical studies (Kujawa and Liberman, 2009). However, for individual diagnosis, random electrical noise such as brain and muscle electrical activities can still lead to high variability in ABR wave-I amplitude across repeated measurements. In addition, the ABR wave-I amplitude is not sensitive to the loss of low-SR SGN fibers, due to the delayed and broad first-spike latency distribution of low-SR fibers (Bourien et al., 2014).

Besides wave amplitude, the shape of ABR/ECochG waves may provide additional information regarding synaptic loss of SGNs. Wave I comes from the summed response of a mixed population of SGN fibers. Due to the effects of the averaging process used with ABR/ECochG, the shape of the wave I averaged response is dependent on the conduction velocity and fiber diameter of the contributing neurons, which vary depending on each fiber's type and location in the cochlea (e.g., Liberman, 1982). High-SR and low-threshold SGN fibers have shorter first-spike latencies than SGN fibers with low-SR and high-threshold fibers (Heil and Irvine, 1997). Compared with high-SR and low-threshold SGNs, low-SR and high-threshold fibers have larger dynamic firing ranges, longer first-spike latencies, and slower conduction velocities (Liberman, 1978; Heil and Irvine, 1997). Subsequently, different SGN fibers may contribute to different parts of ABR wave I shape. Thus, one possible solution to the high variability issue of wave I amplitude is to quantify the shape characteristics of the wave using curvature instead of their amplitudes. Here, we first compared four curvature quantification methods using simulated ABR waves, and identified that the cubic spline method using five data points produced the most accurate quantification. We next evaluated this quantification method with ABR data from an established mouse model of cochlear synaptopathy. Our curvature measurement can quantify curvature changes of three areas of ABR wave 1: the right curve, the peak, and the left curve. This method is much more sensitive and consistent in identifying cochlear synaptic loss in mice than the amplitude and latency measurements. We further tested this curvature method in a different mouse model of conductive hearing loss, and found a different curvature profile for early hearing loss due to middle ear infection in mice with otitis media. This suggests that this curvature method is sensitive to detect cochlear deafferentation, and it is promising to detect other types of hearing loss based on its different curvature profiles.

MATERIALS AND METHODS

Ethics Statement

All mouse studies were approved by the Institutional Animal Care and Use Committee of Northeast Ohio Medical University (NEOMED) in accordance with the National Institutes of Health guidelines.

Animals

The animal data were collected from 4-month-old CBA/CaJ mice (n = 58, 31 males) and 8–9-week-old Ts65Dn mice (n = 12, 6 males) obtained from the Jackson Laboratory (Bar Harbor, ME, United States). For CBA/CaJ mice, after initial ABR and DPOAE threshold testing was conducted to ensure normal hearing, mice were randomly assigned to one of two groups: a control group without noise exposure, and a 96-dB group exposed to a band of noise (8–16 kHz) at 96 dB SPL for 2 h. Mice were then held for 2 weeks post exposure before repeating ABR and DPOAE threshold testing, as well as ABR click testing. For the Ts65Dn mice, similar ABR threshold, ABR click, and DPOAE threshold testing were conducted, as well as tympanometric measurements to assess for otitis media.

Noise Exposures

A free-field noise exposure was used whereby each mouse was unrestrained in a sub-divided cage within a foam-lined, double-walled, sound-isolated room (Industrial Acoustics, North Aurora, IL, United States). The band of noise (8–16 kHz) was generated with custom LabVIEW software, and routed through a power amplifier (Crown CDi1000) to a loudspeaker (Selenium D3500Ti-Nd, JBL, Northridge, CA, United States). Before each exposure, noise levels were calibrated to 96 dB SPL, and during the exposure, the noise level was continually monitored at the center of the cage using a B&K 4153 1/4-inch microphone connected to an amplifier (1–100,000 Hz; Bruel & Kjaer Nexus Amplifier).

Auditory Physiologic Tests

Similar to our previous studies (e.g., Bao et al., 2004, 2013), mice were anesthetized with a solution of ketamine and xylazine

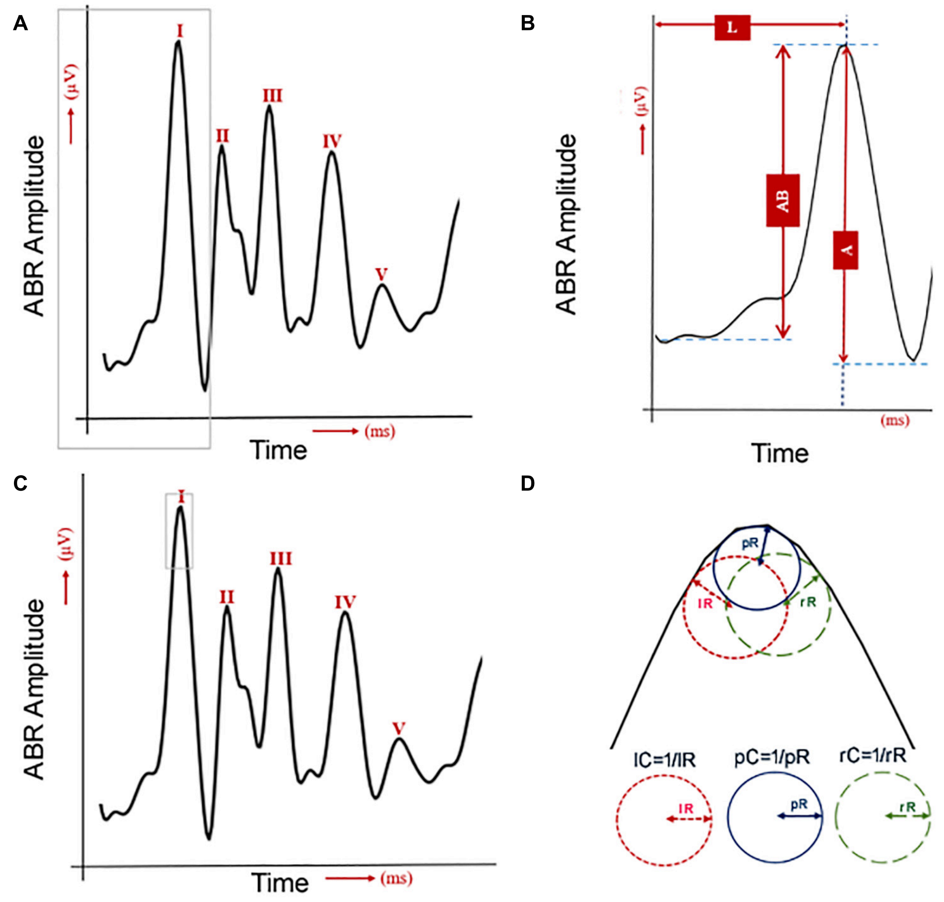

FIGURE 1 | Quantification of six ABR wave-I features. **(A)** One human ABR sample with five waves. The gray lines were used to label the wave I, which is used for the next panel. **(B)** The human ABR wave 1 was commonly analyzed by measurements of latency (L) and amplitude. The amplitude was quantified either by the peak to the baseline (AB) or the peak to the trough (A). **(C)** The same human ABR sample with five waves with the gray lines to label the area for curvature analysis in panel **(D)**. **(D)** Three curvature quantifications for the shape of ABR wave I.

(80/15 mg/kg, i.p.) and positioned dorsally in a custom head holder. Mouse body temperature was maintained at 37.5 ± 1.0°C using an isothermal pad. DPOAEs were measured using an ER10B+ microphone/pre-amplifier (Etymotic Research) and processed with a TDT RZ6/BioSigRZ system (Tucker-Davis Technologies). DPOAEs were elicited with two pure tones, f1 and f2, using an f2/f1 ratio of 1.2, where F2 = 20 kHz, with emissions collected for levels from 90 to 0 dB SPL in 5 dB steps. One hundred sweeps were presented at each test frequency. Input/output functions of DPOAE were quantified and the threshold of DPOAE was defined as the level at which a response could be noted at least 5 dB SPL above the noise floor.

For all ABR testing, three electrodes were placed subdermally behind the test ear (active), the vertex (reference), and the base of the tail (ground). Evoked potentials were collected using a Tucker Davis Technology (TDT) RZ6 processor and BioSigRZ software. Thresholds were obtained by presenting tone bursts at 5, 10, 20, and 40 kHz from 90 dB SPL descending in 5 dB steps to 0 dB SPL or 10 dB below threshold. Tones were 5 ms in duration, 0.5 ms rise/fall, with a repetition rate of 17.1/s, with potentials averaged over 512 repetitions. Threshold was defined as the level where any ABR wave could be identified. ABR responses were also obtained using click stimuli with an initial onset of 0.1 ms presented at 70 and 90 dB peSPL. Clicks were 0.1 ms in duration, of alternating polarity with a repetition rate of 1.9/s. Evoked potentials were averaged over 1024 repetitions and band-pass filtered (100–3,000 Hz).

Curvature Quantification

For the data collected from the click sound stimulation, a computational workflow implemented in Python was used to process the ABR data (**Figure 1**): peak amplitude from trough (A), peak amplitude from baseline (AB), peak latency (L), peak curvature (pC), left curvature (lC), and right curvature (rC). For curvature calculations, four methods were considered (Stoer and Bulirsch, 1992): non-linear least squares (NLLS), Lagrange polynomials (LGP), numerical differentiation (ND), and cubic spline (CS). For a particular data point from an ABR wave, (x, y), the curvature of this point is defined as

$$k = \frac{|x'y'' - y'x''|}{\left[(x')^2 + (y')^2\right]^{3/2}}$$

where the numerical differentiation method finds the partial derivatives based on n data points around (x, y). When y is considered as a function of x, $y = f(x)$, the above formula is simplified to

$$k = \frac{|f''(x)|}{\left[1 + (f'(x))^2\right]^{3/2}}$$

Statistical Analysis

Following feature quantification, statistical analyses were performed using R[1] to determine the significance of the

---

[1] https://www.R-project.org

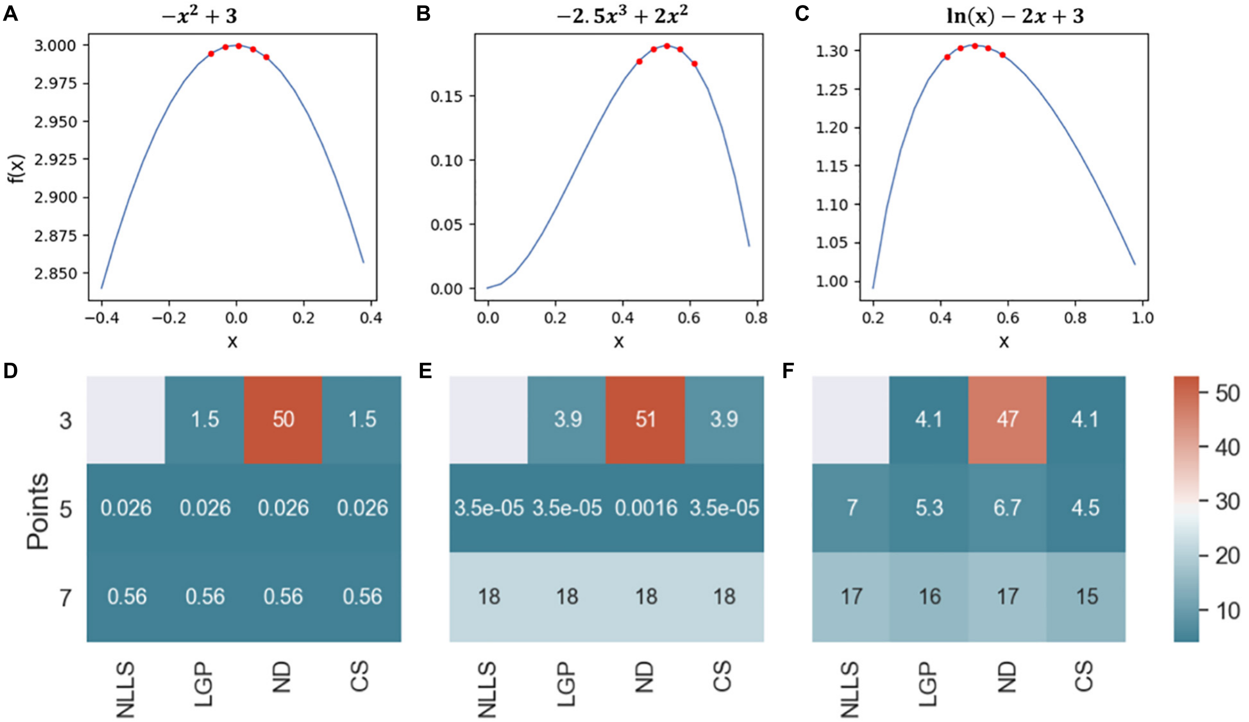

FIGURE 2 | Comparison of four curvature measurements with simulated ABR waves. **(A–C)** Three simulated ABR waves. The five red dots at the peak illustrated how the peak curvature was quantified with five data points. **(D–F)** Three heatmaps were used to summarize the quantification accuracy among four quantification methods.

difference in curvature, amplitude and latency changes between pre- and post-noise exposures (for CBA/CaJ mice) and that between normal and mice with otitis media (for Ts65Dn mice). For detecting possible changes of ABR wave-1, we quantified a total of six features (**Figure 1**). ABR wave-I amplitude was measured in two ways: from the baseline (AB) or from the next trough (A). Its latency was measured from the sound stimulation onset to the wave-I peak (L) (**Figures 1A,B**). Its peak (pC), left (lC), and right curvature (rC) were also quantified (**Figure 1D**). Since two ABR data collections (pre- and post-noise exposure) were made for each CBA/CaJ mouse, a paired *t*-test was applied to evaluate the mean difference in quantified features between the pre- and post-noise exposure. In the detection of hearing loss in otitis media mice, two separate groups of mice (control vs. otitis media) were analyzed and a two-sample *t*-test was used. For all the differential analyses, a significance level of 0.05 was considered.

RESULTS

Comparison Among Four Curvature Quantification Methods

To identify the best curvature quantification method for ABR waves, we first compared the four curvature quantification methods with three simulated ABR waves (**Figures 2A–C**). The three simulated curves were considered for the following characteristics observed in ABR waves: (1) symmetric and non-symmetric shapes, and (2) sampling rate of 24,414.0625 Hz to mimic our ABR recording system (Tucker-Davis Technologies, United States). To cover all possible wave changes around wave peaks, curvature quantification was performed for three, five, or seven points. The quantification accuracy was based on the percent absolute error of the calculated curvature value and the results are summarized in a heatmap (**Figures 2D–F**). For the first simulated ABR curve, the accuracy for all four measurements was the same except for the ND method with 3 data points (**Figure 2D**). For the other two simulated waves, the CS method with five data points produced either equal to or the most accurate results than the other curvature quantification methods. Based on these simulation results, we subsequently chose the CS approach.

Development of Mouse Model for Noise-Induced Cochlear Synaptopathy

Based on previous detailed studies of cochlear synaptopathy in the same mouse strain (e.g., Fernandez et al., 2020; Suthakar and Liberman, 2021), we assigned CBA/CaJ mice to one of two groups: control or noise-exposed (96 dB SPL for 2 h). Hearing function of the mice was quantified by both ABR and DPOAE

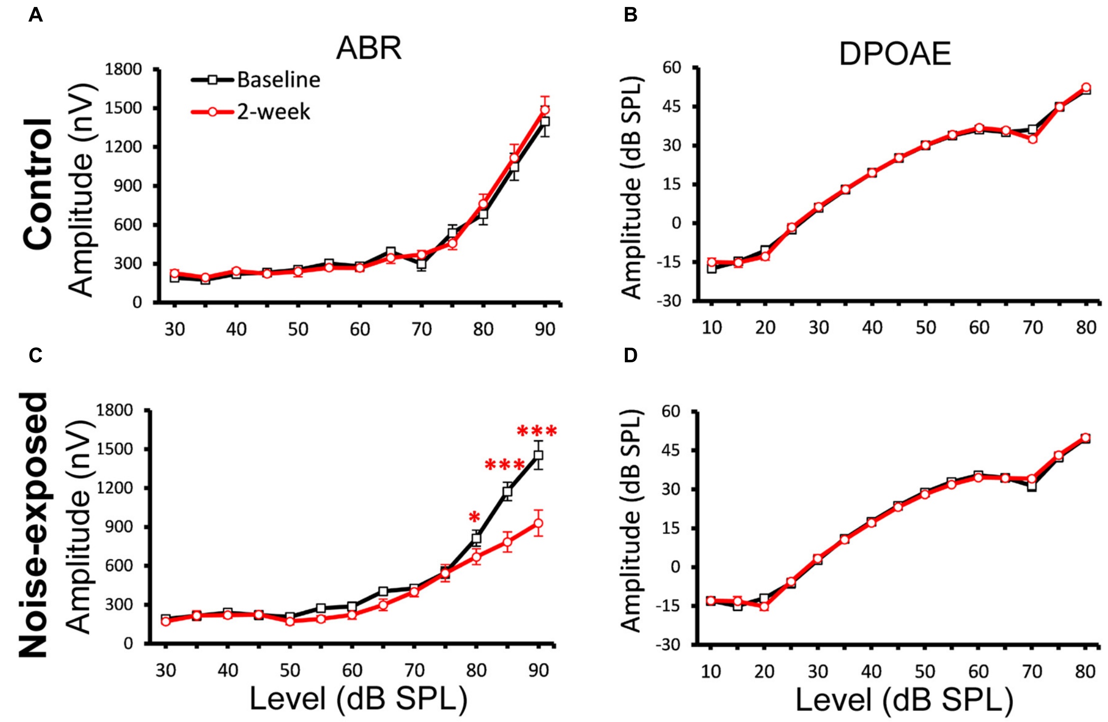

FIGURE 3 | A decrease of ABR Wave-1 supra-threshold amplitudes only in the noise-exposed group. ABR and DPOAE at 20 kHz were tested for both the control and noise-exposed mice before (Baseline) and 2-week after the noise exposure. **(A)** No changes of ABR amplitudes between the baseline and post 2-week measurement in the control mice. **(B)** No change of DPOAE amplitudes in the control mice. **(C)** A significant decrease of ABR amplitudes between the baseline and post 2-week measurement for the noise-exposed mice. **(D)** No change of DPOAE amplitudes in the noise-exposed mice. * $p < 0.05$. *** $p < 0.01$. Data shown are the means ± 1 SEM.

methods before and after the noise exposure to detect temporary threshold shift (TTS; 1 day after noise exposure) and permanent threshold shift (PTS; 2 weeks after noise exposure). Three-factor ANOVAs, with frequency and time as within-subjects effects, revealed a group difference for both ABR threshold [$F(12, 432) = 30.7130$; $p = 2.0787\text{E-}43$] and DPOAE threshold [$F(12, 417) = 33.6826$; $p = 8.4233\text{E-}46$]. For control mice ($n = 19$; 10 males) without noise exposure, no significant TTS or PTS were observed. In contrast, for noise-exposed mice ($n = 25$, 13 males), post-hoc analyses revealed TTS at 10 kHz ($p = 0.0009$, ABR threshold; $p = 0.0058$, DPOAE threshold), 20 kHz ($p = 7.271\text{E-}21$, ABR threshold; $p = 8.8521\text{E-}32$, DPOAE threshold), and 40 kHz ($p = 7.2229\text{E-}52$, ABR threshold; $p = 1.7373\text{E-}52$, DPOAE threshold). The 2-week thresholds of the noise-exposed mice were not significantly different from the pre-exposure thresholds, indicating that none sustained PTS. Thus, mice from the 96-dB noise group had TTS, but no PTS.

In mouse models, it is established that cochlear synaptopathy is highly correlated with reduced ABR wave-1 amplitudes at supra-threshold levels once OHC functions have recovered following noise exposure (Furman et al., 2013; Fernandez et al., 2015, 2020). We subsequently quantified ABR wave-1 and DPOAE amplitude in the same two mouse groups (**Figure 3**). A significant decrease in ABR wave-1 amplitude with suprathreshold sound stimulation was not found in the control group (**Figure 3A**), but was found in the noise-exposed group 2 weeks post noise exposure (**Figure 3C**). Three-factor ANOVAs (group x time x level), with time and stimulus level as within-subjects effects, indicated a significant reduction of ABR wave-1 amplitude at 20 kHz 2 weeks post exposure [$F(26, 1034) = 3.9049$; $p = 1.1221\text{E-}9$]. Bonferroni's multiple comparisons test at each sound intensity/time combination revealed a significant difference at 80 dB SPL ($p = 0.0233$), 85 dB SPL ($p = 1.196\text{E-}9$) and 90 dB SPL ($p = 7.4444\text{E-}16$), while no significant changes in DPOAE amplitude were found for either the control (**Figure 3B**) or the noise-exposed group (**Figure 3D**). Thus, the noise-exposed group showed a typical phenotype of cochlear synaptopathy.

Comparison of Curvature and Amplitude Quantification

To determine which features of ABR wave-1 are strongly associated with cochlear synaptopathy, we compared six quantitative features from ABR data collected with 70 or 90 dB SPL sound stimulation from the same mice pre-noise exposure and 2 weeks post-noise exposure (**Figure 4**). No obvious changes in latency were observed for either group of mice (**Figures 5A,B** first panel). Both amplitude measurements (A and AB) showed similar results, thus, we only present results for the

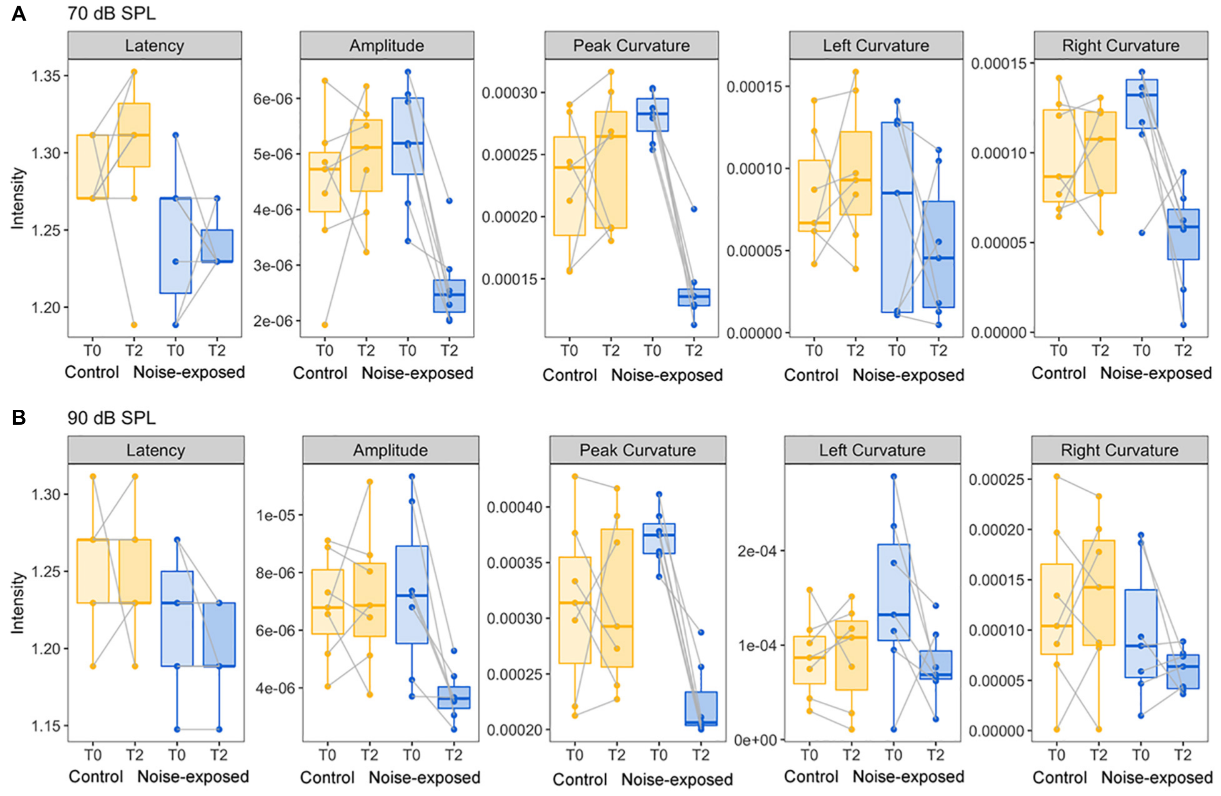

FIGURE 4 | Comparison of five ABR features between control mice and noise-exposed mice. **(A)** For the ABR wave 1 evoked by 70 dB SPL, a decreased of ABR amplitude, peak and right curvature quantifications were found only for mice post noise exposure at 96 dB SPL. **(B)** For the ABR wave 1 evoked by 90 dB SPL, decreases of ABR amplitude, peak, and left curvature quantifications were found only for mice post noise exposure at 96 dB SPL.

peak-to-trough amplitude (A). At 70 dB SPL (**Figure 4A**), for the control group, no obvious changes in these six features were observed between the baseline and 2-week post exposure data, as expected. In contrast, for the noise-exposed group, the amplitude measurement (A) showed a decreased amplitude with a small amount of overlap between pre- and post-exposure data points (the second panel). In contrast, a decreased peak curvature was observed for every noise-exposed mouse with no overlap between pre- and post-noise exposure data (the third pane). A trend of decreased curvature post-exposure was also observed for both the left (lC; the fourth panel) and right sides (rC; the fifth panel) of ABR wave-1. At 90 dB SPL (**Figure 4B**), no differences in these features were observed for the control group. In contrast, for the noise-exposed group, a decreased ABR amplitude (A) was observed with an overlap between pre- and post-exposure, while the pC for the same wave was clearly decreased for every noise-exposed mouse post-exposure. A similar but less consistent trend of curvature decrease was also found for both lC and right rC measures. The same data were statistically analyzed. With 70 dB SPL stimulation (**Table 1**), for the noise-exposed group, the difference in amplitude (A) was significant between pre- and post-noise exposure (p = 0.0008), while the pC quantification provided a better separation between pre- and post-noise exposure ($p < 0.0001$). We also found a significant difference for the noise-exposed group in right curvature (rC) between pre- and post-noise exposure (p = 0.0153). With 90 dB SPL stimulation (**Table 2**), for the noise-exposed group, a significant difference in amplitude (A) was noted between pre- and post-noise exposure (p = 0.0096), while an even more significant difference in the pC measurements between pre- and post-noise exposure was observed (p = 0.0002). In short, at both sound intensities, the curvature measurements were more sensitive than the amplitude measurements in detecting cochlear synaptic loss.

Curvature Quantification in Detecting Hearing Loss of Otitis Media

In order to determine if these observed curvature profiles were specific to cochlear synaptopathy, we repeated the same method in a mouse model of otitis media. Since about 70% of mice with Down syndrome from the Ts65Dn transgenic mouse model develop otitis media at 3 months old (Han et al., 2009), we performed similar ABR and DPOAE threshold tests on Ts65Dn mice at 8–9 weeks old. Among 12 mice tested, six had normal ABR and DPOAE thresholds and tympanograms within the range of normal, and the remainder presented with acute otitis media (AOM). DPOAE thresholds for all AOM mice were below the noise floor and five of the six had elevated ABR thresholds. A statistically significant difference was only found for ABR thresholds (p = 0.004) between the control and AOM mice (**Table 3**). Interestingly, quantitative analysis of their ABR wave-1 click responses showed a pattern different from normal for mice with acute otitis media (**Figure 5**). With 70 dB SPL stimulation (**Table 4**), there were significant differences between the control and AOM mice in amplitude (A; p = 0.0037), pC (p = 0.0143), and lC (p = 0.0332), while with 90 dB

TABLE 1 | Result of the paired t-test for the difference between pre- and post-noise exposure at the 70 dB SPL.

Group	Feature	t-statistic	df	p-value
Control	L	−0.4714	6	0.6540
Control	A	−0.8989	6	0.4033
Control	pC	−0.6170	6	0.5599
Control	lC	−0.7160	6	0.5009
Control	rC	−0.0772	6	0.9409
Noise-exposed	L	0.2810	6	0.7882
Noise-exposed	A	6.2403	6	0.0008*
Noise-exposed	pC	9.5886	6	< 0.0001*
Noise-exposed	lC	0.8323	6	0.4371
Noise-exposed	rC	3.3555	6	0.0153*

*L = latency, A = amplitude, pC = peak curvature, lC = left curvature, rC = right curvature, and df = degrees of freedom. The t-statistic is the ratio of the mean feature difference (T0–T2) to its standard error. A p-value less than the significance level (0.05) is labeled with a *.*

TABLE 2 | Result of the paired t-test for the difference between pre- and post-noise exposure at the 90 dB SPL.

Group	Feature	t-statistic	df	p-value
Control	L	0.2810	6	0.7882
Control	A	−0.3453	6	0.7417
Control	pC	−0.1089	6	0.9168
Control	lC	−0.1201	6	0.9083
Control	rC	−0.4275	6	0.6839
Noise-exposed	L	1.4412	6	0.1996
Noise-exposed	A	3.7451	6	0.0096*
Noise-exposed	pC	8.2330	6	0.0002*
Noise-exposed	lC	1.9179	6	0.1036
Noise-exposed	rC	1.3439	6	0.2276

*L = latency, A = amplitude, pC = peak curvature, lC = left curvature, rC = right curvature, and df = degrees of freedom. The t-statistic is the ratio of the mean feature difference (T0–T2) to its standard error. A p-value less than the significance level (0.05) is labeled with a *.*

TABLE 3 | Tympanometry, DPOAE and ABR data of Ts65Dn transgenic mice.

Group	SC (ml)	TP (-daPa)	DPOAE (dB)	ABR (dB)
Control	2.32	9	40	25
Control	1.32	35	45	30
Control	1.32	43	45	25
Control	1.13	11	45	40
Control	1.15	47	45	25
Control	1.68	19	40	25
Otitis Media	1.16	70	N/A	50
Otitis Media	0.8	27	N/A	55
Otitis Media	0.74	12	N/A	55
Otitis Media	0.83	37	N/A	35
Otitis Media	1.56	20	N/A	65
Otitis Media	0.91	23	N/A	35
p-value	0.06	0.71	N/A	0.004*

*Static compliance (SC) and tympanometry pressure (TP) were obtained from tympanometry. Both DPOAE and ABR data were collected at 20 kHz, a sensitive hearing region for mice. For each measurement, a two-sample t-test between control mice and mice with otitis media was performed. A p-value less than the significance level (0.05) is labeled with a *.*

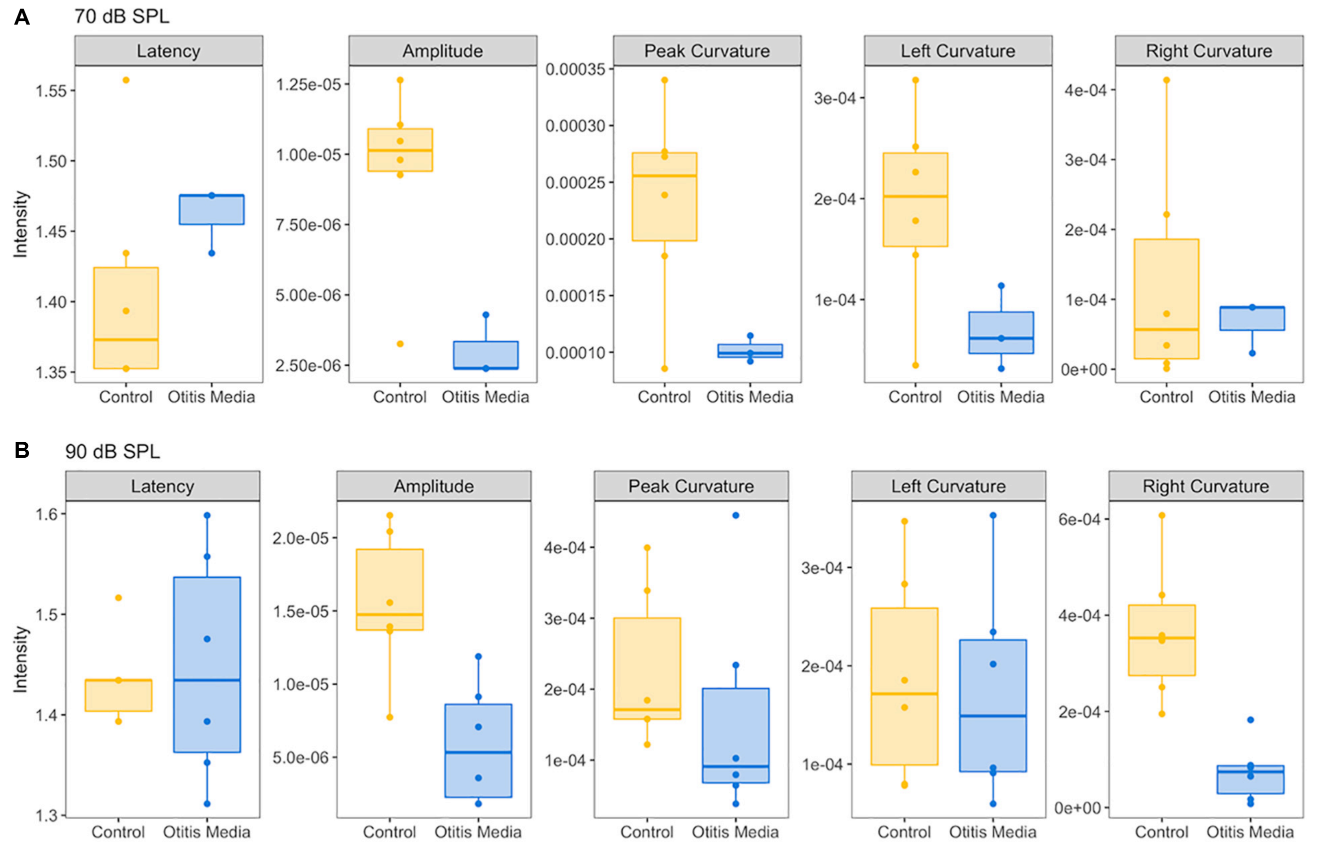

FIGURE 5 | Comparison of five ABR features between control mice and mice with otitis media. **(A)** For the ABR wave 1 evoked by 70 dB SPL, compared to control mice, a decrease of ABR amplitude, peak and left curvature were found for mice with otitis media. **(B)** For the ABR wave 1 evoked by 90 dB SPL, decreases of ABR amplitude and right curvature were found for mice with otitis media.

SPL stimulation, significant differences were only observed for amplitude (A; $p = 0.0052$) and rC ($p = 0.0032$), Thus, the curvature profile for otitis media, which is mainly due to middle ear dysfunction, was different from the curvature profile for cochlear synaptopathy.

TABLE 4 | Result of the two-sample *t*-test for the difference in feature measurements between control and otitis media groups.

Levels	Feature	*t*-statistic	df	*p*-value
70 dB	L	−1.53	6.40	0.173
70 dB	A	4.36	6.69	0.0037*
70 dB	pC	3.58	5.33	0.0143*
70 dB	lC	2.65	6.99	0.0332*
70 dB	rC	0.854	5.97	0.426
90 dB	L	−0.271	6.49	0.795
90 dB	A	3.59	9.65	0.0052*
90 dB	pC	0.842	9.17	0.421
90 dB	lC	0.249	9.99	0.809
90 dB	rC	4.50	6.78	0.0030*

*L = latency, A = amplitude, pC = peak curvature, lC = left curvature, rC = right curvature, and df = degrees of freedom. A p-value less than the significance level (0.05) is labeled with a *.*

DISCUSSION

To address the current failure of detecting cochlear synaptopathy by ABR/ECochG methods, we developed a new method to quantify possible changes in ABR/ECochG wave-1. Instead of relying on amplitude measurements, we focused on curvature measurements, and identified that the cubic spline method calculated with five data points as the most accurate method for assessing changes of ABR wave 1. Using a well-established mouse model of cochlear synaptopathy, we demonstrated that these curvature measurements are more sensitive and consistent in identifying individual mice with cochlear synaptic loss compared to amplitude measurements.

Our findings have directly addressed the high variability of ABR/ECochG wave-I amplitude, which is a major current obstacle in applying ABR/ECochG methods for human diagnosis. Although curvature quantification is well established in other fields, no studies of its application are reported for ABR/ECochG data analysis. Potential advantages of our new approach are: (1) less influenced by background noise compared to more traditional wave peak amplitude analyses, and (2) potentially more sensitive to cochlear synaptic loss of low-SR SGN fibers. Both of these advantages may be the reasons underlying our finding that the curvature method is much more sensitive than the amplitude method. In addition, the change of curvature profiles are different between the mouse model with cochlear synaptopathy and the mouse model with otitis media. Early hearing loss of otitis media is due to the middle ear infection without a significant damage to the cochlea (Trune and Zheng, 2009). Its significant curvature changes are that pC and lC to sound clicks at 70 dB SPL, and only rC to sound clicks at 90 dB SPL. In the mouse model with noise-induced cochlear synaptopathy, pC values are reduced to sound clicks to both 70 and 90 dB SPL, and the rC value is reduced only at 70 dB SPL. Since the major difference between these two animal models is a different cause of hearing loss: synaptic damages vs. middle ear infection, different curvature profiles of ABR wave 1 is most likely associated with these two causes, respectively. However, it would be better to validate by other models of hearing loss. For example, we have found that early hearing loss in cisplatin-induced hearing is associated with mitochondrial loss in SGNs only (Chen et al., 2021), and it would be interesting to apply the same method to identify curvature profiles in this model. In addition, most of noise-induced hearing loss in humans is less likely to cause purely syanptopathy, and may include other cochlear damages such as loss of OHCs (e.g., Fernandez et al., 2020); noise exposure can also create early damage to the extreme base of the cochlea which may influence mass-stiffness properties of the basilar membrane. All these damages may cause possible changes of ABR wave-1 shape. Additional studies are needed to validate our method in these models.

There are several limitations of our study. Due to central neural plasticity (Gold and Bajo, 2014; Lewis et al., 2015), we are aware that cochlear synaptopathy could lead to central plasticity changes, which would result in curvature changes of other ABR waves. In the future, it is worth to carry out a multi-metric approach to the curvature quantification of all major ABR/ECochG waves that reflect activity in both peripheral and central auditory areas (McClaskey et al., 2020). An intrinsic technical issue with this approach would be the reliable identification of multiple functional features associated with cochlear synaptopathy *via* subjective analyses of ABR/ECochG waveform tracings. Recently, machine learning has been developed as an effective statistical technique for identifying multiple features associated with complex phenomena and has been successfully applied in auditory research (e.g., Bramhall et al., 2018). Thus, machine learning may be tested to identify key features in ABR/ECochG waveforms. The other major weakness is a lack of human validation study. It is our general strategy to improve ABR/ECochG data collection and analysis first in well-established animal models, and then validate them in future human studies.

DATA AVAILABILITY STATEMENT

The original contributions presented in the study are included in the article/supplementary material, further inquiries can be directed to the corresponding author.

ETHICS STATEMENT

The animal study was reviewed and approved by the Institutional Animal Care and Use Committee of NEOMED.

AUTHOR CONTRIBUTIONS

JB, SJ, JH, QG, and T-HT were responsible for the experimental design. JB, SJ, JH, BD, SM, ZQ, AL, and T-HT were responsible for data analysis. JB, JH, and T-HT were responsible for providing overall ideas. All authors contributed to the article and approved the submitted version.

FUNDING

This work was supported (in part) by grants from the National Institute on Deafness and Other Communication Disorders (NIDCD) of the National Institutes of Health (NIH), R41 DC017406-01 (JB), the United States Department of the Army W81XWH19C0054 (JB), the 2020 Brain Health Research Institute (BHRI) Blue Award from Kent State University (JB and T-HT), and The Lemon research fund (JB).

ACKNOWLEDGMENTS

We wish to thank Yingying Chen, Christina Palomo, and Grace Szatkowski for preliminary studies, and funding supports from NIDCD, the United States Department of Army, and the BHRI at Kent State University.

REFERENCES

Bao, J., Hungerford, M., Luxmore, R., Ding, D., Qiu, Z., Lei, D., et al. (2013). Prophylactic and therapeutic functions of drug combinations against noise-induced hearing loss. *Hear. Res.* 304, 33–40. doi: 10.1016/j.heares.2013.06.004

Bao, J., Lin, H., Ouyang, Y., Lei, D., Osman, A., Kim, T. W., et al. (2004). Activity-dependent transcription regulation of PSD-95 by neuregulin-1 and Eos. *Nat. Neurosci.* 7, 1250–1258. doi: 10.1038/nn1342

Bharadwaj, H. M., Mai, A. R., Simpson, J. M., Choi, I., Heinz, M. G., and Shinn-Cunningham, B. G. (2019). Non-invasive assays of cochlear synaptopathy – candidates and considerations. *Neuroscience* 407, 53–66. doi: 10.1016/j.neuroscience.2019.02.031

Bourien, J., Tang, Y., Batrel, C., Huet, A., Lenoir, M., Ladrech, S., et al. (2014). Contribution of auditory nerve fibers to compound action potential of the auditory nerve. *J. Neurophysiol.* 112, 1025–1039. doi: 10.1152/jn.00738.2013

Bramhall, N. F., Konrad-Martin, D., McMillan, G. P., and Griest, S. E. (2017). Auditory brainstem response altered in humans with noise exposure despite normal outer hair cell function. *Ear Hear.* 38, e1–e12. doi: 10.1097/AUD.0000000000000370

Bramhall, N. F., McMillan, G. P., Kujawa, S. G., and Konrad-Martin, D. (2018). Use of non-invasive measures to predict cochlear synapse counts. *Hear. Res.* 370, 113–119. doi: 10.1016/j.heares.2018.10.006

Bramhall, N., Beach, E. F., Epp, B., Le Prell, C. G., Lopez-Poveda, E. A., Plack, C. J., et al. (2019). The search for noise-induced cochlear synaptopathy in humans: mission impossible? *Hear. Res.* 377, 88–103. doi: 10.1016/j.heares.2019.02.016

Chen, Y., Bielefeld, E. C., Mellott, J. G., Wang, W., Mafi, A. M., Yamoah, E., et al. (2021). Early physiological and cellular indicators of cisplatin-induced ototoxicity. *J. Assoc. Res. Otolaryngol.* 22, 107–126. doi: 10.1007/s10162-020-00782-z

Fernandez, K. A., Guo, D., Micucci, S., De Gruttola, V., Liberman, M. C., and Kujawa, S. G. (2020). Noise-induced cochlear synaptopathy with and without sensory cell loss. *Neuroscience* 427, 43–57. doi: 10.1016/j.neuroscience.2019.11.051

Fernandez, K. A., Jeffers, P. W., Lall, K., Liberman, M. C., and Kujawa, S. G. (2015). Aging after noise exposure: acceleration of cochlear synaptopathy in "recovered" ears. *J. Neurosci.* 35, 7509–7520. doi: 10.1523/JNEUROSCI.5138-14.2015

Fulbright, A. N. C., Le Prell, C. G., Griffiths, S. K., and Lobarinas, E. (2017). Effects of recreational noise on threshold and suprathreshold measures of auditory function. *Semin. Hear.* 38, 298–318. doi: 10.1055/s-0037-1606325

Furman, A. C., Kujawa, S. G., and Liberman, M. C. (2013). Noise-induced cochlear neuropathy is selective for fibers with low spontaneous rates. *J. Neurophysiol.* 110, 577–586. doi: 10.1152/jn.00164.2013

Gold, J. R., and Bajo, V. M. (2014). Insult-induced adaptive plasticity of the auditory system. *Front. Neurosci.* 8:110. doi: 10.3389/fnins.2014.00110

Grinn, S. K., Wiseman, K. B., Baker, J. A., and Le Prell, C. G. (2017). Hidden hearing loss? No effect of common recreational noise exposure on cochlear nerve response amplitude in humans. *Front. Neurosci.* 11:465. doi: 10.3389/fnins.2017.00465

Guest, H., Munro, K. J., Prendergast, G., Millman, R. E., and Plack, C. J. (2018). Impaired speech perception in noise with a normal audiogram: no evidence for cochlear synaptopathy and no relation to lifetime noise exposure. *Hear. Res.* 364, 142–151. doi: 10.1016/j.heares.2018.03.008

Hall, J. W. III, and Rupp, K. A. (1997). Auditory brainstem response: recent developments in recording and analysis. *Adv. Otorhinolaryngol.* 53, 21–45. doi: 10.1159/000059038

Han, F., Yu, H., Zhang, J., Tian, C., Schmidt, C., Nava, C., et al. (2009). Otitis media in a mouse model for Down syndrome. *Int. J. Exp. Pathol.* 90, 480–488. doi: 10.1111/j.1365-2613.2009.00677.x

Heil, P., and Irvine, D. R. (1997). First-spike timing of auditory-nerve fibers and comparison with auditory cortex. *J. Neurophysiol.* 78, 2438–2454. doi: 10.1152/jn.1997.78.5.2438

Henstridge, C. M., Pickett, E., and Spires-Jones, T. L. (2016). Synaptic pathology: a shared mechanism in neurological disease. *Ageing Res. Rev.* 28, 72–84. doi: 10.1016/j.arr.2016.04.005

Ibrahim, B. A., and Llano, D. A. (2019). Aging and central auditory disinhibition: is it a reflection of homeostatic downregulation or metabolic vulnerability? *Brain Sci.* 9:351. doi: 10.3390/brainsci9120351

John, A., and Reddy, P. H. (2021). Synaptic basis of Alzheimer's disease: focus on synaptic amyloid beta, P-tau and mitochondria. *Ageing Res. Rev.* 65:101208. doi: 10.1016/j.arr.2020.101208

Kobel, M., Le Prell, C. G., Liu, J., Hawks, J. W., and Bao, J. (2017). Noise-induced cochlear synaptopathy: past findings and future studies. *Hear. Res.* 349, 148–154. doi: 10.1016/j.heares.2016.12.008

Kujawa, S. G., and Liberman, M. C. (2009). Adding insult to injury: cochlear nerve degeneration after "temporary" noise-induced hearing loss. *J. Neurosci.* 29, 14077–14085. doi: 10.1523/JNEUROSCI.2845-09.2009

Kujawa, S. G., and Liberman, M. C. (2019). Translating animal models to human therapeutics in noise-induced and age-related hearing loss. *Hear. Res.* 377, 44–52. doi: 10.1016/j.heares.2019.03.003

Lewis, J. D., Kopun, J., Neely, S. T., Schmid, K. K., and Gorga, M. P. (2015). Tone-burst auditory brainstem response wave V latencies in normal-hearing and hearing-impaired ears. *J. Acoust. Soc. Am.* 138, 3210–3219. doi: 10.1121/1.4935516

Liberman, M. C. (1978). Auditory-nerve response from cats raised in a low-noise chamber. *J. Acoust. Soc. Am.* 63, 442–455. doi: 10.1121/1.381736

Liberman, M. C. (1982). The cochlear frequency map for the cat: labeling auditory-nerve fibers of known characteristic frequency. *J. Acoust. Soc. Am.* 72, 1441–1449. doi: 10.1121/1.388677

Liberman, M. C., Epstein, M. J., Cleveland, S. S., Wang, H., and Maison, S. F. (2016). Toward a differential diagnosis of hidden hearing loss in humans. *PLoS One* 11:e0162726. doi: 10.1371/journal.pone.0162726

Lobarinas, E., Salvi, R., and Ding, D. (2020). Gap detection deficits in chinchillas with selective carboplatin-induced inner hair cell loss. *J. Assoc. Res. Otolaryngol.* 21, 475–483. doi: 10.1007/s10162-020-00744-5

McClaskey, C. M., Panganiban, C. H., Noble, K. V., Dias, J. W., Lang, H., and Harris, K. C. (2020). A multi-metric approach to characterizing mouse peripheral auditory nerve function using the auditory brainstem response. *J. Neurosci. Methods* 346:108937. doi: 10.1016/j.jneumeth.2020.108937

Mukherjea, D., Rybak, L. P., Sheehan, K. E., Kaur, T., Ramkumar, V., Jajoo, S., et al. (2011). The design and screening of drugs to prevent acquired sensorineural hearing loss. *Expert Opin. Drug Discov.* 6, 491–505. doi: 10.1517/17460441.2011.562887

Plack, C. J., Léger, A., Prendergast, G., Kluk, K., Guest, H., and Munro, K. J. (2016). Toward a diagnostic test for hidden hearing loss. *Trends Hear.* 20:2331216516657466. doi: 10.1177/2331216516657466

Prendergast, G., Couth, S., Millman, R. E., Guest, H., Kluk, K., Munro, K. J., et al. (2019). Effects of age and noise exposure on proxy measures of cochlear synaptopathy. *Trends Hear.* 23:2331216519877301. doi: 10.1177/2331216519877301

Schaette, R., and McAlpine, D. (2011). Tinnitus with a normal audiogram: physiological evidence for hidden hearing loss and computational model. *J. Neurosci.* 31, 13452–13457. doi: 10.1523/JNEUROSCI.2156-11.2011

Spankovich, C., and Yerraguntla, K. (2019). Evaluation and management of patients with diabetes and hearing loss. *Semin. Hear.* 40, 308–314. doi: 10.1055/s-0039-1697644

Stamper, G. C., and Johnson, T. A. (2015a). Auditory function in normal-hearing, noise-exposed human ears. *Ear Hear.* 36, 172–184. doi: 10.1097/AUD.0000000000000107

Stamper, G. C., and Johnson, T. A. (2015b). Letter to the editor: examination of potential sex influences in auditory function in normal-hearing, noise-exposed human ears. *Ear Hear.* 36, 738–740. doi: 10.1097/AUD.0000000000000228

Stoer, J., and Bulirsch, R. (1992). *Introduction to Numerical Analysis*, 2nd Edn. New York, NY: Springer Verlag.

Suthakar, K., and Liberman, M. C. (2021). Auditory-nerve responses in mice with noise-induced cochlear synaptopathy. *J. Neurophysiol.* 126, 2027–2038. doi: 10.1152/jn.00342.2021

Trune, D. R., and Zheng, Q. Y. (2009). Mouse models for human otitis media. *Brain Res.* 1277, 90–103. doi: 10.1016/j.brainres.2009.02.047

Valero, M. D., Burton, J. A., Hauser, S. N., Hackett, T. A., Ramachandran, R., and Liberman, M. C. (2017). Noise-induced cochlear synaptopathy in rhesus monkeys (*Macaca mulatta*). *Hear. Res.* 353, 213–223. doi: 10.1016/j.heares.2017.07.003

Wu, P. Z., Liberman, L. D., Bennett, K., de Gruttola, V., O'Malley, J. T., and Liberman, M. C. (2019). Primary neural degeneration in the human cochlea: evidence for hidden hearing loss in the aging ear. *Neuroscience* 407, 8–20. doi: 10.1016/j.neuroscience.2018.07.053

Conflict of Interest: JB, JH, BD, and ZQ were employed by Gateway Biotechnology Inc., for this project.

The remaining authors declare that the research was conducted in the absence of any commercial or financial relationships that could be construed as a potential conflict of interest.

frontiers
in Cellular Neuroscience

ORIGINAL RESEARCH
published: 14 March 2022
doi: 10.3389/fncel.2022.857344

Integrative Functional Transcriptomic Analyses Implicate Shared Molecular Circuits in Sensorineural Hearing Loss

Peng Chen[1,2†], Jun-Jun Hao[1†], Meng-Wen Li[1], Jing Bai[1,3], Yuan-Ting Guo[1,2], Zhen Liu[1] and Peng Shi[1,3,4*]*

[1] State Key Laboratory of Genetic Resources and Evolution, Kunming Institute of Zoology, Chinese Academy of Sciences, Kunming, China, [2] Kunming College of Life Science, University of Chinese Academy of Sciences, Kunming, China, [3] School of Future Technology, University of Chinese Academy of Sciences, Beijing, China, [4] Center for Excellence in Animal Evolution and Genetics, Chinese Academy of Sciences, Kunming, China

OPEN ACCESS

Edited by:
Eleonora Napoli,
University of California, Davis,
United States

Reviewed by:
Lukas D. Landegger,
Medizinische Universität Wien, Austria
Alessandra Colciago,
University of Milan, Italy

Correspondence:
Zhen Liu
zhenliu@mail.kiz.ac.cn
Peng Shi
ship@mail.kiz.ac.cn

† These authors have contributed equally to this work

Specialty section:
This article was submitted to Cellular Neuropathology, a section of the journal Frontiers in Cellular Neuroscience

Received: *18 January 2022*
Accepted: *21 February 2022*
Published: *14 March 2022*

Citation:
Chen P, Hao J-J, Li M-W, Bai J, Guo Y-T, Liu Z and Shi P (2022) Integrative Functional Transcriptomic Analyses Implicate Shared Molecular Circuits in Sensorineural Hearing Loss.
Front. Cell. Neurosci. 16:857344.
doi: 10.3389/fncel.2022.857344

Sensorineural hearing loss (SNHL) is referred to as the most common type of hearing loss and typically occurs when the inner ear or the auditory nerve is damaged. Aging, noise exposure, and ototoxic drugs represent three main causes of SNHL, leading to substantial similarities in pathophysiological characteristics of cochlear degeneration. Although the common molecular mechanisms are widely assumed to underlie these similarities, its validity lacks systematic examination. To address this question, we generated three SNHL mouse models from aging, noise exposure, and cisplatin ototoxicity, respectively. Through constructing gene co-expression networks for the cochlear transcriptome data across different hearing-damaged stages, the three models are found to significantly correlate with each other in multiple gene co-expression modules that implicate distinct biological functions, including apoptosis, immune, inflammation, and ion transport. Bioinformatics analyses reveal several potential hub regulators, such as *IL1B* and *CCL2*, both of which are verified to contribute to apoptosis accompanied by the increase of (ROS) in *in vitro* model system. Our findings disentangle the shared molecular circuits across different types of SNHL, providing potential targets for the broad effective therapeutic agents in SNHL.

Keywords: sensorineural hearing loss, aging, noise exposure, ototoxic drugs, common molecular mechanisms, co-expression network

INTRODUCTION

Sensorineural hearing loss (SNHL) refers to a type of hearing loss resulting from the structurally and functionally damaged inner ear and vestibulocochlear nerve, mainly including cochlear hair cells (HCs), stria vascularis (SV), and spiral ganglion neurons (SGNs) (Liberman and Kujawa, 2017). Compared to other kinds of hearing loss, SNHL is usually permanent and accounts for approximately 90% of reported hearing loss cases (Li et al., 2017). Sudden SNHL affects 5 to 27 per 100,000 people each year, with approximately 66,000 new annual cases in the United States (Alexander and Harris, 2013). Among various causes of SNHL, aging, noise exposure, and ototoxic drugs are widely believed to play predominant roles (Liberman and Kujawa, 2017;

Wang and Puel, 2018). Worldwide, more than half of the population aged over 60 years suffer the age-related hearing loss (Gates and Mills, 2005) and ∼16% of the adults with hearing loss are attributed to occupational noise (Nelson et al., 2005). Ototoxicity is well-established toxicity associated with therapeutic agents for causing cochlear impairment and the prevalence of ototoxicity-induced hearing loss ranges from 4 to 90% in patients who have received the therapies with potential ototoxicity (Landier, 2016).

The three types of SNHL above display highly similar pathophysiological characteristics of the damaged or degenerated HCs, SV, and SGNs (Wang et al., 2007; Ding et al., 2012; Breglio et al., 2017; Keithley, 2020), suggesting shared biological mechanisms underlying the SNHL. Although most studies focus on one or two causative factors of SNHL, it is accessible to generalize the shared biological involvements by the clues from those independent studies (Yang et al., 2015; Cheng et al., 2019; Su et al., 2020; Maeda et al., 2021; Taukulis et al., 2021). For example, several biological processes have been suggested to influence apoptosis in cochleae affected by SNHL, such as mitochondrial dysfunction, oxidative stress, inflammation, and additional immunological reaction (Wang and Puel, 2018; Zhang et al., 2021), while autophagy may regulate the survival of HCs and SGNs in such inner ears affected by SNHL (Guo et al., 2021; He et al., 2021). Nevertheless, the validity of the shared biological processes, as well as the jointly involved genes, among different types of SNHL lacks systematic examination.

To address this question, we here created three SNHL mouse models based on aging, noise exposure, and cisplatin ototoxicity, and constructed their cochlear transcriptional co-expression networks during the generation of SNHL models. By identifying the modules with similar gene expression trajectories among different types of SNHL, we assessed the shared biological functions and signaling pathways among the genes involved in these modules, and experimentally confirmed the contributions of hub genes to mechanisms underlying phenotypic changes of SNHL.

RESULTS

Generation of Three Sensorineural Hearing Loss Mouse Models Based on Aging, Noise Exposure, and Ototoxicity

To systematically investigate the shared molecular circuits involved in SNHL, we generated three SNHL models in C57BL/6 mice strain from aging, noise exposure, and cisplatin ototoxicity, respectively (**Figure 1A**). The C57BL/6 mice present the hearing sensitivity reduction ∼6-month old and nearly complete deafness ∼18-month old, thus usually being regarded as an animal model of early-onset age-related hearing loss (Hequembourg and Liberman, 2001). Two-month-old C57BL/6 mice were used to generate other two SNHL models by being exposed to 120 decibel sound pressure level (dB SPL) noises for 2 h (Maeda et al., 2017), and by being intraperitoneally injected a single dose of cisplatin (10 mg/kg) and furosemide (200 mg/kg) (Wang et al., 2004; Li et al., 2011). Furosemide, as a potent loop diuretic, is often used to reduce the nephrotoxicity caused by cisplatin and enhance the entry of ototoxic drugs into the cochleae (Santoso et al., 2003; Ding et al., 2012).

To verify the successful establishment of the three SNHL models, we measured auditory brainstem responses (ABR) and examined the status of cochlear hair cells in the mice at 8- and 12-month age (8Mon and 12Mon), one- and 24-hour post noise exposure (1HPN and 24HPN), as well as one- and 3-day post cisplatin injection (1DPC and 3DPC), respectively (**Figure 1A**). Compared with the controls of 2-month-old (2Mon) C57BL/6 mice without any treatment, the ABR thresholds increased in 8Mon, 1HPN, and 1DPC mice, especially in 12Mon, 24HPN, and 3DPC mice at all examined frequencies (4, 8, 16, 24, and 32 kHz) and the broadband click stimulus (**Figure 1B**). *Myosin VIIa* (MYO7A), a cochlear hair-cell-specific marker, was used to stain the whole-mount cochleae of the three SNHL models (**Figures 1C–F**), indicating that the numbers of MYO7A-positive out hair cells (OHCs) significantly decreased in 8Mon, 1HPN, and 1DPC mice, and further in 12Mon, 24HPN, and 3DPC mice when compared with the controls ($P < 0.05$, two-tailed Student' *t* tests; **Figures 1G–I**). It is notable that more damaged OHCs were observed at the basal region than at the apex when exposed to the excessive intense noises even with relatively low frequencies (120 dB SPL, 4-24 kHz), which may result from the more susceptibility of OHCs at the basal region as shown in the previous studies (Sanz et al., 2015; Miao et al., 2021). In addition, similar to OHCs, the inner hair cells (IHCs) were also generally lost during aging and after the treatments with noise exposure and cisplatin (**Figures 1J–L**). These similar phenotypic alterations of the reduced hearing sensitivity and the damaged cochlear hair cells suggest the successful establishment of the SNHL mouse models based on aging, noise exposure, and cisplatin ototoxicity.

Transcriptome-Wide Gene Co-expression Networks Reflect Shared Molecular Circuits Among Different Sensorineural Hearing Loss Models

We reasoned that transcriptomic data of cochleae from different types of SNHL would inform our understanding of their shared molecular circuits, and thus examined gene expression dynamics during generating SNHL by sequencing cochleae transcriptomes across 2Mon, 8Mon, 12Mon, 1HPN, 24HPN, 1DPC, and 3DPC mice. To ensure the reliability of the data, at least three biological replicates were designed for each sample. We generated a total of 202.3 Gb clean data for cochlear transcriptomes across 27 samples from the above three types of SNHL models (**Supplementary Table 1**). The global relationships among these cochlear transcriptomes were explored through the principal components analysis (PCA). As expected, the samples from the same SNHL model tended to cluster together, suggesting strong commonalities and repeatability of transcriptomic data within each of the three SNHL mouse models (**Figure 2A**). We next performed signed weighted gene co-expression network analysis (WGCNA) (Langfelder and Horvath, 2008) for a total of 17,040 genes with available expression data across 27

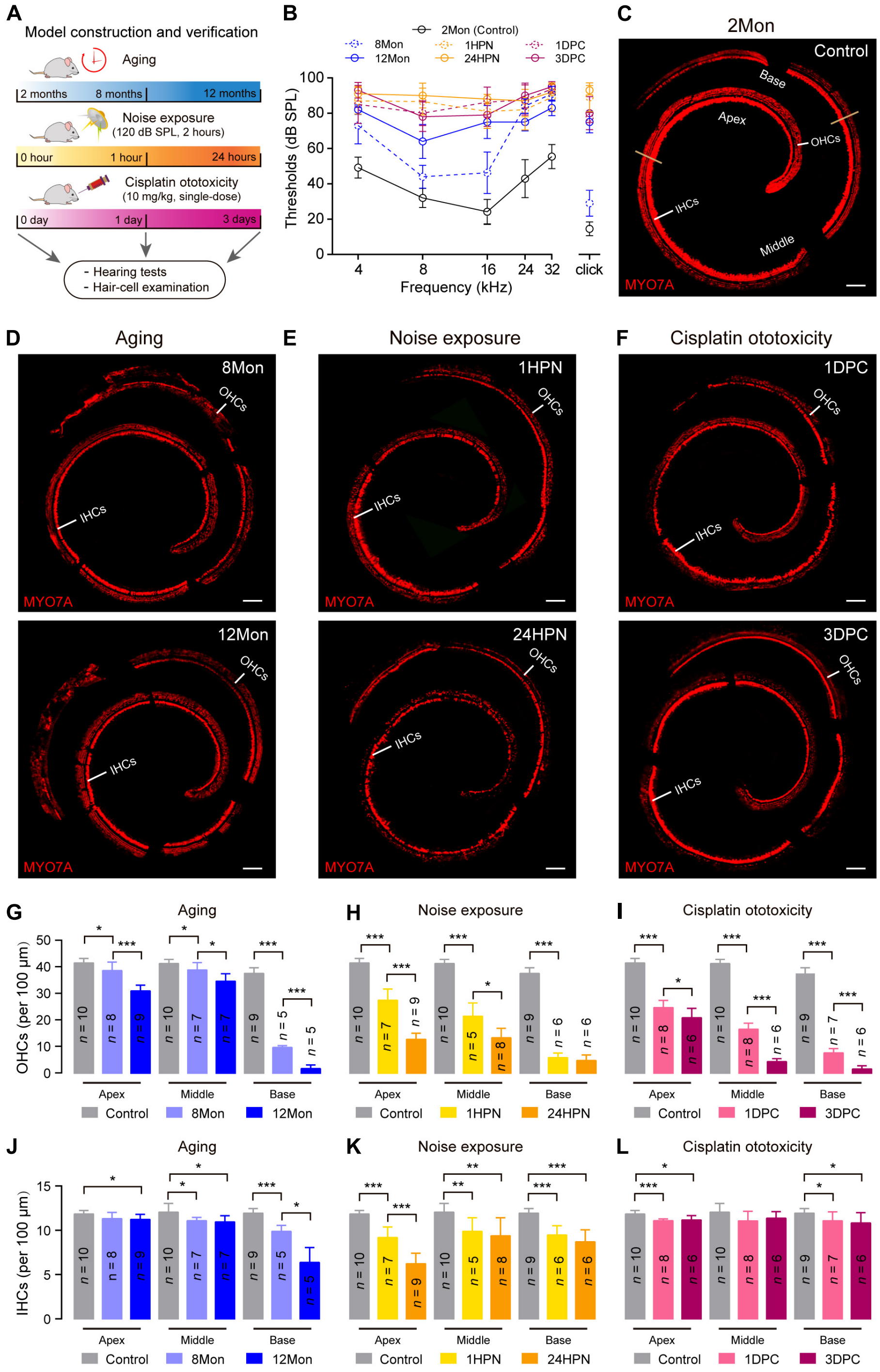

FIGURE 1 | Representative phenotypic transformation in the three types of SNHL mouse models. **(A)** Flowchart of the overall approach to SNHL mouse models. 2 months, 8 months, and 12 months for the aging SNHL model are the actual ages of the mice, while one hour, 24 h, one day, and 3 days are the times after the respective intervention for the 2-month-old mice. **(B)** ABR audiogram in the three types of SNHL mouse models. ABR thresholds of wild type mice at 8 months (8Mon, *n* = 5, dashed-line in blue), 12 months (12Mon, *n* = 5, solid-line in blue), 1 hour post noise exposure (1HPN, *n* = 5, dashed-line in orange), 24 h post noise exposure (24HPN, *n* = 5, solid-line in orange), 1 day post cisplatin injection (1DPC, *n* = 4, dashed-line in purple), 3 days post cisplatin injection (3DPC, *n* = 5, solid-line in purple) show severe hearing loss, compared with wild type mice at 2 months (2Mon, *n* = 12, dashed-line in black). **(C–F)** Representative confocal microscopy images from whole-mount cochleae. The ears of aging and treatments with noise exposure and cisplatin injection exhibited substantial loss of hair cells compared with control ears. Scale bars, 100 μm. **(G–L)** Quantification of survival OHCs and IHCs in the three types of SNHL mouse models. The three types of SNHL mouse models are present in columns with different colors. *n* in the columns shows the numbers of cochleae used for the quantification. All data are shown as Mean ± SD. *$P < 0.05$, **$P < 0.01$, ***$P < 0.001$. *P* values are from two-tailed Student's *t*-tests.

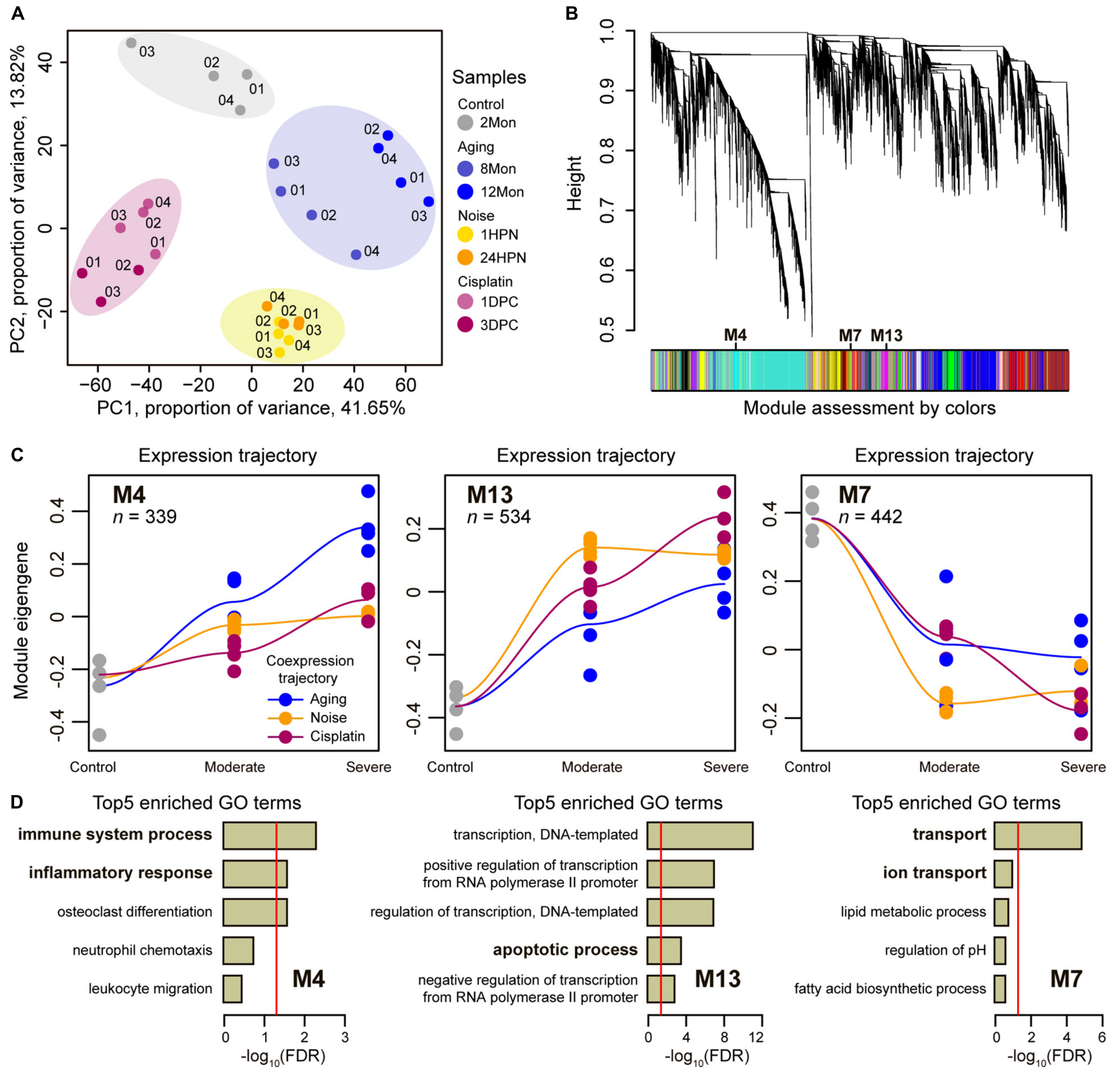

FIGURE 2 | Co-expression network analysis. **(A)** Principal component analysis of cochlear RNA-seq samples in the triad of SNHL. The data revealed that the same SNHL model cochlear samples (represented by colors and labeled numerically) tended to cluster together. **(B)** Network analysis dendrogram showing modules based on the co-expression genes throughout the three types of SNHL mouse models. The colors below give information on module assessment. **(C)** Co-expression trajectory in the highlighted co-regulated modules, including two up-regulated modules (M4 and M13) and one down-regulated module (M7). Trajectories of the three types of SNHL mouse models were plotted by different colors. The fit line represents locally weighted scatterplot smoothing. *n* shows the numbers of the genes in each module. **(D)** Top 5 enriched GO terms of the highlighted co-regulated modules. The reports of $-\log_{10}$ (FDR) present relative enrichment in each module, with the red line at FDR = 0.05.

samples and identified 22 co-expression modules labeled with colors and numbers (**Figure 2B** and **Supplementary Table 2**). The genes within each of these co-expression modules are expected to exhibit highly similar expression patterns during the generation of three types of SNHL models (Langfelder and Horvath, 2008). We investigated each module's trajectory along with the stages of generating SNHL models by calculating the module eigengene (ME) (**Supplementary Figure 2**). The ME is the first principal component of a module and reflects the general expression pattern of the genes within the module (Langfelder and Horvath, 2008). We then calculated the Pearson correlation coefficients (*R*) of ME values for each module between the three types of SNHL above and identified three modules with larger averaged *R* values (> 0.92) than other modules (**Figure 2C** and **Supplementary Table 3**), including two up-regulated modules (M4 and M13) and one down-regulated module (M7). Consequently, the closely aligned gene co-expression patterns between the aging-, noise-, and cisplatin-induced SNHL were suggested in these three modules. Further, we, respectively, assessed biological functions among the genes within each of the three modules by enrichment for Gene Ontology (GO) annotation terms (**Supplementary Tables 4–6**). Top5 GO terms included immune system process and inflammatory response in M4, apoptotic process in M13, and transport and ion transport in M7 (**Figure 2D**), suggesting that the co-up-regulated genes involved in immune systems, inflammatory responses, and apoptotic process, as well as the co-down-regulated genes involved in transport and ion transport play critical roles on the occurrence of SNHL.

Shared Signaling Pathways Associated With Sensorineural Hearing Loss

Although the immune system process, inflammatory response, and apoptotic process were enriched in two distinct up-regulated modules M4 and M13 (**Figure 2D**), these functionally different biological processes can be interactively aroused through some signaling pathways (Mak and Yeh, 2002; Simon, 2003; Fox et al., 2010). We thus hypothesized that shared signaling pathways or molecular regulatory relationships could link the genes within the two up-regulated modules. We first performed Kyoto Encyclopedia of Genes and Genomes (KEGG) enrichment analysis for the genes within M4 and M13. Of the top 5 enriched pathways, NF-kappa B signaling pathway, TNF signaling pathway, and Jak-STAT signaling pathway were found to implicate in immune, inflammatory, and apoptotic processes (**Figure 3A** and **Supplementary Table 7**). We next conducted the protein-protein interaction (PPI) analysis for the co-up-regulated genes within M4 and M13 to provide an independent line of interrogation for the centric profiles. We calculated the degree and the closeness centrality for each node, which are commonly used as centrality measures (Vital-Lopez et al., 2012), and examined their relationships for all nodes to identify hub genes in the network. The top 15 genes in the PPI network were highlighted, which directly interacted with 298 (41.5%) co-up-regulated genes and involved in 840 (22.9%) PPIs (**Figure 3B**). Notably, we found that 9 of the top 15 genes were involved in the NF-kappa B signaling pathway, TNF signaling pathway, and Jak-STAT signaling pathway, including *TNFRSF1A*, *IL1B*, *CCL2*, *MYD88*, *TRAF6*, *STAT3*, *EP300*, *SOCS3*, and *AKT1* (**Figure 3C**). Interestingly, nearly all of these genes (7/9) were associated with the biological functions of immune system process, inflammatory response, and apoptotic process that were determined by the GO enrichment analysis for M4 and M13 (**Figure 3C**).

Similarly, we performed the KEGG enrichment analysis for the genes within the down-regulated M7 and found that oxidative phosphorylation was the most notable KEGG term (**Figure 3D** and **Supplementary Table 8**). The top 15 genes in the PPI network constructed using the co-down-regulated genes in M7 were also highlighted (**Figure 3E**), which directly interacted with 61 (26.2%) co-down-regulated genes and involved 187 (43.2%) PPIs. Among the top 15, 12 genes were involved in mitochondria-related ATP production through oxidative phosphorylation, including *NDUFS1*, *NDUFS5*, *NDUFA5*, *NDUFA9*, *NDUFA11*, *NDUFAB1*, *NDUFB5*, *SDHA*, *UQCRC2*, *COX4I2*, *ATP5B*, and *ATP5J* (**Figure 3F**). Likewise, nearly all of these genes (11/12) were associated with the biological functions of transport and ion transport that were determined by the GO enrichment analysis for M7 (**Figure 3F**).

Experimental Verification for Potential Contributions of *IL1B* and *CCL2* to Sensorineural Hearing Loss

Among the top 15 genes in the PPI network of the up-regulated modules M4 and M13, the pro-inflammatory cytokine *IL1B* and chemokine *CCL2* were found to serve as the connecting links between the TNF signaling pathway, NF-kappa B signaling pathway, and Jak-STAT signaling pathway (**Figure 3C**). Moreover, several previous studies show the increased expression of *IL1B* and *CCL2* after noise exposure, suggesting their crucial roles in generating noise-induced SNHL (Vethanayagam et al., 2016; Zhang et al., 2019; Wang et al., 2020). We next tested whether *IL1B* and *CCL2* also contribute to aging- and ototoxicity-induced SNHL using an *in vitro* model system.

The quantitative real-time polymerase chain reaction (qRT-PCR) was used to verify that both *IL1B* and *CCL2* were significantly up-regulated in the cochleae during creating different types of SNHL mouse models (**Supplementary Figures 3A,B**), as observed in the transcriptome-wide analyses. Next, we applied the house ear institute-organ of Corti 1 (HEI-OC1) cells as an *in vitro* model system for the aging- and ototoxicity-induced SNHL. The HEI-OC1 cells express several cochlear hair-cell-specific markers, such as *myosin VIIa*, *prestin*, *Atoh1*, *BDNF*, *calbindin*, and *calmodulin*, and thus are widely used for investigating the molecular mechanisms of the death or survival of cochlear hair cells (Kalinec et al., 2003, 2016).

Because D-galactose (D-gal) can increase oxidative stress, mitochondrial damage, and apoptosis, which accelerates tissue senescence, the treatment of HEI-OC1 cells with D-gal can largely mimic the alterations of cochlear hair cells during aging (Zhong et al., 2011; Du et al., 2012; He et al., 2020). The D-gal treatment decreased the viability of HEI-OC1 cells in concentration- and time-dependent manners (**Supplementary Figures 4A,B**), revealing that the half-lethal dose of D-gal was 75 mg/ml for 24 h, which was selected for generating the *in vitro* model of aged cochlear hair cells. As observed in the cochleae of aging-induced SNHL mice, both *IL1B* and *CCL2* were expressed significantly more in the HEI-OC1 cells treated with D-gal than without D-gal treatment (**Figure 4A**). When the expression of *IL1B* and *CCL2* was inhibited, the cell viability significantly increased (**Figure 4B**); when *IL1B* and *CCL2* were overexpressed, the cell viability significantly decreased (**Figures 4C,D**).

Similarly, we used the HEI-OC1 cells for testing the roles of *IL1B* and *CCL2* in generating ototoxicity-induced SNHL. The treatment with cisplatin also decreased the cell viability of HEI-OC1 cells in concentration- and time-dependent manners (**Supplementary Figures 4C,D**). The half-lethal dose of cisplatin

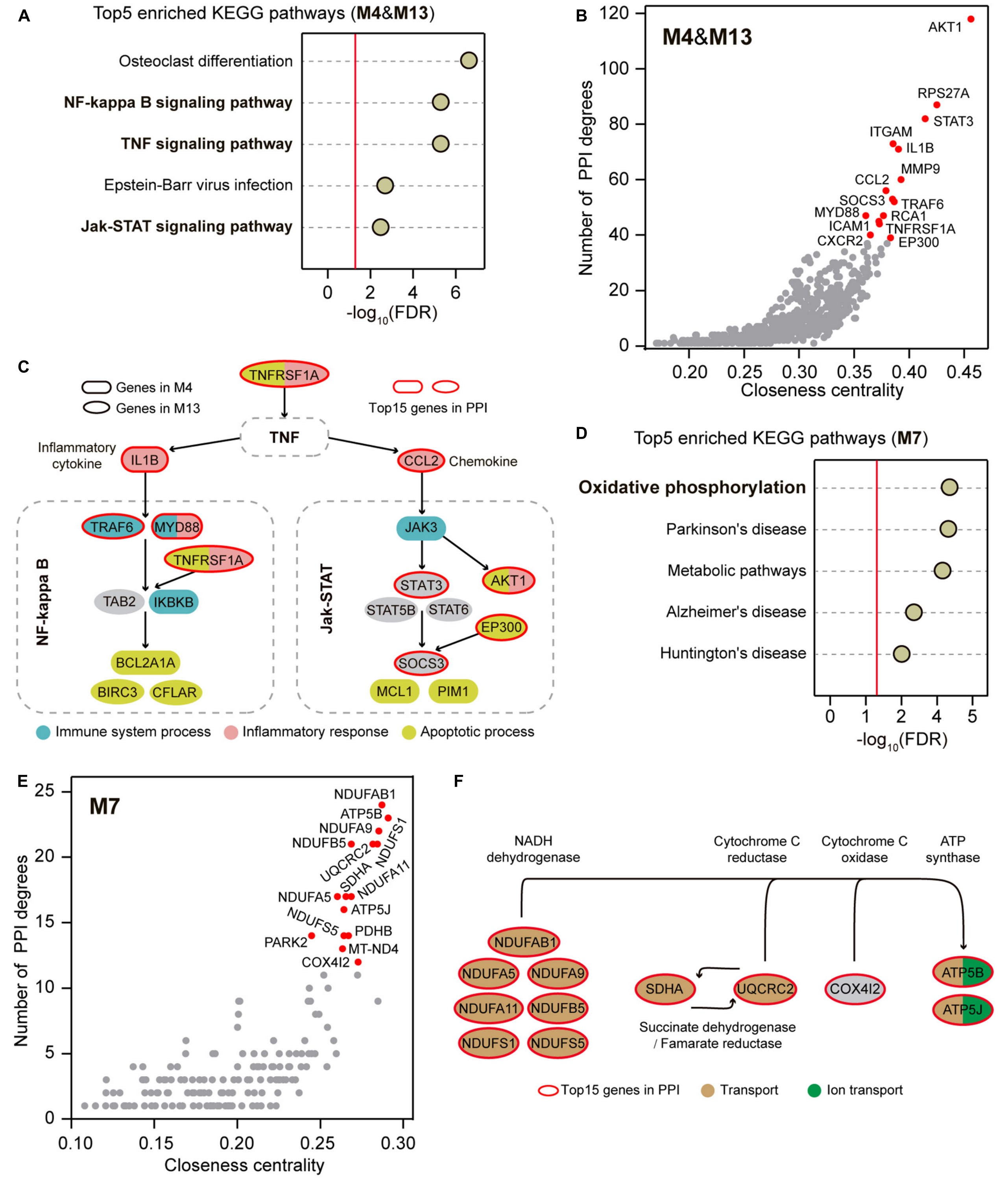

FIGURE 3 | Signaling pathway enrichment and PPI analysis for the co-regulators. **(A)** Top 5 enriched KEGG pathways within M4 and M13. The reports of -$\log_{10}$ (FDR) present relative enrichment with the red line at FDR = 0.05. **(B)** PPI network analysis within M4 and M13. The top 15 highlighted genes are plotted in red. **(C)** Top 15 highlighted some representative genes of M4 and M13 that implicated in a cross-linked pathway composited with the enriched signaling pathways based on KEGG Mapper. The top 15 genes in PPI are marked in red circles and the genes implicated in immune system process, inflammatory response, and apoptotic process are plotted by different colors. **(D)** Top 5 enriched KEGG pathways within M7. The reports of –$\log_{10}$ (FDR) present relative enrichment with the red line at FDR = 0.05. **(E)** PPI network analysis within M7. The top 15 highlighted genes are plotted in red. **(F)** Top 15 highlighted genes of M7 that implicated in oxidative phosphorylation based on KEGG Mapper. The top 15 genes in PPI are marked in red circles and the genes implicated in transport and ion transport are plotted by different colors.

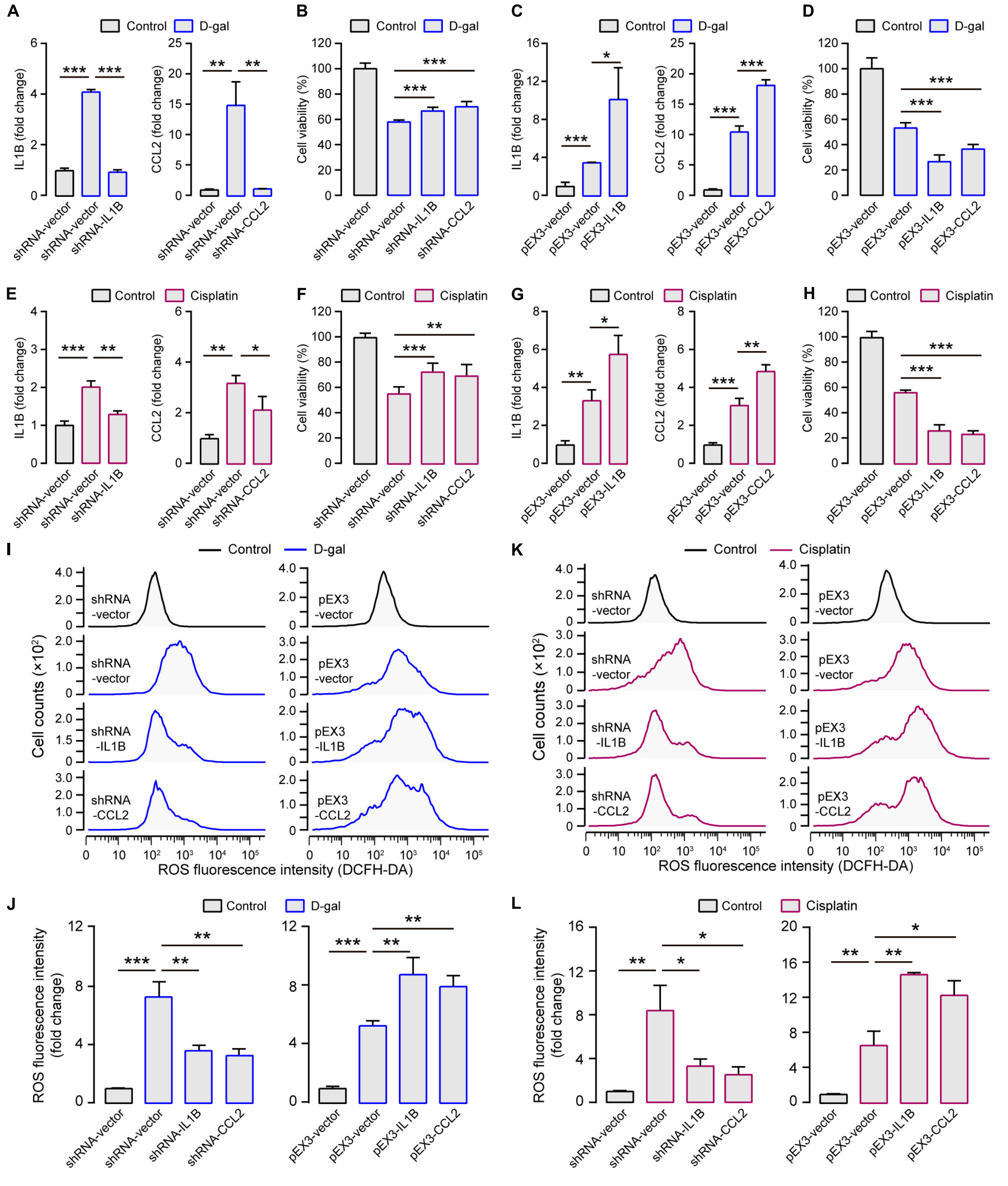

FIGURE 4 | Experimental verification for contributions of *IL1B* and *CCL2* to SNHL. **(A)** In the aging *in vitro* model (treated with D-gal; shown in blue columns), the expression of *IL1B* and *CCL2* increased but decreased when shRNA-IL1B and shRNA-CCL2 were transfected. **(B)** The inhibited expression of *IL1B* and *CCL2* enhanced the cell viability in the aging *in vitro* model. **(C)** Both *IL1B* and *CCL2* overexpression could be elicited after pEX3-IL1B and pEX3-CCL2 transfections and **(D)** this further decreased the cell viability in the aging *in vitro* model. **(E)** In the ototoxicity *in vitro* model (treated with cisplatin; shown in purple columns), the expression of *IL1B* and *CCL2* increased but decreased when shRNA-IL1B and shRNA-CCL2 were transfected. **(F)** The inhibited expression of *IL1B* and *CCL2* enhanced the cell viability in the aging *in vitro* model. **(G)** Both *IL1B* and *CCL2* overexpression could be elicited after pEX3-IL1B and pEX3-CCL2 transfections and **(H)** this further decreased the cell viability in the ototoxicity *in vitro* model. **(I)** Representative cellular distribution with different ROS levels and **(J)** the quantification in *IL1B* and *CCL2* modulation groups in the aging *in vitro* model. **(K)** Representative cellular distribution with different ROS levels and **(L)** the quantification in *IL1B* and *CCL2* modulation groups in the ototoxicity *in vitro* model. In the two *in vitro* models, the levels of intracellular ROS decreased when *IL1B* or *CCL2* were inhibited and increased when *IL1B* or *CCL2* were overexpressed. The gene expression levels were measured by quantitative real-time PCR for each column ($n = 3$). The cell viability was measured by the cell proliferation assay kit for each column ($n = 6$). ROS evaluation was measured by the DCFH-DA kit using the Flow Cytometer for each column ($n = 3$). All the columns are present with Mean ± SD. $^{*}P < 0.05$, $^{**}P < 0.01$, $^{***}P < 0.001$. P values are from two-tailed Student's t-tests.

(50 μM for 48 h) was used for generating the *in vitro* model of cisplatin-induced SNHL. Both *IL1B* and *CCL2* were expressed significantly more in the HEI-OC1 cells treated with cisplatin than without cisplatin treatment (**Figure 4E**). The inhibition of the expression of *IL1B* and *CCL2* increased the cell viability, but the overexpression of the *IL1B* and *CCL2* decreased the cell viability (**Figures 4F–H**). Notably, no cell viability changes were observed when *IL1B* and *CCL2* were inhibited and overexpressed in HEI-OC1 cells without any treatments (**Supplementary Figures 5A,B**). These highly consistent results from the *in vitro* systems of cochlear hair cells strongly support the crucial roles of *IL1B* and *CCL2* in generating the aging- and ototoxicity-induced SNHL.

The expression and activation of *IL1B* and *CCL2* have been reported to closely relate to the production of reactive oxygen species (ROS) (Li et al., 2014; Ansari et al., 2018). ROS can trigger and modulate inflammation and immune responses, and excessive cellular ROS production causes oxidative stress and mitochondrial abnormalities that contribute to the degenerative responsiveness to aging, intense noise, and ototoxic drugs in the auditory system (Someya and Prolla, 2010; Yu et al., 2014; Jing et al., 2015). To test whether the roles of *IL1B* and *CCL2* in generating SNHL are mediated by regulating ROS production, we examined ROS levels in HEI-OC1 cells with different expressions of *IL1B* and *CCL2*. The ROS levels were indeed significantly higher in HEI-OC1 cells treated with D-gal than without any treatments (**Figures 4I,J**). Moreover, the ROS levels significantly decreased when the expression of *IL1B* and *CCL2* was inhibited and increased when the expression of *IL1B* and *CCL2* was enhanced (**Figures 4I,J**). And the similar results were presented in the cisplatin treatment groups (**Figures 4K,L**). These results suggest a general causal link between ROS production and different types of SNHL, and that both *IL1B* and *CCL2* contribute to the production of ROS in different SNHL mouse models.

DISCUSSION

Prior work has documented several biological processes and genes underlying cell death in the cochleae of SNHL, including mitochondrial dysfunction, oxidative stress, inflammation, immune system (Wang and Puel, 2018; Zhang et al., 2021). Most of the studies, however, focused on one or two of the three most causative factors of SNHL, i.e., aging, noise exposure, and ototoxic drugs. In this study, we generated three SNHL mouse models derived from aging, noise exposure, and cisplatin ototoxicity, constructed gene co-expression modules of the cochlear transcriptomes during creating SNHL models and systematically validated the crucial roles of NF-kappa B signaling pathway, Jak-STAT signaling pathway, TNF signaling pathway, and Oxidative phosphorylation in generating SNHL. The *in vitro* experiments demonstrated that the overexpression of *IL1B* and *CCL2* in SNHL increased ROS production, likely leading to apoptosis in the cochleae of SNHL. Together, these findings clarify the shared molecular circuits and genes underlying different types of SNHL.

Besides *IL1B* and *CCL2*, several additional co-regulators were found to be involved in the SNHL-shared inflammatory and immune responses through TNF signaling pathway, NF-kappa B signaling pathway, and Jak-STAT signaling pathway, including *TNFRSF1A*, *TRAF6*, *MYD88*, *AKT1*, *STAT3*, *EP300*, and *SOCS3* (**Figure 3C**). Some of these genes have been identified to be up-regulated in the cochleae of a particular kind of SNHL. For example, the expression levels of *MYD88*, *AKT1*, and *SOCS3* increase after noise exposure (Gratton et al., 2011; Chen et al., 2015; Zhang et al., 2019), and exposure of cochlear explants to the ototoxic drug gentamicin leads to the increased *TNFRSF1A* expression (Bas et al., 2012). Interestingly, some of these regulators are suggested to be recognized as potential targets for ameliorating SNHL. The treatment with IL-1 blockade improves the hearing of 91% of Muckle-Wells-syndrome patients (Kuemmerle-Deschner et al., 2015). Avenanthramide-C reduces *IL1B* and *TNF*-α expression and provides significant protection against noise- and drug-induced SNHL (Umugire et al., 2019). Capsaicin protects against cisplatin-induced SNHL by changing the STAT3/STAT1 expression ratio (Bhatta et al., 2019). Our findings extend the current understanding of the shared biological processes and hub genes in SNHL and provide the elevated probability of discovering the most effective therapeutic and preventive targets across different types of SNHL.

In addition to the shared molecular circuits and regulators, we also identified some prime modules with specific co-expression patterns for each of the three SNHL mouse models. For instance, M6 reflected a down-regulated gene co-expression pattern for the aging-induced SNHL model compared to the noise- and ototoxicity-induced SNHL models. Among the top 5 enriched GO terms for the genes within M6, there were four involved in the regulation of gene transcription (**Supplementary Figure 6A** and **Supplementary Table 9**). M11 and M14, respectively, displayed down- and up-regulated co-expression patterns for the noise-induced SNHL model. Despite no significantly enriched GO terms for the genes within M11, the enriched GO terms for M14 included angiogenesis and steroid metabolic (**Supplementary Figure 6B** and **Supplementary Table 10**). M16 and M21 both presented down-regulated co-expression patterns for the cisplatin-induced SNHL model; the notable GO terms included cell adhesion, immune system process, cell cycle, and cell division (**Supplementary Figure 6C** and **Supplementary Table 11**). These functional involvements have been shown implications for the normal functioning of cochleae more or less (Malgrange et al., 2015; Wang et al., 2019); however, more research is needed before their causal roles in generating SNHL from specific factors is known for certain.

Although we acknowledge that the stages in the three types of SNHL selected for comparison may be artificial, the approaches for shared molecular circuits are reinforced. Our analyses systematically provide evidence for existing the shared molecular circuits in different types of SNHL and highlight the importance of future investigation for the shared molecular circuits in SNHL. Regardless, our analyses suggest some common potential targets of the most effective therapeutic agents for preventing or ameliorating aging-, noise-, and ototoxicity-induced SNHL.

MATERIALS AND METHODS

Animals

C57BL/6 mice were obtained from the Kunming Institute of Zoology Southwest SPF Animal Center. All animal experiments were performed under Animal Use Protocols approved by the Kunming Institute of Zoology Animal Care and Ethics Committee, CAS.

Acoustic Overexposure

Two-month-old mice were continuously exposed to broadband noises (4-24 kHz) at 120 -121 decibel Sound Pressure Level (dB SPL) for 2 h in a small cylindrical cage (706.5 cm^2 × 15 cm.). The noise was delivered by a loudspeaker (HG10044XT; Weijie-Electric, Guangzhou, CN) at a distance of 20 cm above the bottom of the cage. Calibration of noise to target SPL was performed immediately before each noise exposure session to ensure that the SPL varied by $<$ 1 dB across the cage.

Cisplatin Treatment

Two-month-old mice were treated with co-administration of furosemide and cisplatin. All the treatments were performed by intraperitoneal injection. The 200 mg/kg of furosemide (Hongbao, CN) treatment was administered one hour before being intraperitoneally injected with 10 mg/kg of cisplatin (P4394, Sigma- Aldrich). Mice were daily performed by intraperitoneal injection with 1 ml of normal saline for the following 3 days.

Auditory Brainstem Response Measurement

The anesthetized animals with an intraperitoneal injection of sodium pentobarbital (90 mg/kg) were placed on an anti-vibration table in a soundproof room. The recording electrode (a subdermal needle) was inserted at the skull vertex and the reference electrode was placed on a 1-2 mm incision ventroposterior to the external pinna. During ABR recordings, the animal's body temperature was maintained at 37.5°C by a heating pad. Click or tone burst sounds (4, 8, 16, 24, and 32 kHz) with 5 ms duration were delivered from 10 to 90 dB SPL with 5 dB interval at a rate of 10 per second by a calibrated MF1 speaker (TuckerDavis Technologies, Alachua, FL) which was placed ∼2 cm in front of the animal. After being amplified, filtered (100-1000 Hz), and averaged (256 times) by an RZ6 Processor (TuckerDavis Technologies Alachua, FL), the ABR signals were recorded using BioSigRZ software (TuckerDavis Technologies, Alachua, FL). The minimum sound intensity that could elicit a detectable response was defined as the ABR threshold. If no detectable ABR waveforms, the ABR thresholds were arbitrarily defined as 95 dB SPL for statistical analysis.

Cochlear Pathology

After mice were killed with CO_2 inhalation, the cochleae were collected and fixed in 4% paraformaldehyde (PFA) at 4°C overnight and decalcified in 10% ethylene diamine tetraacetic acid (EDTA) solution at room temperature for several days. Then, the cochleae were divided into pieces for whole-mount immunofluorescence. After being infiltrated with 0.3% Triton X-100 (Sigma-Aldrich) for 20 min and blocked with 10% goat serum for one hour, the tissues were applied with rabbit anti-MYO7A (1:500; Proteus BioSciences) at 4°C overnight. After three rinses with PBS, the tissues were incubated in goat anti-rabbit Alexa Fluor 568 (1:2000; Invitrogen) for one hour at room temperature. The samples were mounted in an antifading mountant medium (Cat.#. S2110, Solarbio) after three rinses with PBS. With maximum intensity projections of z-stacks, the confocal images of cochlear hair cells were taken by a microscope (Nikon A1) using a 10 × lens. The numbers of MYO7A-positive cells along 500 μm in each section were counted for statistical analysis. The composite images showing the whole cochlea were constructed by using Adobe Photoshop CC 2019 and Adobe Illustrator CC 2019.

Collection of Cochlear Total RNA

The cochleae were harvested from controls (2-month-old mice), aging-induced SNHL (8-month-old and 12-month-old mice), noise-induced SNHL (2-month-old mice after being exposed to noise for one hour and for 24 h), and cisplatin-induced SNHL (2-month-old mice after being injected with cisplatin for one day and for three days). An individual's bilateral cochleae were collected as a biological replicate. To ensure the reliability and repeatability of our data, at least three replicates were required. After removing the vestibule organ in a Petri dish filled with ice-cold sample protector for RNA/DNA (Cat.#. 9750, TaKaRa), we extracted the total RNA from the remaining cochleae using QIAzol Lysis Reagent (Qiagen Science). The quality and integrity of the purified total RNA with the RNeasy Plus Universal Mini Kit (Cat.#. 73404, Qiagen Science) were examined using Agilent 2100 Bioanalyzer.

Transcriptome Sequencing and Analysis

Total RNA was qualified and quantified using a NanoDrop and Agilent 2100 bioanalyzer (Thermo Fisher Scientific, MA, United States). Approximately 1 μg of total RNA was used to construct cDNA libraries according to the manufacturer's recommendations. All the libraries were sequenced on the MGISEQ2000 platform (BGI-Shenzhen, China) in a paired-end form with 150 bp. The low-quality reads were filtered out using the program of the fastq-quality-filter (from Fastx-Toolkit 0.0.13) with the parameters of -Q 33 -q 20 -p 80. A total of ∼202.3 Gb clean data was obtained and averaged 7.49 Gb high-quality clean reads for 27 samples (**Supplementary Table 1**). The clean reads were mapped onto the mouse genome (version GRCm38) using Tophat 2.1.0 (Kim et al., 2013) with the parameter of –read-mismatches 2. And then, the expected fragments per kilobase of transcript per million fragments (FPKM) of each gene was calculated using cufflinks 2.02 (Trapnell et al., 2010) with the parameter –max-multiread-fraction 0.75 as its expression level. The raw sequence data reported have been deposited both in the Genome Sequence Archive in National Genomics Data Center, China (CRA005119)[1] and in the Gene Expression Omnibus in National Center for Biotechnology Information (GSE196870)[2].

---

[1] https://ngdc.cncb.ac.cn/gsa

[2] www.ncbi.nlm.nih.gov/geo/

Weighted Gene Co-expression Network Analysis

The *R* package of signed weighted gene co-expression network analysis (WGCNA) was used to construct gene co-expression networks (Langfelder and Horvath, 2008). If a gene has > 0.5 FPKM values in less than half of 27 samples, it will be discarded. Finally, a total of 17,040 genes were retained and their FPKM values were logarithmically transformed [$\log_2(\text{FPKM} + 1)$] to generate an integrated expression matrix for constructing co-expression networks with WGCNA. Based on the best soft threshold (power = 15; **Supplementary Figure 1**), a total of 22 co-expression modules across all samples were identified (labeled by color and numerically, **Supplementary Table 2**).

Module Assignment for Shared Molecular Regulation

We investigated each module's trajectory following the stages of SNHL models by calculating the module eigengene (ME), which is the first principal component of a module and reflects the general expression pattern of the genes within the module (**Supplementary Figure 2**). To determine the shared molecular regulation across the three types of SNHL, we calculated the Pearson correlation coefficients (*R*) of ME values for each module between the three types of SNHL induced by aging, noise exposure, and cisplatin injection, respectively (**Supplementary Table 3**). The modules with $R > 0.85$ in any two of the three types of SNHL were considered as closely aligned gene co-expression patterns for shared molecular regulation.

Functional and Pathway Enrichment Analyses and Constructing Protein-Protein Interaction (PPI) Networks

The mouse Gene Ontology (GO) annotations and Kyoto Encyclopedia of Genes and Genomes (KEGG) pathways downloaded from DAVID Bioinformatics Resources 6.8 (david.ncifcrf.gov) were used to assign functional categories to one-to-one orthologous genes. Using all mouse genes as the background, we applied an in-house Fisher's exact test program to perform the statistical analysis. The obtained *P* values were corrected by the false discovery rate (FDR). The maps of the related KEGG pathways were obtained from its official website[3]. We constructed the PPI network using STRING version 11.0[4]. The number of degrees and the closeness centrality value for each gene involved in the networks were calculated by the software Cytoscape 3.8.0 (Shannon et al., 2003).

Cell Culture

The HEI-OC1 cells (Sigma-Aldrich, St. Louis, MO) were cultured in Dulbecco's Modified Eagle's Medium (Gibco, Thermo Fisher) containing 10% fetal bovine serum (Gibco, Thermo Fisher) without antibiotics at 33°C and 5% CO_2. Cells were seeded in a 10 cm plate at a density of 5.0×10^5 cells or a 96-well plate at a density of 1.0×10^4 cells per well and incubated overnight for the next experiments.

Quantitative Real-Time PCR

For Quantitative Real-Time PCR (qRT-PCR), the cochleae of two mice were pooled together to extract total RNA for the SNHL mouse models; the HEI-OC1 cells in a 10 cm plate were collected to extract total RNA for the *in vitro* experiments. The extracted total RNA was reverse transcribed into cDNA using a PrimeScript RT reagent kit with gDNA Eraser (Cat.#. RR047A, Takara, JP). The qRT-PCR assays were performed with GoTaq qPCR Master Mix (Cat.#. A6001, Promega, United States) using Quant-studio 12K Flex (AB Life Technologies), following the conditions: 95°C, 10 min; 95°C, 15 s; 60°C, 1 min; for 40 cycles; 95°C, 15 s; 60°C, 1 min; 95°C 15 s. qRT-PCR data were calculated with the $2^{-\Delta\Delta Ct}$ method and *GAPDH* was used as an endogenous reference control. Primer sequences used in this study were as follows: *IL1B*: Forward 5′- GAGTGTGGATCCCAAGCA AT-3′, Reverse 5′- ACGGAT TCCATGGTGAAGTC-3′; *CCL2*: Forward 5′- TTA AAAACCTGGATCGGAACCAA-3′, Reverse 5′- GCATTAGCT TCAGATTTACGGGT-3′; *GAPDH*: Forward 5′- ACCACCAT GGAGAAGGCC-3′, Reverse 5′- ATTGCTGACAATCTTGAGT GAGT-3′.

Short Hairpin RNA and Plasmid cDNA Transfection

The HEI-OC1 cells in a 10 cm plate were transfected with 10 μg shRNA plasmid or cDNA plasmid in 45 μl of the Lipofectamine 3000, 30 μl P3000, 750 μl Opti-MEM, and 10 ml complete growth medium. The HEI-OC1 cells in a 96-well plate were transfected with 0.2 μg shRNA plasmid or cDNA plasmid in 0.3 μl of the Lipofectamine 3000, 0.2 μl P3000, 10 μl Opti-MEM, and 100 μl complete growth medium. The respective empty plasmid vectors were transfected as controls. After 48 h of transfection, the compound medium was removed and replaced by a complete growth medium with D-galactose or cisplatin. The shRNA-IL1B and shRNA-CCL2 plasmids (GenePharma, CN) were designed to knock down the expression of target genes. The cDNA plasmids of pEX3-IL1B and pEX3-CCL2 (GenePharma, CN) were designed to enhance the gene expression. The target sequence of shRNA is as follows: *IL1B*: 5′-GGACCCATATGAGCTGAAAGC-3′; *CCL2*: 5′-CACCAGCAAGATGATCCCAAT-3′.

Assessment of Cell Viability

The HEI-OC1 cells in a 96-well plate were used for assessing cell viability with Celltiter 96 AQueous One Solution Cell Proliferation Assay (G3581, Promega). After transfection, the cells were treated with cisplatin (P4394, Sigma-Aldrich) or D-galactose (Coolaber, CN) at the indicated concentrations and the designed concentration for indicated periods. After the treatment with drugs, 10 μl compound was added for 2 h. Then, the optical density (OD) values were measured at 450 nm by a Hybrid reader (Synergy H1). The positive control underwent the same procedure without cell-seeding. The averaged OD in

---

[3] www.kegg.jp/kegg/tool/map_pathway2.html

[4] string-db.org/cgi/input

negative control cells was taken as 100% of viability. The relative viability was calculated as (OD experiment - OD positive)/(OD negative – OD positive) × 100. The negative control was the HEI-OC1 cells without any treatment.

Measurement of Reactive Oxygen Species Levels

The cellular Reactive Oxygen Species (ROS) levels were measured by 2,7-Dichlorodihydrofluorescein diacetate (DCFH-DA; GK3611, Genview, CN) staining according to the manufacturer's instructions. The HEI-OC1 cells were incubated with 10 μM DCFH-DA in DMEM for one hour and then washed twice with DMEM. The cells were collected to measure the ROS fluorescent signal intensity by flow cytometry (LSR Fortessa, Becton Dickinson, United States). Flow cytometry analyses were performed with extinction at 502 nm and emission at 530 nm (10,000 cells per sample) and then evaluated with the software FlowJo V10.

DATA AVAILABILITY STATEMENT

The original contributions presented in the study are publicly available. This data can be found here: https://ngdc.cncb.ac.cn/gsa, CRA005119. www.ncbi.nlm.nih.gov/geo/, GSE196870.

ETHICS STATEMENT

The animal study was reviewed and approved by Kunming Institute of Zoology Animal Care and Ethics Committee, CAS.

AUTHOR CONTRIBUTIONS

PC, ZL, and PS designed the project. PC performed ABR recordings and cochleae staining. PC and JB prepared mice and cochlear samples. PC and M-WL performed the qRT-PCR and cell culture experiments. J-JH analyzed the RNA-seq data. Y-TG performed statistical tests. ZL, PC, and PS wrote the manuscript with input from all authors.

FUNDING

This project was supported by grants from the National Natural Science Foundation of China (31930011, 31922010, 32192422, and 31871270), Strategic Priority Research Program of the Chinese Academy of Sciences (XDPB17), National Key Research and Development Program of China (2021YFC2301300), Yunnan Provincial Science and Technology Department (2019FI008), Major Science and Technique Programs in Yunnan Province (202102AA310055), and the Key Research Program of the Chinese Academy of Sciences (KJZD-SW-L11).

ACKNOWLEDGMENTS

We thank Jie Tang for his valuable comments.

SUPPLEMENTARY MATERIAL

The Supplementary Material for this article can be found online at: https://www.frontiersin.org/articles/10.3389/fncel.2022.857344/full#supplementary-material

REFERENCES

Alexander, T. H., and Harris, J. P. (2013). Incidence of sudden sensorineural hearing loss. *Otol. Neurotol.* 34, 1586–1589. doi: 10.1097/MAO.0000000000000222

Ansari, M. Y., Khan, N. M., Ahmad, I., and Haqqi, T. M. (2018). Parkin clearance of dysfunctional mitochondria regulates ROS levels and increases survival of human chondrocytes. *Osteoarthritis Cartilage* 26, 1087–1097. doi: 10.1016/j.joca.2017.07.020

Bas, E., Van De Water, T. R., Gupta, C., Dinh, J., Vu, L., Martínez-Soriano, F., et al. (2012). Efficacy of three drugs for protecting against gentamicin-induced hair cell and hearing losses. *Br. J. Pharmacol.* 166, 1888–1904. doi: 10.1111/j.1476-5381.2012.01890.x

Bhatta, P., Dhukhwa, A., Sheehan, K., Al Aameri, R. F. H., Borse, V., Ghosh, S., et al. (2019). Capsaicin Protects Against Cisplatin Ototoxicity by Changing the STAT3/STAT1 Ratio and Activating Cannabinoid (CB2) Receptors in the Cochlea. *Sci. Rep.* 9:4131. doi: 10.1038/s41598-019-40425-9

Breglio, A. M., Rusheen, A. E., Shide, E. D., Fernandez, K. A., Spielbauer, K. K., McLachlin, K. M., et al. (2017). Cisplatin is retained in the cochlea indefinitely following chemotherapy. *Nat. Comm.* 8:1654. doi: 10.1038/s41467-017-01837-1

Chen, J., Yuan, H., Talaska, A. E., Hill, K., and Sha, S. H. (2015). Increased Sensitivity to Noise-Induced Hearing Loss by Blockade of Endogenous PI3K/Akt Signaling. *J. Assoc. Res. Otolaryngol.* 16, 347–356. doi: 10.1007/s10162-015-0508-x

Cheng, C., Wang, Y., Guo, L., Lu, X., Zhu, W., Muhammad, W., et al. (2019). Age-related transcriptome changes in Sox2+ supporting cells in the mouse cochlea. *Stem Cell Res. Ther.* 10:365. doi: 10.1186/s13287-019-1437-0

Ding, D., Allman, B. L., and Salvi, R. (2012). Review: ototoxic Characteristics of Platinum Antitumor Drugs. *Anat. Record Adv. Integr. Anat. Evol. Biol.* 295, 1851–1867. doi: 10.1002/ar.22577

Du, Z., Yang, Y., Hu, Y., Sun, Y., Zhang, S., Peng, W., et al. (2012). A long-term high-fat diet increases oxidative stress, mitochondrial damage and apoptosis in the inner ear of D-galactose-induced aging rats. *Hear. Res.* 287, 15–24. doi: 10.1016/j.heares.2012.04.012

Fox, S., Leitch, A. E., Duffin, R., Haslett, C., and Rossi, A. G. (2010). Neutrophil apoptosis: relevance to the innate immune response and inflammatory disease. *J. Innate Immun.* .2, 216–227. doi: 10.1159/000284367

Gates, G. A., and Mills, J. H. (2005). Presbycusis. *The Lancet* 366, 1111–1120. doi: 10.1016/s0140-6736(05)67423-5

Gratton, M. A., Eleftheriadou, A., Garcia, J., Verduzco, E., Martin, G. K., Lonsbury-Martin, B. L., et al. (2011). Noise-induced changes in gene expression in the cochleae of mice differing in their susceptibility to noise damage. *Hear. Res.* 277, 211–226. doi: 10.1016/j.heares.2010.12.014

Guo, L., Cao, W., Niu, Y., He, S., Chai, R., and Yang, J. (2021). Autophagy Regulates the Survival of Hair Cells and Spiral Ganglion Neurons in Cases of Noise, Ototoxic Drug, and Age-Induced Sensorineural Hearing Loss. *Front. Cell Neurosci.* 15:760422. doi: 10.3389/fncel.2021.760422

He, Z. H., Li, M., Fang, Q. J., Liao, F. L., Zou, S. Y., Wu, X., et al. (2021). FOXG1 promotes aging inner ear hair cell survival through activation of the autophagy pathway. *Autophagy* 17, 4341–4362. doi: 10.1080/15548627.2021.1916194

He, Z. H., Zou, S. Y., Li, M., Liao, F. L., Wu, X., Sun, H. Y., et al. (2020). The nuclear transcription factor FoxG1 affects the sensitivity of mimetic aging hair cells to inflammation by regulating autophagy pathways. *Redox Biol.* 28:101364. doi: 10.1016/j.redox.2019.101364

Hequembourg, S., and Liberman, M. C. (2001). Spiral ligament pathology: a major aspect of age-related cochlear degeneration in C57BL/6 mice. *J. Assoc. Res. Otolaryngol.* 2, 118–129. doi: 10.1007/s101620010075

Jing, W., Zongjie, H., Denggang, F., Na, H., Bin, Z., Aifen, Z., et al. (2015). Mitochondrial mutations associated with aminoglycoside ototoxicity and hearing loss susceptibility identified by meta-analysis. *J. Med. Genet.* 52, 95–103. doi: 10.1136/jmedgenet-2014-102753

Kalinec, G., Thein, P., Park, C., and Kalinec, F. (2016). HEI-OC1 cells as a model for investigating drug cytotoxicity. *Hear. Res.* 335, 105–117. doi: 10.1016/j.heares.2016.02.019

Kalinec, G. M., Webster, P., Lim, D. J., and Kalinec, F. (2003). A cochlear cell line as an in vitro system for drug ototoxicity screening. *Audiol. Neurootol.* 8, 177–189. doi: 10.1159/000071059

Keithley, E. M. (2020). Pathology and mechanisms of cochlear aging. *J. Neurosci. Res.* 98, 1674–1684. doi: 10.1002/jnr.24439

Kim, D., Pertea, G., Trapnell, C., Pimentel, H., Kelley, R., and Salzberg, S. L. (2013). TopHat2: accurate alignment of transcriptomes in the presence of insertions, deletions and gene fusions. *Genom. Biol.* 14:R36. doi: 10.1186/gb-2013-14-4-r36

Kuemmerle-Deschner, J. B., Koitschev, A., Tyrrell, P. N., Plontke, S. K., Deschner, N., Hansmann, S., et al. (2015). Early detection of sensorineural hearing loss in Muckle-Wells-syndrome. *Pediatr. Rheumatol. Online J.* 13:43. doi: 10.1186/s12969-015-0041-9

Landier, W. (2016). Ototoxicity and cancer therapy. *Cancer* 122, 1647–1658. doi: 10.1002/cncr.29779

Langfelder, P., and Horvath, S. (2008). WGCNA: an R package for weighted correlation network analysis. *Bmc Bioinform.* 9:559. doi: 10.1186/1471-2105-9-559

Li, L., Chao, T., Brant, J., O'Malley, B. Jr., Tsourkas, A., and Li, D. (2017). Advances in nano-based inner ear delivery systems for the treatment of sensorineural hearing loss. *Adv. Drug Deliv. Rev.* 108, 2–12. doi: 10.1016/j.addr.2016.01.004

Li, X., Xu, Q., Wu, Y., Li, J., Tang, D., Han, L., et al. (2014). A CCL2/ROS autoregulation loop is critical for cancer-associated fibroblasts-enhanced tumor growth of oral squamous cell carcinoma. *Carcinogenesis* 35, 1362–1370. doi: 10.1093/carcin/bgu046

Li, Y., Ding, D., Jiang, H., Fu, Y., and Salvi, R. (2011). Co-administration of cisplatin and furosemide causes rapid and massive loss of cochlear hair cells in mice. *Neurotox. Res.* 20, 307–319. doi: 10.1007/s12640-011-9244-0

Liberman, M. C., and Kujawa, S. G. (2017). Cochlear synaptopathy in acquired sensorineural hearing loss: manifestations and mechanisms. *Hear. Res.* 349, 138–147. doi: 10.1016/j.heares.2017.01.003

Maeda, Y., Kariya, S., Uraguchi, K., Takahara, J., Fujimoto, S., Sugaya, A., et al. (2021). Immediate changes in transcription factors and synaptic transmission in the cochlea following acoustic trauma: a gene transcriptome study. *Neurosci. Res.* 165, 6–13. doi: 10.1016/j.neures.2020.05.001

Maeda, Y., Omichi, R., Sugaya, A., Kariya, S., and Nishizaki, K. (2017). Cochlear Transcriptome Following Acoustic Trauma and Dexamethasone Administration Identified by a Combination of RNA-seq and DNA Microarray. *Otol. Neurotol.* 38, 1032–1042. doi: 10.1097/mao.0000000000001373

Mak, T. W., and Yeh, W. C. (2002). Signaling for survival and apoptosis in the immune system. *Arthritis Res* 4(Suppl. 3), S243–S252. doi: 10.1186/ar569

Malgrange, B., Varela-Nieto, I., de Medina, P., and Paillasse, M. R. (2015). Targeting cholesterol homeostasis to fight hearing loss: a new perspective. *Front. Aging Neurosci.* 7:3. doi: 10.3389/fnagi.2015.00003

Miao, L., Zhang, J., Yin, L., and Pu, Y. (2021). TMT-Based Quantitative Proteomics Reveals Cochlear Protein Profile Alterations in Mice with Noise-Induced Hearing Loss. *Int. J. Environ .Res. Public Health* 19:382. doi: 10.3390/ijerph19010382

Nelson, D. I., Nelson, R. Y., Concha-Barrientos, M., and Fingerhut, M. (2005). The global burden of occupational noise-induced hearing loss. *Am. J. Ind. Med.* 48, 446–458. doi: 10.1002/ajim.20223

Santoso, J. T., Lucci, J. A. III, Coleman, R. L., Schafer, I., and Hannigan, E. V. (2003). Saline, mannitol, and furosemide hydration in acute cisplatin nephrotoxicity: a randomized trial. *Cancer Chemother. Pharmacol.* 52, 13–18. doi: 10.1007/s00280-003-0620-1

Sanz, L., Murillo-Cuesta, S., Cobo, P., Cediel-Algovia, R., Contreras, J., Rivera, T., et al. (2015). Swept-sine noise-induced damage as a hearing loss model for preclinical assays. *Front. Aging Neurosci.* 7:7. doi: 10.3389/fnagi.2015.00007

Shannon, P., Markiel, A., Ozier, O., Baliga, N. S., Wang, J. T., Ramage, D., et al. (2003). Cytoscape: a software environment for integrated models of biomolecular interaction networks. *Genom. Res.* 13, 2498–2504. doi: 10.1101/gr.1239303

Simon, H. U. (2003). Targeting apoptosis in the control of inflammation. *Eur. Respir. J.* 44, 20s–21s. doi: 10.1183/09031936.03.00000603b

Someya, S., and Prolla, T. A. (2010). Mitochondrial oxidative damage and apoptosis in age-related hearing loss. *Mech. Ageing Dev.* 131, 480–486. doi: 10.1016/j.mad.2010.04.006

Su, Z., Xiong, H., Liu, Y., Pang, J., Lin, H., Zhang, W., et al. (2020). Transcriptomic analysis highlights cochlear inflammation associated with age-related hearing loss in C57BL/6 mice using next generation sequencing. *PeerJ.* 8:e9737. doi: 10.7717/peerj.9737

Taukulis, I. A., Olszewski, R. T., Korrapati, S., Fernandez, K. A., Boger, E. T., Fitzgerald, T. S., et al. (2021). Single-Cell RNA-Seq of Cisplatin-Treated Adult Stria Vascularis Identifies Cell Type-Specific Regulatory Networks and Novel Therapeutic Gene Targets. *Front. Mol. Neurosci.* 14:718241. doi: 10.3389/fnmol.2021.718241

Trapnell, C., Williams, B. A., Pertea, G., Mortazavi, A., Kwan, G., van Baren, M. J., et al. (2010). Transcript assembly and quantification by RNA-Seq reveals unannotated transcripts and isoform switching during cell differentiation. *Nat. Biotechnol.* 28, 511–515. doi: 10.1038/nbt.1621

Umugire, A., Lee, S., Kim, D., Choi, M., Kim, H.-S., and Cho, H.-H. (2019). Avenanthramide-C prevents noise- and drug-induced hearing loss while protecting auditory hair cells from oxidative stress. *Cell Death Discov.* 5:115. doi: 10.1038/s41420-019-0195-1

Vethanayagam, R. R., Yang, W., Dong, Y., and Hu, B. H. (2016). Toll-like receptor 4 modulates the cochlear immune response to acoustic injury. *Cell Death Dis.* 7:e2245. doi: 10.1038/cddis.2016.156

Vital-Lopez, F. G., Memisevic, V., and Dutta, B. (2012). Tutorial on biological networks. *Wiley Interdiscip. Rev. Data Mining Knowledge Discov.* 2, 298–325. doi: 10.1002/widm.1061

Wang, J., Ladrech, S., Pujol, R., Brabet, P., Van De Water, T. R., and Puel, J. L. (2004). Caspase inhibitors, but not c-Jun NH2-terminal kinase inhibitor treatment, prevent cisplatin-induced hearing loss. *Cancer Res.* 64, 9217–9224. doi: 10.1158/0008-5472.Can-04-1581

Wang, J., Pignol, B., Chabrier, P.-E., Saido, T., Lloyd, R., Tang, Y., et al. (2007). A novel dual inhibitor of calpains and lipid peroxidation (BN82270) rescues the cochlea from sound trauma. *Neuropharmacology* 52, 1426–1437. doi: 10.1016/j.neuropharm.2007.02.007

Wang, J., and Puel, J.-L. (2018). Toward Cochlear Therapies. *Physiol. Rev.* 98, 2477–2522. doi: 10.1152/physrev.00053.2017

Wang, Q., Shen, Y., Hu, H., Fan, C., Zhang, A., Ding, R., et al. (2020). Systematic Transcriptome Analysis of Noise-Induced Hearing Loss Pathogenesis Suggests Inflammatory Activities and Multiple Susceptible Molecules and Pathways. *Front. Genet.* 11:968. doi: 10.3389/fgene.2020.00968

Wang, X., Zhang, J., Li, G., Sai, N., Han, J., Hou, Z., et al. (2019). Vascular regeneration in adult mouse cochlea stimulated by VEGF-A(165) and driven by NG2-derived cells ex vivo. *Hear. Res.* 377, 179–188. doi: 10.1016/j.heares.2019.03.010

Yang, S., Cai, Q., Bard, J., Jamison, J., Wang, J., Yang, W., et al. (2015). Variation analysis of transcriptome changes reveals cochlear genes and their associated functions in cochlear susceptibility to acoustic overstimulation. *Hear. Res.* 330, 78–89. doi: 10.1016/j.heares.2015.04.010

Yu, J., Wang, Y., Liu, P., Li, Q., Sun, Y., and Kong, W. (2014). Mitochondrial DNA common deletion increases susceptibility to noise-induced hearing loss in a mimetic aging rat model. *Biochem. Biophys. Res. Commun.* 453, 515–520. doi: 10.1016/j.bbrc.2014.09.118

Zhang, G., Zheng, H., Pyykko, I., and Zou, J. (2019). The TLR-4/NF-κB signaling pathway activation in cochlear inflammation of rats with noise-induced hearing loss. *Hear. Res.* 379, 59–68. doi: 10.1016/j.heares.2019.04.012

Zhang, Y., Li, Y., Fu, X., Wang, P., Wang, Q., Meng, W., et al. (2021). The Detrimental and Beneficial Functions of Macrophages After Cochlear Injury. *Front. Cell Dev. Biol.* 9:631904. doi: 10.3389/fcell.2021.631904

Zhong, Y., Hu, Y. J., Yang, Y., Peng, W., Sun, Y., Chen, B., et al. (2011). Contribution of common deletion to total deletion burden in mitochondrial DNA from inner ear of d-galactose-induced aging rats. *Mutat. Res.* 712, 11–19. doi: 10.1016/j.mrfmmm.2011.03.013

Conflict of Interest: The authors declare that the research was conducted in the absence of any commercial or financial relationships that could be construed as a potential conflict of interest.

frontiers | Frontiers in Cellular Neuroscience

ORIGINAL RESEARCH
published: 04 May 2022
doi: 10.3389/fncel.2022.859882

Stiffening of Circumferential F-Actin Bands Correlates With Regenerative Failure and May Act as a Biomechanical Brake in the Mammalian Inner Ear

Mark A. Rudolf[1], Anna Andreeva[2], Christina E. Kim[1], Anthony C.-J. DeNovio[1], Antoan N. Koshar[1], Wendy Baker[1], Alexander X. Cartagena-Rivera[3] and Jeffrey T. Corwin[1,4]*

[1] Department of Neuroscience, University of Virginia School of Medicine, Charlottesville, VA, United States, [2] School of Sciences and Humanities, Nazarbayev University, Nur-Sultan, Kazakhstan, [3] Section on Mechanobiology, National Institute of Biomedical Imaging and Bioengineering, National Institutes of Health, Bethesda, MD, United States, [4] Department of Cell Biology, University of Virginia School of Medicine, Charlottesville, VA, United States

OPEN ACCESS

Edited by:
Brad Walters,
University of Mississippi Medical Center, United States

Reviewed by:
Jian Zuo,
Creighton University, United States
Karen Litwa,
East Carolina University, United States

***Correspondence:**
Jeffrey T. Corwin
jtc2k@virginia.edu

Specialty section:
This article was submitted to Non-Neuronal Cells, a section of the journal Frontiers in Cellular Neuroscience

Received: 21 January 2022
Accepted: 06 April 2022
Published: 04 May 2022

Citation:
Rudolf MA, Andreeva A, Kim CE, DeNovio AC-J, Koshar AN, Baker W, Cartagena-Rivera AX and Corwin JT (2022) Stiffening of Circumferential F-Actin Bands Correlates With Regenerative Failure and May Act as a Biomechanical Brake in the Mammalian Inner Ear. Front. Cell. Neurosci. 16:859882. doi: 10.3389/fncel.2022.859882

The loss of inner ear hair cells causes permanent hearing and balance deficits in humans and other mammals, but non-mammals recover after supporting cells (SCs) divide and replace hair cells. The proliferative capacity of mammalian SCs declines as exceptionally thick circumferential F-actin bands develop at their adherens junctions. We hypothesized that the reinforced junctions were limiting regenerative responses of mammalian SCs by impeding changes in cell shape and epithelial tension. Using micropipette aspiration and atomic force microscopy, we measured mechanical properties of utricles from mice and chickens. Our data show that the epithelial surface of the mouse utricle stiffens significantly during postnatal maturation. This stiffening correlates with and is dependent on the postnatal accumulation of F-actin and the cross-linker Alpha-Actinin-4 at SC-SC junctions. In chicken utricles, where SCs lack junctional reinforcement, the epithelial surface remains compliant. There, SCs undergo oriented cell divisions and their apical surfaces progressively elongate throughout development, consistent with anisotropic intraepithelial tension. In chicken utricles, inhibition of actomyosin contractility led to drastic SC shape change and epithelial buckling, but neither occurred in mouse utricles. These findings suggest that species differences in the capacity for hair cell regeneration may be attributable in part to the differences in the stiffness and contractility of the actin cytoskeletal elements that reinforce adherens junctions and participate in regulation of the cell cycle.

Keywords: hair cell, utricle, regeneration, F-actin (filamentous actin), epithelial mechanics, alpha actinin 4, atomic force microscopy – AFM, micropipette aspiration (MPA)

INTRODUCTION

Permanent hearing loss affects more than 400 million people worldwide, and studies indicate that vestibular dysfunctions affect roughly one third of adults (Agrawal et al., 2009; World Health Organization [WHO], 2018). The loss of sensory hair cells (HCs) in the inner ear is a major irreversible cause of these sensory deficits. HCs are vulnerable to loud sound, ototoxic drugs, and aging, and are not effectively replaced in humans and other mammals (Nadol, 1993). In contrast, HC loss in fish, amphibians, and birds causes neighboring supporting cells (SCs) to divide and produce progeny that can differentiate into replacement HCs, and in some cases convert directly into HCs (Corwin and Cotanche, 1988; Baird et al., 1996). What accounts for the difference in regenerative capacity has remained unclear.

Studies of epithelial repair have shown that mechanical forces arising from cell loss propagate through cell-cell junctions, increasing tension in the cortical cytoskeletons and changing the shapes of neighboring cells, which activates mechanosensitive signaling molecules such as YAP/TAZ and leads to cell proliferation (Rauskolb et al., 2014; Benham-Pyle et al., 2015). Past research has shown that the intercellular junctions of SCs in the chicken utricle contain little or no E-cadherin and are associated with thin circumferential "belts" of F-actin as are epithelial cells in general. In contrast, utricular SCs in mice and humans develop E-cadherin-rich junctions that are bracketed by exceptionally wide and thick regions of circumferential F-actin (Burns et al., 2008; Burns and Corwin, 2013). Throughout this article we use the term "F-actin bands" as a more appropriate descriptor for the exceptionally robust structures in mouse SCs. The growth of the circumferential F-actin bands in SCs of the mouse utricle strongly correlates to declines in the capacity for the cells to change shape ($R = -0.989$) and proliferate ($R = -0.975$) in culture (Burns et al., 2008; Collado et al., 2011b). HC loss and SC shape change also have been found to activate YAP in SCs of the chicken utricle, but lead to little or no nuclear accumulation in the mouse utricle (Rudolf et al., 2020; Borse et al., 2021). Those findings suggested that the thin F-actin belts in non-mammalian SCs might more readily permit shape changes and proliferation, whereas the thick F-actin bands in mammalian SCs could restrict or slow deformations, thereby reducing signals that can evoke proliferative responses.

To test our hypothesis that the thick F-actin bands limit deformation of mammalian SCs, we measured stiffness of the epithelial surface in utricles from mice and chickens of various ages using atomic force microscopy (AFM) and micropipette aspiration. The measurements revealed that the mouse utricular epithelium stiffens postnatally, particularly at SC junctions. F-actin and the cross-linker Alpha-Actinin-4 substantially contribute to the measured stiffness. In stark contrast, chicken utricles remained relatively compliant. Analysis of cell shape revealed that the apical domains of chicken SCs elongate and align throughout development. Inhibition of myosin II contractility led to dramatic expansion of chicken SC surfaces, but it did not affect the size and regular shapes of mouse SCs. The results indicate that the exceptionally thick and cross-linked circumferential F-actin bands stiffen mammalian SCs and appear likely to limit the mechanical signals produced during cell loss, whereas the compliant SCs in birds exhibit collective mechanical behavior that is favorable for epithelial repair.

MATERIALS AND METHODS

Animals and Dissection of Vestibular Organs

All animals were handled in accordance with protocols approved by the Animal Care and Use Committee at the University of Virginia (protocol 18350718) and NIH guidelines for animal use (protocol 1254-18). Utricles from embryonic day 16 (E16), postnatal day zero (P0), or adult (>6 week old) mice were used with staging of embryos according to The Atlas of Mouse Development (Kaufman, 1992). Swiss Webster mice were obtained from Charles River Laboratories. Transgenic mice that express a γ-actin and green fluorescent protein fusion (γ-actin–GFP) were generated in the laboratory of Dr. Andrew Matus (Fischer et al., 1998). Mice with whole-body knockout of *Alpha-Actinin-4 (Actn4* KO) were generated in the laboratory of Dr. Martin Pollak (Kos et al., 2003). Fertilized White Leghorn (W-36) eggs were obtained from Hy-Line and incubated at 37°C in a humidified chamber with rocking until E18, after which eggs were incubated without rocking. Embryos were staged according to morphometric features (Hamburger and Hamilton, 1951). Animals of either sex were used for all experiments.

For tissue harvest, labyrinths were dissected from temporal bones in ice-cold, HEPES-buffered DMEM/F-12 (Thermo Fisher Scientific), utricles were isolated, and the roof and the otoconia were mechanically removed.

Generation of *Actn4* Conditional Knockout Mice

To generate $Actn4^{flox/flox}$ mice, frozen sperm from $Actn4^{TM1a(EUCOMM)Wtsi}$ mice (Mouse Genome Informatics ID: 4441842) were obtained from the European Mouse Mutant Archive (EMMA) (EM:05964). The $Actn4^{TM1a(EUCOMM)Wtsi}$ mice harbor a loxP site downstream of *Actn4* exon 5 at position 28615171 of chromosome 7 (Build GRCm39), as well as an L1L2_gt1 cassette upstream of exon 5 at position 28614391, which contains an FRT-flanked lacZ/neomycin sequence followed by a loxP site. The Genetically Engineered Murine Model core at the University of Virginia performed *in vitro* fertilization to rederive the line, as previously described (Takeo and Nakagata, 2011). The conditional knockout line was then generated per the EMMA protocol. Briefly, FLP germline deleter mice were crossed with the $Actn4^{TM1a(EUCOMM)Wtsi}$ mice to excise the FRT-flanked lacZ/neomycin sequence, producing mice with an allele of *Actn4* in which the critical exon 5 is floxed. The resulting $Actn4^{flox/flox}$ mice were crossed to 129(Cg)-$Foxg1^{TM1(cre)Skm}$/J mice (*Foxg1-Cre*, Jackson Laboratory stock 004337) which express Cre recombinase in the embryonic forebrain and otic vesicle (Hébert and McConnell, 2000), producing $Actn4^{flox/flox}$;*Foxg1-Cre* (*Actn4* cKO) mice. $Actn4^{flox/flox}$ mice were genotyped using the following primers:

5′-AACTCAGGATGGAGTTGGGC-3′ (common forward), 5′-TGGATGTGGGTGATCTTTGC-3′ (wild type reverse), and 5′-TCGTGGTATCGTTATGCGCC-3′ (floxed reverse). An amplicon measuring 455 bp signifies a wild type allele of *Actn4*, and an amplicon of 184 bp signifies a floxed allele. *Foxg1-Cre* mice were genotyped using the following primers: 5′-AGAACCTGAAGATGTTCGCG-3′ (*Cre* forward) and 5′-GGCTATACGTAACAGGGTGT-3′ (*Cre* reverse). An amplicon measuring 328 bp signifies the presence of a *Cre* allele.

Organ Culture

Utricles dissected from mice and chickens under aseptic conditions were transferred to glass-bottom dishes (Mat-Tek) or Willco dishes (Willco Wells) coated with Cell-Tak (1 μL air-dried onto the glass; BD Biosciences #354240) and adhered with the stromal side down. Utricles were cultured in DMEM/F-12 + HEPES with 1% fetal bovine serum (FBS; Invitrogen) and 10 μg/ml Ciprofloxacin (Bayer) at 37°C and 5% CO_2. In some experiments, cytochalasin D (Sigma-Aldrich), blebbistatin (Calbiochem), or streptomycin sulfate (Sigma) were added to the culture medium at the concentrations and durations indicated below.

Micropipette Aspiration

To measure the mechanical stability of sensory epithelia from chickens and mice of various ages, we adapted micropipette aspiration to quantify tissue-level resistance to deformation in utricles. This technique enables direct observation of deformation lengths produced by a calibrated suction, and can be applied in length scales ranging from single cells (Hochmuth, 2000) to whole embryos (Porazinski et al., 2015). Two types of micropipettes were fabricated from borosilicate glass tubes on a Sutter Instruments puller: "stabilizing pipettes" were scored with a tile and broken to a clean edge of 50–100 μm internal diameter, and "aspiration pipettes" were scored with a tile and broken to a clean edge of 22.5 μm internal diameter (which spans ∼5 HCs). The tip of the aspiration micropipette was dipped in Sigmacote (Sigma SL2) and allowed to dry before use in order to minimize adhesion to debris.

On the day of tissue harvest, utricles for micropipette aspiration measurement were cultured atop 0.08 μm Nucleopore filters (Whatman) at the meniscus of the culture medium. On the following day, utricles were transferred to a glass-bottom POCR chamber (Zeiss) containing DMEM/F12 + HEPES supplemented with 5% FBS, and the utricle was adhered to the Cell-Tak-coated glass with the stromal side down. Under an upright microscope with a heated stage set to 37°C, the utricle was visualized with a 2× objective and partially lifted from the glass using fine forceps, with one edge remaining adhered to the glass. The "stabilizing" pipette of 50–100 μm internal diameter was positioned via a micromanipulator into contact with the stromal side of the utricle and held the macular surface parallel to the optical axis (**Figure 1A**). The second, "aspiration" micropipette of 22.5 μm internal diameter was used for micropipette aspiration measurements of the apical surface. Water-filled tubing connected each micropipette to an open-barreled syringe (water reservoir) that was raised or lowered to control suction and serve as a manometer. A 60×, 0.9 NA water immersion objective and differential interference contrast were used to visualize the utricle's apical surface and the tip of the micropipette.

To perform a measurement, the meniscus of the water reservoir was initially held at the same height as the utricle, so that no suction pressure would be present upon contact. Then, a micromanipulator was used to bring the aspiration pipette into light contact with the sensory epithelium's apical surface. The water reservoir was then lowered to apply a ramped negative pressure, resulting in deformation of the apical surface that could be visualized with differential interference contrast video microscopy (**Figures 1B,C**; **Supplementary Movie 1**). Specifically, the water reservoir was lowered at a rate of 3 cm/s for 10 s (equivalent to a negative pressure ramp of 3 cm H_2O/s or ∼300 Pa/s), and then held with the meniscus 30 cm below the height of the utricle (equivalent to a negative pressure of 30 cm H_2O or ∼3 kPa) for an additional 10 s. As the utricle's apical surface deformed during that process, images of the deformation were acquired at 1 s increments using a SPOT Idea CMOS camera. After the 20 s acquisition, the final deformation length was measured in a blinded fashion using FIJI software (Schindelin et al., 2012). Each utricle was measured at least three times, and the individual measurements from each utricle were averaged to generate a single value of deformation length, which was considered a single independent observation for statistical analysis.

Elastic Young's modulus (*E*; Pa) was calculated using a simple continuum model that treats the tissue as a homogeneous, incompressible, linear-elastic half space (Theret et al., 1988; González-Bermúdez et al., 2019):

$$E_{tissue} = \Delta P \frac{3\varphi_p}{2\pi} \frac{R_p}{L_p}$$

In this equation, the applied pressure gradient ΔP was 30 cm H_2O (2942 Pa), the pipette wall thickness parameter φ_p was set to 2.1, the pipette inner radius R_p was 11.25 μm, and L_p was the measured deformation length (μm). The average deformation length was used to calculate one value of *E* per utricle, which was considered a single independent observation for statistical analysis.

Atomic Force Microscopy

Atomic force microscopy (AFM) measurements were conducted for utricular sensory epithelia of CD-1 mice (Charles River Laboratories) and embryonic Delaware chickens (B & E eggs, PA). To comply with the language of the animal protocol at the NIH, utricles were harvested exclusively from embryonic and not post-hatch chickens. Eggs were incubated at 37.5°C in an automatic rocking incubator (Brinsea), and all embryos were terminated prior to hatching at E21. Utricles were freshly dissected as above and mounted on glass-bottom dishes (HBST-5040, Willco Wells) precoated with 2 μl of Cell-Tak (Corning) and immersed in Leibovitz media (L-15, 21083-027, Life Technologies). AFM measurements were obtained on a Bioscope Catalyst AFM system (Bruker) mounted on an inverted

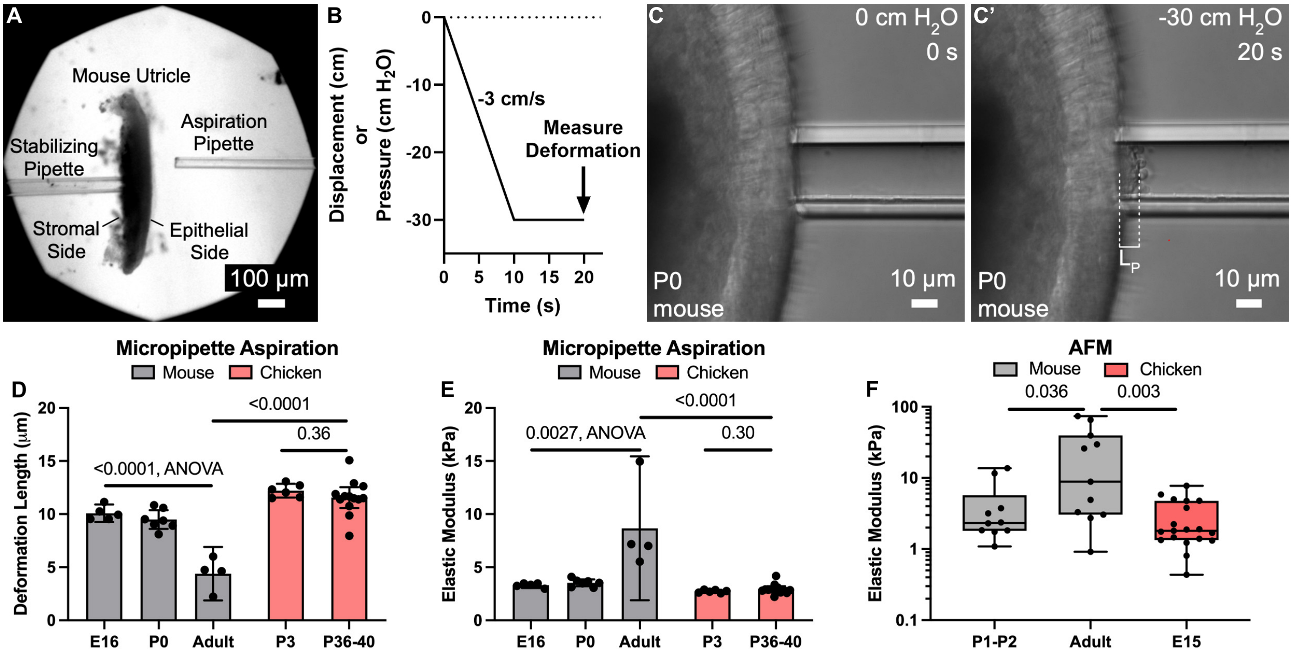

FIGURE 1 | Micropipette aspiration and AFM measurements reveal that the apical surface of utricles from mature mice are significantly more resistant to deformation than those of newborn mice and chickens. **(A)** Low magnification image of a mouse utricle prior to micropipette aspiration. A stabilizing pipette ∼50–100 μm in diameter (left) was used to apply light suction on the "stromal side" to maintain the utricle in place. Another pipette 22.5 μm (∼5 cell apices) in diameter (right) was used to apply a defined negative pressure to the epithelial surface of the utricle. **(B)** The negative pressure was ramped from 0 cm H_2O to –30 cm H_2O over a span of 10 s, and then maintained at –30 cm H_2O for an additional 10 s. The deformation length of the apical surface was after the full 20 s "pull" was recorded. **(C,C')** High magnification images of the apical surface of a P0 mouse utricle during application of negative pressure, producing a deformation of length L_P. **(D)** Plot of mean deformation length of utricles from mice and chickens of various ages. Error bars denote 95% confidence intervals. Dots represent an average of at least three measurements from a single utricle. *P*-values are listed from unpaired *t*-tests or ANOVA. **(E)** Plot of elastic moduli as measured by micropipette aspiration of the utricular epithelial surface, as calculated from the deformation lengths in **(D)**. Error bars denote 95% confidence intervals, and each dot represents one utricle. *P*-values are listed from unpaired *t*-tests or ANOVA. **(F)** Boxplot in logarithmic scale of elastic moduli as measured by AFM of the utricular epithelial surface. Each dot represents the average elastic modulus obtained from an eight-point line scan. *P*-values are indicated from Mann-Whitney tests.

Axiovert 200M microscope (Zeiss) equipped with a confocal laser scanning microscope (510 Meta, Zeiss) and a 40× objective lens (0.95 NA, Plan-Apochromat, Zeiss). Explants were maintained at 37°C using a Bruker heated stage. For tissue-level measurements, line scans of eight points spaced between 500 nm and 1 μm apart were obtained from the apical surface of the sensory epithelium. We used soft silicon nitride Bruker MLCT AFM probes with nominal tip radius of 20 nm. The MLCT cantilevers were precalibrated by using the AFM built-in thermal method, yielding spring constants between 0.07 and 0.12 N/m. For some experiments, sheets of utricular sensory epithelium were obtained by incubating the utricles in 0.5% thermolysin at 37°C for 15 min, and mechanically separating the epithelium from the underlying stroma. PeakForce Tapping (PFT) Quantitative Imaging mode was used for high-resolution measurements, as has been performed previously for living inner ear tissues (Theret et al., 1988; Cartagena-Rivera et al., 2019; González-Bermúdez et al., 2019; Katsuno et al., 2019). The AFM probe specially designed for live cell imaging (PFQNM-LC, Bruker) has a tip height of 17 μm, controlled tip radius of 65 nm, and opening angle of 15°. The cantilevers (Bruker, PFQNM-LC-A-CAL) were precalibrated right after manufacturing by Bruker using a laser Doppler vibrometer. We confirmed the precalibration by Bruker using the AFM built-in thermal tuning method, and the obtained spring constant range of the cantilevers was between 0.06 and 0.08 N/m. For PFT-AFM imaging, we used a driving frequency of 500 Hz and drive amplitudes of 500 to 650 nm. The scan speed used was 0.5 Hz. The PeakForce feedback was set between 800 pN and 1.2 nN. The elastic Young's modulus (stiffness) calculations for both AFM modalities used in this study were performed using NanoScope Analysis software (Bruker). The elastic Young's modulus (E) was computed by fitting each force-distance curve with the Sneddon's contact mechanics model for indenting an infinite isotropic elastic half-space with a conical indenter:

$$F_{Sneddon} = (8E\ tan\frac{\alpha}{3}\ \pi)\delta^2$$

In this equation, F is the applied force, α is the tip half-opening angle, and δ is the sample mean indentation. A single value of E was obtained for each line scan by averaging the eight values that comprised each line scan. One line scan was considered an independent replicate for statistical analysis.

Immunohistochemistry

Utricles were fixed in 4% paraformaldehyde for 1 h at room temperature or Shandon Glyo-Fixx overnight at 4°C. After washing in PBS with 0.1% Triton X-100 (PBST), utricles were blocked in 10% normal goat serum (Vector) in PBST for 2 h at room temperature. Primary antibodies were incubated with 2% normal goat serum at 4°C overnight. After washing in PBST, secondary antibodies were added in 2% normal goat serum and incubated for 2 h at room temperature. Where indicated below, AlexaFluor-conjugated phalloidin (1:100) and Hoechst 33452 (1:500) were incubated along with secondary antibodies to detect actin and nuclei. After washing in PBST, samples were mounted in Prolong Diamond and imaged using a Zeiss 880 confocal microscope or a Zeiss Axiovert 200M widefield microscope. Primary antibodies used included: Rabbit anti-Calretinin (Millipore Sigma AB5054, 1:200), mouse anti-N-cadherin (BD Biosciences 610920, 1:200), rabbit anti-ZO-1 (Thermo Fisher Scientific 40-2200, 1:200), rabbit anti-Chick Occludin (generous gift from Shoichiro Tsukita, 1:200), mouse anti-Spectrin (Millipore MAB1622, 1:200), rabbit anti-phospho-Histone H3 (Ser10) (Millipore 06-570, 1:400), rabbit anti-Cingulin (Zymed 36-4401, 1:200), and rabbit anti-Filamin A (Abcam ab51217, 1:200).

RNA Extraction and Quantitative PCR

To extract RNA, 10 mouse utricles or 2–4 chicken utricles were harvested, pooled, and dissolved in 500 μL TRI-reagent (Molecular Research Center). RNA was precipitated using 2 μL of polyacryl carrier (Molecular Research Center) per the manufacturer's protocol, and cDNA was generated with a High-Capacity RNA-to-cDNA kit (Applied Biosystems). Quantitative PCR was performed using SensiMix SYBR Green and Fluorescein kit (Quantace) on a MyIQ/iCycler (Bio-Rad). Two technical replicates were used for each run. The Miner algorithm was used to analyze gene expression (Zhao and Fernald, 2005). For mouse utricles, *Ppia* (also known as *Cyclophilin A*) served as an endogenous reference gene (forward primer, CAGTGCTCAGAGCTCGAAAGT; reverse primer, GTGTTCTTCGACATCACGGC), and *Actn4* was the target gene (forward primer, TCCACTTACAGACATCGTGAACACA; reverse primer, GCATGGTAGAAGCTGGACACATAT). For chicken utricles, *ACTB* served as an endogenous reference gene (forward primer, CCGGCTCTGACTGACCGCGT; reverse primer, GGCATCGTCCCCGGCGAAAC), and *ACTN4* was the target gene (forward primer, ACGGAGCGCCATGGTGGATT; reverse primer, AGCAGCAGGTCTCGGTCCCA). Three biological replicates were acquired for mouse samples, and two biological replicates were acquired for chicken samples. An unpaired t-test was used for statistical comparison of gene expression between different ages.

Measurement of Macular Area

After performing micropipette aspiration measurements, utricles of adult control and *Actn4 cKO* mice were labeled with phalloidin and imaged on a Zeiss 880 confocal microscope. Maximum intensity projections were generated in FIJI, and outlines of the utricular maculae were hand-drawn by using stereociliary bundles to determine the macular border. The macular areas of the left and right utricles were averaged together to produce one value of macular area per mouse, which was considered an independent biological replicate for statistical analysis.

Transmission Electron Microscopy

Transmission electron microscopy (TEM) images of the apical junctional region of utricles from *Actn4* KO mice were obtained as previously described (Burns et al., 2008). Briefly, mice were euthanized as above, and within 3 min a fixative solution composed of 3% glutaraldehyde in 0.15 M sodium cacodylate buffer at pH 7.4 was injected into the superior semicircular canal to replace the endolymph. The labyrinth was then isolated and fixed overnight at 4°C. Then the utricle was dissected in 0.15 M cacodylate buffer and post-fixed in 1% osmium-tetroxide. The tissue was dehydrated in a graded ethanol series and infiltrated with Epon 812 (Electron Microscopy Sciences, Hatfield, PA, United States). Thin sections were cut in the plane parallel to the epithelial surface with a diamond knife. Sections were collected on copper grids and stained 5 min with lead citrate, 15 min with uranyl acetate, and 5 min with lead citrate. A JEOL 1230 transmission electron microscope was used for imaging.

Cell Shape Measurements

Supporting cell apical junctions were visualized by immunostaining for ZO-1 or N-cadherin in mouse utricles and immunostaining for cingulin, occludin, or N-cadherin in chicken utricles. For cell shape measurements, five images were acquired per utricle with 30 contiguous SCs quantified from the center of each image, all of which were pooled and considered an independent observation. Mouse utricles were imaged in five standardized locations (lateral extrastriolar, anterior, medial, posterior, and central (striolar) regions). All images of the chicken utricle were acquired in the large, medial extrastriolar region.

All image analysis was done using FIJI. First, SC apical domains were hand-traced from high-magnification images of the utricular apical surface, with 30 contiguous cells analyzed from the center of each image. The apical domain area of each SC was measured. Then, each SC apical domain was fit to an ellipse using the software's built-in function, which provided the length of each apical domain's major axis, minor axis, and angular orientation. Elongation (length:width ratio) was calculated from the ratio of the major and minor axes of each apical domain. The intercellular alignment for a given image was calculated using the following equation, where n is the number of apical domains analyzed in the image (30), θ_{med} is the median ellipse orientation for a given image, and θ_i is the orientation of ellipse i.

$$Intercellular\ alignment = \frac{1}{n}\sum_{i=1}^{n} |\theta_{med} - \theta_i|$$

Using this definition, perfectly aligned cells have a value of 0° deviation from the median angle, and randomly aligned cells have an intercellular alignment approaching 45° deviation from the median angle.

Measurement of Cell Division Orientation

To measure cell division orientation in the developing chicken utricle, utricles were harvested at E14 and immunostained for phospho-histone H3 (PH3) to label dividing cells and spectrin to label the cuticular plates of HCs. Using an Axiovert 200M inverted microscope, cells in metaphase and anaphase were identified. Each mitotic figure was imaged together with nearby HC cuticular plates, which were used to determine the local axis of HC polarity. The division axis of a cell in metaphase was determined by drawing a line that spanned the metaphase plate, measuring its angle in FIJI, and adding 90° to account for the fact that metaphase cells divide perpendicular to the orientation of their metaphase plate. The division axis of a cell in anaphase was determined by drawing a line from one pole to the other and measuring its angle in FIJI. The local axis of HC polarity was determined by averaging the polarity of the six HCs closest to each mitotic figure. Each HC's polarity was measured by drawing a line that bisected its spectrin-labeled cuticular plate and terminated at the fonticulus, and the resulting angle was measured in FIJI. The difference between each cell's division axis and the axis of local HC polarity was recorded as "degrees deviation from local HC polarity." Using this definition, the cell division orientation can range from 0° (division axis parallel to the local axis of HC polarity) to 90° (division axis perpendicular to the local axis of HC polarity).

To measure cell division orientation in the regenerating chicken utricle, utricles from P2 chickens were harvested and cultured 24 h in medium containing 1 mM streptomycin sulfate to ablate HCs. Utricles were then transferred to a dish containing standard culture medium and incubated an additional 48 h prior to fixation. Anti-cingulin was used to label cell junctions, and Hoechst 33342 was used to label nuclei. The orientations of dividing cells in metaphase or anaphase were measured as described above. Because HCs were ablated, the orientation of cell divisions was measured with respect to the long axis of neighboring SCs, which aligns with the axis of HC polarity. To do this, the apical domains of the six closest SCs were outlined using cingulin immunoreactivity and fit to an ellipse using FIJI. Then, the orientations of the major axes of the ellipses were averaged together. The difference between a given cell's division axis and the local axis of SC elongation was recorded as "degrees deviation from local SC elongation." Using this definition, the cell division orientation can range from 0° (division axis parallel to the local axis of SC elongation) to 90° (division axis perpendicular to the local axis of SC elongation).

Time-Lapse Imaging

Chicken utricles were harvested and incubated in culture medium containing 100 nM SiR-actin (Cytoskeleton CY-SC006) for 6 h to label F-actin. They were then transferred to DMEM/F-12 + HEPES containing 3 μM FM1-43FX (Thermo Fisher F35355) for 3 min to label HCs. For imaging, utricles were transferred to a Zeiss POCR chamber with a 42 mm coverglass that contained DMEM/F-12 + HEPES supplemented with 10% FBS. A wax barrier bisected the chamber for the simultaneous imaging of two utricles. Utricles were immobilized HC-side down with a miniature "harp" (gold wire threaded with fine nylon) as previously described (Bird et al., 2010). Then, the imaging chamber was placed on a 37°C heated stage insert supplemented with 5% CO_2. Just prior to image acquisition, blebbistatin was spiked into one side of the bisected chamber at a final concentration of 50 μM, and DMSO was added to the second side as a vehicle control. The time-lapse was acquired on a Zeiss 880 confocal microscope, with z-stacks obtained at 10 min intervals for a duration of 9 h.

Statistics

GraphPad Prism 9 software was used for statistical tests. Unpaired student's t-tests or Mann-Whitney tests were used for pairwise comparisons. ANOVA was used to analyze comparisons among three or more groups, and Tukey's test was applied where indicated. The Kolmogorov-Smirnov (KS) test was used to test whether cell division orientations were randomly oriented, with a uniform distribution as the null hypothesis. Unless otherwise stated, bar graphs display mean ± 95% confidence interval, with dots denoting independent biological replicates. Test statistics, sample sizes, degrees of freedom, and p-values are reported in the Results, on graphs, or in the figure legends. For all tests, a p-value less than 0.05 was considered statistically significant.

RESULTS

Utricular Sensory Epithelia of Mature Mice Are More Resistant to Deformation Than Those of Developing Mice and Chickens

To test the hypothesis that the surface of the sensory epithelium would become more resistant to deformation as mice develop and mature, we used the customized micropipette aspiration described above in utricles from E16, P0, or adults > 6 weeks old (**Figures 1A–C**). Similar deformation lengths were measured in E16 and P0 mouse utricles (10.1 ± 0.8 μm and 9.5 ± 0.9 μm, mean ± 95% confidence interval), corresponding to tissue-level elastic moduli of 3.3 ± 0.3 kPa and 3.5 ± 0.3 kPa, respectively. In contrast, utricles from adults deformed less than half as much (4.4 ± 2.5 μm; $p < 0.0001$, $F_{(2,13)} = 38.16$, ANOVA, $n = 4–7$ utricles per condition, **Figure 1D**), which corresponds to a 2.5-fold increase in elastic modulus compared to that measured in utricles from newborn mice (8.7 ± 6.8 kPa; $p = 0.0027$, $F_{(2,13)} = 2.24$, ANOVA, $n = 4–7$ utricles per condition, **Figure 1E**).

To compare the stiffness of mouse utricles to measurements from a non-mammalian vertebrate that readily regenerates hair cells, we applied the same technique in utricles from P3 and P36-40 chickens. Despite the age difference, the measurements of mean deformation lengths showed no significant difference (12.2 ± 0.7 μm vs. 11.6 ± 1.0 μm, $p = 0.36$, $t_{(17)} = 0.93$, unpaired t-test, $n = 6–13$ utricles per condition, **Figure 1D**), and no significant difference in calculated elastic moduli (2.7 ± 0.1 kPa vs. 2.9 ± 0.3 kPa, $p = 0.31$, $t_{(17)} = 1.06$, unpaired t-test, $n = 6–13$ utricles per condition, **Figure 1E**). Moreover, the deformation lengths of P36-40 chicken utricles were 2.6-fold greater than those measured for adult mice ($p < 0.0001$, $t_{(15)} = 7.7$, unpaired t-test,

$n = 4–13$ utricles per condition, **Figure 1D**), which corresponds to an elastic modulus ~1/3 of that for their mammalian counterparts ($p < 0.0001$, $t_{(15)} = 7.2$, unpaired *t*-test, $n = 4–13$ utricles per condition, **Figure 1E**).

To independently assess surface mechanical properties of utricles from neonatal mice, adult mice, and embryonic chickens, we used AFM. Consistent with the results from micropipette aspiration, AFM yielded a median elastic modulus for the utricles from adult mice that was 3.8-fold greater than that for P1-2 mice (8.8 kPa vs. 2.3 kPa, $p = 0.036$, Mann-Whitney test, $n = 10–11$ line scans per condition, **Figure 1F**) and 4.9-fold greater than that for utricles from E15 chickens (8.8 kPa vs. 1.8 kPa, $p = 0.0033$, Mann-Whitney test, $n = 11–19$ line scans per condition, **Figure 1F**). When we used AFM to measure the surface of delaminated sheets of utricular epithelium, values obtained were not significantly different than the AFM measurements from the surfaces of utricles which contained the underlying stroma (mouse: $p = 0.43$, chicken: $p = 0.46$, Mann-Whitney test, $n = 6–19$ line scans per condition, **Supplementary Figure 1**). This indicates that the original measurements made in utricles containing the stroma reflect the mechanical properties of the sensory epithelium itself. Furthermore, calculated elastic moduli from micropipette aspiration measurements were not significantly different than those obtained from AFM (P0-P2 mice: 3.5 kPa vs. 2.3 kPa median elastic modulus, $p = 0.23$, $p = 0.95$, Mann-Whitney test, $n = 4–11$ measurements). Taken together, the data indicate that maturational changes in the mouse utricle result in the sensory epithelium developing greater resistance to deformation than the sensory epithelium of the chicken utricle, where we did not detect postembryonic stiffening.

F-Actin Depolymerization and Deletion of *Actn4* Reduce the Stiffness of Mature Mouse Utricles

High-resolution AFM measurements and topography mapping at the epithelial surface of utricles from neonatal and adult mice revealed apical protrusions corresponding to HC stereociliary bundles (**Figures 2A,C**). In adult mouse utricles, the measured elastic moduli at the intercellular junctions of SCs often exceeded 100 kPa with maximum peaks reaching ~300 kPa (**Figures 2D,E**), while corresponding regions in P2 mouse utricles rarely exceeded 50 kPa (**Figures 2B,E**). The results indicate that the intercellular junctions in mouse vestibular SCs become significantly stiffer with age, and thus more resistant to changes in cell shape.

Imaging during micropipette aspiration measurements in utricles from P0 and adult γ-actin–GFP mice showed that F-actin at the apices of SCs is deformed, consistent with a hypothesized contribution to stiffness (**Supplementary Movie 2**). To test whether the stiffness of the mouse utricular epithelium is dependent on F-actin, we cultured utricles from adult mice in the presence of 100 nM cytochalasin D for 24 h, which depolymerized the F-actin bands in SCs (**Figures 3A,B**; Burns and Corwin, 2014). Micropipette aspiration revealed that cytochalasin D treatment resulted in a nearly 40% increase in deformation length over DMSO controls (7.3 ± 0.7 vs. 5.3 ± 1.1 μm, $p = 0.002$, $t_{(12)} = 3.94$, unpaired *t*-test, $n = 7$ utricles per condition, **Figures 3C–E**), corresponding to a 24% decrease in elastic modulus (6.5 ± 1.1 vs. 4.6 ± 0.5 kPa, $p = 0.002$, $t_{(12)} = 3.91$, unpaired *t*-test, $n = 7$ utricles per condition, **Figure 3F**). Thus, F-actin substantially stiffens the utricular epithelium in adult mice.

Next, we investigated the expression of actin-binding genes in mouse utricles using RT-qPCR. We observed that *Alpha-Actinin-4* (*Actn4*), which cross-links actin filaments and tethers them to cadherin-catenin complexes at adherens junctions (Tang and Brieher, 2012), increases 2.4-fold from P0 to P83 ($p < 0.0001$, $t_{(4)} = 18.3$, $n = 3$ replicates, **Supplementary Figure 2A**). Consistent with this, examination of publicly available RNA sequencing data of mouse utricular sensory epithelia revealed a 1.4-fold increase in *Actn4* expression between E17 and P9 ($p = 0.0114$, $t_{(4)} = 4.43$, $n = 3$ replicates, **Supplementary Figure 2B**; Gnedeva and Hudspeth, 2015). We detected the ortholog *ACTN4* in chicken utricles by RT-qPCR but found no significant change in expression between the ages of P0 and P30-60 ($p = 0.28$, $t_{(2)} = 1.46$, $n = 2$ replicates, **Supplementary Figure 2A**).

We observed that Actn4 localizes to the exceptionally thick circumferential F-actin bands in mouse SCs (**Figures 3G,I**). To characterize the effect of *Actn4* on the morphology of the F-actin bands, we used *Actn4* KO mice that have whole-body deletion of the *Actn4* gene (Kos et al., 2003). Since mice with homozygous deletion of *Actn4* rarely survived past weaning age (21/175, 12%), we obtained TEM images from utricles of P23 *Actn4* KO and wild-type mice. Deletion of *Actn4* reduced the density of the perijunctional F-actin network as can be seen in **Supplementary Figure 3**.

To circumvent the perinatal lethality of whole-body *Actn4* deletion, we generated conditional knockout mice in which *Actn4* deletion is restricted to the embryonic forebrain and other discrete head structures, including the otic vesicle (*Actn4* cKO, see section "Materials and Methods"). *Actn4* cKO mice were viable and fertile, and showed no significant difference in the area of the utricular sensory epithelia compared to $Actn4^{flox/flox}$ littermate controls (1098 ± 62 vs. 1126 ± 85 μm^2, $p = 0.43$, $t_{(6)} = 0.85$, unpaired *t*-test, $n = 4$ adult mice per condition, **Supplementary Figure 4**). Conditional deletion of *Actn4* in vestibular SCs was confirmed by immunostaining, which showed that morphology of the F-actin bands was disrupted in utricles where the cross-linker was absent (**Figures 3H,J**).

To test whether *Actn4* cross-linking within the F-actin bands stiffens the utricular epithelium, we performed micropipette aspiration on utricles from aged (16–24 months) *Actn4* cKO mice and littermate controls. The epithelial surface of the utricles from *Actn4* cKO mice deformed 19% more than $Actn4^{flox/flox}$ littermate controls (5.4 ± 0.4 vs. 4.5 ± 0.6 μm, $p = 0.012$, $t_{(18)} = 2.79$, unpaired *t*-test, $n = 10$ utricles per condition, **Figure 3K**). That corresponds to an 18% reduction in elastic modulus (6.4 ± 0.4 vs. 7.6 ± 0.8 kPa, $p = 0.005$, $t_{(18)} = 3.22$, unpaired *t*-test, $n = 10$ utricles per condition, **Figure 3L**). The results thus far showed that the mouse utricular epithelium stiffens as it matures, that the apical junctions are sites of particular stiffness, and that stiffness depends on both the F-actin bands and Alpha-Actinin-4. Contrasting with that, the F-actin belts of SCs in the chicken utricular epithelium remain thin,

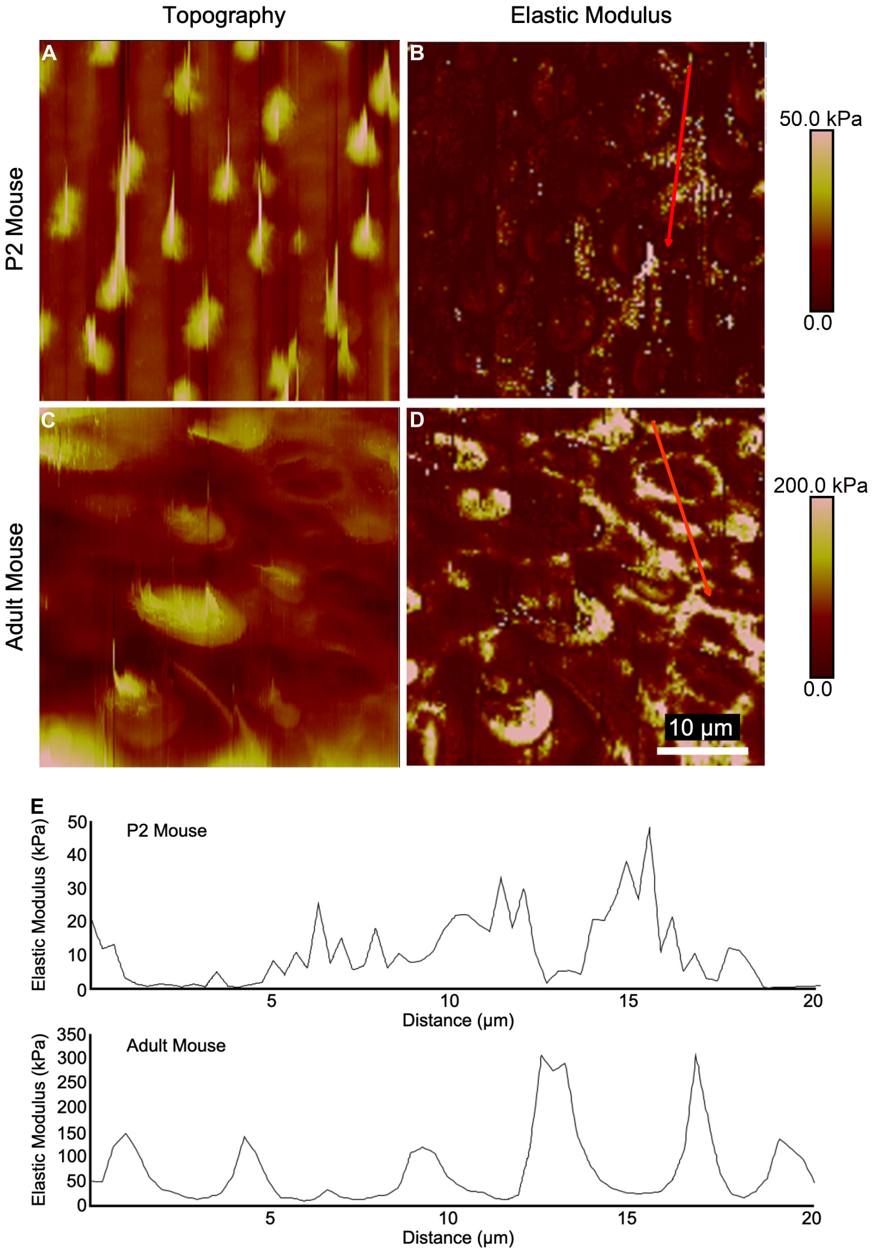

FIGURE 2 | High-resolution AFM measurements of utricular sensory epithelia from neonatal and adult mice show elevated stiffness at intercellular junctions. **(A,C)** Topography mapping of the utricular surface from P2 and adult mice reveals locations of hair bundles. **(B,D)** Elastic modulus mapping of the utricular surface shows elevated stiffnesses in regions corresponding to HC cuticular plates and intercellular junctions. **(E)** Line scans depicting elastic modulus along the red traces in **(B,D)**.

readily regenerate HCs even as adults, and are considerably more compliant than their counterparts in mice.

Supporting Cell Elongation in the Chicken Utricle Provides Evidence of Anisotropic Tissue Tension

The shapes of epithelial cells reflect a balance of forces from internal hydrostatic pressure, adhesion, and actomyosin contractility (Mao and Baum, 2015). In the course of this investigation, we observed that SC surfaces in wild-type mice resemble regular polygons, while those in chickens are elongated (**Supplementary Figures 5A,E**). To determine whether and how differences in cell surface shapes arose during development, we measured the outlines of SC surfaces at multiple developmental timepoints, quantifying changes in SC area, elongation, and alignment (**Supplementary Figures 5A–I**).

In mouse utricles, the area enclosed by the surface outline of the average SC increased by ~80% from E16 through adulthood ($p = 0.0008$, $F_{(2,8)} = 20.0$, ANOVA, $n = 3–4$ utricles per

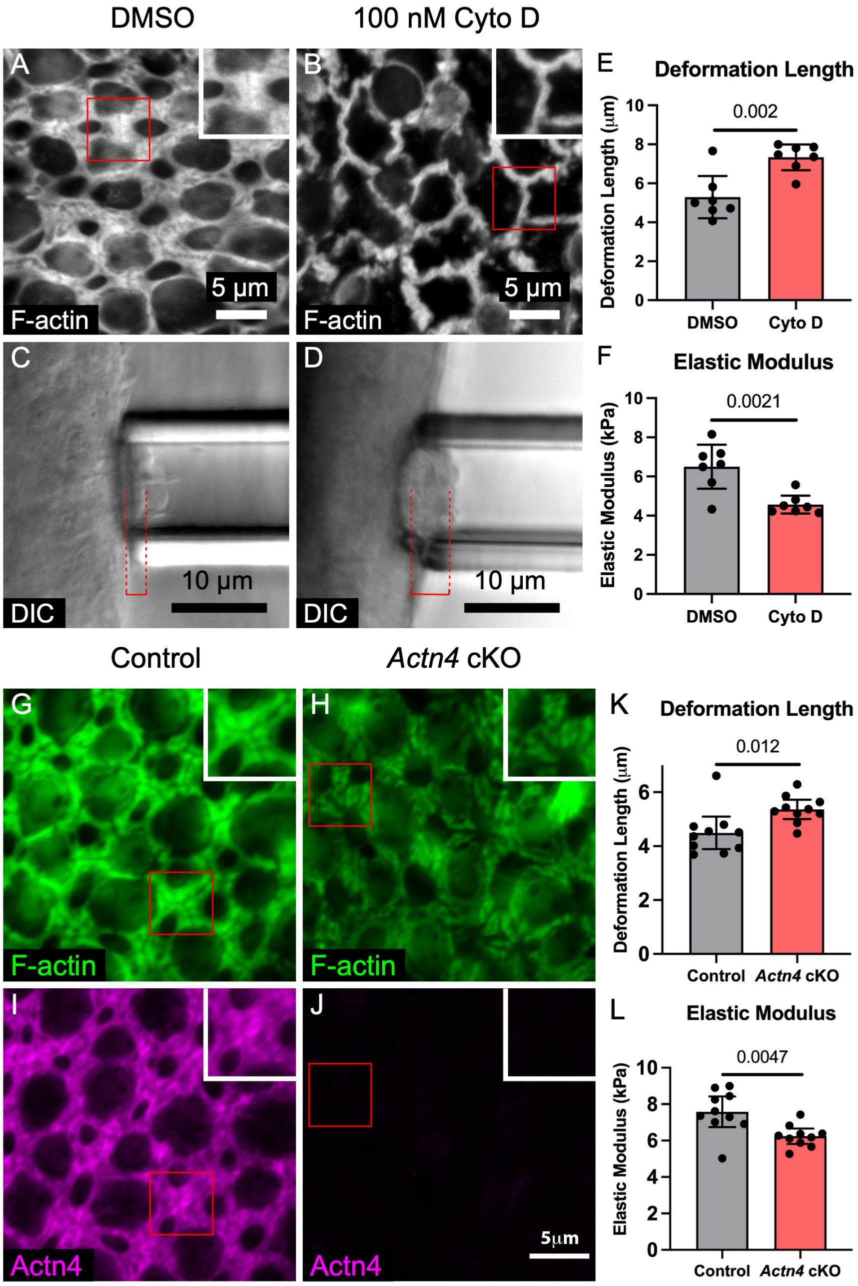

FIGURE 3 | F-actin depolymerization and deletion of the cross-linker *Actn4* each disrupt the morphology of the circumferential F-actin bands in SCs of adult mouse utricles and reduce stiffness of the apical surface. **(A,B)** Representative images of phalloidin-labeled F-actin in utricles from adult mice that were cultured for 24 h in DMSO or 100 nM cytochalasin D (Cyto D), an F-actin depolymerizing agent. Insets depict higher-magnification views of a SC-SC junction. **(C,D)** Micropipette aspiration of utricles from adult mice that were cultured in DMSO or 100 nM Cyto D for 24 h. Red dashed lines denote the deformation lengths. **(E)** Blinded quantification revealed that the mean deformation length of utricles cultured in Cyto D was significantly greater than that of DMSO-treated controls. Dots represent an average of at least three measurements from a single utricle. **(F)** Quantification of elastic modulus revealed a significant difference in stiffness. **(G,H)** Circumferential F-actin bands were normal in utricles of control *Actn4*$^{flox/flox}$ mice, but those in *Actn4* cKO mice had disrupted morphology. **(I,J)** Actn4 immunostaining labeled the F-actin bands in control mice, but the F-actin bands in Actn4 cKO mice had sharply reduced immunoreactivity. **(K,L)** Quantification of deformation length and elastic modulus from micropipette aspiration of utricles from *Actn4* cKO mice and littermate controls. All data are shown as mean ± 95% confidence interval.

condition, **Figures 4A–C,H,I**). The average area of chicken SCs also grew with developmental age, increasing ∼50% from E7 to P0 (p = 0.001, $F_{(3,16)}$ = 9.05, ANOVA, n = 3–7 utricles per condition, **Figures 4D–I**).

Differences in surface structure between mouse and chicken SCs became more apparent when we assessed elongation. The surfaces of mouse SCs maintained fairly regular shapes, with the length:width ratios of cell outlines increasing by just ∼8%

between E16 and adulthood (E16: 1.4 ± 0.01, Adult: 1.6 ± 0.1, $p = 0.044$, $F_{(2,8)} = 4.7$, ANOVA, $n = 3–4$ utricles per condition, **Figure 4H**). In contrast, SC surfaces in embryonically developing chickens became progressively elongated. By P0, the length:width ratio of chicken SCs averaged 4.2 ± 0.9, more than twice the ratio for SCs at E7 ($p = 0.001$, $F_{(3,16)} = 25.5$, ANOVA, $n = 3–7$ utricles per condition, **Figure 4H**).

By observing the orientation of HC cuticular plates, which we immunostained using an antibody to spectrin, we determined the local axis of planar HC polarity. Immunostaining for spectrin and occludin revealed that chicken SCs are elongated and aligned parallel to the local axis of planar HC polarity (**Supplementary Figure 5J**). At E7, the deviation of the average SC from the local median angle was 23° ± 6° but the average deviation shrank to just 7° ± 1° by P0 ($p < 0.0001$, $F_{(3,18)} = 39.9$, ANOVA, $n = 3–7$ utricles per condition, **Figure 4H**). In contrast, mouse SCs did not exhibit detectable alignment with age (E16: 24° ± 6°, Adult: 24° ± 9°, $p = 0.18$, $F_{(2,8)} = 2.1$, ANOVA, $n = 3–4$ utricles per condition, **Figure 4H**).

The measurements show that the regular polygonal apical surfaces of SCs in mouse utricles approximate a standard, low-energy configuration. In contrast, SCs in the developing

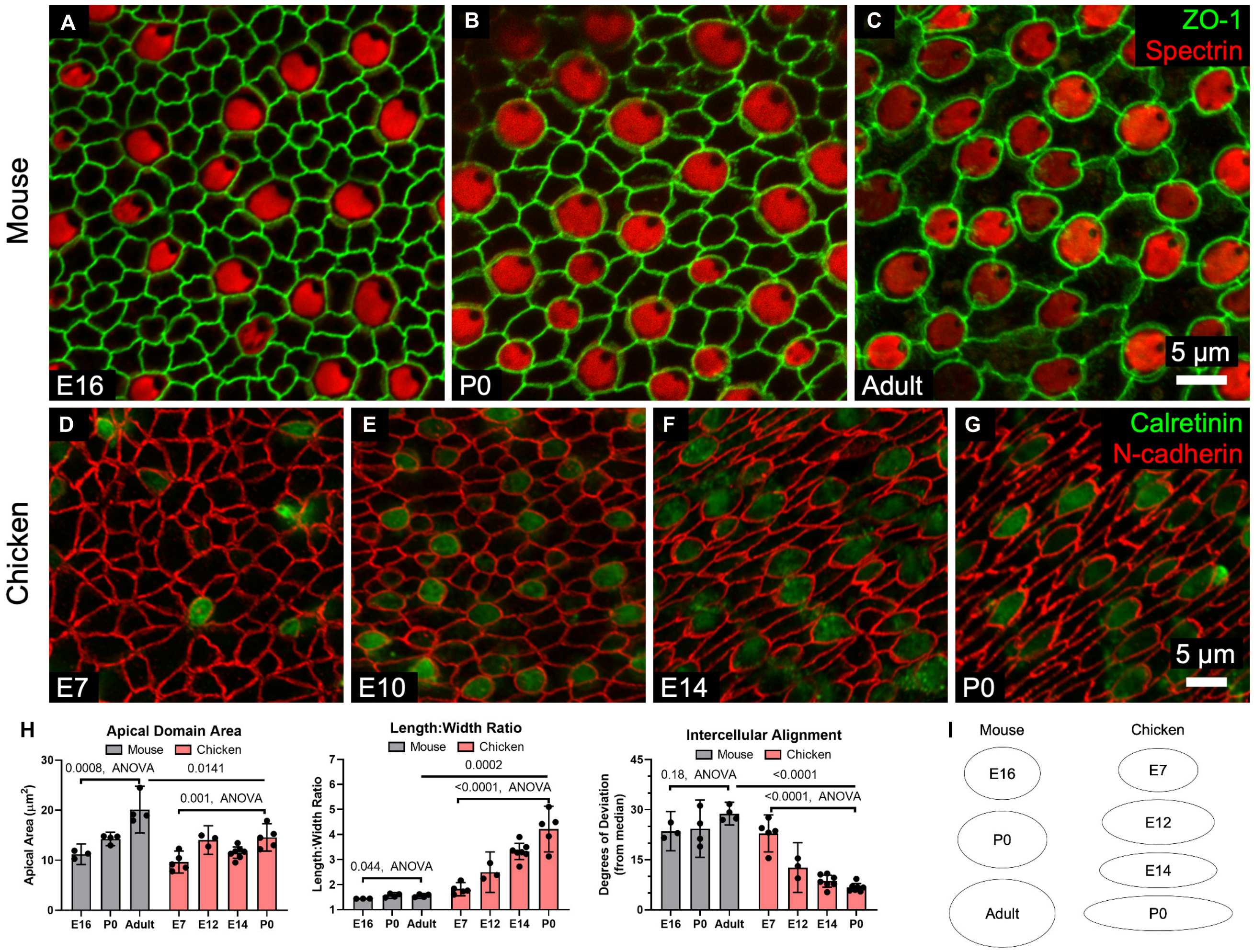

FIGURE 4 | SCs in mouse utricles do not undergo dramatic shape changes during development and postnatal maturation, whereas those in chickens become elongated and locally aligned during development. **(A–C)** Confocal images of utricles from mice of various ages. Images are from the striolar region. **(D–G)** Confocal images of utricles from chickens of various ages. **(H)** Quantification reveals that SC apical domains become significantly larger over time (Mouse: $p = 0.0008$, $F_{(2,8)} = 20.0$, ANOVA, $n = 3–4$ utricles per condition; Chicken: $p = 0.001$, $F_{(3,16)} = 9.05$, ANOVA, $n = 3–7$ utricles per condition). The mean SC area was significantly greater in adult mice than P0 chickens ($p = 0.0141$, $t_{(7)} = 3.2$, unpaired t-test, $n = 4–5$ utricles per condition). Both mouse and chicken SCs became significantly more elongated with age (Mouse: $p = 0.044$, $F_{(2,8)} = 4.7$, ANOVA, $n = 3–4$ utricles per condition; Chicken: $p = 0.001$, $F_{(3,16)} = 25.5$, ANOVA, $n = 3–7$ utricles per condition), though elongation was significantly greater in P0 chicken SCs compared to SCs in adult mice ($p = 0.0002$, $t_{(7)} = 7.1$, unpaired t-test, $n = 4–5$ utricles per condition). Alignment did not significantly change in mouse SCs with age ($p = 0.18$, $F_{(2,8)} = 2.1$, ANOVA, $n = 3–4$ utricles per conditions), but significantly increased with age in chicken SCs ($p < 0.0001$, $F_{(3,18)} = 39.9$, ANOVA, $n = 3–7$ utricles per condition). SCs of the P0 chicken utricle were significantly more aligned than those of adult mouse utricles ($p < 0.0001$, $t_{(9)} = 21.9$, unpaired t-test, $n = 4–7$ utricles per condition). **(I)** The average shapes of SC apical domains in mouse and chicken utricles are depicted as ellipses to denote relative area and length:width ratio.

chicken utricle become elongated and collectively aligned with the planar polarity axis, which is a higher-energy configuration and likely results from anisotropic forces in the epithelium.

Normal Supporting Cell Shape Requires Maintained Actomyosin Contractility in the Utricles of Chickens, but Not in Mice

The contractile force of non-muscle myosin II on the junction-associated F-actin belt is an important determinant of cell shape in epithelia (Ebrahim et al., 2013). Mouse and chicken utricles both express non-muscle myosin II isoforms as illustrated by RNA-sequencing data (**Supplementary Figure 2C**; Ku et al., 2014; Gnedeva and Hudspeth, 2015). We hypothesized that myosin II contractility influences the shape of vestibular SC surfaces. To test this, we cultured P0 chicken utricles in the presence of either DMSO or 50 μM blebbistatin, an inhibitor of non-muscle myosin II contractility, for 24 h before fixing and immunostaining for N-cadherin and calretinin to label cell junctions and HCs, respectively. Confocal microscopy showed a normal, approximately planar sensory epithelium surface in each of the DMSO-treated utricles, but the sensory epithelium in each of the utricles cultured in blebbistatin developed a striking series of ridges and valleys, which we refer to as "ruffles" (**Figures 5A,B**). The ruffles were regularly spaced ∼25 μm apart and fanned out laterally, paralleling the local axis of HC polarity. *Z*-axis projections from confocal microscopy revealed that the

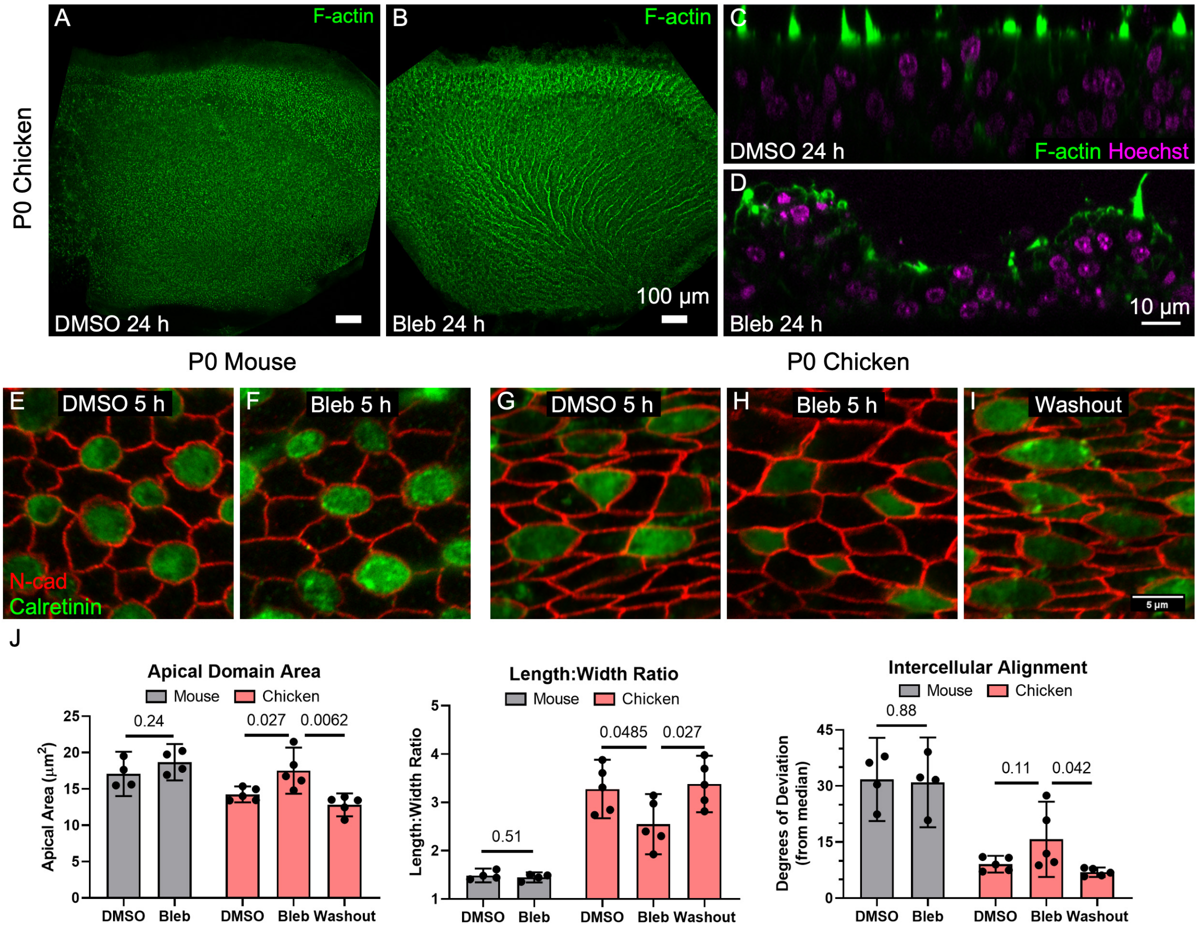

FIGURE 5 | Inhibition of non-muscle myosin II activity led to dramatic expansion of SC apical domains in utricles of P0 chickens but had no detectable effect on the shapes of SCs in P0 mouse utricles. **(A,B)** Chicken utricles were cultured for 24 h in the presence of DMSO **(A)** or 50 μm blebbistatin **(B)**. Blebbistatin treatment resulted in a "ruffled" appearance of the epithelial surface. **(C,D)** Z-projections depicting buckling of the epithelium after blebbistatin treatment. **(E–I)** Utricles from P0 mice and P0 chickens were cultured for 5 h in the presence of 50 μM blebbistatin or DMSO vehicle control before fixation. Some blebbistatin-treated utricles of P0 chickens were rinsed and fixed after a total of 16 h (Washout, **I**). **(J)** Quantification revealed that in SCs of mouse utricles, blebbistatin treatment did not lead to significant differences in apical domain area ($p = 0.24$, $t_{(6)} = 1.30$, unpaired *t*-test, $n = 4$ utricles per condition), length:width ratio ($p = 0.51$, $t_{(6)} = 0.70$, unpaired *t*-test, $n = 4$ utricles per condition), or intercellular alignment ($p = 0.88$, $t_{(6)} = 0.15$, unpaired *t*-test, $n = 4$ utricles per condition) compared to controls treated with DMSO. In contrast, blebbistatin treatment significantly affected SC area ($p = 0.027$, $t_{(8)} = 2.7$, $n = 5$ utricles per condition) and length:width ratio ($p = 0.0485$, $t_{(8)} = 2.3$, $n = 5$ utricles per condition) in chicken utricles, with alignment not reaching statistical significance ($p = 0.11$, $t_{(8)} = 1.8$, $n = 5$ utricles per condition). Upon washout of blebbistatin, changes to SC area ($p = 0.0062$, $t_{(8)} = 3.7$, $n = 5$ utricles per condition), elongation ($p = 0.027$, $t_{(8)} = 2.3$, $n = 5$ utricles per condition), and intercellular alignment ($p = 0.042$, $t_{(8)} = 2.7$, $n = 5$ utricles per condition) were reversible.

epithelial surface of the blebbistatin-treated utricles had buckled (**Figures 5C,D**).

To determine how this dramatic change in sensory epithelium form came about, we recorded images from P0 chicken utricles in time-lapse microscopy after labeling with SiR-actin, a cell-permeable live-cell probe that is highly specific for F-actin. At the start of image acquisition, DMSO was spiked into the medium containing a chicken utricle in one half of a two-compartment imaging chamber, and blebbistatin was spiked into the medium around another chicken utricle in the other chamber at a final concentration of 50 μM. The shapes of SCs in the DMSO-treated utricles did not change during the 9 h time-lapse (**Supplementary Movie 3**), while the apical surfaces of SCs in the blebbistatin-treated utricles began to expand noticeably starting at ∼3 h. We expected that shape changes would occur stochastically, but instead the time-lapse recordings revealed SC surfaces changing shape and size in concert with their neighbors. When the time-lapse images encompassed larger areas of the sensory epithelium it became apparent that the cellular surface expansion was propagating across the epithelium, suggesting a wavefront of SC surface relaxation. Measurements of SC surface outlines showed that the expansion of SCs was anisotropic, with the short axis of the SC surfaces increasing 1.1 ± 0.2 μm on average, which was more than three times the 0.3 ± 0.5 μm average increase in the long axis (p = 0.006, $t_{(29)}$ = 3.0, paired t-test, n = 30 cells). We conclude that a previously unrecognized requirement for actomyosin contractility maintains anisotropic tension and normal supporting cell surface shapes in the chicken utricular epithelium, since inhibition of myosin II contractility quickly led to anisotropic SC expansion that resulted in buckling of the sensory epithelium.

To further quantify the effect, we cultured utricles from chickens and mice in the presence of DMSO or 50 μM blebbistatin for 5 h. At that point, most cultures were either fixed and processed for immunohistochemistry, but some blebbistatin-treated utricles were cultured for 16 h before rinsing and fixation. The 5-h blebbistatin treatment of P0 chicken utricles resulted in a 20% increase in SC area and a 20% decrease in the average SC length:width ratio (area: p = 0.027, $t_{(8)}$ = 2.7; length:width ratio: p = 0.0485, $t_{(8)}$ = 2.3; alignment: p = 0.11, $t_{(8)}$ = 1.8, unpaired t-test, n = 5 utricles per condition, **Figures 5G–J**). Upon washout, the effects of blebbistatin on SCs in the chicken utricle were reversible (area: p = 0.0062, $t_{(8)}$ = 3.7; length:width ratio: p = 0.027, $t_{(8)}$ = 2.3; alignment: p = 0.042, $t_{(8)}$ = 2.7, unpaired t-test, n = 5 utricles per condition, **Figures 5G–J**).

In contrast to the dramatic effects we observed in the chicken utricle, blebbistatin treatments of P0 mouse utricles produced no detectable differences in SC area, elongation, or alignment (area: p = 0.24, $t_{(6)}$ = 1.30; length:width ratio: p = 0.51, $t_{(6)}$ = 0.70; alignment: p = 0.88, $t_{(6)}$ = 0.15, unpaired t-test, n = 4 utricles per condition, **Figures 5E,F,J**). We repeatedly tested this in our laboratory but have not found any experimental conditions under which blebbistatin inhibition of myosin II in mouse utricles causes substantial changes in SC shape or leads to epithelial buckling.

Since chickens are precocious at hatching and newborn mice are altricial, P0 chicken utricles may be at a more advanced developmental stage than P0 mouse utricles. For that reason, we repeated the experiment using blebbistatin treatment of P75 mouse utricles, which yielded no detectable differences in SC area or intercellular alignment (area: p = 0.46, $t_{(6)}$ = 0.80; alignment: p = 0.11, $t_{(6)}$ = 1.90, n = 4 utricles), and a minimal 5% reduction in length:width ratio (p = 0.031, $t_{(6)}$ = 2.80, n = 4 utricles, **Supplementary Figure 6**). The results show that the sizes and shapes of F-actin-stiffened apical domains of SCs in mouse utricles are maintained independent of non-muscle myosin II contractility. In sharp contrast, the more readily deformable SCs in the chicken utricle require continuous actomyosin contractility to maintain their distinct elongated and aligned surface shapes.

Supporting Cells in Chicken Utricles Divide Perpendicular to Hair Cell Polarity During Development and Regeneration

In epithelial monolayers that experience anisotropic tensional stress, cell divisions typically occur with the cleavage plane orthogonal to the cell's long axis, so the division of an elongate cell results in two less elongated cells and reduced tensional stress (Wyatt et al., 2015). The propensity for elongated cells to divide along that axis is known as "Hertwig's rule" (Hertwig, 1884). To determine whether the cell divisions of elongated SCs in the chicken utricle are oriented in a non-random manner, we harvested utricles at E14 and immunostained them with anti-phospho-Histone 3 (PH3), which binds to condensed chromatin during mitosis. The orientations of 119 cells that were in metaphase or anaphase were analyzed with reference to the local axis of HC polarity, as determined by spectrin immunostaining (**Figures 6A–D**). The measured sample of cell division orientations was clearly non-random (p = 1.512e^{-10}, D = 0.313, KS test, n = 119 cells, **Figure 6I**). We were surprised to see that the majority of mitotic figures were oriented orthogonal to the planar axis of HC polarity, so the cleavage plane of the ensuing cell divisions would occur parallel to the SC's long axis in violation of "Hertwig's rule" (**Figures 6A,B**).

To test whether regenerative cell divisions orient similarly, we harvested utricles from P2 chickens and killed HCs by culturing the utricles in the presence of 1 mM streptomycin for 24 h, prior to washout and culturing 48 h more in control medium before fixation. Orientations of 141 mitotic figures in metaphase and anaphase were measured relative to the local axis of SC elongation, which is aligned with the axis of HC polarity (**Supplementary Figure 5J**). As in development, regenerative cell divisions were not randomly oriented (p = 2.368e^{-8}, D = 0.254, KS test, n = 141 cells, **Figure 6I**). Rather, the majority of mitotic figures were oriented such that the cleavage plane would be parallel to the SC's long axis (**Figures 6E–I**). Thus, in development and regeneration, and contrary to "Hertwig's rule," cell divisions in chicken utricles tend to orient in a manner that would appear to contribute to, rather than dissipate, anisotropic tensional stress.

DISCUSSION

Auditory SCs in mammals develop highly specialized morphologies and are positioned in precisely ordered rows along the organ of Corti, making them significantly different

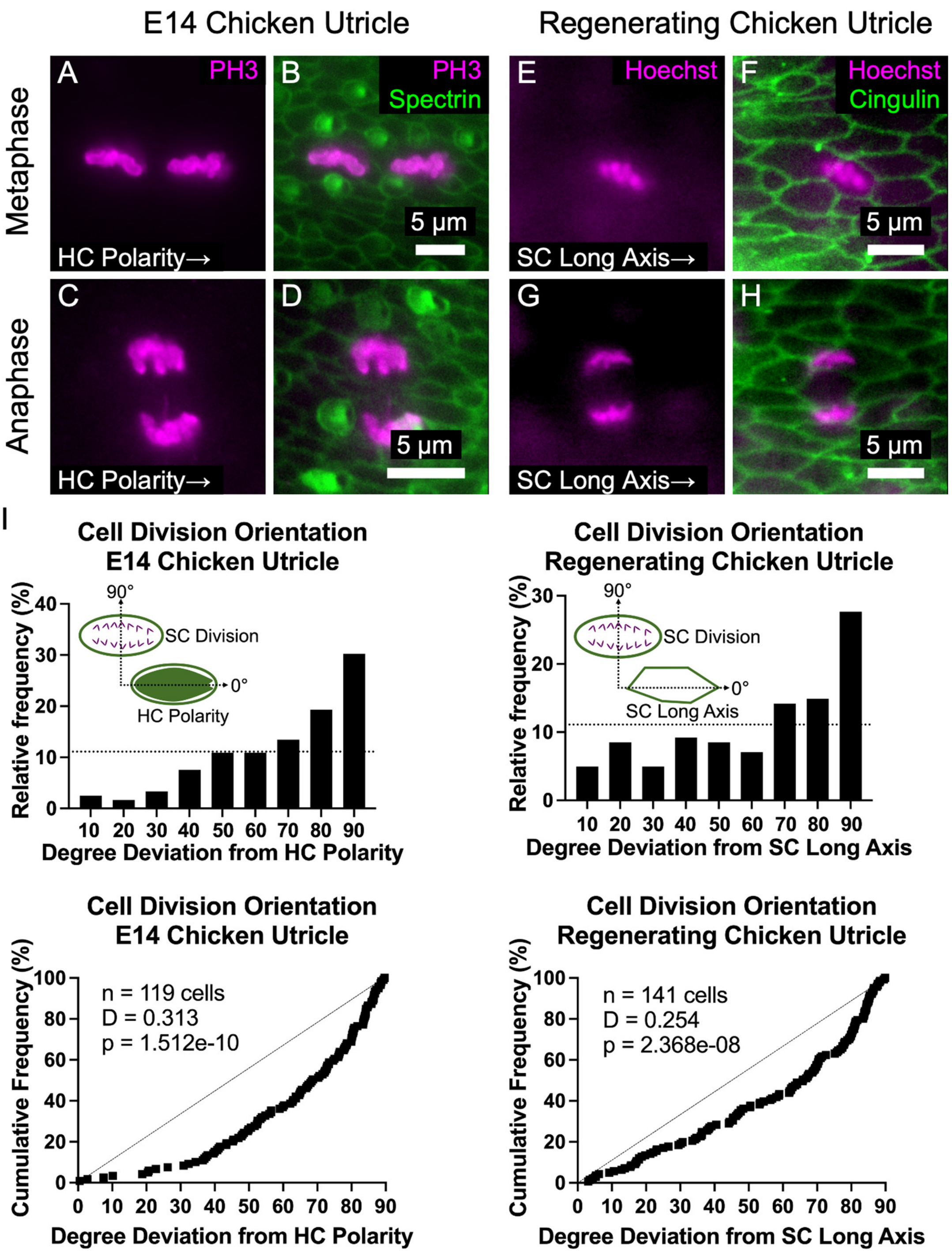

FIGURE 6 | The majority of supporting cell divisions in the developing and regenerating chicken utricle are oriented such that the division axis is perpendicular to the axes of HC polarity and SC elongation. **(A–D)** The orientation of PH3-labeled mitotic figures in metaphase **(A,B)** and anaphase **(C,D)** were measured with respect to the local axis of HC polarity, as visualized by spectrin immunostaining. **(E–H)** To determine whether regenerative cell divisions were oriented, utricles from P2 chickens were cultured in 1 mM streptomycin for 24 h to ablate HCs and fixed after a total of 72 h. Due to the high efficiency of HC killing with this approach, no HCs are present in the images. Images of cells in metaphase **(E,F)** and anaphase **(G,H)** were acquired with Hoechst labeling of cell nuclei, and the orientation of mitotic figures was measured with respect to the local axis of SC elongation, as visualized by cingulin immunostaining. **(I)** *Top:* Histograms of cell division orientation during development and regeneration. The bins have a width of 10 degrees and the *x*-axis labels denote the upper boundary of each bin. The dashed lines denote a uniform distribution (i.e., randomly oriented divisions). *Bottom:* Cumulative distribution functions of cell division orientation during development and regeneration. Dashed lines denote randomly oriented cell divisions. KS tests revealed that the measured cell division orientations were significantly non-random during development (p = 1.512e-10, D = 0.313, n = 119 cells) and regeneration (p = 2.368e-8, D = 0.254, n = 141 cells).

from their less specialized counterparts in the auditory epithelia of fish, amphibians, reptiles, and birds. SCs in the vestibular organs of humans and other mammals closely resemble those of non-mammals in overall form and positioning, but they lack the high capacity for regenerative replacement of lost HCs that allows non-mammals to quickly recover sensory function. There are, however, two cellular specializations that distinguish vestibular SCs in mammals from those in nearly all non-mammals: The first to be recognized in mammalian SCs was the exceptionally robust circumferential F-actin bands, which grow in thickness until they occupy 89% of the average SC area at the level of the adherens junction (Meyers and Corwin, 2007; Burns et al., 2008). The second recognized specialization was E-cadherin, which is expressed at high levels in the adherens junctions and basolateral membranes of mammalian SCs but is absent or expressed at very low levels in the SCs and vestibular epithelia of birds, turtles, amphibians, bony fish, and sharks (Collado et al., 2011b; Burns et al., 2013). Those observations and the results of prior experiments led to two hypotheses: that the highly reinforced, E-cadherin-rich junctions in mature mammalian vestibular epithelia might dampen local intraepithelial tension changes that arise when cells are lost, and that such dampening of those mechanical signals might reduce the capacity for mammalian SCs to respond to HC losses by changing shape and participating in regenerative proliferation (Meyers and Corwin, 2007; Burns and Corwin, 2013).

Prior to this study, there was a lack of direct evidence as to whether the reinforced adherens junctions of mammalian SCs affect the mechanical properties of the utricular epithelium. Our results show that accumulation of F-actin and the expression of Alpha-Actinin-4 at SC-SC junctions stiffen the utricular epithelium substantially as mice mature. Stiffness measured in the mouse sensory epithelium was considerably greater than our measurements from the highly regenerative chicken utricle, where the F-actin belts remain thin throughout life. While blebbistatin-mediated inhibition of non-muscle myosin II contractility produced no detectable changes in the shape or surface area of SCs in mouse utricles, in chicken utricles it caused SC shape change, dramatic expansion of SC surfaces, and buckling of the sensory epithelium. Taken together, our findings show that the utricular sensory epithelium in chickens behaves as a mechanical syncytium, with deformable SCs collectively responding to changes in intraepithelial tension such as those produced when cells are lost from the epithelium. Epithelial cell loss deforms nearby cells, changing tension in their cortical F-actin and intercellular junctions (Karsch et al., 2017), which can activate mitogenic YAP-TEAD signaling (Rauskolb et al., 2014; Benham-Pyle et al., 2015). The mechanical differences measured in this study are consistent with unexplained species differences in SC responses and HC regeneration. When HCs in chicken ears die, nearby, compliant SCs rapidly change shape, which is associated with robust nuclear accumulation of YAP and subsequent S-phase entry (Cotanche, 1987; Corwin and Cotanche, 1988; Bird et al., 2010; Collado et al., 2011a; Rudolf et al., 2020).

In contrast with the properties of utricular epithelium in chickens, the mechanical properties of the utricular sensory epithelium in the mouse are dominated by stiffness that depends in part on exceptionally thick and cross-linked F-actin bands at the level of SC junctions. It appears likely that the apical domain stiffness of mammalian supporting cells limits and blunts dynamic mechanical signals produced during cell loss and restricts collective mechanical behavior that can govern more effective epithelial repair. Consistent with this, the progressive stiffening of adherens junctions in mouse SCs correlates with reduced rates of shape change and proliferation, and with restricted responses to HC loss observed by time-lapse microscopy that are limited to just the closest neighboring SCs (Meyers and Corwin, 2007; Collado et al., 2011a; Burns and Corwin, 2014).

In another study, we recently reported that treatments with EGF and a GSK3β inhibitor cause significant thinning of the circumferential F-actin bands in SCs throughout the sensory epithelium in utricles cultured from adult mice (Kozlowski et al., 2020). With time, treatment with EGF and a GSK3β inhibitor caused depletion of E-cadherin at the junctions between SCs located within the striola and resulted in significant SC proliferation that was restricted to the striola. It is noteworthy that thinning of F-actin bands occurred throughout the entire sensory epithelium in those adult utricles but was not in itself sufficient to trigger proliferation. It remains to be determined whether thinning of the F-actin is required for E-cadherin depletion at SC-SC junctions in adult mouse utricles and why the effect on E-cadherin levels was restricted to just the striolar SCs. Our data suggest that treatments with EGF and a GSK3β inhibitor would reduce the stiffness of SCs in the adult mouse utricle, but it remains unknown whether that would cause those SCs to be more responsive to inhibition of myosin II contractility or better able to activate YAP-TEAD signaling. Further studies are required to investigate whether mouse models that have enhanced regenerative capacity have SCs with thinner F-actin bands, greater compliance, and heightened YAP-TEAD signaling.

We did not identify mechanisms that underlie the mouse utricle's lack of sensitivity to blebbistatin inhibition of myosin II contractility (**Figure 5**). One possibility is that presence of Actn4 or other actin cross-linkers such as Filamin A and Tropomodulin 1, which also localize to the F-actin bands (data not shown), could reduce the efficiency of actomyosin contractility (Ennomani et al., 2016). Interestingly, blebbistatin treatments are reported to induce expansion of SC surfaces in cochleae explanted from embryonic and newborn mice (Ebrahim et al., 2013; Cohen et al., 2020), where circumferential F-actin bands are not as thick as in utricular SCs (Burns et al., 2008, 2013). The thinner F-actin bands in SCs of the developing cochlea may be important for convergent extension, cell intercalation, and other morphogenic movements that are essential to the development of the organ of Corti's precise patterning (Cohen et al., 2020). The circumferential F-actin bands of Deiters cells and pillar cells thicken postnatally (Burns et al., 2013), and the epithelial surface becomes stiffer (Szarama et al., 2012; Chen et al., 2021), but it remains to be determined whether SCs in the cochleae of older mice become insensitive to blebbistatin treatment.

The findings presented here suggest that the thick circumferential F-actin bands could have provided two selective advantages during mammalian evolution. Stiffness conferred by the thick F-actin bands may have contributed to enhanced fidelity of HC mechanoelectrical transduction, particularly at high sound frequencies where the sensitivity of numerous mammalian species greatly exceeds that in birds and other non-mammals. The thick F-actin bands of mammalian SCs also appear likely to have imparted an energetic advantage, since the maintenance of mammalian SC shape does not rely on constitutively maintained, ATP-dependent activity of non-muscle myosin II, as shown in the blebbistatin results. In contrast, SCs of the utricles of birds appear to require continuous expenditure of ATP to sustain myosin II contractility that maintains their compact apical domains, surface shapes and sizes, as well as the planar form of the chicken utricular epithelium, which changes dramatically when myosin II contraction is inhibited. Both potential advantages warrant further exploration, as does the possibility that the mechanical properties and responses of SCs in chicken vestibular epithelia may be shared with the vestibular epithelia in reptiles, amphibians, bony fish, and sharks that also retain thin circumferential F-actin belts throughout life and express little or no E-cadherin in the sensory epithelium (Burns et al., 2013).

The progressive elongation and alignment of SCs in the embryonic chicken utricle is a hallmark of accumulating anisotropic tensile stress. Typically, cell divisions are oriented such that the cleavage plane occurs perpendicular to the cell's long axis (Hertwig, 1884), which reduces anisotropic stress (Campinho et al., 2013; Wyatt et al., 2015). Yet, contrary to "Hertwig's rule," during development and in regeneration SC mitoses in the chicken utricle are oriented such that the cleavage will be parallel to the cell's long axis (**Figure 6**). The results suggest that the cell divisions and subsequent cell growth would increase anisotropic stress. Time-lapse microscopy and other measures will be needed to confirm or refute that hypothesis. An intriguing possibility is that the orientation of the SC divisions promotes the accumulation and maintenance of tissue anisotropic stress that could contribute to the planar polarization or the refinement of HC orientation.

While the downregulation of developmental pathways such as Wnt, Notch, and SoxC has appropriately garnered attention in efforts to explain the reduced regenerative capacity of mammalian HC epithelia (Gnedeva and Hudspeth, 2015; Maass et al., 2015; Wang et al., 2015), the measurements and experimental findings reported above suggest that it would be wise to more fully investigate the unique cytological features and expression patterns that arose in SCs as mammals evolved. The results here sharpen mechanistic understanding of how the junctional reinforcement in mammalian SCs may limit regenerative responses, with exceptionally thick circumferential F-actin bands providing stiffness and the potential to act as a "biomechanical brake" that limits deformations, actomyosin-generated tension, and the propagation of tension changes in mammalian HC epithelia. High levels of E-cadherin may not only provide strong intercellular adhesion, but may collaborate as a "biochemical brake" that sequesters mitogenic signaling molecules at adherens junctions, as recent evidence suggests (Kozlowski et al., 2020). These mechanisms may explain, in part, why mammalian SCs largely remain in a state of proliferative quiescence after HC loss, whereas SCs in non-mammals readily replace HCs, enabling recovery of hearing and balance function.

DATA AVAILABILITY STATEMENT

The raw data supporting the conclusions of this article will be made available by the authors, without undue reservation.

ETHICS STATEMENT

The animal studies were reviewed and approved by the Animal Care and Use Committee at the University of Virginia (protocol 18350718) and National Institutes of Health guidelines for animal use (protocol 1254-18).

AUTHOR CONTRIBUTIONS

MR, AA, AC-R, and JC designed the research and edited the manuscript. MR, AA, CK, AD, AK, WB, and AC-R performed the research. MR, CK, AD, AK, WB, and AC-R analyzed the data. MR wrote the first draft of the manuscript. All authors contributed to the manuscript revision, read and approved the submitted version.

FUNDING

This work was supported by National Institute on Deafness and Other Communication Disorders/National Institutes of Health R01 DC000200 to JC, National Institute on Deafness and Other Communication Disorders/National Institutes of Health F30 DC016806 to MR. AC-R was also supported by the National Institutes of Health (NIH) Intramural Research Program of the National Institute of Biomedical Imaging and Bioengineering (grant # ZIA EB000094) as well as the National Institutes of Health Distinguished Scholars Program.

ACKNOWLEDGMENTS

We thank Wenhao Xu and the Genetically Engineered Murine Model Core at the University of Virginia for rederiving the $Actn4^{TM1a(EUCOMM)Wtsi}$ mouse line. We thank Matthew Kelley and Weise Chang at the National Institute on Deafness and Other Communication Disorders for kindly providing fertilized chicken eggs and mice for AFM experiments. We thank Jung-Bum Shin and Harald Sontheimer at the University of Virginia Department of Neuroscience for helpful discussions and logistical support.

SUPPLEMENTARY MATERIAL

The Supplementary Material for this article can be found online at: https://www.frontiersin.org/articles/10.3389/fncel.2022.859882/full#supplementary-material

REFERENCES

Agrawal, Y., Carey, J. P., Della Santina, C. C., Schubert, M. C., and Minor, L. B. (2009). Disorders of Balance and Vestibular Function in US Adults: Data From the National Health and Nutrition Examination Survey, 2001-2004. *Arch. Inter. Med.* 169:938. doi: 10.1001/archinternmed.2009.66

Baird, R. A., Steyger, P. S., and Schuff, N. R. (1996). Mitotic and Nonmitotic Hair Cell Regeneration in the Bullfrog Vestibular Otolith Organsa. *Ann. N.Y. Acad. Sci.* 781, 59–70. doi: 10.1111/j.1749-6632.1996.tb15693.x

Benham-Pyle, B. W., Pruitt, B. L., and Nelson, W. J. (2015). Mechanical strain induces E-cadherin-dependent Yap1 and β-catenin activation to drive cell cycle entry. *Science* 348, 1024–1027. doi: 10.1126/science.aaa4559

Bird, J. E., Daudet, N., Warchol, M. E., and Gale, J. E. (2010). Supporting cells eliminate dying sensory hair cells to maintain epithelial integrity in the avian inner ear. *J. Neurosci.* 30, 12545–12556. doi: 10.1523/JNEUROSCI.3042-10.2010

Borse, V., Barton, M., Arndt, H., Kaur, T., and Warchol, M. E. (2021). Dynamic patterns of YAP1 expression and cellular localization in the developing and injured utricle. *Sci. Rep.* 11:2140. doi: 10.1038/s41598-020-77775-8

Burns, J. C., and Corwin, J. T. (2013). A historical to present-day account of efforts to answer the question, "What puts the brakes on mammalian hair cell regeneration?". *Hear. Res.* 297, 52–67. doi: 10.1016/j.heares.2013.01.005

Burns, J. C., and Corwin, J. T. (2014). Responses to Cell Loss Become Restricted as the Supporting Cells in Mammalian Vestibular Organs Grow Thick Junctional Actin Bands That Develop High Stability. *J. Neurosci.* 34, 1998–2011. doi: 10.1523/JNEUROSCI.4355-13.2014

Burns, J. C., Collado, M. S., Oliver, E. R., and Corwin, J. T. (2013). Specializations of intercellular junctions are associated with the presence and absence of hair cell regeneration in ears from six vertebrate classes. *J. Comp. Neurol.* 521, 1430–1448. doi: 10.1002/cne.23250

Burns, J., Christophel, J. J., Collado, M. S., Magnus, C., Carfrae, M., and Corwin, J. T. (2008). Reinforcement of cell junctions correlates with the absence of hair cell regeneration in mammals and its occurrence in birds. *J. Comp. Neurol.* 511, 396–414. doi: 10.1002/cne.21849

Campinho, P., Behrndt, M., Ranft, J., Risler, T., Minc, N., and Heisenberg, C.-P. (2013). Tension-oriented cell divisions limit anisotropic tissue tension in epithelial spreading during zebrafish epiboly. *Nat. Cell Biol.* 15, 1405–1414. doi: 10.1038/ncb2869

Cartagena-Rivera, A. X., Gal, S. L., Richards, K., Verpy, E., and Chadwick, R. S. (2019). Cochlear outer hair cell horizontal top connectors mediate mature stereocilia bundle mechanics. *Sci. Adv.* 5:eaat9934. doi: 10.1126/sciadv.aat9934

Chen, T., Rohacek, A. M., Caporizzo, M., Nankali, A., Smits, J. J., Oostrik, J., et al. (2021). Cochlear supporting cells require GAS2 for cytoskeletal architecture and hearing. *Dev. Cell* 56, 1526.e–1540.e. doi: 10.1016/j.devcel.2021.04.017

Cohen, R., Amir-Zilberstein, L., Hersch, M., Woland, S., Loza, O., Taiber, S., et al. (2020). Mechanical forces drive ordered patterning of hair cells in the mammalian inner ear. *Nat. Commun.* 11:5137. doi: 10.1038/s41467-020-18894-8

Collado, M. S., Burns, J. C., Meyers, J. R., and Corwin, J. T. (2011a). Variations in Shape-Sensitive Restriction Points Mirror Differences in the Regeneration Capacities of Avian and Mammalian Ears. *PLoS One* 6:e23861. doi: 10.1371/journal.pone.0023861

Collado, M. S., Thiede, B. R., Baker, W., Askew, C., Igbani, L. M., and Corwin, J. T. (2011b). The postnatal accumulation of junctional E-cadherin is inversely correlated with the capacity for supporting cells to convert directly into sensory hair cells in mammalian balance organs. *J. Neurosci.* 31, 11855–11866. doi: 10.1523/JNEUROSCI.2525-11.2011

Corwin, J. T., and Cotanche, D. A. (1988). Regeneration of sensory hair cells after acoustic trauma. *Science* 240, 1772–1774. doi: 10.1126/science.3381100

Cotanche, D. A. (1987). Regeneration of hair cell stereociliary bundles in the chick cochlea following severe acoustic trauma. *Hear. Res.* 30, 181–195. doi: 10.1016/0378-5955(87)90135-3

Ebrahim, S., Fujita, T., Millis, B. A., Kozin, E., Ma, X., Kawamoto, S., et al. (2013). NMII forms a contractile transcellular sarcomeric network to regulate apical cell junctions and tissue geometry. *Curr. Biol.* 23, 731–736. doi: 10.1016/j.cub.2013.03.039

Ennomani, H., Letort, G., Guérin, C., Martiel, J.-L., Cao, W., Nédélec, F., et al. (2016). Architecture and Connectivity Govern Actin Network Contractility. *Curr. Biol.* 26, 616–626. doi: 10.1016/j.cub.2015.12.069

Fischer, M., Kaech, S., Knutti, D., and Matus, A. (1998). Rapid actin-based plasticity in dendritic spines. *Neuron* 20, 847–854. doi: 10.1016/s0896-6273(00)80467-5

Gnedeva, K., and Hudspeth, A. J. (2015). SoxC transcription factors are essential for the development of the inner ear. *PNAS* 112, 14066–14071. doi: 10.1073/pnas.1517371112

González-Bermúdez, B., Guinea, G. V., and Plaza, G. R. (2019). Advances in Micropipette Aspiration: Applications in Cell Biomechanics. Models, and Extended Studies. *Biophys. J.* 116, 587–594. doi: 10.1016/j.bpj.2019.01.004

Hamburger, V., and Hamilton, H. L. (1951). A series of normal stages in the development of the chick embryo. *J. Morphol.* 88, 49–92.

Hébert, J. M., and McConnell, S. K. (2000). Targeting of cre to the Foxg1 (BF-1) locus mediates loxP recombination in the telencephalon and other developing head structures. *Dev. Biol.* 222, 296–306. doi: 10.1006/dbio.2000.9732

Hertwig, O. (1884). Das Problem der Befruchtung und der Isotropie des Eies, eine Theorie der Vererbung. *Jenaische Zeitschrift fur Naturwissenschaft* 18, 276–318.

Hochmuth, R. M. (2000). Micropipette aspiration of living cells. *J. Biomechan.* 33, 15–22. doi: 10.1016/S0021-9290(99)00175-X

Karsch, S., Kong, D., Großhans, J., and Janshoff, A. (2017). Single-Cell Defects Cause a Long-Range Mechanical Response in a Confluent Epithelial Cell Layer. *Biophys. J.* 113, 2601–2608. doi: 10.1016/j.bpj.2017.10.025

Katsuno, T., Belyantseva, I. A., Cartagena-Rivera, A. X., Ohta, K., Crump, S. M., Petralia, R. S., et al. (2019). TRIOBP-5 sculpts stereocilia rootlets and stiffens supporting cells enabling hearing. *JCI Insight* 4:e128561. doi: 10.1172/jci.insight.128561

Kaufman, M. H. (1992). *The Atlas of Mouse Development*. Amsterdam: Elsevier Science.

Kos, C. H., Le, T. C., Sinha, S., Henderson, J. M., Kim, S. H., Sugimoto, H., et al. (2003). Mice deficient in α-actinin-4 have severe glomerular disease. *J. Clin. Invest.* 111, 1683–1690. doi: 10.1172/JCI200317988

Kozlowski, M. M., Rudolf, M. A., and Corwin, J. T. (2020). EGF and a GSK3 Inhibitor Deplete Junctional E-cadherin and Stimulate Proliferation in the Mature Mammalian Ear. *J. Neurosci.* 40, 2618–2632. doi: 10.1523/JNEUROSCI.2630-19.2020

Ku, Y.-C., Renaud, N. A., Veile, R. A., Helms, C., Voelker, C. C. J., Warchol, M. E., et al. (2014). The Transcriptome of Utricle Hair Cell Regeneration in the Avian Inner Ear. *J. Neurosci.* 34, 3523–3535. doi: 10.1523/JNEUROSCI.2606-13.2014

Maass, J. C., Gu, R., Basch, M. L., Waldhaus, J., Lopez, E. M., Xia, A., et al. (2015). Changes in the regulation of the Notch signaling pathway are temporally correlated with regenerative failure in the mouse cochlea. *Front. Cell Neurosci.* 9:110. doi: 10.3389/fncel.2015.00110

Mao, Y., and Baum, B. (2015). Tug of war—The influence of opposing physical forces on epithelial cell morphology. *Dev. Biol.* 401, 92–102. doi: 10.1016/j.ydbio.2014.12.030

Meyers, J. R., and Corwin, J. T. (2007). Shape change controls supporting cell proliferation in lesioned mammalian balance epithelium. *J. Neurosci.* 27, 4313–4325. doi: 10.1523/JNEUROSCI.5023-06.2007

Nadol, J. B. (1993). Hearing loss. *N. Engl. J. Med.* 329, 1092–1102. doi: 10.1056/NEJM199310073291507

Porazinski, S., Wang, H., Asaoka, Y., Behrndt, M., Miyamoto, T., Morita, H., et al. (2015). YAP is essential for tissue tension to ensure vertebrate 3D body shape. *Nature* 521, 217–221. doi: 10.1038/nature14215

Rauskolb, C., Sun, S., Sun, G., Pan, Y., and Irvine, K. D. (2014). Cytoskeletal Tension inhibits Hippo signaling through an Ajuba-Warts complex. *Cell* 158, 143–156. doi: 10.1016/j.cell.2014.05.035

Rudolf, M. A., Andreeva, A., Kozlowski, M. M., Kim, C. E., Moskowitz, B. A., Anaya-Rocha, A., et al. (2020). YAP Mediates Hair Cell Regeneration in Balance Organs of Chickens. But LATS Kinases Suppress Its Activity in Mice. *J. Neurosci.* 40, 3915–3932. doi: 10.1523/JNEUROSCI.0306-20.2020

Schindelin, J., Arganda-Carreras, I., Frise, E., Kaynig, V., Longair, M., Pietzsch, T., et al. (2012). Fiji: an open-source platform for biological-image analysis. *Nat. Methods* 9, 676–682. doi: 10.1038/nmeth.2019

Szarama, K. B., Gavara, N., Petralia, R. S., Kelley, M. W., and Chadwick, R. S. (2012). Cytoskeletal changes in actin and microtubules underlie the developing surface mechanical properties of sensory and supporting cells in the mouse cochlea. *Development* 139, 2187–2197. doi: 10.1242/dev.073734

Takeo, T., and Nakagata, N. (2011). Reduced glutathione enhances fertility of frozen/thawed C57BL/6 mouse sperm after exposure to methyl-beta-cyclodextrin. *Biol. Reprod.* 85, 1066–1072. doi: 10.1095/biolreprod.111.092536

Tang, V. W., and Brieher, W. M. (2012). α-Actinin-4/FSGS1 is required for Arp2/3-dependent actin assembly at the adherens junction. *J. Cell Biol.* 196, 115–130. doi: 10.1083/jcb.201103116

Theret, D. P., Levesque, M. J., Sato, M., Nerem, R. M., and Wheeler, L. T. (1988). The Application of a Homogeneous Half-Space Model in the Analysis of Endothelial Cell Micropipette Measurements. *J. Biomech. Eng.* 110, 190–199. doi: 10.1115/1.3108430

Wang, T., Chai, R., Kim, G. S., Pham, N., Jansson, L., Nguyen, D.-H., et al. (2015). Lgr5+ cells regenerate hair cells via proliferation and direct transdifferentiation in damaged neonatal mouse utricle. *Nat. Commun.* 6:6613. doi: 10.1038/ncomms7613

World Health Organization [WHO] (2018). *Global estimates on prevalence of hearing loss. WHO | Estimates*. Available online at: http://www.who.int/deafness/estimates/en/ [Accessed Aug 2 2019]

Wyatt, T. P. J., Harris, A. R., Lam, M., Cheng, Q., Bellis, J., Dimitracopoulos, A., et al. (2015). Emergence of homeostatic epithelial packing and stress dissipation through divisions oriented along the long cell axis. *Proc. Natl. Acad. Sci. U.S.A.* 112, 5726–5731. doi: 10.1073/pnas.1420585112

Zhao, S., and Fernald, R. D. (2005). Comprehensive algorithm for quantitative real-time polymerase chain reaction. *J. Comput. Biol.* 12, 1047–1064. doi: 10.1089/cmb.2005.12.1047

Conflict of Interest: The authors declare that the research was conducted in the absence of any commercial or financial relationships that could be construed as a potential conflict of interest.

frontiers | Frontiers in Cellular Neuroscience

ORIGINAL RESEARCH
published: 17 June 2022
doi: 10.3389/fncel.2022.876805

Vestibular Hair Cells Require CAMSAP3, a Microtubule Minus-End Regulator, for Formation of Normal Kinocilia

Josephine O'Donnell[1] and Jing Zheng[1,2]*

[1] Department of Otolaryngology, Feinberg School of Medicine, Northwestern University, Chicago, IL, United States,
[2] Knowles Hearing Center, Northwestern University, Evanston, IL, United States

Kinocilia are exceptionally long primary sensory cilia located on vestibular hair cells, which are essential for transmitting key signals that contribute to mammalian balance and overall vestibular system function. Kinocilia have a "9+2" microtubule (MT) configuration with nine doublet MTs surrounding two central singlet MTs. This is uncommon as most mammalian primary sensory cilia have a "9+0" configuration, in which the central MT pair is absent. It has yet to be determined what the function of the central MT pair is in kinocilia. Calmodulin-regulated spectrin-associated protein 3 (CAMSAP3) regulates the minus end of MTs and is essential for forming the central MT pair in motile cilia, which have the "9+2" configuration. To explore the role of the central MT pair in kinocilia, we created a conditional knockout model (cKO), *Camsap3*-cKO, which intended to eliminate CAMSAP3 in limited organs including the inner ear, olfactory bulb, and kidneys. Immunofluorescent staining of vestibular organs demonstrated that CAMSAP3 proteins were significantly reduced in *Camsap3*-cKO mice and that aged *Camsap3*-cKO mice had significantly shorter kinocilia than their wildtype littermates. Transmission electron microscopy showed that aged *Camsap3*-cKO mice were in fact missing that the central MT pair in kinocilia more often than their wildtype counterparts. In the examination of behavior, wildtype and *Camsap3*-cKO mice performed equally well on a swim assessment, right-reflex test, and evaluation of balance on a rotarod. However, *Camsap3*-cKO mice showed slightly altered gaits including reduced maximal rate of change of paw area and a smaller paw area in contact with the surface. Although *Camsap3*-cKO mice had no differences in olfaction from their wildtype counterparts, *Camsap3*-cKO mice did have kidney dysfunction that deteriorated their health. Thus, CAMSAP3 is important for establishing and/or maintaining the normal structure of kinocilia and kidney function but is not essential for normal olfaction. Our data supports our hypothesis that CAMSAP3 is critical for construction of the central MT pair in kinocilia, and that the central MT pair may be important for building long and stable axonemes in these kinocilia. Whether shorter kinocilia might lead to abnormal vestibular function and altered gaits in older *Camsap3*-cKO mice requires further investigation.

Keywords: CAMSAP3, kinocilia, "9+2" configuration, gait, vestibular function, kidney dysfunction

Edited by:
Bernd Fritzsch,
The University of Iowa, United States

Reviewed by:
Katie Kindt,
National Institutes of Health (NIH),
United States
Kristen Rak,
Comprehensive Hearing Center,
Germany

****Correspondence:***
Jing Zheng
jzh215@northwestern.edu

Specialty section:
This article was submitted to
Non-Neuronal Cells,
a section of the journal
Frontiers in Cellular Neuroscience

Received: *15 February 2022*
Accepted: *30 May 2022*
Published: *17 June 2022*

Citation:
O'Donnell J and Zheng J (2022)
Vestibular Hair Cells Require
CAMSAP3, a Microtubule Minus-End
Regulator, for Formation of Normal
Kinocilia.
Front. Cell. Neurosci. 16:876805.
doi: 10.3389/fncel.2022.876805

INTRODUCTION

Cilia, found on cell surfaces, are microtubule (MT)-based organelles that play essential roles for cell development, proliferation, differentiation, migration, signal transduction, etc. The structure, length, and function of cilia must be tightly regulated because their dysfunction is associated with numerous diseases collectively called ciliopathy disorders (Lee and Gleeson, 2011; Falk et al., 2015; Reiter and Leroux, 2017; Andreu-Cervera et al., 2021; Lee and Ostrowski, 2021). Based on their mobility, cilia are divided into two types: motile cilia and non-motile cilia like primary cilia. Motile cilia beat rhythmically to transport fluids across epithelia, while non-motile, as known as primary cilia, serve as sensory organelles gathering information about their environment. The majority of motile cilia in mammals are composed of MTs in the "9+2" configuration, i.e., nine doublet MTs surrounding two central singlet MTs. In contrast, most of the primary sensory cilia in mammals do not have central MT pairs, and instead, their axonemes have a "9+0" configuration.

Vestibular kinocilia, located on hair cells of the vestibular organ, are primary sensory cilia present throughout the murine lifespan. Compared to other primary sensory cilia, vestibular kinocilia are exceptionally long, some being 3–4 times longer than adjacent microvilli called stereocilia (Xue and Peterson, 2006). The actin-based stereocilia and MT-based kinocilia on vestibular hair cells are connected by lateral links and tip links (**Figure 3B**). Because of their length, the tips of vestibular kinocilia reach into the overlying otoconial layer. This structural arrangement allows vestibular kinocilia to transmit positions and movements of the head by change the otoconial membrane mass to the adjacent stereocilia, which generate electrical signals in sensory hair cells and ultimately controls mammalian balance and awareness of spatial orientation. As such, the mechanical properties and length of vestibular kinocilia play important roles in determining the operating range of the vestibular system (Spoon and Grant, 2011, 2013; Nam, 2018). Unlike most of primary sensory cilia, vestibular kinocilia have the "9+2" configuration, a common configuration found in motile cilia (Wersall et al., 1965; Rosenhall and Engstrom, 1974; Choksi et al., 2014). Unlike the outer 9 MT doublets, the central MT pair is not continuous with MT triplets in the basal body (Lechtreck et al., 2013). In motile cilia, the central MTs and their MT-associated proteins are required for the synchronized motion needed to remove debris (Loreng and Smith, 2017). The function of central MTs in primary cilia remains unknown. Primary cilia on olfactory sensory neurons and vestibular hair cells have the longest axoneme in mammals. Intriguingly, both cilia have the "9+2" configuration, which leads us to suspect that the central MT pair may be essential for the formation of the long axoneme.

Calmodulin-regulated spectrin-associated protein 3 (CAMSAP3), also called Marshalin (Zheng et al., 2013), is a MT minus-end regulator. Because CAMSAP3 can interact with other proteins through its protein-protein interaction domains, it has been reported to play several regulatory roles through interactions with multiple proteins (Meng et al., 2008; Goodwin and Vale, 2010; Toya et al., 2016; Gibieža et al., 2021). For example, CDH23 is an adhesive protein that plays crucial roles for hearing and balance. The C isoform of CDH23 can directly bind to CAMSAP3 and modifies CAMSAP3-associated MT networks (Takahashi et al., 2016). In addition, CAMSAP3 is involved in the formation of MTs from non-centrosomal MT organizing centers (MTOCs). CAMSAP3-coated MTs are stable and can be used to seed tubulin polymerization at non-centrosomal sites (Jiang et al., 2014, 2018; Zenker et al., 2017). We recently discovered that CAMSAP3 is necessary to form the central MT pairs in motile cilia (Robinson et al., 2020). In the *Camsap3*$^{\mathrm{tm}1a/tm1a}$ mice, the global knockdown (KD) of CAMSAP3 expression is associated with impaired ciliary motion, leading to phenotypes of Primary Ciliary Dyskinesia (PCD), which includes hydrocephalus, subfertility, and impaired mucociliary clearance. Dysfunctional mucociliary clearance leads to hyposmia, anosmia, rhinosinusitis, and otitis media. We occasionally noticed *Camsap3*$^{\mathrm{tm}1a/tm1a}$ mice (*Camsap3*-KD for short) with a head tilt to one side. Therefore, we suspect that CAMSAP3 is also needed to construct the central MT pair in kinocilia on vestibular hair cells and predict that the central MT pair in vestibular kinocilia is essential to establish the long and stable cilia required for vestibular function.

CAMSAP3 is expressed ubiquitously in mice. The global KD and global knockout (KO) CAMSAP3 in mice could potentially affect all cells that express CAMSAP3. Indeed, removal of *Camsap3* gene from a mouse genome leads to global *Camsap3*-KO mice dying prematurely (Muroyama et al., 2018). Even the *Camsap3*-KD mice, which reduce CAMSAP3 expression through RNA processing (Testa et al., 2004; White et al., 2013) without deleting any exons of *Camsap3* gene, showed some degree of embryonic lethality, sub-infertility, hydrocephalus, anosmia or hyposmia, sinusitis, respiratory distress, otitis media, and hearing loss (Perez-Garcia et al., 2018; Ingham et al., 2019; Robinson et al., 2020). To investigate the function of CAMSAP3 in a reliable living mouse model, we created a conditional knockout (cKO) mouse model known as *Camsap3*$^{\mathrm{tm}1d/tm1d}$ (*Camsap3*-cKO for short) for tissue specific cKO by using Cre-loxP system.

Camsap3-cKO would allow us to examine CAMSAP3's role in vestibular hair cells without influence from other health issues. Tg*Pax2-Cre* mouse line is widely used to establish cKO mouse models for inner ear (Pan et al., 2011; Cox et al., 2012; Wiwatpanit et al., 2018). In this transgenic mouse line, *IRES-Cre* was inserted into *Pax2* (paired box gene 2), a transcription factor that is crucial in the developmental and proliferation of multiple cells and organs. *Cre* expression was detected at E8.5 in the otic placode in the *Pax2-Cre* mouse line (Ohyama and Groves, 2004), which is earlier than when hair cell differentiation typically occurs (around E13.5) (Mbiene et al., 1984). Thus, we created *Camsap3*-cKO by crossing Tg*Pax2-Cre* mice with *Camsap3*$^{\mathrm{tm}1c/tm1c}$ (fl/fl), aiming to eliminate CAMSAP3 expression in *Cre*-expressed tissues, which include most of the cells in the inner ear, midbrain, cerebellum, the olfactory bulb, and kidneys (Ohyama and Groves, 2004). If CAMSAP3 is important for establishing normal vestibular kinocilia as we predict, we expect *Camsap3*-cKO mice to show behaviors associated with vestibular dysfunction. Different assessments, including Rotarod balance tests, DigiGait analyses, along with anatomical examination, were used to characterize the vestibular functions of *Camsap3*-cKO mice. We also evaluated olfactory function and monitored kidney health in order to determine whether removing CAMSAP3 causes detrimental effects outside of our expected outcomes in the vestibular system. Our data suggests that CAMSAP3 has an important role in establishing or maintaining normal vestibular kinocilia and kidney function, but is not essential for the task of olfactory bulbs.

MATERIALS AND METHODS

Creation of *Camsap3*-cKO Mice

All experiments utilizing animals were approved by the Institutional Animal Care and Use Committees of Northwestern University and in accordance with the National Institutes of Health guidelines. Animals were housed in Northwestern's Center for Comparative Medicine facilities.

The *Camsap3*$^{\mathrm{tm1}a(EUCOMM)\ Wtsi}$ (referred to as *Camsap3*-KD) mouse model was obtained from the Wellcome Trust Sanger Institute. The original *Camsap3*-KD line on the C57B6N background was re-derived on FVB murine backgrounds to increase their viability (Robinson et al., 2020). As shown in **Figure 1A**, a *Camsap3*-KD mouse was created using the "knockout first, conditional-ready" strategy (Skarnes et al., 2011). A targeted trap allele was inserted into the intron between the exon 6 and 7 of the *Camsap3* gene to knock out *Camsap3* expression through RNA processing (Testa et al., 2004; White et al., 2013) without deleting any exons. To create a cKO mouse model, *Camsap3*-KD mice were first crossed with B6-Tg(CAG-FLPe)36 (Kanki et al., 2006) to delete the *neo* and *LacZ* cassettes flanked by FRT sites and create *Camsap3*$^{\mathrm{tm1}c}$ (floxed allele), a strain of pseudo-wildtype (WT) mice. This WT *Camsap3*^{tm1c} floxed line was further crossed with the Tg*Pax2*^{Cre} mouse line, Tg(Pax2-*Cre*)1Akg/Mmnc (MMRRC stock number 10569) (Ohyama and Groves, 2004) to create a conditional knockout mouse model: Tg*Pax2*$^{Cre/+}$; *Camsap3*$^{\mathrm{tm1}c/tm1c}$ and their WT littermates: Tg*Pax2*$^{Cre+/+}$;*Camsap3*$^{\mathrm{tm1}c/tm1c}$. We call this mouse model *Camsap3*$^{\mathrm{tm1}d/tm1d}$ (null allele) *Camsap3*-cKO for short. All animals were maintained by heterotypic breeding, and the genotypes were determined by detecting the inserted cassettes in mouse tail samples performed by Transnetyx (Cordova, TN, United States).

Since *Cre* expression was limited in a few tissues including the inner ear, olfactory bulb, and kidneys of Tg*Pax2*^{Cre} mice, the exon 7 of *camsap3* was expected to be fully removed from these tissues of *Camsap3*-cKO mice. To verify the exon 7 exclusion, genomic DNA was purified from the inner ear of WT and *Camsap3*-cKO mice using the QIAamp DNA FFPE Tissue Kit (Qiagen). PCR was used to verify the exon 7 exclusion using the PCR Master Mix (Thermo Fisher Scientific, A44647100) with forward primer L1L2-BactP-MD-F (GCTGGCGCCG GAACC) and reverse primer C3Floxed5-R (TTGGCCTGGGGAACATGAC). Conditions for the thermal cycler were: step 1–95°C, 2 min; step 2–95°C, 30 s; step 3–55°C, 30 s, step 4–72°C, 90 s; repeat steps 2–4, 35 × ; step 5–72°C, 10 min. Expected sizes were 1,307 base pairs (bp) for WT, and 199 bp for *Camsap3*-cKO mice. Both male and female mice were used in all experiments.

Evaluation of Vestibular Function

Swimming Test

WT mice and their *Camsap3*-cKO littermates were placed in a 5-gallon bucket filled with room temperature water and were required to swim for 3 min. Behavior was observed, and any abnormal behavior was recorded. The swim test protocol was a modified version of a protocol described previously (Hardisty-Hughes et al., 2010).

Right Reflex Test

We modified a protocol described previously (Pau et al., 2004) to assess right reflexes. WT mice and their *Camsap3*-cKO littermates were placed in a clear plastic box (1″ × 2″ × 5″). The box was quickly flipped upside down and the time it took each mouse to flip themselves back upright was recorded.

Rotarod Test

The rotarod test was created by Dunham and Miya (1957) to assess neuromuscular function in rodents and is commonly used to assess balance (Jones et al., 2018). The Rotarod apparatus (TSE Systems, Chesterfield, MO, United States) was used to assess balance in *Camsap3*-cKO and their WT littermates. Following the Jones et al. (2018) protocol, mice were placed on a rotating beam and their time to fall (TTF) was recorded. Mice were tested 3 at a time with their cage mates. The rotarod was set to start rotating at a speed of 5 rpm and accelerate to a top speed of 44 rpm over the course of 300 s (the maximum duration of the trial). The mice were given 10-min trial intervals and tested again. Ten *Camsap3*-cKO mice and 10 WT littermates completed eight trials, with the first three trials functioning as an acclimation and familiarization period. The final five trials were recorded for analysis.

Gait Analysis

The DigiGait$^{\mathrm{TM}}$ Imaging System apparatus (Mouse Specifics Inc., Framingham, MA, United States) consists of a motorized transparent treadmill belt sitting above a digital camera which records the ventral view (**Supplementary Movie 1**). WT mice and their *Camsap3*-cKO littermates were placed on the treadmill one at a time and were required to run. The mice were then evaluated at treadmill speeds of 10, 17, and 24 cm/s. The DigiGait assay was run by Northwestern Behavioral Phenotyping Core. The DigiGait Imaging System software allowed us to examine 52 different aspects of each mouse's gait (Rostosky and Milosevic, 2018). The analysis software can detect slight differences in angles, lengths, and speeds of the paws and strides of the mice. The key behaviors we were interested in, shown in **Supplementary Figures 1**, **2**, included: swing to stance ratio, paw angle, gait symmetry, stance width, step angle, breaking duration, stride length, the ataxia

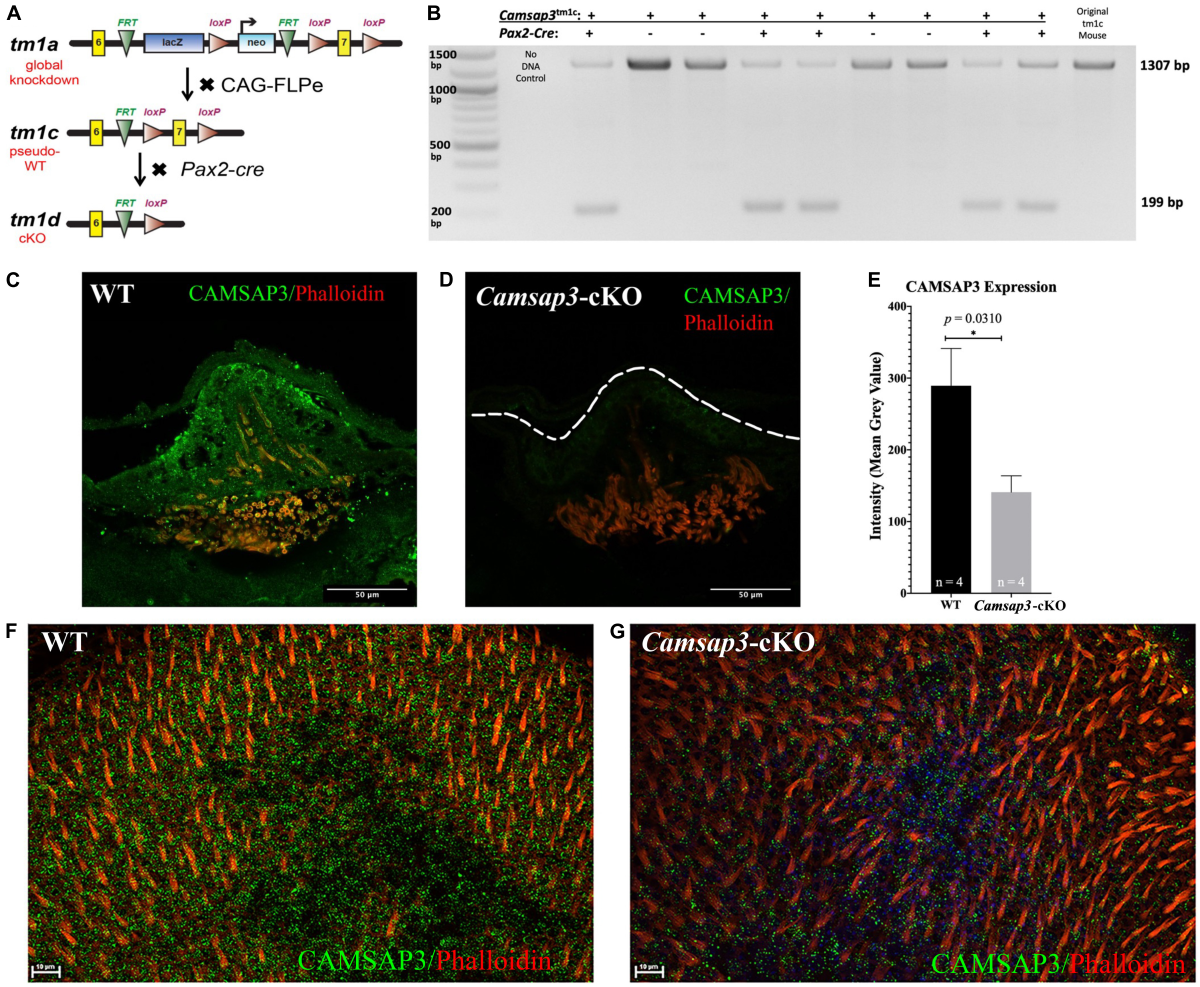

FIGURE 1 | Creation and validation of the *Camsap3*-cKO mouse. **(A)** A schematic diagram of the *Camsap3* knockout first targeting strategy and conversion of tm1a (KO first) to tm1c (floxed), and tm1d (cKO) alleles, respectively. Tg*Pax2*$^{Cre/+}$; *Camsap3*$^{tm1c/tm1c}$ mice, known as *Camsap3*-cKO, are a cKO model for the vestibular organ. **(B)** The exon 7 of *Camsap3* execution was validated by PCR genotyping. The inner ear genomic DNA of offspring derived from crossing Tg*Pax2*^{Cre} and *Camsap3*$^{tm1c/tm1c}$ were isolated and used for PCR (*n* = 9 from two separate litters). No DNA and floxed allele *Camsap3*$^{tm1c/tm1c}$ were used as the negative and positive controls. The bands were expected to be 1307 bp for WT (Tg*Pax2*$^{Cre+/+}$; *Camsap3*$^{tm1c/tm1c}$) and 199 bp for *Camsap3*-cKO mice. **(C–G)** CAMSAP3 protein expression in the vestibular system as examined by immunofluorescence. **(C,D)** Representative immunofluorescent images of a crista from WT **(C)** and *Camsap3*-cKO **(D)** mouse at P75 were shown. The dashed line outlines the edge of the crista of a *Camsap3*-cKO mouse. Scale Bars = 50 µm. **(E)** Vestibular cells from *Camsap3*-cKO mice had significantly less CAMSAP3 staining than their WT counterparts. The bars represent mean ± SD. *Statistically significant difference ($p = 0.03$). WT and *Camsap3*-cKO mice littermate (P75) replicates (n) were as indicated. **(F,G)** Representative confocal maximum projection of z-stack images taken from whole-mounts utricle samples of a WT **(F)** and a *Camsap3*-cKO mouse **(G)**. More CAMSAP3 staining dots were found on the apical surface of WT utricle compared to those on *Camsap3*-cKO mouse. Scale Bars = 10 µm. Antibodies: anti-Camsap3 (Green), phalloidin (Red).

coefficient, paw area, and the maximum change in paw area (maximum dA/dt).

Immunofluorescence and Microscopy

The inner ears, olfactory bulbs, and olfactory mucosa in nasal cavities were collected from WT mice and their *Camsap3*-cKO littermates for immunofluorescence as previously described (Sekerka et al., 2011; Robinson et al., 2020). Briefly, samples were immersion fixed in 4% formaldehyde in phosphate buffered solution (PBS). Some samples underwent whole mount preparation, in which the utricles and cristae were further dissected out and used for immunostaining. Other samples were cryosectioned before staining. These samples were first decalcified in 0.125M EDTA for 2 days. Decalcified samples were then placed in a series of sucrose solutions in 1X PBS (10–30%) then two changes of Tissue-Tek Optimal Cutting Temperature (OCT) Embedding Medium (Sakura Finetek, 4583), and embedded in fresh OCT. The inner ear samples were then sectioned into 12 micrometer thick slices, and post-fixed in 2% formaldehyde for 10 min and blocked at room temperature for 1 h in blocking solution: 5% goat serum, 2% Triton X-100 in Tris-buffered saline (TBS). The following primary antibodies were used for immunostaining: anti-Camsap3 (Robinson et al., 2020) at 1:2500, anti-acetylated tubulin at 1:500 (Thermo Fisher

Scientific 32-2700, AB_2533073). Samples were incubated with primary antibodies at 4°C overnight. The next day samples were then washed in PBS and incubated with appropriate fluorophore-conjugated secondary antibodies, including goat anti-rabbit Alexa 488 at 1:500 (Thermo Fisher Scientific 32-2700, AB_143165), goat anti-mouse Alexa Fluor 488 (RRID: AB_2556548), goat anti-mouse IgG2b Alexa 647 at 1:500 (Thermo Fisher Scientific AB_143165), Hoechst at 1:1000 (Thermo Fisher Scientific, H3570), and Phalloidin-Alexa 568 at 1:2000 (Thermo Fisher Scientific 21838, AB_2532159), or Phalloidin-Alexa 647 at 1:400 (Thermo Fisher Scientific A22287) for 2.5 h at room temperature. The stained samples were subsequently mounted in Fluoromount Aqueous Mounting Medium (Sigma, F4680). When mounting the whole mount utricle samples, a 0.12 mm deep Secure-Seal spacer (Thermo Fisher Scientific, S24735) was placed between the slide and the cover glass in order to avoid destruction of the vestibular kinocilia on hair cells. Immunostained samples were imaged using a Nikon C2 or A1R+ confocal microscope using objects of a plan Apo VC 20×/0.75 DIC N2 (Nikon) and a plan Apo 60×/1.4 oil (Nikon). All images were taken as 12-bit, which allows for 0–4,095 range. For vestibular kinocilia length measurement, Z-stacks images were captured from the apical surface of utricle hair cells to the tip of vestibular kinocilia (from the position "A" extended to "C-D" shown in **Figure 3B**) using the optical section (0.5 μm). These Z-stack images were then reconstructed into 3D images, which were analyzed using Imaris 8 (Bitplane) and Nikon NIS Element software. Mean gray value, the sum of the gray values of all the pixels in the selection divided by the number of pixels, was measured using FIJI.

Transmission Electron Microscopy

Utricles from WT mice and their *Camsap3*-cKO littermates were dissected out and immersion fixed in 0.1 M sodium cacodylate buffer pH 7.3, containing 2% paraformaldehyde and 2.5% glutaraldehyde for at least 24 h and post-fixed with 2% osmium tetroxide followed by 3% uranyl acetate. Tissues were then dehydrated in ascending grades of ethanol, transitioned with propylene oxide and embedded in resin mixture from the Embed 812 kit, cured in a 60°C oven. Samples were sectioned on a UCT ultramicrotome (Leica Microsystems). To identify regions of interest 1 μm thick sections were collected, stained with Toluidine Blue O and examined by light microscopy. 70 nm tissue sections were collected on 200 mesh copper grids and stained with uranyl acetate and Reynolds lead citrate, and examined using a FEI Tecnai G2 Spirit Transmission Electron Microscope. The number of MTs in kinocilium was counted and sorted by structure: "9+2," "9+0," "8+2," or "8+0." The first number indicates the numbers of MT doublets outlying, and the second number implies the amount of MTs in the center.

Evaluation of Olfaction

The Buried Food Test was used to evaluate olfaction in mice (Yang and Crawley, 2009; Robinson et al., 2020). WT mice and their *Camsap3*-cKO littermates were food restricted but provided water *ad libitum* for 24 h prior to testing. Mice were given a piece of a Nutter Butter cookie during this day to familiarize the mice with its scent. Testing was performed during daylight, starting at 9 AM. The base of a Sterilite translucent storage box (cage) [47 cm (L) × 37.8 cm (W) × 28.3 cm (H)] was filled with bedding to a depth of 3 cm. Each mouse was placed in an acclimation bin which was identical to the testing bin in every way, with the exception of no food being present, and were given 5 min to adjust to the enclosure. Mice were then transferred individually to the testing cage, which had ∼ 0.5 g of Nutter Butter cookie hidden in the center of the cage under the bedding. As soon as the mouse entered the testing bin a stopwatch was started and the latency to find (LTF) the cookie was recorded. Following the experiment, mice were returned to their home cages and given their full allotment of food.

RESULTS

Camsap3-cKO Is a *Camsap3* Conditional Knockout Model for the Vestibular Organ

As previously reported, the global KD mice, *Camsap3*-KD, were born with smaller bodies along with sub-infertility, hydrocephalus, anosmia or hyposmia, sinusitis, respiratory distress, otitis media, and hearing loss (Perez-Garcia et al., 2018; Ingham et al., 2019; Robinson et al., 2020). In contrast to *Camsap3*-KD, *Camsap3*-cKO had normal fertility and a normal appearance comparable to their WT littermates regardless of their sex prior to 4 months of age, The normal appearance of *Camsap3*-cKO was not surprising as *Camsap3* was expected to be eliminated only in the inner ear, midbrain, cerebellum, olfactory bulb, and the kidneys (Ohyama and Groves, 2004). To test whether the exon 7 of *Camsap3* was indeed removed from the genome of affected cells, we performed PCR genotyping using genomic DNA isolated from the inner ear, where *Cre* was expressed to remove the floxed exon 7 of *Camsap3*. As shown in **Figure 1B**, in all *Camsap3*-cKO mice (*Pax2-Cre* positive), the expected short fragments (199 bps) were detected, but not in mice without the *Pax2-Cre* allele (*Pax2-Cre* negative) or original homozygous *Camsap3*^{tm1c} mice. We noted that the long PCR band, 1307 bp, was also detected in *Camsap3*-cKO mice with low intensity. As we did not perform cardiac perfusion before extracting genomic DNA from the inner ear, we suspected that cells from the circular bloodstream in the inner ear could contribute to the long PCR bands as the genomic DNA from these cells were not affected by *Pax2-Cre* expression. It is also possible that the exon 7 of *Camsap3* was not completely removed from all cells in the inner ear. To verify whether *Camsap3* was expressed in the vestibular hair cells, we performed immunofluorescence using vestibular organs collected from *Camsap3*-cKO and their WT littermates, with the ages of postnatally day (P) 23 to 260. In WT, CAMSAP3 expression was found in the vestibular organ including the hair cells in cristae (**Figure 1C**), utricle (**Figure 1F**), and saccule (data not shown). CAMSAP3 expression in *Camsap3*-cKO was absent or reduced in vestibular cells from *Camsap3*-cKO mice as shown in **Figures 1D,G**. CAMSAP3 staining was expressed in both hair cells and their surrounding supporting cells in vestibular organs from WT samples. CAMSAP3 signals were more concentrated in the apical cortical area of the WT vestibular organ (**Figure 1C**).

Such distribution patterns are unsurprising as CAMSAP3 is needed at apical cortical area of epithelial cells to establish the intercellular connection and orient the apical-to-basal polarity of microtubule arrays (Meng et al., 2008; Toya et al., 2016). We further quantified CAMSAP3 staining intensities in the apical cortical area that included both vestibular hair cells and supporting cells. The mean gray value (intensity) of CAMSAP3 staining in these areas were measured using FIJI software. As shown in **Figure 1E**, CAMSAP3 expression was significantly decreased in the hair cell area and supporting cells from *Camsap3*-cKO mice, with CAMSAP3 expression in *Camsap3*-cKO mice equaling 48.74% of expression in WT mice at P75 (p = 0.031, unpaired t-test, n = 4). In sum, we created a cKO model that significantly reduced CAMSAP3 proteins in the vestibular system.

Camsap3-cKO Mice Have Abnormal Kinocilia on Vestibular Hair Cells

To investigate CAMSAP3's role in establishing kinocilia on the vestibular hair cells, utricles collected from *Camsap3*-cKO mice (3 male) and their WT littermates (3 male) around 1-year old (P296-P384) were examined using immunofluorescent staining of anti-acetylated tubulin and phalloidin, which labeled vestibular kinocilia (green) and stereocilia (red, dash lines), respectively (**Figure 2A**). We measured the length of kinocilia on vestibular hair cells of utricles from *Camsap3*-cKO mice and their WT littermates at the most anterior portion for consistency (**Figure 2B**). From each mouse sample, the length of kinocilium was measured from base to tip in micrometers. Great care was taken to exclude vestibular kinocilia whose full length was not captured in the confines of the reconstructed 3D image. The average length of the vestibular kinocilia, in mean ± SD, were 20.39 μm ± 3.21 for WT and 17.16 μm ± 3.03 for *Camsap3*-cKO (**Figure 2C**). An unpaired t-test revealed a significant reduction in vestibular kinocilia length in *Camsap3*-cKO mice when compared with their WT littermates ($p < 0.0001$).

Our previous work demonstrated that CAMSAP3 was needed for *de novo* formation of the central MT pair in a "9+2" configuration observed in the axons of motile cilia (Robinson et al., 2020). To test whether CAMSAP3 was also needed for formation of the central MT pair in the kinocilia on vestibular hair cells, we first examined the connection between CAMSAP3 and basal bodies by immunofluorescence. The basal bodies that extend to 9 peripheral MT doublets were labeled by anti-γ-tubulin, and phalloidin was used to label the actin-based stereocilia that were adjacent to the kinocilium. As shown in **Figure 3A**, a group of Z-stack images taken from the apical surface of utricle hair cells (the position "A" shown in **Figure 3B**) showed two vestibular kinocilia labeled by γ-tubulin (arrows). A stereocilia bundle was next to one of kinocilia, indicating these cells were hair cells from an utricle. Similar to other epithelial cells, CAMSAP3 punctuates (green) were found on the apical surface of hair cells. Two CAMSAP3-stained green dots (arrows) were colocalized with two basal bodies (red dots). As the focus pointing moved step by step (0.5 μm/per section) from the apical surface toward the nucleus, green CAMSAP3 dots (arrows in **Figure 3A**) in both vestibular kinocilia disappeared before the red basal bodies punctuates, suggesting that CAMSAP3 was at the base of vestibular kinocilia just above the basal bodes, as illustrated in **Figure 3B**. Such a close connection between CAMSAP3 and basal bodies was of particular interest because CAMSAP3 is not a centrosome- or basal bodies-bound protein. In fact, CAMSAP3 was not observed in the basal bodies of primary cilia with "9+0" MT configuration (Robinson et al., 2020). More importantly, the close association between γ-tubulin and CAMSAP3 was comparable to that observed in motile cilia with "9+2" MT configuration (Robinson et al., 2020; Saito et al., 2021), suggesting that CAMSAP3 was also involved in *de novo* formation of the central MT pair in the kinocilia on the vestibular hair cells.

To further verify the role of CAMSAP3 in formation of the central MT pair in vestibular kinocilia, the MT structure

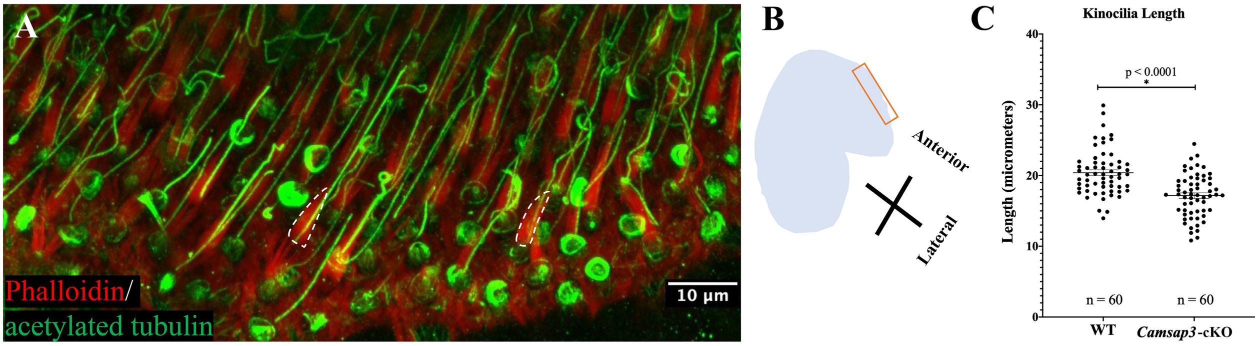

FIGURE 2 | Kinocilia on utricles hair cells from *Camsap3*-cKO are shorter than their WT littermates. **(A)** A representative 3D-reconstruction from z-stacks images of bundles of stereocilia (red) and kinocilia (green) located on the apical surface of hair cells from an utricle of a WT mouse (P386). Antibodies: anti-acetylated tubulin (Green), phalloidin (Red). The dashed line outlines the edge of actin-based stereocilia bundles. Scale Bar = 10 μm. **(B)** A schematic diagram showing the region over which Z-stack images of utricle hair cells were collected. **(C)** Quantification of kinocilia length collected from male WT (n = 3) and male *Camsap3*-cKO littermates (n = 3) with ages ranging from 10- to 13-month. Each dot represented one kinocilium. Bars represent mean ± SD. Kinocilia on utricles hair cells from *Camsap3*-cKO were statistically significant shorter than WT (p < 0.0001). *Statistically significant difference.

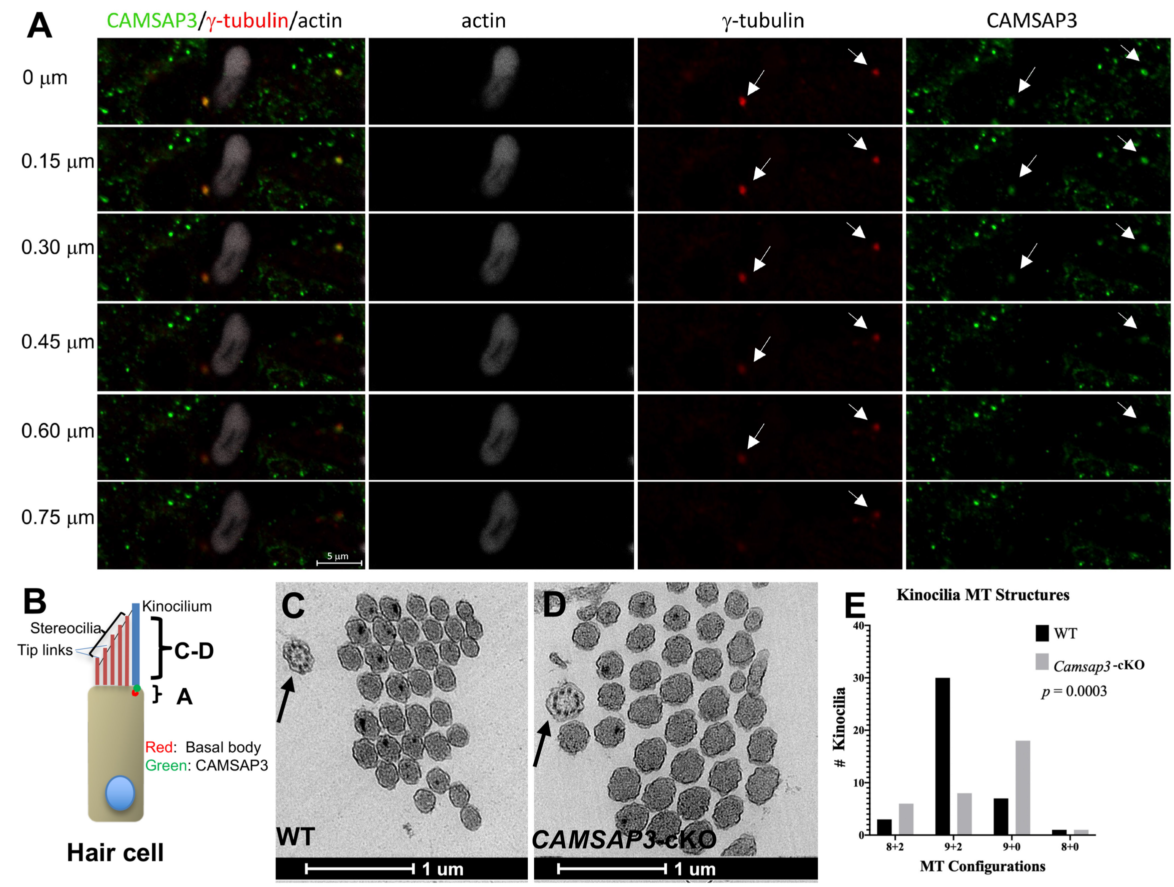

FIGURE 3 | CAMSAP3 contributes to the formation of central MT pairs in axonemes of kinocilia on utricle hair cells. **(A)** The overlaps between CAMSAP3 (green) and basal bodies (red) were displayed by a group of consecutive Z-stack kinocilia images taken from a whole mount utricle sample of WT (P42). Z-stack images were captured using the optical section (0.5 µm) starting from the apical surface of utricle hair cells toward its nucleus. Antibodies: anti-CAMSAP3 (Green), anti-γ-tubulin (red), phalloidin (white). Scale Bars = 5 µm. Two basal bodies of kinocilia were indicated by arrows. **(B)** A schematic diagram illustrates the region over which Z-stack images of kinocilia immunostaining A, and TEM images C-D were collected. **(C,D)** Representative TEM images show transverse sections of kinocilia on utricle hair cells from 8-month-old WT with a "9+2" configuration (black arrow) **(C)**, and a "9+0" configuration (black arrow) for their *Camsap3*-cKO littermates **(D)**. Scale Bars = 1 µm. **(E)** The distribution of MT arrangements for both WT and *Camsap3*-cKO mice was compared. Distribution of the MT configurations between WT and KO was significantly different as analyzed by a Kolmogorov–Smirnov test (*p* = 0.0003).

differences between WT and *Camsap3*-cKO vestibular kinocilia were then evaluated using TEM (**Figures 3C–E**). We examined 42 axoneme structures (the position "C-D" shown in **Figure 3B**) from 8-month-old WT mice and 33 axonemes from their *Camsap3*-cKO littermates. The "9+2" configuration here includes 9 MT doublets peripherally and two MT singlets or amorphous material with higher electron density (darker) at the center of axonemes. This is demonstrated in a transverse section of WT vestibular kinocilia (**Figure 3C**, indicated by an arrow). The "9+0" configuration lacks the central MTs structure and electron-dense materials as seen in the *Camsap3*-cKO image in **Figure 3D**. More than 71% of vestibular kinocilia from WT mice have "9+2" configuration, while only 24% vestibular kinocilia from *Camsap3*-cKO mice showed similar structure. The majority of *Camsap3*-cKO vestibular kinocilia (55%) have the "9+0" configuration. In addition, irregular configurations, "8+2" and "8+0," were found in both WT (12%) and *Camsap3*-cKO (21%). Distribution of the MT configurations between WT and KO was statistically significant different as analyzed using a Kolmogorov-Smirnov distribution comparison test (*p* = 0.0003). Our data suggests that vestibular kinocilia of *Camsap3*-cKO were more likely missing the central MT pair than WT vestibular kinocilia.

Kinocilia are known to be essential for establishing the orientation of stereocilia bundles on hair cells. Data collected from P23 to 13-month showed that vestibular kinocilia were present on the vestibular hair cells of *Camsap3*-cKO mice just as their WT littermates. In addition, the shape and orientation of stereocilia on vestibular hair cells from *Camsap3*-cKO were quantitatively similar to those on WT mice despite the vestibular kinocilia from *Camsap3*-cKO mice were shorter and more likely to miss the central MT pair (**Figures 2**, **3**). We also investigated the impact of CAMSAP3 on the orientation of stereocilia bundles by comparing auditory hair cells from WT and *Camsap3*-cKO mice with matched ages and sexes. As shown in **Supplementary Figure 3**, the orientation of stereocilia bundles on auditory hair cells from *Camsap3*-cKO mice were comparable to those on WT auditory hair cells. This data is not surprising because most of kinocilia on auditory hair cells are with "9+0" configuration (Sobkowicz et al., 1995), and CAMSAP3 signals do not co-localize with the basal bodies where "9+0" axonemes are originated (Robinson et al., 2020). In summary, CAMSAP3 is unlikely to have a significant impact on cochlear kinocilia and the orientation of stereocilia.

Body Weight Differences Between Wildtype and *Camsap3*-cKO Mice Arise as Mice Age

In our original measurements of young mice, ranging from 1 to 4 months old, there was no weight difference between *Camsap3*-cKO mice and their WT littermates (**Figure 4A**). This phenotype differs from KD mice, *Camsap3*-KD, which were born smaller than their WT littermates (Robinson et al., 2020). Since we did not notice obvious body weight differences like those observed in the global *Camsap3*-KD mice, we assumed that their weights remained comparable. Though there were no obvious weight differences between WT and *Camsap3*-cKO mice when mice were less than 4-month old, weight differences emerged in 8-month old mice (**Figure 4A**). For mice 8 months and older (P237–P388), the average male WT mouse weighed (mean ± SD) 39.61 g ± 8.703 (*n* = 21), and the average male *Camsap3*-cKO mouse weighed 26.49 g ± 4.904 (*n* = 13). For female mice older than 8 months, the average WT mouse weighed 30.56 g ± 4.687 (*n* = 8), and the average female *Camsap3*-cKO mouse weighed 22.38 g ± 1.727 (*n* = 7). WT mice older than 8-month were significantly larger than the *Camsap3*-cKO mice regardless their sex (**Figure 4**).

Camsap3-cKO Mice Do Not Have Notable Vestibular Dysfunction

Since CAMSAP3 was essential to build or maintain normal structure of vestibular kinocilia (**Figures 2**, **3**), we further investigated whether shorter kinocilia on vestibular hair cells caused vestibular dysfunction. Vestibular dysfunction can manifest as issues with balance or gait abnormalities. In their home cages, *Camsap3*-cKO mice did not show obvious head tilt, walked normally, and were indistinguishable from their WT littermates. To assess the vestibular function of *Camsap3*-cKO mice, we performed multiple methods aiming to detect more subtle abnormalities. The simplest methods of testing vestibular functions include a swim test and a right-reflex test (Hardisty-Hughes et al., 2010). The swim test aims to determine if the mice could properly swim in a straight line and keep themselves upright. After assessing 26 WT (14 male and 12 female), and 27 *Camsap3*-cKO (14 male and 13 female) mice, ages ranging from P22 to P388, we found that there were no notable differences between the *Camsap3*-cKO and WT mice regarding their ability to swim. The right-reflex test assesses whether the mice can re-right themselves when flipped upside down. The same group of 26 WT and 27 *Camsap3*-cKO mice completed the right-reflex test. We found no difference in performance between the WT and *Camsap3-cKO* mice as each of the mice was able to flip themselves back to upright immediately (within 1 s). Subsequently, we analyzed the balance ability of *Camsap3*-cKO mice by rotarod apparatus. On the Rotarod, we assessed

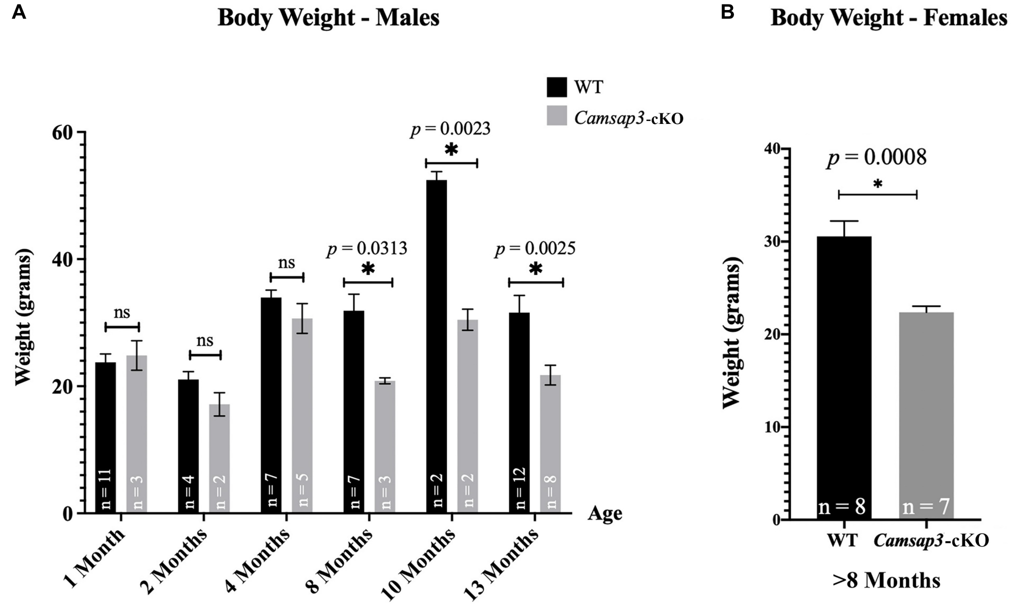

FIGURE 4 | Weight differences between WT and *Camsap3*-cKO mice. **(A)** Male *Camsap3*-cKO mice weigh less than their WT counterparts after the age of 8-month, while no body weight difference was observed in mice younger than 4-month old. Mice were weighed prior to euthanasia at ages P36–P388. ns, not statistically significant difference. **(B)** Female *Camsap3*-cKO mice aged 8–13 months weigh less than their WT counterparts. For both male and female mice, the weights of old WT and *Camsap3*-cKO mice were significantly different. *p*-values for each age group of mice were as indicated. *Statistically significant difference.

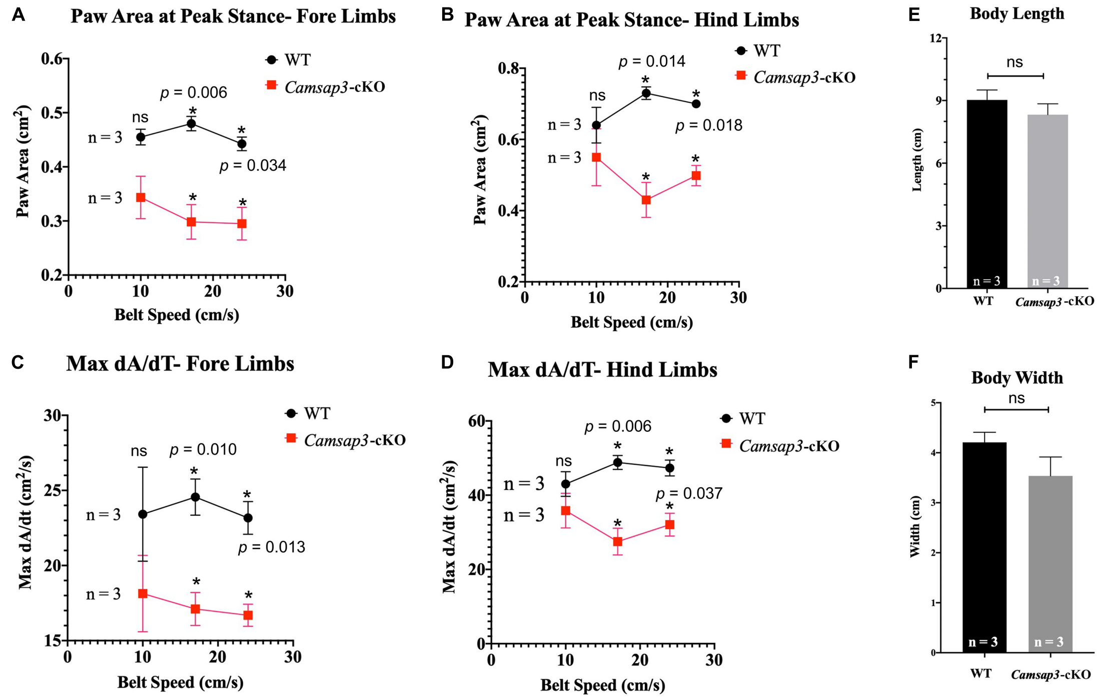

FIGURE 5 | Gait differences between WT and *Camsap3*-cKO mice. Two litters of mice, ages P130–P133, were tested using the DigiGait Imaging System. Multiple *t*-tests revealed that Paw Area **(A,B)** and Max dA/dt **(C,D)** were significantly different between WT and *Camsap3*-cKO mice (*p*-values for each speed were as indicated). Bars represent mean ± SD. **(E)** Unpaired *t*-tests showed that there was no body length difference between male WT and *Camsap3*-cKO mice (ns, $p = 0.1572$). **(F)** Unpaired *t*-tests showed that there was also no body width difference between male WT and *Camsap3*-cKO mice (ns, $p = 0.0539$). $N = 3$ for both WT and *Camsap3*-cKO mice. *Statistically significant difference.

12 WT (6 male and 6 female) and 8 *Camsap3*-cKO (5 male and 3 female) mice, ages P37–P153, and found that there was no significant difference in TTF between the two groups (data not shown).

Camsap3-cKO Mice Have Slightly Altered Gaits

The vestibular function of *Camsap3*-cKO mice was also examined using the DigiGait Imaging System (Berryman et al., 2009). Since mice older than 8-month *Camsap3*-cKO mice were lighter than their WT littermates (**Figure 4A**), mice at 4 months old were selected for gait measurement. At this age, gait was fully developed (Akula et al., 2020; Rahn et al., 2021), and *Camsap3*-cKO mice were not significantly lighter than their WT littermates (**Figure 4A**). The assessed litter consisted of 6 male mice: 3 WT and 3 *Camsap3*-cKO. We collected data from these mice using the DigiGait^{TM} Imaging System. Of all the aspects of gait analyzed by the DigiGait analysis software, most showed no significant difference between the WT and *Camsap3*-cKO mice. Some of the results were shown in the **Supplementary Figures 1**, **2**). Two aspects of gait with significantly differences were paw area at peak stance and maximum dA/dt (**Figure 5**). Paw area (cm^2) is the maximal paw area captured by the camera and corresponds with the time of "peak stance" (**Supplementary Figure 1**). When compared to their WT littermates, *Camsap3*-cKO mice had smaller areas of their paws in contact with the treadmill for both fore and hind limbs regardless of running speeds (**Figures 5A,B**). For example, at a speed of 17 cm/s, the paw area that *Camsap3*-cKO mice used to touch the treadmill was 62.1% (fore limbs) and 58.9% (hind limbs) of the paw area WT mice used. Maximum dA/dt (cm^2/s) is the maximal rate of change of paw area in contact with the treadmill belt during the braking phase. At a low treadmill speed (10 cm/s), there was no substantial difference between the WT and *Camsap3*-cKO mice in their dA/dt for both fore and hind lambs. However, as the treadmill speeds increased, the difference between the WT and *Camsap3*-cKO mice became more apparent. At a high treadmill speed (24 cm/s), the maximum dA/dt decreased in *Camsap3*-cKO mice's hind limbs (−10.5%), while WT mice had increased maximum dA/dt (+10.0%). Similar to paw area, maximum dA/dt in *Camsap3*-cKO mice were always slower than their WT littermates independent of walking speed. These differences exist despite there being no difference in the body length, width (**Figures 5E,F**), and weight (**Figure 4A**) between the WT and *Camsap3*-cKO mice.

Older *Camsap3*-cKO Mice Have Renal Abnormalities

In Tg*Pax2*^{Cre} mouse line, *Cre* was detected in the embryonic kidney since the 12-somite stage to remove the floxed allele (Ohyama and Groves, 2004). Since CAMSAP3 is essential to orienting the apical-to-basal polarity of MT arrays in epithelial cells (Toya et al., 2016), we suspected that kidney function might be affected in *Camsap3*-cKO mice. Therefore, both kidneys were prepared out of euthanized WT and cKO mice with ages of P22–P339. Since the kidney-to-body weight ratio has been commonly used to predict kidney function (Hughes et al., 1999; Mitsuhata et al., 2021), we weighed 19 WT mice and 7 *Camsap3*-cKO mice and their kidneys. Kidney weight as a proportion of body weight was recorded. Female mice that had previously given birth were excluded. Interestingly, we found that *Camsap3*-cKO mice, especially the males, had statistically significant heavier

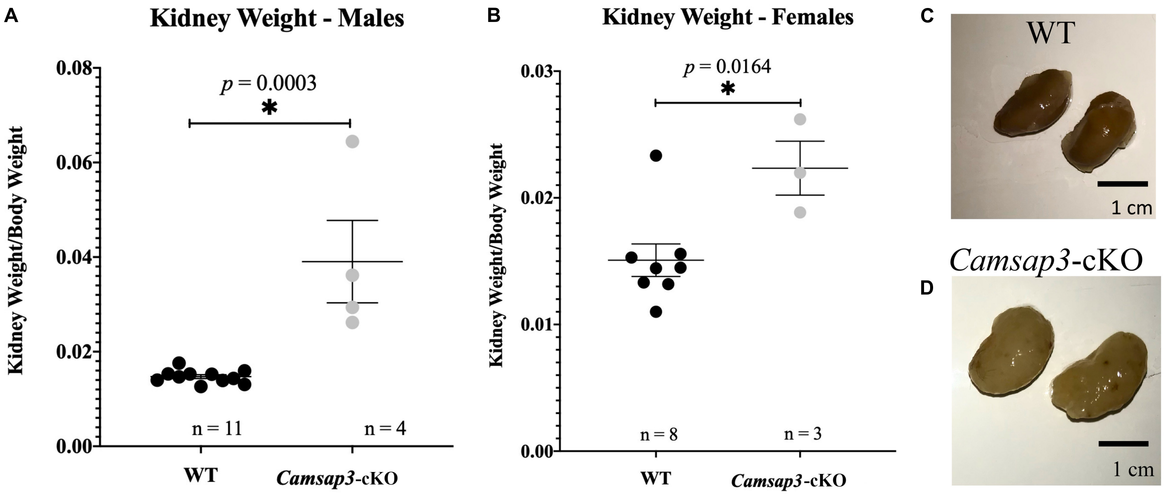

FIGURE 6 | Renal abnormalities in *Camsap3*-cKO mice. **(A,B)** The kidney-to-body weight ratio in male **(A)** and female **(B)**. Unpaired *t*-tests revealed that *Camsap3*-cKO mice (P22-P339) showed a statistically significant increase in their kidney-to-body weight ratio relative to their WT counterparts. *p*-values for each age group of mice were as indicated. Bars represent mean ± SD. **(C,D)** Representative kidney images taken from male, 1-year-old WT **(C)** and *Camsap3*-cKO littermate **(D)**. Kidneys from the *Camsap3*-cKO mouse were hypertrophic and discolored. *Statistically significant difference.

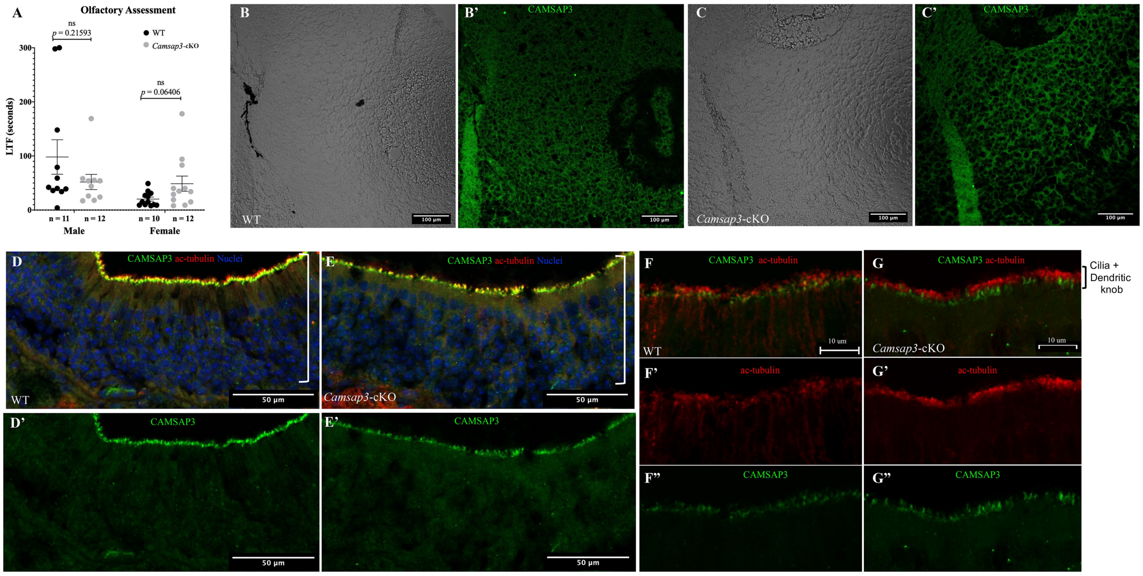

FIGURE 7 | WT and *Camsap3*-cKO mice show no differences in olfaction. **(A)** No differences in the reaction time of the sense of smell between WT and *Camsap3*-cKO mice. Bars represent mean ± SD. Unpaired *t*-tests revealed no significant (ns) differences between WT and *Camsap3*-cKO mice in male or female mice. **(B,C)** CAMSAP3 had little expression in olfactory bulbs regardless of genotype, WT **(B)** or *Camsap3*-cKO **(C)**. The representative images were taken from female WT and their *Camsap3*-cKO littermates at P180. **(B',C')** were the cells shown in **(B,C)** stained with anti-Camsap3 (green). **(D–G)** CAMSAP3 was expressed in olfactory sensory neurons (OSN) in both WT and *Camsap3*-cKO mice. Olfactory mucosa in the nasal cavity from WT **(D,F)** and *Camsap3*-cKO **(E,G)** mice were stained with anti-Camsap3 (green), anti-acetylated tubulin (red, olfactory cilia, and nerve fibers), and Hoechst 33342 (blue, nuclei). **(F,G)** were images with higher magnification showing olfactory cilia and dendritic knobs layers on OSNs. **(D',E',F",G")** Showed the anti-CAMSAP3 (green) channel in **(D–G)**. **(F',G')** Showed anti-acetylated tubulin (red) channel in **(F,G)**. "[" Marks the OSN layer in the olfactory epithelium. Scale Bars = 100 μm **(B,C)**, 50 μm **(D,E)**, 10 μm **(F,G)**.

kidneys (as a function of body weight) than their WT littermates (**Figure 6**). In male WT mice, their kidneys made up (mean ± SD) 1.47 ± 0.13% of their body weight, and in male *Camsap3*-cKO mice, their kidneys equaled 3.90 ± 1.5% of their body weight (**Figure 6A**). In female WT mice, their kidneys made up 1.51 ± 0.34% of their body weight, while in female *Camsap3*-cKO mice, their kidneys equaled 2.23 ± 0.30% of their body weight (**Figure 6B**). Kidneys from the *Camsap3*-cKO mice were hypertrophic and discolored (**Figure 6C**). Such a phenotype was similar to those observed in CAMSAP3-mutant knocking in mice model $Camsap3^{dc/dc}$, in which exons 14–17 of *Camsap3* were removed from the genome of $Camsap3^{dc/dc}$ mice (Toya et al., 2016). Exons 14–17 encode the key MT binding domain of CAMSAP3, CKK domain. Because the mutant CAMSAP3 without the CKK domain is incapable of binding to MTs to form proper MT network in the epithelial cells in kidney, $Camsap3^{dc/dc}$ mice developed malfunction of kidneys with cyst at the proximal convoluted tubules starting at E17.5 even though kidney had normal appearance at P21 (Mitsuhata et al., 2021). Since renal dysfunction often caused body weight loss (Hickman and Swan, 2010), the deterioration of kidneys observed in *Camsap3*-cKO may contribute to the small body size of *Camsap3*-cKO mice older than 8-month (**Figure 4**). In consequence, health issues arose, and these mice became thin, hunched, and moved slowly. These health issues prevented further investigation of CAMSAP3's impact on vestibular function in *Camsap3*-cKO mice that were older than 13 months of age.

Camsap3-cKO Mice Maintain Normal Olfaction

Since *Cre* was expressed in the olfactory bulb in Tg$Pax2^{Cre}$ mouse line to remove the floxed *Camsap3* exon 7, we investigated whether *Camsap3*-cKO had normal olfaction. Olfaction evaluation was performed for WT (11 male and 10 female) and *Camsap3*-cKO mice (12 male and 12 female) from 8 litters of mice, ages P55–P313. Mice were placed in a large container filled with bedding, and their latency to find (LTF) a buried Nutter Butter cookie was recorded. As shown in **Figure 7A**, WT and textitCamsap3-cKO mice took equal amounts of time to find the buried cookie. There was no significant difference between WT and *Camsap3*-cKO mice regardless their sex. We then examined CAMSAP3 expression in the olfactory bulb. Olfactory bulbs from P180 WT and *Camsap3*-cKO littermates were collected and stained with anti-Camsap3. As shown in **Figures 7B,C**, there was little CAMSAP3 expression in cells located in olfactory bulbs from both the WT and *Camsap3*-cKO mice, suggesting that CAMSAP3 has a minimal role in olfactory bulbs. We also compared CAMSAP3 expression in olfactory sensory neurons, where CAMSAP3 was abundantly expressed (Robinson et al., 2020). As shown in **Figures 7D–G**, CAMSAP3 was abundantly expressed in olfactory sensory neurons located in the nasal olfactory epithelia in both the WT and *Camsap3*-cKO mice. CAMSAP3 expression in olfactory sensory neurons is not affected in *Camsap3*-cKO mice and remained concentrated at dendritic knobs under the olfactory cilia (**Figures 7F,G**). In other words, CAMSAP3 expression in cells involved in olfaction were not changed in *Camsap3*-cKO mice compared to their WT littermates. Given the equivalent CAMSAP3 expression in cells involved in olfaction (**Figures 7B–G**), it was unsurprising that the *Camsap3*-cKO mice performed equally as well as WT mice on the open-field olfaction assessment.

DISCUSSION

Kinocilia on vestibular hair cells have MTs arranged in a "9+2" configuration that differs from most primary sensory cilia. Unlike the central MT pair in motile cilia, the function of the central MT pair in primary sensory cilia, including vestibular kinocilia, remains unknown. Our data shows that CAMSAP3 is located at the base of vestibular kinocilia (**Figure 3**). Removing or reducing CAMSAP3 in vestibular hair cells leads to abnormal kinocilia, which have shorter axonemes (**Figure 2**) and are more often missing the central MT pair (**Figure 3**). Since CAMSAP3 is required for *de novo* formation of the central MT pair for the "9+2" configuration in motile cilia (Robinson et al., 2020; Saito et al., 2021), it is likely that lacking CAMSAP3 and CAMSAP3-stabilized MTs in vestibular hair cells also prevents the central MT pair formation in vestibular kinocilia. This likely leads to the shortened vestibular kinocilia observed in *Camsap3*-cKO mice (**Figure 2**). In addition, *Camsap3*-cKO mice have more irregular configurations (8+2, 8+0) in vestibular kinocilia than their WT littermates. Although a very small portion of irregular MT configuration is commonly found in WT cilia, an increased proportion of irregular MT configurations in cilia was often associated with damage or degeneration of cilia (Piorunek et al., 2008). With increased irregular MT configurations and decreased "9+2" configuration in vestibular kinocilia from *Camsap3*-cKO, our data suggests that the central MT pair in vestibular kinocilia is important in establishing and/or maintaining the long axonemes observed in vestibular kinocilia.

Despite their abnormal vestibular kinocilia formation, *Camsap3*-cKO mice do not have notable vestibular dysfunction such as slower right-reflexes, inferior balance, and gait asymmetries (Hardisty-Hughes et al., 2010; Lu et al., 2011; Kopecky et al., 2012; Mathur et al., 2015). Such incoherent results between morphological data and behavioral assays are not uncommon, as many other mutant mice with damaged hair cells or neurons in the vestibular organ showed no detectable vestibular dysfunction (Jones and Jones, 2014). Since balance is achieved and maintained by multiple systems including the vestibular system, vision, proprioception, and central nervous system, it is possible that the *Camsap3*-cKO mice are able to retain normal vestibular function because of compensation or adaptation by the central nervous system and other peripheral systems. In addition, the central MT pairs are not completely eliminated from all kinocilia on vestibular hair cells from *Camsap3*-cKO mice as shown in **Figure 3E**. We suspect that *Camsap3* might not be completely removed from all cells in the vestibular organ. It is also possible that CAMSAP3's role is compensated for by other members of CAMSAP family, such as CAMSAP2, which compensates for CAMSAP3 to maintain

MT networks (Tanaka et al., 2012). Nevertheless, *Camsap3*-cKO mice did show slightly altered gaits in their paw area at peak stance and maximum dA/dt. Assessment of paw placement during walking is often used to evaluate pain (Griffioen et al., 2015; Deuis et al., 2017), pain-killer medicines (Brings et al., 2021), diseases (Bernardes and Oliveira, 2017), and recovery of injuries including both peripheral and central nerve injury (Neumann et al., 2009; Heinzel et al., 2020). Mice with numbers of disorders decrease their paw area to form "tip-toe walking" patterns (Furusawa et al., 1996; Moskovitz et al., 2001). Such phenotypes are also found in humans, particularly in children. An underdeveloped or poor vestibular system is believed to contribute to some of the idiopathic toe walking cases observed in children (Montgomery and Gauger, 1978; Chu and Anderson, 2020). *Camsap3*-cKO mice also decreased their paw area in both hind paws that come into contact with the surface (**Figure 5**). It is, therefore, tempting to speculate that altered gaits observed in *Camsap3*-cKO mice is the consequence of shorter vestibular kinocilia due to a lack of CAMSAP3 and central MTs in their axoneme. However, vascular calcification can also cause tiptoe walking in mice (Okawa et al., 1998), and kidney disease is one etiology for vascular calcification (Palit and Kendrick, 2014). Although there is no evidence suggesting that *Camsap3* expression is changed in the somatosensory system of *Camsap3*-cKO mice, but the midbrain and cerebellum may reduce CAMSAP3 expression due to *Cre* expression in these issues. Changed CAMSAP3 expression in the midbrain and cerebellum may interfere with the somatosensory information process that might lead to alternated gaits in *Camsap3*-cKO.

Balance disequilibrium is a significant contributor to falls in the elderly. The most common cause of balance dysfunction is due to abnormal hair cells from the vestibular sensory epithelia of the vestibular organ. Because of malfunction of kidneys in *Camsap3*-cKO mice, we were not able to investigate the impact of CAMSAP3 on the vestibular function in older mice due to their health issues. Different *Camsap3* transgenic mouse models without damaged kidneys may be needed to investigate impact of CAMSAP3 and the central MT pair of kinocilia on vestibular function. In addition, it might be worthwhile to examine the vestibulo-ocular reflex (VOR) of *Camsap3* transgenic mice using video-oculography. Video-oculography quantifies eye movement data to evaluate vestibular function, and could highlight vestibular issues that we were not able to capture in this study.

In summary, our data suggest that CAMSAP3 is critical for construction of the central MT pair in vestibular kinocilia, which may be essential for building long and stable axonemes in these kinocilia on vestibular hair cells. Whether abnormal vestibular kinocilia of *Camsap3*-cKO mice could directly lead to vestibular function requires further investigation.

DATA AVAILABILITY STATEMENT

The original contributions presented in this study are included in the article/**Supplementary Material**, further inquiries can be directed to the corresponding author.

ETHICS STATEMENT

The animal study was reviewed and approved by the Institutional Animal Care and Use Committees of Northwestern University.

AUTHOR CONTRIBUTIONS

JZ designed and performed some of the experiments and analyzed the data. JO'D performed some of the experiments and analyzed some of the data. JO'D and JZ wrote the manuscript. Both authors contributed to the article and approved the submitted version.

FUNDING

This work was supported by the American Hearing Research Foundation and a Hugh Knowles Leadership Fund Award to JZ. Gait Analysis was performed by the Northwestern University Behavioral Phenotyping Core. Imaging was conducted at the Northwestern University Center for Advanced Microscopy, which was supported by the NCI CCSG P30 CA060553. The re-derived *Camsap3*-KD line on the FVB murine background was conducted at Transgenic and Targeted Mutagenesis Laboratory of Northwestern University.

ACKNOWLEDGMENTS

We thank Alan M. Robinson, Satoe Takahashi, Yingjie Zhou, and Craig Weiss (Northwestern University) for their guidance and advice on several experiments, as well as MaryAnn Cheatham (Northwestern University) for creating *Camsap3*-cKO mice, and Jaime Garcia-Anoveros and Donna Whitlon (Northwestern University) for providing reagents.

SUPPLEMENTARY MATERIAL

The Supplementary Material for this article can be found online at: https://www.frontiersin.org/articles/10.3389/fncel.2022.876805/full#supplementary-material

REFERENCES

Akula, S. K., McCullough, K. B., Weichselbaum, C., Dougherty, J. D., and Maloney, S. E. (2020). The trajectory of gait development in mice. *Brain Behav*. 10:e01636. doi: 10.1002/brb3.1636

Andreu-Cervera, A., Catala, M., and Schneider-Maunoury, S. (2021). Cilia, ciliopathies and hedgehog-related forebrain developmental disorders. *Neurobiol. Disease* 150:105236. doi: 10.1016/j.nbd.2020.105236

Bernardes, D., and Oliveira, A. L. R. (2017). Comprehensive catwalk gait analysis in a chronic model of multiple sclerosis subjected to treadmill exercise training. *BMC Neurol*. 17:160. doi: 10.1186/s12883-017-0941-z

Berryman, E. R., Harris, R. L., Moalli, M., and Bagi, C. M. (2009). Digigait quantitation of gait dynamics in rat rheumatoid arthritis model. *J. Musculoskelet Neuronal. Interact*. 9, 89–98.

Brings, V. E., Payne, M. A., and Gereau, R. W. (2021). Paw placement during walking is altered by analgesic doses of opioids and post-surgical injury in mice. *bioRxiv* doi: 10.1101/2021.12.15.4728182012

Choksi, S. P., Lauter, G., Swoboda, P., and Roy, S. (2014). Switching on cilia: transcriptional networks regulating ciliogenesis. *Development* 141, 1427–1441. doi: 10.1242/dev.074666

Chu, V., and Anderson, L. (2020). Sensory-Processing Differences in ChildrenWith Idiopathic ToeWalking (ITW). *Am. J. Occup. Therapy* 74:74115051301. doi: 10.5014/ajot.2020.74S1-PO3205

Cox, B. C., Liu, Z., Lagarde, M. M., and Zuo, J. (2012). Conditional gene expression in the mouse inner ear using Cre-loxP. *J.Assoc. Res. Otolaryngol.* 13, 295–322. doi: 10.1007/s10162-012-0324-5

Deuis, J. R., Dvorakova, L. S., and Vetter, I. (2017). Methods Used to Evaluate Pain Behaviors in Rodents. *Front. Mole. Neurosci.* 10:284. doi: 10.3389/fnmol.2017.00284

Dunham, N. W., and Miya, T. S. (1957). A note on a simple apparatus for detecting neurological deficit in rats and mice. *J. Am. Pharm. Assoc. Am. Pharm. Assoc.* 46, 208–209. doi: 10.1002/jps.3030460322

Falk, N., Losl, M., Schroder, N., and Giessl, A. (2015). Specialized Cilia in Mammalian Sensory Systems. *Cells* 4, 500–519. doi: 10.3390/cells4030500

Furusawa, N., Baba, H., Imura, S., and Fukuda, M. (1996). Characteristics and mechanism of the ossification of posterior longitudinal ligament in the tip-toe walking Yoshimura (twy) mouse. *Eur. J. Histochem.* 40, 199–210.

Gibieža, P., Peterman, E., Hoffman, H. K., Engeleburg, S. V., Skeberdis, V. A., and Prekeris, R. (2021). Rab14/MACF2 complex regulates endosomal targeting during cytokinesis. *Mole. Biol.Cell* 32, 554–566. doi: 10.1091/mbc.E20-09-0607

Goodwin, S. S., and Vale, R. D. (2010). Patronin regulates the microtubule network by protecting microtubule minus ends. *Cell* 143, 263–274. doi: 10.1016/j.cell.2010.09.022

Griffioen, M. A., Dernetz, V. H., Yang, G. S., Griffith, K. A., Dorsey, S. G., and Renn, C. L. (2015). Evaluation of Dynamic Weight Bearing for Measuring Nonevoked Inflammatory Hyperalgesia in Mice. *Nurs. Res.* 64, 81–87. doi: 10.1097/NNR.0000000000000082

Hardisty-Hughes, R. E., Parker, A., and Brown, S. D. (2010). A hearing and vestibular phenotyping pipeline to identify mouse mutants with hearing impairment. *Nat. Protoc.* 5, 177–190. doi: 10.1038/nprot.2009.204

Heinzel, J., Swiadek, N., Ashmwe, M., Rührnößl, A., Oberhauser, V., Kolbenschlag, J., and Hercher, D. (2020). Automated gait analysis to assess functional recovery in rodents with peripheral nerve or spinal cord contusion injury. *J. Vis. Exp.* 164:e61852. doi: 10.3791/61852

Hickman, D. L., and Swan, M. (2010). Use of a body condition score technique to assess health status in a rat model of polycystic kidney disease. *J. Am. Assoc. Lab. Anim. Sci*. 49, 155–159.

Hughes, C. B., Bergstralh, E. J., Larson, T. S., Stegall, M. D., and Velosa, J. A. (1999). Kidney Weight (Kw) and Body Weight (Bw) Ratios Predict Glomerular Filtration Rate (GFR) in Transplant Recipients. *Transplantation* 67:S156. doi: 10.1097/00007890-199904150-00626

Ingham, N. J., Pearson, S. A., Vancollie, V. E., Rook, V., Lewis, M. A., Chen, J., et al. (2019). Mouse screen reveals multiple new genes underlying mouse and human hearing loss. *PLoS Biol.* 17:e3000194. doi: 10.1371/journal.pbio.3000194

Jiang, K., Faltova, L., Hua, S., Capitani, G., Prota, A. E., Landgraf, C., et al. (2018). Structural Basis of Formation of the Microtubule Minus-End-Regulating CAMSAP-Katanin Complex. *Structure* 26, 375–382.e4. doi: 10.1016/j.str.2017.12.017

Jiang, K., Hua, S., Mohan, R., Grigoriev, I., Yau, K. W., Liu, Q., et al. (2014). Microtubule minus-end stabilization by polymerization-driven CAMSAP deposition. *Dev. Cell* 28, 295–309. doi: 10.1016/j.devcel.2014.01.001

Jones, S. M., and Jones, T. A. (2014). Genetics of peripheral vestibular dysfunction: lessons from mutant mouse strains. *J. Am. Acad. Audiol*. 25, 289–301. doi: 10.3766/jaaa.25.3.8

Jones, S. M., Vijayakumar, S., Dow, S. A., Holt, J. C., Jordan, P. M., and Luebke, A. E. (2018). Loss of α-Calcitonin Gene-Related Peptide (αCGRP) Reduces Otolith Activation Timing Dynamics and Impairs Balance. *Front. Mole. Neurosci.* 11:289. doi: 10.3389/fnmol.2018.00289

Kanki, H., Suzuki, H., and Itohara, S. (2006). High-efficiency CAG-FLPe deleter mice in C57BL/6J background. *Exp. Anim*. 55, 137–141. doi: 10.1538/expanim.55.137

Kopecky, B., Decook, R., and Fritzsch, B. (2012). Mutational ataxia resulting from abnormal vestibular acquisition and processing is partially compensated for. *Behav. Neurosci*. 126, 301–313. doi: 10.1037/a0026896

Lechtreck, K. F., Gould, T. J., and Witman, G. B. (2013). Flagellar central pair assembly in Chlamydomonas reinhardtii. *Cilia* 2:15. doi: 10.1186/2046-2530-2-15

Lee, J. E., and Gleeson, J. G. (2011). A systems-biology approach to understanding the ciliopathy disorders. *Genome Med*. 3:59. doi: 10.1186/gm275

Lee, L., and Ostrowski, L. E. (2021). Motile cilia genetics and cell biology: big results from little mice. *Cell. Mole. Life Sci.* 78, 769–797. doi: 10.1007/s00018-020-03633-5

Loreng, T. D., and Smith, E. F. (2017). The Central Apparatus of Cilia and Eukaryotic Flagella. *Cold Spring Harb. Perspect Biol.* 9:a028118. doi: 10.1101/cshperspect.a028118

Lu, Y.-C., Wu, C.-C., Shen, W.-S., Yang, T.-H., Yeh, T.-H., Chen, P.-J. I, et al. (2011). Establishment of a knock-in mouse model with the SLC26A4 c.919-2A>G mutation and characterization of its pathology. *PloS one*. 6, e22150–e22150. doi: 10.1371/journal.pone.0022150

Mathur, P. D., Vijayakumar, S., Vashist, D., Jones, S. M., Jones, T. A., and Yang, J. (2015). A study of whirlin isoforms in the mouse vestibular system suggests potential vestibular dysfunction in DFNB31-deficient patients. *Hum. Mole. Gene*. 24, 7017–7030. doi: 10.1093/hmg/ddv403

Mbiene, J. P., Favre, D., and Sans, A. (1984). The pattern of ciliary development in fetal mouse vestibular receptors. A qualitative and quantitative SEM study. *Anat Embryol*. 170, 229–238. doi: 10.1007/BF00318726

Meng, W., Mushika, Y., Ichii, T., and Takeichi, M. (2008). Anchorage of microtubule minus ends to adherens junctions regulates epithelial cell-cell contacts. *Cell* 135, 948–959. doi: 10.1016/j.cell.2008.09.040

Mitsuhata, Y., Abe, T., Misaki, K., Nakajima, Y., Kiriya, K., Kawasaki, M., et al. (2021). Cyst formation in proximal renal tubules caused by dysfunction of the microtubule minus-end regulator CAMSAP3. *Sci. Rep*. 11:5857. doi: 10.1038/s41598-021-85416-x

Montgomery, P., and Gauger, J. (1978). Sensory Dysfunction in Children Who Toe Walk. *Physical. Therapy*. 58, 1195–1204. doi: 10.1093/ptj/58.10.1195

Moskovitz, J., Bar-Noy, S., Williams, W. M., Requena, J., Berlett, B. S., and Stadtman, E. R. (2001). Methionine sulfoxide reductase (MsrA) is a regulator of antioxidant defense and lifespan in mammals. *Proc.Nat. Acad. Sci.U. S. A*. 98, 12920–12925. doi: 10.1073/pnas.231472998

Muroyama, A., Terwilliger, M., Dong, B., Suh, H., and Lechler, T. (2018). Genetically induced microtubule disruption in the mouse intestine impairs intracellular organization and transport. *Mole. Biol. Cell* 29, 1533–1541. doi: 10.1091/mbc.E18-01-0057

Nam, J. H. (2018). An operating principle of the turtle utricle to detect wide dynamic range. *Hearing Res.* 360, 31–39. doi: 10.1016/j.heares.2017.09.015

Neumann, M., Wang, Y., Kim, S., Hong, S. M., Jeng, L., Bilgen, M., et al. (2009). Assessing gait impairment following experimental traumatic brain injury in mice. *J. Neurosci. Met*. 176, 34–44. doi: 10.1016/j.jneumeth.2008.08.026

Ohyama, T., and Groves, A. K. (2004). Generation of Pax2-Cre mice by modification of a Pax2 bacterial artificial chromosome. *Genesis* 38, 195–199. doi: 10.1002/gene.20017

Okawa, A., Nakamura, I., Goto, S., Moriya, H., Nakamura, Y., and Ikegawa, S. (1998). Mutation in Npps in a mouse model of ossification of the posterior longitudinal ligament of the spine. *Nat. Gene*. 19, 271–273. doi: 10.1038/956

Palit, S., and Kendrick, J. (2014). Vascular calcification in chronic kidney disease: role of disordered mineral metabolism. *Curr. Pharm. Design*. 20, 5829–5833. doi: 10.2174/1381612820666140212194926

Pan, N., Jahan, I., Kersigo, J., Kopecky, B., Santi, P., Johnson, S., et al. (2011). Conditional deletion of Atoh1 using Pax2-Cre results in viable mice without differentiated cochlear hair cells that have lost most of the organ of Corti. *Hearing Res*. 275, 66–80. doi: 10.1016/j.heares.2010.12.002

Pau, H., Hawker, K., Fuchs, H., De Angelis, M. H., and Steel, K. P. (2004). Characterization of a new mouse mutant, flouncer, with a balance defect and inner ear malformation. *Otol Neurotol*. 25, 707–713. doi: 10.1097/00129492-200409000-00010

Perez-Garcia, V., Fineberg, E., Wilson, R., Murray, A., Mazzeo, C. I., Tudor, C., et al. (2018). Placentation defects are highly prevalent in embryonic lethal mouse mutants. *Nature* 555, 463–468. doi: 10.1038/nature26002

Piorunek, T., Marszalek, A., Biczysko, W., Gozdzik, J., Cofta, S., and Seget, M. (2008). Correlation between the stage of cystic fibrosis and the level of morphological changes in adult patients. *J. Physiol. Pharmacol*. 59, 565–572.

Rahn, R. M., Weichselbaum, C. T., Gutmann, D. H., Dougherty, J. D., and Maloney, S. E. (2021). Shared developmental gait disruptions across two mouse models of neurodevelopmental disorders. *J. Neurodev. Disorders*. 13:10. doi: 10.1186/s11689-021-09359-0

Reiter, J. F., and Leroux, M. R. (2017). Genes and molecular pathways underpinning ciliopathies. *Nat. Rev. Mole. Cell Biol*. 18, 533–547. doi: 10.1038/nrm.2017.60

Robinson, A. M., Takahashi, S., Brotslaw, E. J., Ahmad, A., Ferrer, E., Procissi, D., et al. (2020). CAMSAP3 facilitates basal body polarity and the formation of the central pair of microtubules in motile cilia. *Proc.Nat. Acad. Sci. U. S. A*. 117, 13571–13579. doi: 10.1073/pnas.1907335117

Rosenhall, U., and Engstrom, B. (1974). Surface Structures of the Human Vestibular Sensory Regions. *Acta oto-Laryngologica*. 77, 3–18. doi: 10.1080/16512251.1974.11675749

Rostosky, C. M., and Milosevic, I. (2018). Gait analysis of age-dependent motor impairments in mice with neurodegeneration. *J. Vis. Exp*. 136:57752. doi: 10.3791/57752

Saito, H., Matsukawa-Usami, F., Fujimori, T., Kimura, T., Ide, T., Yamamoto, T., et al. (2021). Tracheal motile cilia in mice require CAMSAP3 for the formation of central microtubule pair and coordinated beating. *Mole. Biol. Cell*. 32:ar12. doi: 10.1091/mbc.E21-06-0303

Sekerka, G., Richter, C.-P., and Bartles, J. (2011). Roles of the Espin Actin-Bundling Proteins in the Morphogenesis and Stabilization of Hair Cell Stereocilia Revealed in CBA/CaJ Congenic Jerker Mice. *PLoS Gene*. 7:e1002032. doi: 10.1371/journal.pgen.1002032

Skarnes, W. C., Rosen, B., West, A. P., Koutsourakis, M., Bushell, W., Iyer, V., et al. (2011). A conditional knockout resource for the genome-wide study of mouse gene function. *Nature* 474, 337–342. doi: 10.1038/nature10163

Sobkowicz, H. M., Slapnick, S. M., and August, B. K. (1995). The kinocilium of auditory hair cells and evidence for its morphogenetic role during the regeneration of stereocilia and cuticular plates. *J. Neurocytol*. 24, 633–653. doi: 10.1007/BF01179815

Spoon, C., and Grant, W. (2011). Biomechanics of hair cell kinocilia: experimental measurement of kinocilium shaft stiffness and base rotational stiffness with Euler-Bernoulli and Timoshenko beam analysis. *J. Exp. Biol*. 214, 862–870. doi: 10.1242/jeb.051151

Spoon, C., and Grant, W. (2013). Biomechanical measurement of kinocilium. *Met. Enzymol*. 525, 21–43. doi: 10.1016/B978-0-12-397944-5.00002-X

Takahashi, S., Mui, V. J., Rosenberg, S. K., Homma, K., Cheatham, M. A., and Zheng, J. (2016). Cadherin 23-C Regulates Microtubule Networks by Modifying CAMSAP3's Function. *Sci. Rep*. 6, 28706. doi: 10.1038/srep28706

Tanaka, N., Meng, W., Nagae, S., and Takeichi, M. (2012). Nezha/CAMSAP3 and CAMSAP2 cooperate in epithelial-specific organization of noncentrosomal microtubules. *Proc.Nat. Acad. Sci.U. S. A*. 109, 20029–20034. doi: 10.1073/pnas.1218017109

Testa, G., Schaft, J., van der Hoeven, F., Glaser, S., Anastassiadis, K., Zhang, Y., et al. (2004). A reliable lacZ expression reporter cassette for multipurpose, knockout-first alleles. *Genesis*. 38, 151–158. doi: 10.1002/gene.20012

Toya, M., Kobayashi, S., Kawasaki, M., Shioi, G., Kaneko, M., Ishiuchi, T., et al. (2016). CAMSAP3 orients the apical-to-basal polarity of microtubule arrays in epithelial cells. *Proc.Nat. Acad. Sci.U. S. A*. 113, 332–337. doi: 10.1073/pnas.1520638113

Wersall, J., Flock, A., and Lundquist, P. G. (1965). Structural basis for directional sensitivity in cochlear and vestibular sensory receptors. *Cold Spring Harb. Symp. Quant. Biol*. 30, 115–132. doi: 10.1101/SQB.1965.030.01.015

White, J. K., Gerdin, A. K., Karp, N. A., Ryder, E., Buljan, M., Bussell, J. N., et al. (2013). Genome-wide generation and systematic phenotyping of knockout mice reveals new roles for many genes. *Cell* 154, 452–464. doi: 10.1016/j.cell.2013.06.022

Wiwatpanit, T., Lorenzen, S. M., Cantú, J. A., Foo, C. Z., Hogan, A. K., Márquez, F., et al. (2018). Trans-differentiation of outer hair cells into inner hair cells in the absence of INSM1. *Nature*. 563, 691–695. doi: 10.1038/s41586-018-0570-8

Xue, J., and Peterson, E. H. (2006). Hair bundle heights in the utricle: differences between macular locations and hair cell types. *J. Neurophysiol*. 95, 171–186. doi: 10.1152/jn.00800.2005

Yang, M., and Crawley, J. N. (2009). Simple behavioral assessment of mouse olfaction. *Curr. Protoc. Neurosci*. 8:8.24. doi: 10.1002/0471142301.ns0824s48

Zenker, J., White, M. D., Templin, R. M., Parton, R. G., Thorn-Seshold, O., Bissiere, S., et al. (2017). A microtubule-organizing center directing intracellular transport in the early mouse embryo. *Science* 357, 925–928. doi: 10.1126/science.aam9335

Zheng, J., Furness, D., Duan, C., Miller, K. K., Edge, R. M., Chen, J., et al. (2013). Marshalin, a microtubule minus-end binding protein, regulates cytoskeletal structure in the organ of Corti. *Biol. Open* 2, 1192–1202. doi: 10.1242/bio.20135603

Conflict of Interest: The authors declare that the research was conducted in the absence of any commercial or financial relationships that could be construed as a potential conflict of interest.

frontiers | Frontiers in Cellular Neuroscience

TYPE Original Research
PUBLISHED 16 September 2022
DOI 10.3389/fncel.2022.841864

Regenerated hair cells in the neonatal cochlea are innervated and the majority co-express markers of both inner and outer hair cells

Mitchell L. Heuermann[1], Sophia Matos[1,2], Deborah Hamilton[2] and Brandon C. Cox[1,2]*

[1]Department of Otolaryngology, Southern Illinois University School of Medicine, Springfield, IL, United States, [2]Department of Pharmacology, Southern Illinois University School of Medicine, Springfield, IL, United States

OPEN ACCESS

EDITED BY
Bernd Fritzsch,
The University of Iowa, United States

REVIEWED BY
Patricia White,
University of Rochester Medical Center, United States
Alan G. Cheng,
Stanford University, United States
Guoqiang Wan,
Nanjing University, China

*CORRESPONDENCE
Brandon C. Cox
bcox@siumed.edu

SPECIALTY SECTION
This article was submitted to Non-Neuronal Cells, a section of the journal Frontiers in Cellular Neuroscience

RECEIVED 22 December 2021
ACCEPTED 29 August 2022
PUBLISHED 16 September 2022

CITATION
Heuermann ML, Matos S, Hamilton D and Cox BC (2022) Regenerated hair cells in the neonatal cochlea are innervated and the majority co-express markers of both inner and outer hair cells. *Front. Cell. Neurosci.* 16:841864. doi: 10.3389/fncel.2022.841864

After a damaging insult, hair cells can spontaneously regenerate from cochlear supporting cells within the first week of life. While the regenerated cells express several markers of immature hair cells and have stereocilia bundles, their capacity to differentiate into inner or outer hair cells, and ability to form new synaptic connections has not been well-described. In addition, while multiple supporting cell subtypes have been implicated as the source of the regenerated hair cells, it is unclear if certain subtypes have a greater propensity to form one hair cell type over another. To investigate this, we used two CreER mouse models to fate-map either the supporting cells located near the inner hair cells (inner phalangeal and border cells) or outer hair cells (Deiters', inner pillar, and outer pillar cells) along with immunostaining for markers that specify the two hair cell types. We found that supporting cells fate-mapped by both CreER lines responded early to hair cell damage by expressing Atoh1, and are capable of producing regenerated hair cells that express terminal differentiation markers of both inner and outer hair cells. The majority of regenerated hair cells were innervated by neuronal fibers and contained synapses. Unexpectedly, we also found that the majority of the laterally positioned regenerated hair cells aberrantly expressed both the outer hair cell gene, oncomodulin, and the inner hair cell gene, vesicular glutamate transporter 3 (VGlut3). While this work demonstrates that regenerated cells can express markers of both inner and outer hair cells after damage, VGlut3 expression appears to lack the tight control present during embryogenesis, which leads to its inappropriate expression in regenerated cells.

KEYWORDS

hair cell regeneration, inner hair cells, outer hair cells, hair cell development, fate mapping, oncomodulin, VGlut3

Introduction

The organ of Corti, located within the cochlea of the inner ear, contains the intricate anatomy required for hearing. It is comprised of three rows of outer hair cells, one row of inner hair cells, various supporting cell subtypes, and innervating fibers of spiral ganglion neurons. Whereas inner hair cells act as mechanoelectric transducers that encode sound waves into spiral ganglion neuronal action potentials, outer hair cells amplify sound input to increase frequency specificity and the dynamic range of hearing (reviewed in Dallos, 2008). Both types of hair cells form afferent synaptic connections with spiral ganglion neurons, although these differ in function and number. Each inner hair cell forms synapses with multiple type I afferent spiral ganglion neurons (Liberman, 1980; Bohne et al., 1982; Stamataki et al., 2006), although each type I afferent will synapse with only one inner hair cell (Spoendlin, 1969; Kiang et al., 1982; Liberman, 1982). Type I neurons are responsible for carrying action potentials toward the ascending auditory pathway (Reijntjes and Pyott, 2016). Type II spiral ganglion neurons form synapses with outer hair cells (Huang et al., 2012; Martinez-Monedero et al., 2016; Elliott et al., 2021). Although their function is less understood, they are proposed to have a nociceptive function in response to mechanical or noise trauma (Weisz et al., 2009; Flores et al., 2015; Liu et al., 2015).

Hearing loss is multifactorial and can include insults from noise exposure, aging, genetic disorders, and ototoxic drugs. It is among the most prevalent diseases, with an estimated 1.5 billion individuals affected (Gbd 2019 Hearing Loss Collaborators, 2021). Because of this, there has been a keen interest in treating or reversing hearing loss. As most forms of hearing damage culminate with the loss of hair cells, much of this research has focused on regenerating new hair cells. While the mammalian cochlea can spontaneously regenerate its hair cells at neonatal ages (White et al., 2006; Bramhall et al., 2014; Cox et al., 2014; Hu et al., 2016), no regeneration occurs after the first postnatal week (Oesterle et al., 2008; Cox et al., 2014; Maass et al., 2015).

A number of studies have demonstrated that supporting cells act as the progenitor cells that form new hair cells during regeneration using two mechanisms. First, with direct transdifferentiation, a supporting cell changes fate to a hair cell without leaving quiescence. Second, with mitotic regeneration, a supporting cell divides, and one or both daughter cells differentiate into hair cells (Rubel et al., 2013; Bramhall et al., 2014; Cox et al., 2014). At least eight subtypes of supporting cells have been identified in the mammalian cochlea, including Claudius cells, Hensen's cells, Deiters' cells, inner and outer pillar cells, inner phalangeal cells, border cells and greater epithelial ridge cells (Raphael and Altschuler, 2003; Jahan et al., 2015). Available evidence suggest that multiple supporting cell subtypes are capable of regenerating hair cells, although it is debated whether certain subtypes have a greater propensity over others (Bramhall et al., 2014; McGovern et al., 2019). In addition, two studies have shown that regenerated hair cells can differentiate into an outer hair cell fate (Bramhall et al., 2014; Cox et al., 2014); yet it is unknown how many reach terminal differentiation and whether inner hair cells can also be replaced. Furthermore, while regenerated hair cells formed in non-mammalian vertebrates contain synapses and are innervated (Duckert and Rubel, 1990; Ryals and Westbrook, 1994), the capacity for innervation in regenerated hair cells in mammals has not been explored. Each of these questions is of vital importance to understand the extent to which spontaneous regeneration drives cochlear repair.

Here, we investigated the terminal differentiation and innervation of regenerated hair cells in the neonatal mouse cochlea using CreER mouse models to fate-map either the supporting cells surrounding inner hair cells (inner phalangeal and border cells) or those that neighbor outer hair cells (Deiters', inner pillar, and outer pillar cells). We found that supporting cells fate-mapped by both CreER lines were capable of producing regenerated hair cells that expressed terminal differentiation markers of inner and outer hair cells, the majority of which were innervated by neuronal fibers and contained synapses. In addition, the majority of regenerated cells in the lateral compartment (where outer hair cells are normally located) showed aberrant expression of both oncomodulin (an outer hair cell marker) and vesicular glutamate transporter 3 (VGlut3) (an inner hair cell marker).

Results

To investigate whether different supporting cells subtypes can produce regenerated cells that differentiate into inner or outer hair cell fates, we used two CreER lines (*Prox1*^{CreERT2} and *Plp-CreER*^{T}) that were paired with the reporter, *Rosa26*$^{CAG-loxP-stop-loxP-tdTomato}$ (*Rosa26*^{tdTomato}) for fate-mapping. When injected with tamoxifen at postnatal day (P) 0, *Prox1*^{CreERT2}:*Rosa26*^{tdTomato} mice have previously been shown to selectively label inner pillar (~33%), outer pillar (~78%), and Deiters' (~78%) cells (**Figures 1A,C–C"**; Yu et al., 2010; Liu et al., 2012; McGovern et al., 2017), while *Plp-CreER*^{T}:*Rosa26*^{tdTomato} mice primarily labeled inner phalangeal and border cells (~73%), as well as a small number of inner pillar (~7%), outer pillar (~9%), and Deiters' cells (~11%) (**Figures 1B,D–D"**; Gómez-Casati et al., 2010; McGovern et al., 2017). These two lines (*Prox1*^{CreERT2}:*Rosa26*^{tdTomato} and *Plp-CreER*^{T}:*Rosa26*^{tdTomato}) were then crossed with *Pou4f3*^{DTR} mice which express the human diphtheria toxin receptor (DTR) specifically in hair cells using the *Pou4f3* promoter. Administration of diphtheria toxin (DT) to mice carrying the *Pou4f3*^{DTR} allele then leads to selective hair cell death. *Prox1*^{CreERT2}:*Rosa26*^{tdTomato}:*Pou4f3*^{DTR} and *Plp-CreER*^{T}:*Rosa26*^{tdTomato}:*Pou4f3*^{DTR} mice (referred to hereafter as *DTR:Prox1*^{CreERT2} and *DTR:Plp-CreER*^{T}) served as the experimental groups, while their littermates lacking the *Pou4f3*^{DTR} allele (and therefore not susceptible to DT-induced hair cell damage) were used as controls. All mice were injected with tamoxifen (3 mg/40 g, intraperitoneally) on P0, thereby inducing tdTomato expression in the specific supporting cell subtypes described above and with DT (6.25 ng/g, intramuscularly) on P1 to cause selective death of the hair cells and induce subsequent hair cell regeneration, as previously described (Cox et al., 2014). Cochleae were harvested on P3-P10 and the entire organ of Corti was analyzed from apex to base using immunostaining and confocal microscopy. To identify regenerated cells that differentiated toward either an inner or outer hair cell fate, we labeled all hair cells using anti-myosin VIIA (Myo7A) antibodies and used additional antibodies that were specific to inner or outer hair cells. Regenerated hair cells (Myo7a-positive) were identified based on tdTomato expression, which was controlled by the supporting cell-specific CreER lines. In *Plp-CreER*^{T} control samples at P7, we observed an average of 1.6 ± 0.8 tdTomato-positive outer hair cells and 0.4 ± 0.4 tdTomato-positive inner hair cells (n = 5), whereas *Prox1*^{CreERT2} controls had an average of 13.4 ± 1.7 tdTomato-positive outer hair cells and no tdTomato-positive inner hair cells (n = 7). All tdTomato-positive hair cells in control samples were located almost exclusively at apical-most portion of each cochlea. Similar to previous reports (Cox et al., 2014; McGovern et al., 2019), the vast majority of the regenerate HCs (tdTomato-positive/Myo7a-positive cells) were located in the apical turn.

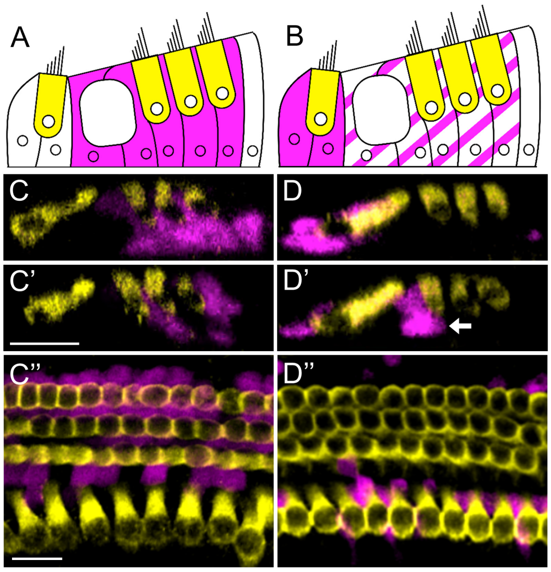

FIGURE 1
Prox1^{CreERT2} and *Plp-CreER*^{T} label different groups of cochlear supporting cell subtypes. **(A,B)** Illustration of a cochlear cross-section with one row of inner and three rows of outer hair cells (yellow) and tdTomato-positive (magenta) supporting cells labeled by *Prox1*^{CreERT2} **(A)** or *Plp-CreER*^{T} **(B)**. **(C–D'')** Representative images from the apical turn of *Prox1*^{CreERT2}*:Rosa26*^{tdTomato} **(C–C'')** and *Plp-CreER*^{T}*:Rosa26*^{tdTomato} **(D–D'')** mice at P7. All mice were injected with tamoxifen at P0 to induce tdTomato expression in various groups of supporting cells. Samples were immunostained with anti-Myo7a (yellow) to label all hair cells, and tdTomato was detected using endogenous fluorescence (magenta). *Prox1*^{CreERT2} labels primarily pillar and Deiters' cells **(A,C–C'')**, whereas *Plp-CreER*^{T} labels primarily inner phalangeal and border cells (solid magenta in **B**), along with a small number of pillar and Deiters' cells (striped magenta in **B**) **(B,D–D'')**. White arrow **(D')** indicates an outer pillar cell labeled by *Plp-CreER*^{T}. Panels **(C–D')** are optical cross-sections and panels **(C''–D'')** are top-down views. All scale bars: 20 μm.

A large number of supporting cells respond to hair cell damage by expressing Atoh1, but only a fraction of these cells mature to express myosin VIIA

We first sought to compare the response to hair cell damage among supporting cell subtypes using expression of *Atoh1*, the first known gene to be turned on in a cell differentiating into a hair cell fate (Bermingham et al., 1999). *DTR:Prox1*^{CreERT2} and *DTR:Plp-CreER*^{T} mice were bred with *Atoh1*$^{GFP/+}$ mice, which is a knock-in reporter line that creates an ATOH1-GFP fusion protein (Rose et al., 2009). Both groups were treated with tamoxifen on P0 and DT on P1, and temporal bones were collected on P3. Endogenous GFP fluorescence was augmented with anti-GFP antibodies. In control *Prox1*^{CreERT2} and *Plp-CreER*^{T} samples at P3, Atoh1 expression was seen exclusively in Myo7a-positive hair cells, with only three Atoh1-positive supporting cells observed among three control cochleae (**Figures 2A–A'''**). Next, we examined experimental mice that had hair cell damage to quantify tdTomato-positive supporting cells that expressed ATOH1-GFP, but lacked the more mature hair cell marker, Myo7a (**Figures 2B–C'''**). At P3, there was a larger number of supporting cells that expressed ATOH1-GFP after hair cell damage in *DTR:Plp-CreER*^{T} mice (162.8 ± 11.7, n = 5) compared to *DTR:Prox1*^{CreERT2} mice (125.4 ± 7.8, n = 5, p = 0.0031 determined using a two-way ANOVA followed by a Sidak's *post-hoc* test) (**Figure 2D**). When converted to a percentage (using the total number of Tomato-positive supporting cells from each CreER line), only 13.2 ± 0.9% of the Cre-positive supporting cells in *DTR:Plp-CreER*^{T} mice and 5.3 ± 0.3% of the Cre-positive supporting cells in *DTR:Prox1*^{CreERT2} mice expressed Atoh1-GFP (n = 5; **Figure 2E**). However comparing across cochlear turns, *DTR:Prox1*^{CreERT2} mice showed a decreasing gradient of Atoh1-GFP-positive/Tomato-positive cells from apex to base (74.4 ± 7.9 in apex, 41.4 ± 5.8 in middle, and 9.6 ± 2.6 in base, n = 5, p = 0.0051 determined using a two-way ANOVA followed by a Sidak's *post-hoc* test), but there was no difference among turns in the *DTR:Plp-CreER*^{T} mice (**Figure 2E**). This may

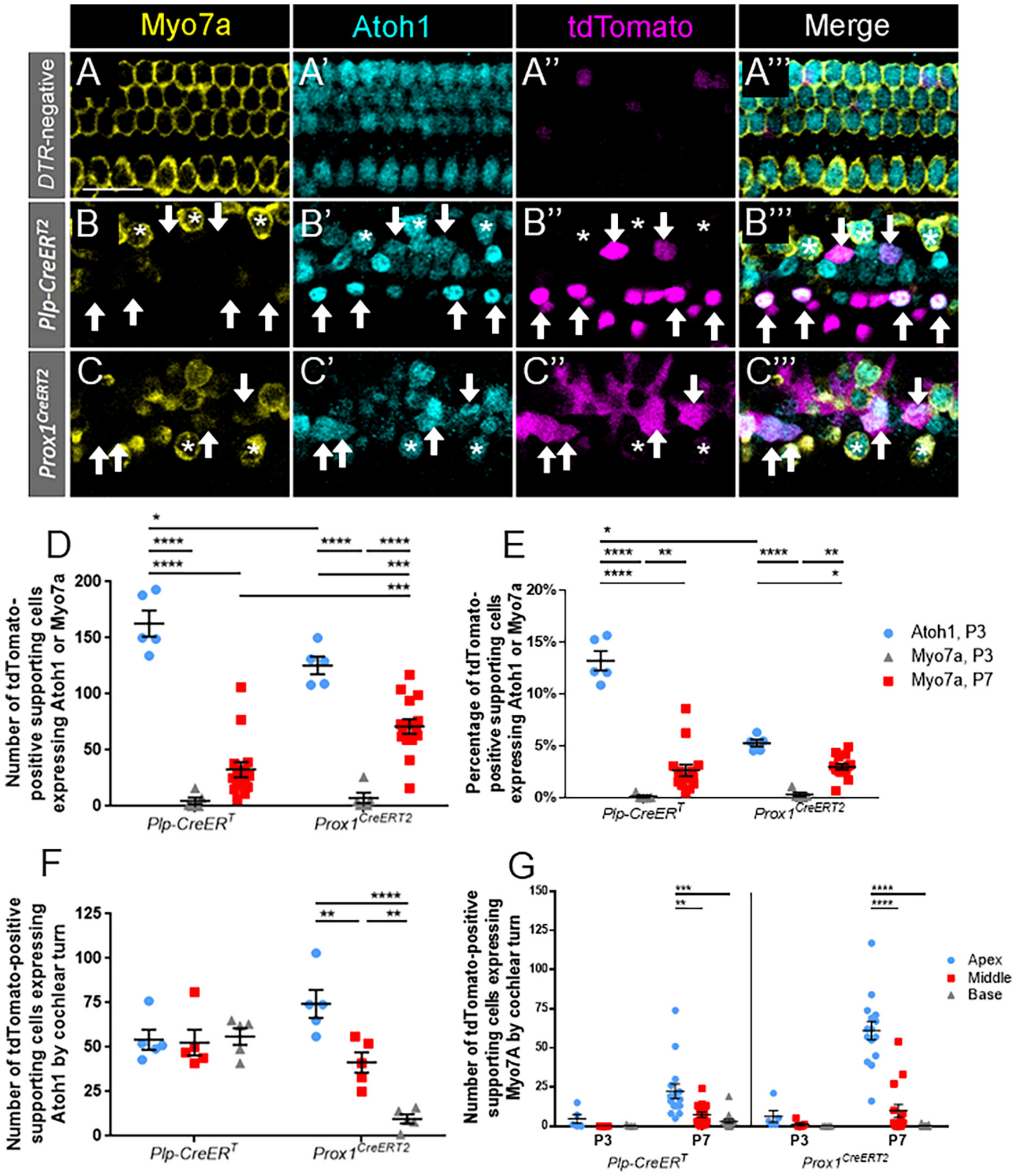

FIGURE 2

A significant proportion of Atoh1-positive supporting cells at P3 do not mature to Myo7a-positive regenerated hair cells by P7. **(A–C''')** Representative confocal slice images from the apical turn of *Atoh1*$^{GFP/+}$ **(A–A''')**, *Plp-CreER*^{T}*:Rosa26*^{tdTomato}*:Pou4f3*^{DTR}*:Atoh1*$^{GFP/+}$ **(B–B''')** and *Prox1*^{CreERT2}*:Rosa26*^{tdTomato}*:Pou4f3*^{DTR}*:Atoh1*$^{GFP/+}$ **(C–C''')** mice at P3. All mice were injected with tamoxifen at P0 to induce tdTomato expression in various groups of supporting cells and with DT at P1 to induce hair cell damage. Samples were immunostained with anti-Myo7a antibodies (yellow) to label all hair cells and anti-GFP antibodies (blue) to detect Atoh1 expression as an early marker of hair cell conversion. tdTomato was detected using endogenous fluorescence (magenta). Arrows indicate Atoh1-positive/Myo7a-negative/tdTomato -positive fate-mapped supporting cells. Asterisks indicate Myo7a-positive/tdTomato-negative cells that are hair cells which survived the DT-mediated damage. Note that in controls all Atoh1-postive cells also expressed Myo7a. Scale bars: 25 μm. **(D)** The supporting cell populations fate-mapped by *Plp-CreER*^{T} produced significantly more cells expressing Atoh1 than those fate-mapped by *Prox1*^{CreERT2}. A significant number of the hair cell progenitors from both populations of supporting cells did not mature to Myo7a-positive regenerated hair cells by P7, although the number of Myo7a-positive regenerated hair cells present at P7 was significantly greater for in the *Prox1*^{CreERT2} group compared the *Plp-CreER*^{T} group. **(E)** Data from panel **(D)** normalized to the total number of Tomato-positive supporting cells in each mouse model. **(F)** When stratified by cochlear turn at P3, there were similar numbers of Atoh1-positive, *Plp-CreER*^{T}-positive supporting cells in each turn, but there was a decreasing gradient of Atoh1-positive, *Prox1*^{CreERT2}-positive supporting cells from apex to base. **(G)** Supporting cell populations in both CreER lines produced significantly more regenerated hair cells in the apex compared to the middle and basal turns at P7, but there were no differences across cochlear turns at P3. Data are presented as mean ± SEM for $n = 5–15$. *$p < 0.05$; **$p < 0.01$; ***$p < 0.001$; ****$p < 0.0001$ determined using two-way ANOVA with a Sidak's *post-hoc* test.

suggest that supporting cells in the medial compartment remain plastic for a longer time period than the lateral supporting cells. Also at P3, a similar, but very small number of cells co-expressed tdTomato and Myo7a in both CreER lines (4.8 ± 3.1 for *Plp-CreER*^{T} vs. 7.4 ± 4.7 for *Prox1*^{CreERT}, $n = 5$; **Figure 2D**), which is less than 0.5% of the total Tomato-positive supporting cells in each CreER line ($n = 5$; **Figure 2E**).

We then determined the number of tdTomato-positive supporting cells that progressed to express Myo7a at P7 (**Figure 2D**). Numbers of regenerating, Myo7a-positive/Tomato-positive hair cells fate-mapped by *Prox1*^{CreERT2} were two-fold greater than those fate-mapped by *Plp-CreER*^{T} at P7 (71.1 ± 6.5 vs. 32.7 ± 6.8, $n = 15$, $p < 0.0001$ determined using a two-way ANOVA followed by a Sidak's *post-hoc* test). When converted to a percentage, this accounts for ~2.5–3% of the Tomato-positive supporting cells in each CreER line ($n = 5$; **Figure 2E**). When comparing across cochlear turns, both *DTR:Plp-CreER*^{T} and *DTR:Prox1*^{CreERT2} mice showed a decreasing gradient of Myo7a-positive/Tomato-positive cells from apex to base (*DTR:Plp-CreER*^{T}: 22.3 ± 4.7 in apex, 7.3 ± 1.7 in middle, and 3.1 ± 1.2 in base, $n = 15$, $p = 0.003$; *DTR:Prox1*^{CreERT2}: 61.1 ± 5.9 in apex, 9.8 ± 4.1 in middle, and 0.2 ± 0.1 in base; $n = 15$, $p < 0.0001$ determined using a two-way ANOVA followed by a Sidak's *post-hoc* test) (**Figure 2G**). Compared to the number of ATOH1-GFP-positive supporting cells at P3, cells expressing tdTomato and Myo7a at P7 were 2–4 fold less in both models (162.8 ± 11.7 ATOH1-GFP/tdTomato, $n = 5$ vs. 32.7 ± 6.8 Myo7a/tdTomato, $n = 15$ for *Plp-CreER*^{T}, $p < 0.0001$, and 125.4 ± 7.8 ATOH1-GFP/tdTomato, $n = 5$ vs. 71.1 ± 6.5 Myo7a/tdTomato, $n = 15$ for *Prox1*^{CreERT2}, $p < 0.0001$ determined using a two-way ANOVA followed by a Sidak's *post-hoc* test) (**Figure 2D**). This suggests that a significant number of supporting cells respond to hair cell damage by expressing Atoh1, but they have not yet completed the transdifferentiation process by P7.

Oncomodulin expression is seen in a similar number and percentage of regenerated hair cells derived from all supporting cell subtypes

To identify immature outer hair cells, cochlear sections were costained with oncomodulin (also called parvalbumin-β) and Myo7a. Oncomodulin is a calcium binding protein that has been previously shown to be selectively expressed in immature outer hair cells beginning as early as P2 (Hackney, 2005; Simmons et al., 2010; Tong et al., 2016). In control *Prox1*^{CreERT2} and *Plp-CreER*^{T} samples at P7, oncomodulin expression was specific to outer hair cells, with only one oncomodulin-positive inner hair cell observed among three control cochleae, and no expression detected in supporting cells (**Figures 3A–A'''**). Robust oncomodulin expression was also seen at P7 in regenerated hair cells (tdTomato-positive/Myo7a-positive) fate-mapped by both CreER lines (**Figures 3B–C'''**). There were no Tomato-positive/Myo7a-negative cells that expressed oncomodulin in any of the control or experimental samples. Quantification of total numbers of oncomodulin-positive regenerated hair cells (tdTomato-positive/Myo7a-positive) were similar for both CreER lines (**Figure 3D**; 32.2 ± 4.7 for *DTR:Prox1*^{CreERT2} vs. 33.6 ± 16.9 for *DTR:Plp-CreER*^{T}, $n = 5$, determined using an unpaired Student's *t*-test), and remained similar when the counts were normalized to the total number of regenerated hair cells (tdTomato-positive/Myo7a-positive) in each sample (**Figure 3E**; 66.0 ± 7.1% for *DTR:Prox1*^{CreERT2} vs. 42.7 ± 14.7% for *DTR:Plp-CreER*^{T}, $n = 5$, determined using an unpaired Student's *t*-test). This suggests that both subsets of supporting cells have an equivalent capacity to differentiate toward an outer hair cell fate.

Prestin expression increases with age and becomes proportionally higher in regenerated hair cells derived from lateral compartment supporting cells

To identify terminally differentiated outer hair cells, cochlear sections were costained with prestin and Myo7a. Prestin, the cytoplasmic motor protein important for the cochlear amplifier function, has been previously shown to be a reliable marker for mature outer hair cells, and it is not expressed in supporting cells or inner hair cells (Liberman et al., 2002; Fang et al., 2012; Bramhall et al., 2014; Cox et al., 2014). Previous work demonstrated that some spontaneously regenerated hair cells in the neonatal cochlea can express prestin (Bramhall et al., 2014; Cox et al., 2014).

Like oncomodulin, prestin was specifically expressed in outer hair cells of control *Prox1*^{CreERT2} and *Plp-CreER*^{T} samples at P7, with no prestin-positive inner hair cells or supporting cells seen among the three control cochleae (**Figures 4A–A'''**). Similar to oncomodulin, prestin was also expressed in regenerated hair cells (tdTomato-positive/Myo7a-positive) derived from both subsets of supporting cells. However, at P7, prestin expression appeared faint (**Figures 4B–C'''**) and there were low numbers and percentages of prestin-positive regenerated hair cells (tdTomato-positive/Myo7a-positive) (**Figures 4F,G**). Therefore, we also examined samples at P10 (**Figures 4D–E'''**), where prestin staining was stronger (**Figures 4D',E'** vs. **Figures 4B',C'**). Regenerated hair cells derived from *Prox1*^{CreERT2}-labeled supporting cells (in the lateral compartment) showed a significantly higher number of prestin-positive hair cells at P10 compared to P7 (64.6 ± 21.5 vs. 16.2 ± 7.6, $n = 5$, $p = 0.0130$ determined using a two-way ANOVA followed by a Sidak's *post-hoc* test), but there was no difference in the number of cells expressing prestin between P7 and P10 in the *DTR:Plp-CreER*^{T} mice (**Figure 4F**). At P10, there were

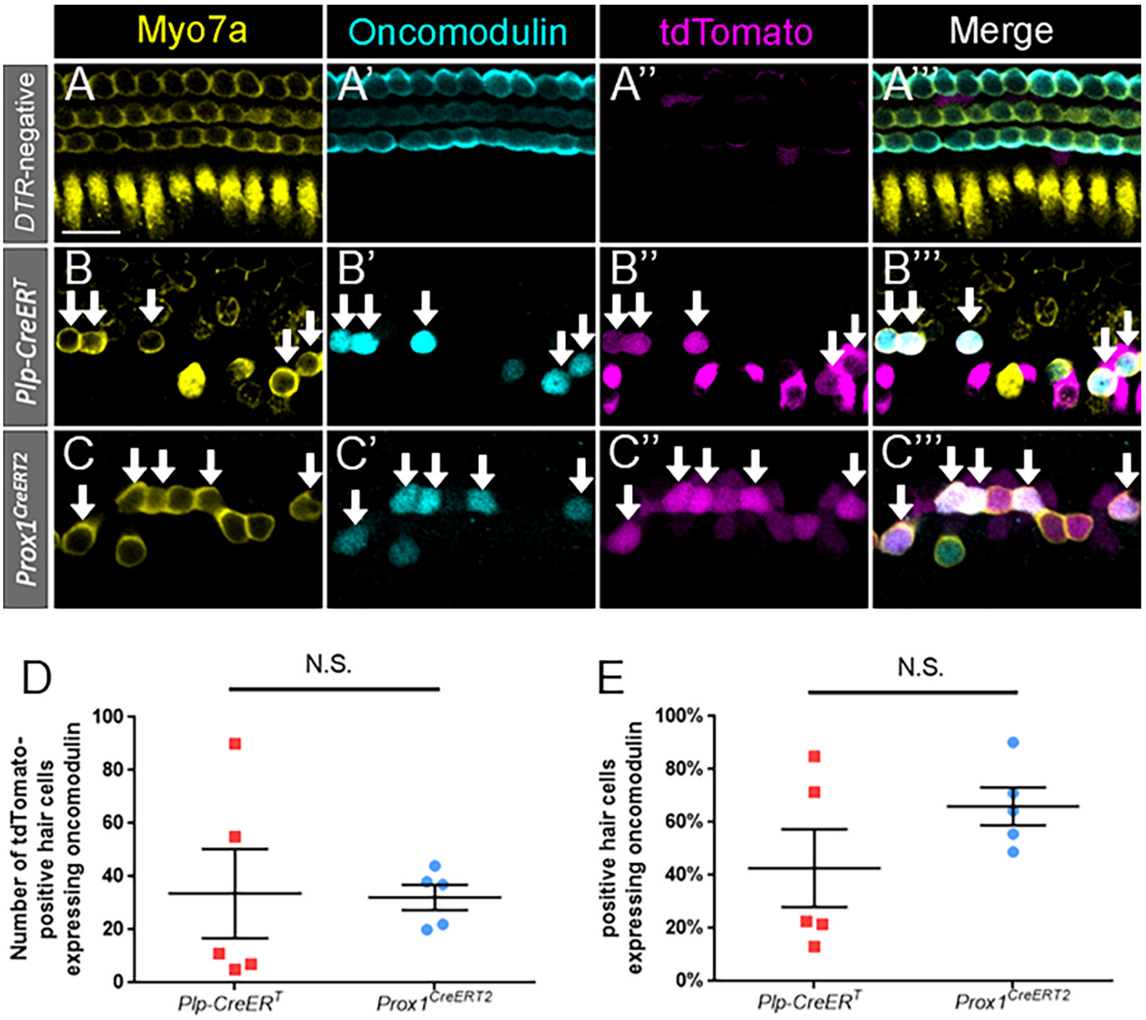

FIGURE 3

Oncomodulin is expressed in a similar number and percentage of regenerated hair cells across supporting cell subtypes. **(A–C''')** Representative confocal slice images from the middle turn of $Pou4f3^{DTR}$-negative **(A–A''')** and apical turns of $Plp\text{-}CreER^{T}$:$Rosa26^{tdTomato}$:$Pou4f3^{DTR}$ **(B–B''')** and $Prox1^{CreERT2}$:$Rosa26^{tdTomato}$:$Pou4f3^{DTR}$ **(C–C''')** mice at P7–P8 that were injected with tamoxifen at P0 to induce tdTomato expression in the two supporting cell subpopulations and with DT at P1 to induce hair cell damage. Samples were immunostained with anti-Myo7a antibodies (yellow) to label all hair cells and anti-oncomodulin antibodies (blue) to label immature outer hair cells. tdTomato was detected using endogenous fluorescence (magenta). Arrows indicate Myo7a-positive/oncomodulin-positive/tdTomato-positive cells that are regenerated, fate-mapped outer hair cells. Scale bar: 25 μm. **(D)** There was no significant difference in the total number of regenerated hair cells expressing oncomodulin between the supporting cell populations targeted by the two CreER lines. **(E)** When normalized to the total number of tdTomato-positive/Myo7a-positive cells, there was no significant difference in the percentage of oncomodulin-positive regenerated hair cells between the supporting cell populations targeted by the two CreER lines. Significance was determined using an unpaired Student's *t*-test. Data are presented as mean ± SEM; $n = 5$. N.S., not significant.

also more prestin-positive regenerated hair cells (tdTomato-positive/Myo7a-positive) in $DTR\text{:}Prox1^{CreERT2}$ samples than $DTR\text{:}Plp\text{-}CreER^{T}$ samples (64.6 ± 21.5 vs. 8.4 ± 2.4, $n = 5$, $p = 0.0065$ determined using a two-way ANOVA followed by a Sidak's *post-hoc* test) (**Figure 4F**). Likewise, when the data were converted to a percentage [to normalize it to the total number of regenerated hair cells (tdTomato-positive/Myo7a-positive)], regenerated hair cells derived from $Prox1^{CreERT2}$-labeled supporting cells (in the lateral compartment) showed a significantly higher percentage of prestin-positive hair cells at P10 compared to P7 (99.5 ± 0.4% vs. 50.0 ± 21.2%, $n = 5$, $p = 0.0325$ determined using a two-way ANOVA followed by a Sidak's *post-hoc* test), and compared to those derived from $Plp\text{-}CreER^{T}$-labeled supporting cells at P10 (99.5 ± 0.4% vs. 36.5 ± 7.0%, $n = 5$, $p = 0.0031$ determined using a two-way ANOVA followed by a Sidak's *post-hoc* test) (**Figure 4G**). There were no Tomato-positive/Myo7a-negative cells that expressed prestin in any of the control or experimental samples. These data suggest that similar to normal development, it takes several days after Myo7a expression for prestin to be expressed in

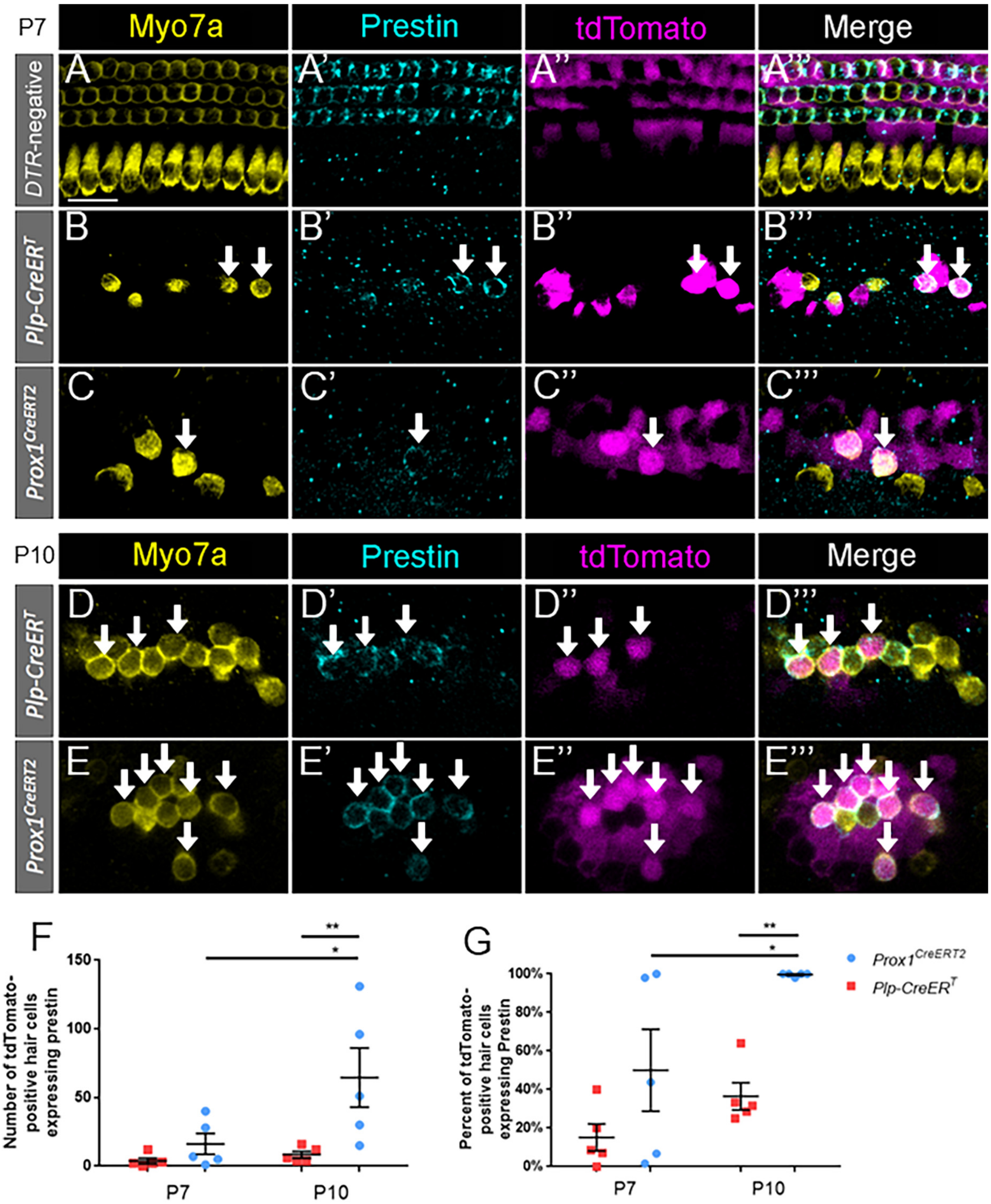

FIGURE 4

Prestin expression in regenerated hair cells increases with age and is proportionally higher in pillar and Deiters' cells. **(A–E''')** Representative confocal slice images from the middle turn of *Pou4f3*^{DTR}-negative **(A–A''')** and from the apical turn of *Plp-CreER*^{T}*:Rosa26*^{tdTomato}*:Pou4f3*^{DTR} **(B–B''',D–D''')** and *Prox1*^{CreERT2}*:Rosa26*^{tdTomato}*:Pou4f3*^{DTR} **(C–C''',E–E''')** mice at P7–P8 **(A–C''')** and P10 **(D–E''')** that were injected with tamoxifen at P0 to induce tdTomato expression in the two supporting cell subpopulations and with DT at P1 to induce hair cell damage. Samples were immunostained with anti-Myo7a antibodies (yellow) to label hair cells and anti-prestin antibodies (blue) to label mature outer hair cells. tdTomato was detected using endogenous fluorescence (magenta). Arrows indicate Myo7a-positive/prestin-positive/tdTomato-positive cells that are regenerated, fate-mapped mature outer hair cells. Scale bars: 25 μm. **(F)** A significantly greater number of prestin-positive regenerated hair cells were seen in the supporting cells located in the lateral compartment and fate-mapped by *Prox1*^{CreERT2} between P7 and P10 and between the supporting cell populations targeted by the two CreER lines at P10. **(G)** Data from panel **(F)** normalized to the total number of Tomato-positive/Myo7a-positive cells in each mouse model. *$p < 0.05$; **$p < 0.01$, determined using two-way ANOVA with a Sidak's *post-hoc* test. Data are presented as mean ± SEM; $n = 5$. N.S., not significant.

regenerated outer hair cells, and prestin-positive regenerated hair cells are preferentially produced by supporting cells originating in the lateral compartment, which neighbor the endogenous outer hair cells.

VGlut3 is expressed in hair cells regenerated from all supporting cell subtypes

To identify terminally differentiated inner hair cells, cochlear sections were costained with VGlut3 and Myo7a. VGlut3 is responsible for transport of cytoplasmic glutamate into presynaptic vesicles of inner hair cells, and is not normally expressed in outer hair cells or supporting cells (Seal et al., 2008; Liu et al., 2014; Strenzke et al., 2016). We confirmed this expression pattern of VGlut3 in our control *Prox1*^{CreERT2} and *Plp-CreER*^{T} samples at P7 (**Figures 5A–A'''**); no VGlut3-positive outer hair cells or supporting cells were seen among three control cochleae. Like the outer hair cell markers, VGlut3 expression was also seen in regenerated hair cells (tdTomato-positive/Myo7a-positive) fate-mapped by both *Prox1*^{CreERT2} and *Plp-CreER*^{T} at P7 (**Figures 5B–C'''**). There were no Tomato-positive/Myo7a-negative cells that expressed VGlut3 in any of the control or experimental samples. While regenerated

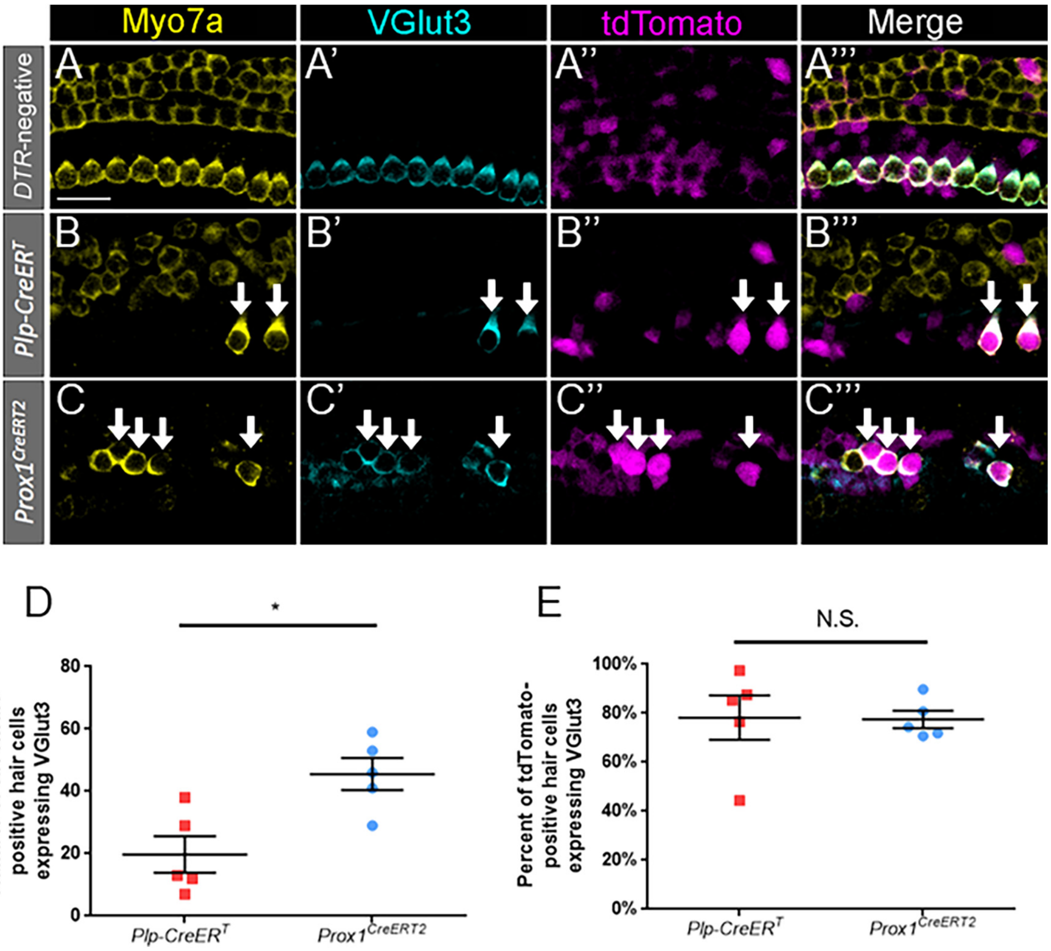

FIGURE 5
VGlut3 is expressed in a similar proportion of regenerated hair cells across supporting cell subtypes. **(A–C''')** Representative confocal slice images from the apical turn of *Pou4f3*^{DTR}-negative **(A–A''')**, middle turn of *Plp-CreER*^{T}:*Rosa26*^{tdTomato}:*Pou4f3*^{DTR} **(B–B''')**, and apical turn of *Prox1*^{CreERT2}:*Rosa26*^{tdTomato}:*Pou4f3*^{DTR} **(C–C''')** mice at P7–P8 that were injected with tamoxifen at P0 to induce tdTomato expression in the two supporting cell subpopulations and with DT at P1 to induce hair cell damage. Samples were immunostained with anti-Myo7a antibodies (yellow) to label hair cells and anti-VGlut3 antibodies (blue) to label mature inner hair cells. tdTomato was detected using endogenous fluorescence (magenta). Arrows indicate Myo7a-positive/VGlut3-positive/tdTomato-positive cells that are regenerated, fate-mapped mature inner hair cells. Scale bars: 25 μm. **(D)** Significantly more regenerated hair cells derived from supporting cells in the lateral compartment and fate-mapped by *Prox1*^{CreERT2} expressed VGlut3. **(E)** When normalized to the total number of tdTomato-positive/Myo7a-positive cells, there was no significant difference in the percentage of VGlut3-positive regenerated hair cells between the supporting cell populations targeted by the two CreER lines. *$p < 0.05$, determined using an unpaired Student's *t*-test. Data are presented as mean ± SEM; $n = 5$. N.S., not significant.

hair cells (tdTomato-positive/Myo7a-positive) of *Prox1*^{CreERT2} supporting cell origin had a greater number of VGlut3-positive cells than those of *Plp-CreER*^{T} origin (45.6 ± 5.2 vs. 19.8 ± 5.9, $n = 5$, $p = 0.0108$ determined using an unpaired Student's *t*-test) (**Figure 5D**), when normalized to the total number of regenerated hair cells (tdTomato-positive/Myo7a-positive), there was a similar percentage of VGlut3-positive cells in both CreER lines (77.5 ± 3.5% and 78.2 ± 9.1%, $n = 5$) (**Figure 5E**). This suggests that both subsets of supporting cells have an equivalent capacity to differentiate toward an inner hair cell fate.

Some regenerated hair cells aberrantly express inner and outer hair cell markers simultaneously

Given the high percentage of regenerated cells (tdTomato-positive/Myo7a-positive) that expressed oncomodulin and VGlut3 in both of the CreER lines (**Figures 3E**, **5E**), we hypothesized that some cells expressed both of these genes. To test this, *DTR:Prox1*^{CreERT2} and *DTR:Plp-CreER*^{T} cochlear samples were stained with both oncomodulin and VGlut3 at P7. Regenerated hair cells were identified by tdTomato expression combined with expression of either or both oncomodulin and VGlut3.

We observed a significant number of regenerated hair cells (tdTomato-positive) that expressed VGlut3 without oncomodulin in both lines (*DTR:Prox1*^{CreERT2}: 20.0 ± 6.3; *DTR:Plp-CreER*^{T}: 29.4 ± 6.7, $n = 5$) (**Figures 6A–E**). Conversely, an exceedingly low number of oncomodulin-positive regenerated hair cells (tdTomato-positive) expressed oncomodulin without VGlut3 (*DTR:Prox1*^{CreERT2}: 2.0 ± 1.0; *DTR:Plp-CreER*^{T}: 1.2 ± 1.0, $n = 5$) (**Figures 6A–E**). Within the *DTR:Prox1*^{CreERT2} cochleae, there was a significantly greater number of regenerated hair cells expressing both VGlut3 and oncomodulin than those expressing oncomodulin alone (27.4 ± 4.9 vs. 2.0 ± 1.0, $n = 5$, $p = 0.0118$, determined using two-way ANOVA followed by a Sidak's *post-hoc* test) (**Figures 6A–E**). Within the *DTR:Plp-CreER*^{T} cochleae, there was a significantly greater number of regenerated hair cells expressing VGlut3 alone or both VGlut3 and oncomodulin than those expressing oncomodulin alone (24.8 ± 9.0 vs. 1.2 ± 1.0, $n = 5$, $p = 0.0050$ and 29.4 ± 6.7 vs. 1.2 ± 1.0, $n = 5$, $p = 0.0201$, determined using two-way ANOVA followed by a Sidak's *post-hoc* test) (**Figures 6A–E**). When the data were normalized to the total number of regenerated hair cells (tdTomato-positive cells that co-expressed either VGlut3 or oncomodulin), a similar percentage of cells expressing both oncomodulin and VGlut3 were seen in both CreER lines (*Prox1*^{CreERT2}: 59.3 ± 12.2%; *DTR:Plp-CreER*^{T}: 43.9 ± 9.9%, $n = 5$, determined using an unpaired Student's *t*-test) (**Figure 6F**).

Since *Plp-CreER*^{T} is expressed in ∼7–11% of inner pillar, outer pillar, and Deiters' cells in addition to the supporting cells in the medial compartment (**Figures 1B,D,D'**; McGovern et al., 2017), we closely examined the location of the regenerated hair cells, using the tunnel of Corti as a landmark (**Figures 6A–A''',C–C'''**). Regenerated hair cells that expressed both oncomodulin and VGlut3 simultaneously were most commonly found within the lateral compartment (*Prox1*^{CreERT2}: 23.8 ± 4.0; *Plp-CreER*^{T}: 21.6 ± 9.8, $n = 5$), and were rarely seen in the medial compartment (*Prox1*^{CreERT2}: 3.6 ± 1.4; *Plp-CreER*^{T}: 3.2 ± 1.0, $n = 5$) in both CreER lines (**Figures 6B–B''',D–D'''**). While the regenerated hair cells that expressed VGlut3 without oncomodulin were found exclusively medial to the tunnel of Corti, the cells that expressed oncomodulin without VGlut3 were almost exclusively observed in the lateral compartment. When the data were normalized to the total number of regenerated hair cells (tdTomato-positive cells that co-expressed either VGlut3 or oncomodulin), a similar percentage of cells expressing both oncomodulin and VGlut3 were seen in the lateral compartment of both CreER lines (*Prox1*^{CreERT2}: 87.7 ± 3.8%; *DTR:Plp-CreER*^{T}: 77.0 ± 9.0%, $n = 5$, determined using an unpaired Student's *t*-test). This suggests that VGlut3 expression is not properly controlled in the neonatal cochlea, thus many regenerated hair cells may develop as hybrids, expressing markers of both inner and outer hair cells.

Regenerated hair cells from both mouse lines form new synaptic connections

Hair cell types also differ in their innervation patterns with afferent spiral ganglion neurons. To identify synapses and innervation with regenerated hair cells, cochlear sections of both CreER lines at P7 were stained with either anti-C-terminal binding protein 2 (CtBP2) (**Figures 7A–B'''**) or anti-neuron-specific class III β-tubulin (Tuj1) (**Figures 7C–D'''**). CtBP2 is an important component of the ribbon synapses that are found in both inner and outer hair cells (Schmitz, 2009; Uthaiah and Hudspeth, 2010; Becker et al., 2018). Tuj1 is an important structural component of spiral ganglion neurites (Sekerková et al., 2008). In the *DTR:Plp-CreER*^{T}- and *DTR:Prox1*^{CreERT2}-labeled regenerated hair cells (tdTomato-positive/Myo7a-positive) at P7, 81.8 and 96.8% had numerous CtBP2-positive puncta, respectively, while 95.2 and 98.0% of regenerated hair cells had direct contact with at least one Tuj1-positive neurite.

We next categorized tdTomato-positive hair cells as being in the medial or lateral compartments depending on their position relative to the tunnel of Corti (**Figures 6A–A''',C–C'''**). At P7, each *DTR:Plp-CreER*^{T} cochleae contained 16.6 ± 4.2 medially positioned and 4.6 ± 0.9 laterally positioned tdTomato-positive hair cells, contrasting *DTR:Prox1*^{CreERT2} cochleae, which each contained 4.0 ± 0.8 medially positioned cells and 77.8 ± 8.0 laterally positioned cells. Using the 10

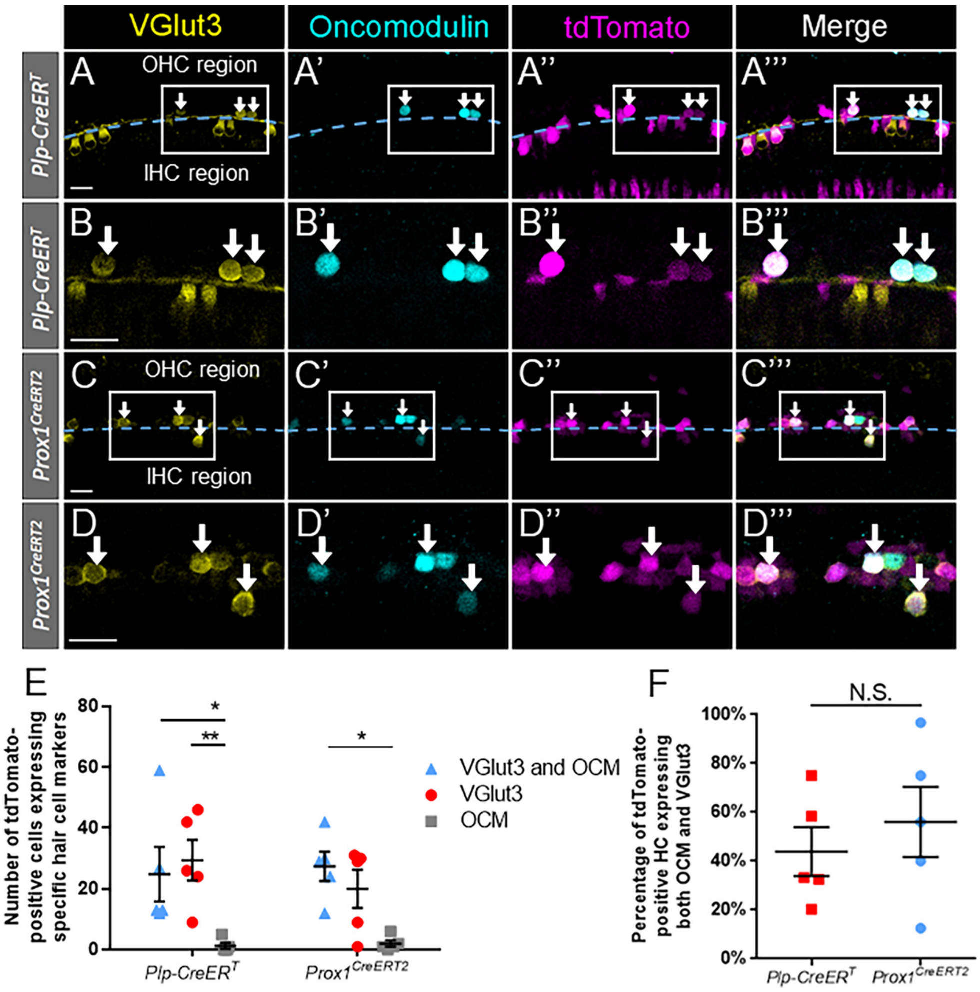

FIGURE 6

A large proportion of regenerated hair cells expressed both oncomodulin and VGlut3 across supporting cell subtypes. **(A–C''')** Representative confocal slice images from the apical turn of *Plp-CreER*^{T}*:Rosa26*^{tdTomato}*:Pou4f3*^{DTR} **(A–B''')** and *Prox1*^{CreERT2}*:Rosa26*^{tdTomato}*:Pou4f3*^{DTR} **(C–D''')** mice at P7–P8 that were injected with tamoxifen at P0 to induce tdTomato expression in the two supporting cell subpopulations and with DT at P1 to induce hair cell damage. Samples were immunostained with anti-VGlut3 antibodies (yellow) as a marker of mature inner hair cells and anti-oncomodulin antibodies (blue) as a marker of immature outer hair cells. tdTomato was detected using endogenous fluorescence (magenta). Arrows indicate VGlut3-positive/oncomodulin-positive/tdTomato-positive cells that are regenerated, fate-mapped hair cells. **(A–A''',C–C''')** Based on their location relative to the tunnel of Corti (dashed blue line), regenerated hair cells were classified as being located in the lateral compartment (upper half of image) or the medial compartment (lower half of image) position. Boxes outline the location where higher magnification images **(B–B''', D–D''')** were taken. All scale bars: 25 µm. **(E)** In both population of supporting cells, a significantly greater number of regenerated hair cells (Tomato-positive) expressed both VGlut3 and oncomodulin (blue triangles) compared to those expressing only oncomodulin (gray squares). For regenerated hair cells fate-mapped by *Plp-CreER*^{T}, the number of cells expressing only VGlut3 (red circles) also significantly exceeded those expressing only oncomodulin. **(F)** When normalized to the total number of tdTomato-positive hair cells, there was no significant difference in the percentage of VGlut3-positive/oncomodulin-positive regenerated hair cells between the supporting cell populations targeted by the two CreER lines. *$p < 0.05$; **$p < 0.01$, determined using two-way ANOVA with a Sidak's *post-hoc* test. Data are presented as mean ± SEM; $n = 5$. N.S., not significant.

most apical regenerated hair cells (tdTomato-positive/Myo7a-positive) in each compartment, we quantified the number of synapses per regenerated hair cell by counting CtBP2-positive puncta. In some cases there were less than 10 regenerated hair cells in a compartment, so we used all cells present in that sample/compartment for the quantifications. Medial compartment tdTomato-positive hair cells had significantly more CtBP2-positive ribbon synapses than lateral compartment tdTomato-positive cells in both the *DTR:Plp-CreER*^{T} and *DTR:Prox1*^{CreERT2} lines (Figure 7E; 31.2 ± 3.4 vs. 22.6 ± 1.3 for *DTR:Plp-CreER*^{T}, $n = 5$, $p = 0.0128$ and 28.8 ± 1.0 vs. 15.6 ± 0.9 for *DTR:Prox1*^{CreERT2}, $n = 5$, $p = 0.0004$ determined using two-way ANOVA followed by a Sidak's *post-hoc* test). Furthermore, lateral compartment regenerated hair cells fate-mapped by *DTR:Plp-CreER*^{T} had more CtBP2-positive puncta per cell than those fate-mapped by *DTR:Prox1*^{CreERT2}

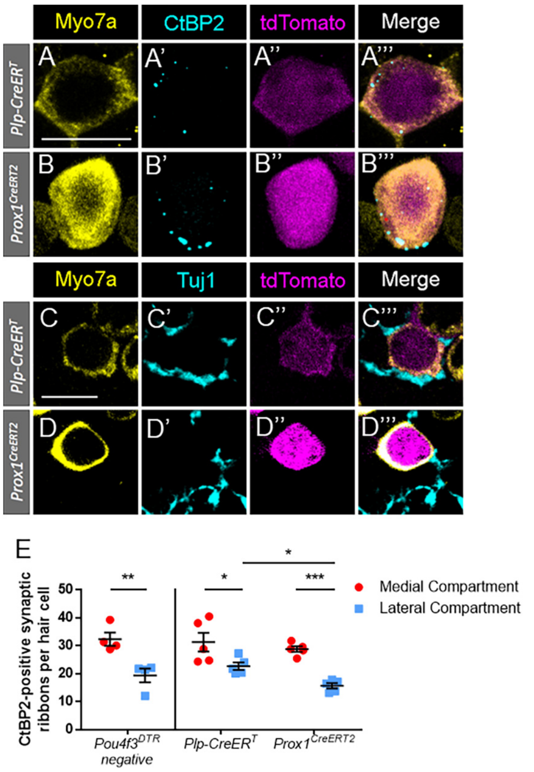

FIGURE 7

Regenerated hair cells formed ribbon synapses and were innervated by Tuj1-positive neurites at P7. **(A–D''')** Representative confocal slice images from the apical turn of *Plp-CreER*^{T}*:Rosa26*^{tdTomato}*:Pou4f3*^{DTR} **(A–A''',C–C''')** and *Prox1*^{CreERT2}*:Rosa26*^{tdTomato}*:Pou4f3*^{DTR} **(B–B''',D–D''')** mice at P7–P8 that were injected with tamoxifen at P0 to induce tdTomato expression in the two supporting cell subpopulations and with DT at P1 to induce hair cell damage. Samples were immunostained with anti-Myo7a antibodies (yellow) to label hair cells and anti-CtBP2 antibodies (blue, **A–B'''**) to label synaptic ribbons or anti-Tuj1 antibodies (blue, **C–D'''**) to label neurites of the spiral ganglion. tdTomato was detected using endogenous fluorescence (magenta). Scale bars: 10 μm. **(E)** In the *Pou4f3*^{DTR}-negative controls, there were significant more ribbon synapses in the inner hair cells located in the medial compartment (red circles) than the outer hair cells located the in the lateral compartment (blue squares). For the *DTR:Prox1*^{CreERT2} and *DTR:Plp-CreER*^{T} mice, hair cells were classified as located in the medial or lateral compartment based on their location relative to the tunnels of Corti (see **Figures 6A–A''',C–C'''**). Similar to the control dataset, significantly more synaptic ribbons were seen in regenerated hair cells (Myo7a-poitive/Tomato-positive) located in the medial compartment compared to the lateral compartment for both CreER lines. In addition, there were a greater number of CtBP2-positive puncta in the lateral compartment regenerated hair cells fate-mapped by *Plp-CreER*^{T} than those fate-mapped by *Prox1*^{CreERT2}. $*p < 0.05$; $**p < 0.01$; $***p < 0.001$, determined using an unpaired Student's *t*-test. Data are presented as mean ± SEM; $n = 4–5$.

(22.6 ± 1.3 vs. 15.6 ± 0.9, $n = 5$, $p = 0.415$ determined using two-way ANOVA followed by a Sidak's *post-hoc* test). In P7 control samples (*Pou4f3*^{DTR}*-negative*), there were also more ribbon synapses in inner hair cells (located in the medial compartment) compared to outer hair cells (located in the lateral compartment) (32.3 ± 2.36 vs. 19.3 ± 2.44, $N = 4$, $p = 0.0086$ determined using a Student's *t*-test). However, there was no differences in the number of ribbon synapses per hair cell between controls and either CreER line for either compartment (**Figure 7E**). These synapse numbers are similar to the number of CtBP2-positive synaptic ribbons reported previously at P0-P3 during normal cochlear development (Huang et al., 2012), but greater than what is present in adult mice (Thiers et al., 2008; Becker et al., 2018; Chen et al., 2021), suggesting that at P7 hair cells have yet to undergone synaptic pruning.

Discussion

While hair cells expressing markers of terminal differentiation have been reported in models where supporting cells were reprogrammed to induce hair cell regeneration (Liu et al., 2014; Lee et al., 2020; Chen et al., 2021), examples of this in spontaneously regenerated hair cells is limited. Previous work showed that some spontaneously regenerated hair cells can express the terminal outer hair cell marker prestin, but there is no evidence of inner hair cell replacement (Bramhall et al., 2014; Cox et al., 2014). Our work here, which includes cells that were regenerated by both mitotic regeneration and direct transdifferentiation, demonstrates that spontaneously regenerated hair cells are able to express markers of inner or outer hair cells, including their terminal differentiation markers, VGlut3 and prestin, respectively. In addition, a large number of supporting cells responded to hair cell damage by expressing Atoh1, within 2 days of the injury, yet the number of these cells that progressed to express Myo7a was significantly reduced in both CreER lines. The lack of progression toward a hair cell fate may be explained by recent findings which suggest that the targets of Atoh1 are not accessible in many neonatal supporting cells, or there may be a critical level of *Atoh1* expression needed to induce transdifferentiation in a feed-forward fashion through expression of *Pou4f3* (Yu et al., 2021).

VGlut3 is mis-expressed in regenerated hair cells originating from supporting cells in the lateral compartment

Interestingly, when we co-stained for VGlut3 and oncomodulin simultaneously, we observed that the majority of the oncomodulin-positive, VGlut3-positive regenerated cells were found in the lateral compartment (87.7 ± 3.8% for *DTR:Prox1*^{CreERT2} and 77.0 ± 9.0% for *DTR:Plp-CreER*^{T}, $N = 5$) While very few regenerated cells expressed oncomodulin alone, we found that about a quarter of regenerated cells expressed VGlut3 alone in each CreER line, with these cells located exclusively in the medial compartment.

The finding of these outer compartment hybrid cells suggests that the cues that control regulation of inner hair cell genes and differentiation are reduced or are no longer present in the neonatal cochlea. *Atoh1* and *Pou4f3* have been shown to be important for induction of a general cochlear hair cell fate. Two additional transcription factors, Ikaros family zinc finger 2 (*Ikzf2*) (which encodes the protein Helios) and insulinoma-associated protein 1 (*Insm1*) have recently been implicated in further differentiation toward an outer hair cell fate (Chessum et al., 2018; Wiwatpanit et al., 2018; Sun et al., 2021) and *Tbx2* has been implicated in promoting an inner hair cell fate (García-Añoveros et al., 2022). *Ikzf2* is expressed starting at P4, and persists in fully mature outer hair cells. It is thought to play a role in promoting an outer hair cell fate by downregulating genes that are inner hair cell-specific, and upregulating outer hair cell-specific genes (Chessum et al., 2018). Conversely, *Insm1* is expressed only transiently from embryonic day (E) 15.5 to P2 in outer hair cells (Lorenzen et al., 2015). It is also thought to help promote an outer hair cell fate by repressing inner hair cell-specific genes and preventing embryonic hair cells from responding to pro-inner hair cell signaling gradients. Deletion of *Insm1* during embryonic development caused differentiation of some hair cells in the lateral compartment into inner hair cells in a decreasing gradient from the medial to lateral compartments (Wiwatpanit et al., 2018). The recently described opposing medial-lateral gradients of Activin A and Follistatin may represent two such gradients driving this process (Prajapati-DiNubila et al., 2019). Given that the induction of hair cell damage in our work occurred at P1, which is near the end of normal *Insm1* expression, it is possible that spontaneously regenerating hair cells in the lateral compartment lacked appropriate expression of *Insm1* and were thus susceptible to molecular gradients driving an inner hair cell fate, leading to the inappropriate expression of VGlut3 that we observed. Another potential explanation is that the hybrid cells (VGlut3-positive/oncomodulin-positive/Tomato-positive) are original hair cells that survived the DT-mediated damage. However this is unlikely since there was only ∼1 Tomato-positive hair cell in $Plp\text{-}CreER^{T}$ mice and ∼13 Tomato-positive hair cells in $Prox1^{CreERT2}$ mice and 30–40 hybrid cells present in both mouse models.

It is unclear what properties these hybrid cells might possess. It is also possible that the VGlut3 mis-expression induced cell death, since previous reports showed that most regenerated hair cells do not survive into adulthood (Cox et al., 2014). Although examples of cell transdifferentiation are seen in other organ systems, such as the liver and pancreas (Shen et al., 2003; Yanger et al., 2013), to the best of our knowledge similar evidence of healthy, regenerated cells co-expressing markers of other distinct, neighboring cell types has not been reported. Rather, inappropriate expression of proteins is often discussed within the context of dysplasia or malignancy (Qie and Diehl, 2016; Kent and Leone, 2019).

Regenerated hair cells express mature inner and outer hair cell markers, and the type of marker expressed does not depend on the supporting cell subtype of origin

A recent single cell RNA-seq study showed that the inner phalangeal cells located in the medial compartment of the organ of Corti have a very different molecular profile than the pillar and Deiters' cells located in the lateral compartment (Kolla et al., 2020). We attempted to determine whether supporting cells in closest proximity to each hair cell subtype would be more likely to produce the same type of regenerated hair cell (i.e., are the supporting cells that neighbor each hair cell type pre-programmed to follow a specific fate). Contrary to our hypothesis, we found that there were no differences in the percentage of regenerated hair cells from the two CreER lines that expressed markers of an immature outer hair cell fate (by expressing oncomodulin) or a mature inner hair cell fate (by expressing VGlut3). Conversely, there was a greater proportion of $Prox1^{CreERT2}$–labeled regenerated cells that expressed the terminal outer hair cell gene, prestin. Importantly, these experiments were performed with only one type-specific hair cell marker, along with the general hair cell marker, Myo7a. While this allowed us to characterize differentiated cells as a proportion of all regenerated cells labeled by a specific CreER line, our subsequent finding of hybrid cells suggests that experiments performed with only one type-specific marker did not reliably define a pure inner or outer hair cell phenotype. While our single-marker findings contradict with a recent report by Chen et al. (2021) in which hair cells induced by over-expression of *Gfi1*, *Pou4f3*, and *Atoh1* produced cells expressing prestin only when pillar and Deiters' cells were targeted, and produced cells expressing VGlut3 only when inner phalangeal and border cells were targeted, these studies examined VGlut3 and prestin separately. In addition, the different results from these two studies may have been caused by changes that occurred in the organ of Corti after DT-induced hair cell damage, which was present in our experiment, but not in the Chen et al. (2021) study, or were due to the age of the supporting cells being studied.

Plasticity differences between supporting cell subtypes in the medial and lateral compartments

While there was no difference in the percentage of regenerated hair cells (Myo7a-positive/Tomato-positive cells) from the two CreER lines, there were differences in the percentage of supporting cells from each population that turned on the early hair cell gene, Atoh1, after hair cell damage. Specifically, there were ∼2 fold more *Plp-CreER*^{T}-positive supporting cells that expressed Atoh1 after damage and this may suggest that supporting cells in the medial compartment, located near inner hair cells, retain their plasticity and capacity to respond to hair cell damage longer than other supporting cell subtypes. When looking at cochlear development, this may seem surprising since the hair cells and supporting cells in the medial compartment differentiate from progenitor cells before the cells in the lateral compartment (Morrison et al., 1999; Lanford et al., 2000; Driver et al., 2013), and thus one might predict that the medial cells are more mature at neonatal ages.

It is well documented that the supporting cells in the base of the cochlea begin the maturation process 1–2 days before the cells in the apex (Hallworth et al., 2000; Jensen-Smith et al., 2003; Szarama et al., 2012) and that the majority of regenerated hair cells are located in the apical turn of the cochlea where supporting cells are less mature (Bramhall et al., 2014; Cox et al., 2014; Atkinson et al., 2018; McGovern et al., 2019), Similar to previous reports (Atkinson et al., 2018), the *Prox1*^{CreERT2}–labeled supporting cells in the lateral compartment followed this gradient showing a decline in the number of Atoh1-positive cells from the apex to the base. However there was no gradient of Atoh1 expression seen for the *Plp-CreER*^{T}-labeled supporting cells, which also supports the idea that medial supporting cells remain plastic for a longer period of time.

Spontaneously regenerated hair cells form new synaptic connections

Contact with Tuj1-positive neurites and formation of CtBP2-positive synaptic boutons was seen in the vast majority of regenerated hair cells, suggesting that the replacement hair cells form new synaptic connections. During normal embryogenesis and the early postnatal period, the number of synaptic ribbons in each hair cell increases gradually. Inner hair cells reach a peak of 50–55 CtBP2-positive puncta around P3, whereas outer hair cells reach a peak of 45–50 CtBP2-positive puncta around P6. Both subsets of hair cells are then subject to synaptic pruning until ∼P12, at which time they reach adult levels (Huang et al., 2012). In adult mice, the number of CtBP2 puncta has been reported to be approximately 15–20 per inner hair cell (Thiers et al., 2008; Becker et al., 2018; Chen et al., 2021) and 1–2 per outer hair cell (Thiers et al., 2008). The number of CtBP2-positive synaptic ribbons seen in regenerated hair cells in our experiments at P7 are similar to the numbers of ribbon synapses seen in the first few postnatal days during normal development, based on data from both with our control samples and published data. This is logical since the regenerated cells had just differentiated from supporting cells a few days prior, and suggests that the synaptic pruning process has not yet occurred. Additionally, lateral compartment regenerated cells contained significantly less synapses than the medial compartment cells, which follows the normal pattern of synapse counts seen in normal inner and outer hair cells.

In summary our study showed that regenerated hair cells expressing terminal differentiation markers of both inner and outer hair cells could be produced from either subset of fate-mapped supporting cells, and that these regenerated cells contained synaptic boutons and neuronal connections. Our work also suggests that the regulatory factors guiding terminal hair cell differentiation are altered during the first week of neonatal life, as evidenced by aberrant expression of VGlut3 in regenerating cells located in the lateral, outer hair cell compartment. Further work is needed to elucidate the processes that guide hair cell differentiation into subtypes, as replicating these processes during regeneration will likely be necessary to form functional, mature inner and outer hair cells.

Materials and methods

Animals

Plp-CreER^{T} mice (stock #5975, Doerflinger et al., 2003), *Rosa26*^{tdTomato} mice, also referred to as Ai14 (stock #7914, Madisen et al., 2010), and *Atoh1*$^{GFP/+}$ mice (stock #13593, Rose et al., 2009) were obtained from The Jackson Laboratory. *Pou4f3*^{DTR} mice (Golub et al., 2012; Tong et al., 2015) were provided by Dr. Ed Rubel (University of Washington, Seattle, WA, USA). *Prox1*^{CreERT2} mice (Srinivasan et al., 2007) were provided by Dr. Guillermo Oliver (St. Jude Children's Research Hospital, Memphis, TN, USA). Both of these strains are now available at The Jackson Laboratory. Transnetyx, Inc., performed all genotyping. Mice of both genders were used, and all animal work was performed in accordance with approved animal protocols from the Institutional Animal Care and Use Committee at Southern Illinois University School of Medicine.

Substances given to animals

tdTomato expression was induced in supporting cell subgroups by intraperitoneal injection of 3 mg/40 g tamoxifen (Sigma-Aldrich, St. Louis, MO, USA) in 100% corn oil (Sigma-Aldrich, St Louis, MO, USA) given at P0. Hair cell death was induced by intramuscular injection of 6.25 ng/g DT (List Biological Laboratories, Inc., Campbell, CA, USA) given at P1.

Immunostaining

Neonatal pups were euthanized under isoflurane anesthesia (Piramal Enterprises Limited, Telangana, India) between P3-P10 and cochleae were subsequently harvested and post-fixed in 4% paraformaldehyde (Polysciences, Inc., Warrington, PA, USA) for ∼2 h at room temperature. Samples were then transferred to 10 mM phosphate buffered saline (PBS) (Sigma-Aldrich, St. Louis, MO, USA) and stored at 4°C. Whole mount dissection was performed with cochleae dissected into 3 turns of equal length. Sections were placed in a 48-well plate for free floating immunostaining as previously described (Montgomery and Cox, 2016). The following primary antibodies were used: rabbit anti-myosin VIIa (Myo7a) (1:200, cat#25-6790, Proteus Biosciences, Ramona, CA, USA), goat anti-prestin (1:200, cat#sc-22692, Santa Cruz Biotechnology, Inc., Dallas, TX, USA), mouse anti-CtBP2 IgG1 (1:500, cat#BDB612044, Fisher, Hampton, NH, USA), mouse anti-Tuj1 IgG2a (1:500, cat#801201, BioLegend, San Diego, CA, USA), chicken anti-GFP (1:1,000, cat#ab13970, Abcam, Cambridge, United Kingdom), goat anti-oncomodulin (1:200, cat#sc-7446, Santa Cruz Biotechnology, Inc., Dallas, TX, USA), mouse anti-VGlut3 IgG2a (1:200, cat#135211, Synaptic Systems, Göttingen, Germany), and rabbit anti-VGlut3 (1:500, cat#135203, Synaptic Systems, Göttingen, Germany). Alexa fluor-conjugated secondary antibodies (Invitrogen, Thermo Fisher Scientific, Carlsbad, CA, USA) were used at 1:1000 dilution and nuclei were stained with Hoechst (1:2000, Fisher, Hampton, NH, USA). Samples were mounted on slides using Prolong Gold (Fisher, Hampton, NH, USA).

Cell counts

Confocal imaging was performed using the Zeiss LSM800 (Zeiss, Oberkochen, Germany), and images were processed using Zen Blue (Zeiss, Oberkochen, Germany) software. All Myo7a-positive/tdTomato-positive cells (regenerated hair cells) were quantified and assessed for expression of the various markers along the entire length of the cochlea for both experimental and control groups. Regenerated hair cells that expressed specific markers of inner or outer hair cells were normalized to the total number of Myo7a-positive, tdTomato-positive cells in each cochlea. In **Figure 2**, all tdTomato-positive supporting cells throughout the cochlea that expressed ATOH1-GFP or Myo7a were included in the quantifications. In **Figure 2E**, total numbers of Tomato-positive supporting cells in each CreER line were taken from McGovern et al. (2019) to generate the percentages. In **Figure 5**, regenerated hair cells were identified by tdTomato expression combined with expression of either or both oncomodulin and VGlut3 (since Myo7a was not used in this experiment). For quantification of CtBP2-positive synapses in **Figure 7**, up to 10 regenerated hair cells (Myo7a-positive, tdTomato-positive) in each compartment (medial and lateral) were assessed in each cochlea. When more than 10 cells in each compartment were present in a single cochlea, the 10 most apical cells were used for synapse quantification.

Statistical analysis

All data are presented as mean ± SEM and the *n*-value represents the number of mice included in the study in which one cochlea from each mouse was used for each experiment. Statistical tests were performed using GraphPad Prism 6.02 and are described in the figure legends.

Data availability statement

The original contributions presented in this study are included in the article/supplementary material, further inquiries can be directed to the corresponding author.

Ethics statement

The animal study was reviewed and approved by Institutional Animal Care and Use Committee at Southern Illinois University School of Medicine.

Author contributions

MH performed the experiments and data analysis, as well as contributed to the experimental design under the supervision of BC. DH and SM performed the experiments and edited the manuscript. BC conceived the project idea and together with MH wrote and edited the manuscript. All authors contributed to the article and approved the submitted version.

Funding

This work was supported by a grant from the NIDCD (R01 DC014441 to BC). The Southern Illinois University School of Medicine Research Imaging Facility is supported by a grant from the Office of Naval Research (N00014-15-1-2866).

Acknowledgments

We thank Guillermo Oliver at St. Jude Children's Research Hospital for providing the *Prox1*^{CreERT2} mouse line and Ed Rubel at the University of Washington for providing the *Pou4f3*^{DTR} mouse line.

Conflict of interest

BC was a consultant for Turner Scientific, LLC and has sponsored research contracts with Decibel Therapeutics, Inc., and Otonomy, Inc.

The remaining authors declare that the research was conducted in the absence of any commercial or financial relationships that could be construed as a potential conflict of interest.

Publisher's note

References

Atkinson, P. J., Dong, Y., Gu, S., Liu, W., Najarro, E. H., Udagawa, T., et al. (2018). Sox2 haploinsufficiency primes regeneration and Wnt responsiveness in the mouse cochlea. *J. Clin. Invest.* 128, 1641–1656. doi: 10.1172/JCI97248

Becker, L., Schnee, M. E., Niwa, M., Sun, W., Maxeiner, S., Talaei, S., et al. (2018). The presynaptic ribbon maintains vesicle populations at the hair cell afferent fiber synapse. *eLife* 7:e30241. doi: 10.7554/eLife.30241

Bermingham, N. A., Hassan, B. A., Price, S. D., Vollrath, M. A., Ben-Arie, N., Eatock, R. A., et al. (1999). Math1: An essential gene for the generation of inner ear hair cells. *Science* 284, 1837–1841. doi: 10.1126/science.284.5421.1837

Bohne, B. A., Kenworthy, A., and Carr, C. D. (1982). Density of myelinated nerve fibers in the chinchilla cochlea. *J. Acoust. Soc. Am.* 72, 102–107. doi: 10.1121/1.387994

Bramhall, N. F., Shi, F., Arnold, K., Hochedlinger, K., and Edge, A. S. B. (2014). Lgr5-positive supporting cells generate new hair cells in the postnatal cochlea. *Stem Cell Rep.* 2, 311–322. doi: 10.1016/j.stemcr.2014.01.008

Chen, Y., Gu, Y., Li, Y., Li, G.-L., Chai, R., Li, W., et al. (2021). Generation of mature and functional hair cells by co-expression of Gfi1, Pou4f3, and Atoh1 in the postnatal mouse cochlea. *Cell Rep.* 35:109016. doi: 10.1016/j.celrep.2021.109016

Chessum, L., Matern, M. S., Kelly, M. C., Johnson, S. L., Ogawa, Y., Milon, B., et al. (2018). Helios is a key transcriptional regulator of outer hair cell maturation. *Nature* 563, 696–700. doi: 10.1038/s41586-018-0728-4

Cox, B. C., Chai, R., Lenoir, A., Liu, Z., Zhang, L., Nguyen, D.-H., et al. (2014). Spontaneous hair cell regeneration in the neonatal mouse cochlea *in vivo*. *Development* 141, 1599–1599. doi: 10.1242/dev.109421

Dallos, P. (2008). Cochlear amplification, outer hair cells and prestin. *Curr. Opin. Neurobiol.* 18, 370–376. doi: 10.1016/j.conb.2008.08.016

Doerflinger, N. H., Macklin, W. B., and Popko, B. (2003). Inducible site-specific recombination in myelinating cells. *Genesis* 35, 63–72. doi: 10.1002/gene.10154

Driver, E. C., Sillers, L., Coate, T. M., Rose, M. F., and Kelley, M. W. (2013). The Atoh1-lineage gives rise to hair cells and supporting cells within the mammalian cochlea. *Dev. Biol.* 376, 86–98. doi: 10.1016/j.ydbio.2013.01.005

Duckert, L. G., and Rubel, E. W. (1990). Ultrastructural observations on regenerating hair cells in the chick basilar papilla. *Hear. Res.* 48, 161–182. doi: 10.1016/0378-5955(90)90206-5

Elliott, K. L., Kersigo, J., Lee, J. H., Jahan, I., Pavlinkova, G., Fritzsch, B., et al. (2021). Developmental changes in peripherin-eGFP expression in spiral ganglion neurons. *Front. Cell. Neurosci.* 15:678113. doi: 10.3389/fncel.2021.678113

Fang, J., Zhang, W.-C., Yamashita, T., Gao, J., Zhu, M.-S., and Zuo, J. (2012). Outer hair cell-specific prestin-CreERT2 knockin mouse lines. *Genesis* 50, 124–131. doi: 10.1002/dvg.20810

Flores, E. N., Duggan, A., Madathany, T., Hogan, A. K., Márquez, F. G., Kumar, G., et al. (2015). A non-canonical pathway from cochlea to brain signals tissue-damaging noise. *Curr. Biol.* 25, 606–612. doi: 10.1016/j.cub.2015.01.009

García-Añoveros, J., Clancy, J. C., Foo, C. Z., García-Gómez, I., Zhou, Y., Homma, K., et al. (2022). Tbx2 is a master regulator of inner versus outer hair cell differentiation. *Nature* 605, 298–303. doi: 10.1038/s41586-022-04668-3

Gbd 2019 Hearing Loss Collaborators (2021). Hearing loss prevalence and years lived with disability, 1990-2019: Findings from the Global Burden of Disease Study 2019. *Lancet* 397, 996–1009. doi: 10.1016/S0140-6736(21)00516-X

Golub, J. S., Tong, L., Ngyuen, T. B., Hume, C. R., Palmiter, R. D., Rubel, E. W., et al. (2012). Hair cell replacement in adult mouse utricles after targeted ablation of hair cells with diphtheria toxin. *J. Neurosci.* 32, 15093–15105. doi: 10.1523/JNEUROSCI.1709-12.2012

Gómez-Casati, M. E., Murtie, J., Taylor, B., and Corfas, G. (2010). Cell-specific inducible gene recombination in postnatal inner ear supporting cells and glia. *J. Assoc. Res. Otolaryngol.* 11, 19–26. doi: 10.1007/s10162-009-0191-x

Hackney, C. M. (2005). The concentrations of calcium buffering proteins in mammalian cochlear hair cells. *J. Neurosci.* 25, 7867–7875. doi: 10.1523/JNEUROSCI.1196-05.2005

Hallworth, R., McCoy, M., and Polan-Curtain, J. (2000). Tubulin expression in the developing and adult gerbil organ of Corti. *Hear. Res.* 139, 31–41. doi: 10.1016/S0378-5955(99)00165-3

Hu, L., Lu, J., Chiang, H., Wu, H., Edge, A. S. B., and Shi, F. (2016). Diphtheria toxin-induced cell death triggers wnt-dependent hair cell regeneration in neonatal mice. *J. Neurosci.* 36, 9479–9489. doi: 10.1523/JNEUROSCI.2447-15.2016

Huang, L.-C., Barclay, M., Lee, K., Peter, S., Housley, G. D., Thorne, P. R., et al. (2012). Synaptic profiles during neurite extension, refinement and retraction in the developing cochlea. *Neural Dev.* 7:38. doi: 10.1186/1749-8104-7-38

Jahan, I., Pan, N., Elliott, K. L., and Fritzsch, B. (2015). The quest for restoring hearing: Understanding ear development more completely. *BioEssays* 37, 1016–1027. doi: 10.1002/bies.201500044

Jensen-Smith, H. C., Eley, J., Steyger, P. S., Ludueña, R. F., and Hallworth, R. (2003). Cell type-specific reduction of β tubulin isotypes synthesized in the developing gerbil organ of Corti. *J. Neurocytol.* 32, 185–197. doi: 10.1023/b:neur.0000005602.18713.02

Kent, L. N., and Leone, G. (2019). The broken cycle: E2F dysfunction in cancer. *Nat. Rev. Cancer* 19, 326–338. doi: 10.1038/s41568-019-0143-7

Kiang, N. Y. S., Rho, J. M., Northrop, C. C., Liberman, M. C., and Ryugo, D. K. (1982). Hair-cell innervation by spiral ganglion cells in adult cats. *Science* 217, 175–177. doi: 10.1126/science.7089553

Kolla, L., Kelly, M. C., Mann, Z. F., Anaya-Rocha, A., Ellis, K., Lemons, A., et al. (2020). Characterization of the development of the mouse cochlear epithelium at the single cell level. *Nat. Commun.* 11:2389. doi: 10.1038/s41467-020-16113-y

Lanford, P. J., Shailam, R., Norton, C. R., Ridley, T., and Kelley, M. W. (2000). Expression of Math1 and HES5 in the Cochleae of Wildtype and Jag2 Mutant Mice. *J. Assoc. Res. Otolaryngol.* 1, 161–171. doi: 10.1007/s101620010023

Lee, S., Song, J.-J., Beyer, L. A., Swiderski, D. L., Prieskorn, D. M., Acar, M., et al. (2020). Combinatorial Atoh1 and Gfi1 induction enhances hair cell regeneration in the adult cochlea. *Sci. Rep.* 10:21397. doi: 10.1038/s41598-020-78167-8

Liberman, M. C. (1980). Morphological differences among radial afferent fibers in the cat cochlea: An electron-microscopic study of serial sections. *Hear. Res.* 3, 45–63. doi: 10.1016/0378-5955(80)90007-6

Liberman, M. C. (1982). Single-neuron labeling in the cat auditory nerve. *Science* 216, 1239–1241. doi: 10.1126/science.7079757

Liberman, M. C., Gao, J., He, D. Z. Z., Wu, X., Jia, S., and Zuo, J. (2002). Prestin is required for electromotility of the outer hair cell and for the cochlear amplifier. *Nature* 419, 300–304.

Liu, C., Glowatzki, E., and Fuchs, P. A. (2015). Unmyelinated type II afferent neurons report cochlear damage. *Proc. Natl. Acad. Sci. U.S.A.* 112, 14723–14727. doi: 10.1073/pnas.1515228112

Liu, Z., Fang, J., Dearman, J., Zhang, L., and Zuo, J. (2014). *In vivo* generation of immature inner hair cells in neonatal mouse cochleae by ectopic atoh1 expression. *PLoS One* 9:e89377. doi: 10.1371/journal.pone.0089377

Liu, Z., Owen, T., Fang, J., Srinivasan, R. S., and Zuo, J. (2012). *In vivo* notch reactivation in differentiating cochlear hair cells induces Sox2 and Prox1 expression but does not disrupt hair cell maturation. *Dev. Dyn.* 241, 684–696. doi: 10.1002/dvdy.23754

Lorenzen, S. M., Duggan, A., Osipovich, A. B., Magnuson, M. A., and García-Añoveros, J. (2015). Insm1 promotes neurogenic proliferation in delaminated otic progenitors. *Mech. Dev.* 138, 233–245. doi: 10.1016/j.mod.2015.11.001

Maass, J. C., Gu, R., Basch, M. L., Waldhaus, J., Lopez, E. M., Xia, A., et al. (2015). Changes in the regulation of the Notch signaling pathway are temporally correlated with regenerative failure in the mouse cochlea. *Front. Cell. Neurosci.* 9:110. doi: 10.3389/fncel.2015.00110

Madisen, L., Zwingman, T. A., Sunkin, S. M., Oh, S. W., Zariwala, H. A., Gu, H., et al. (2010). A robust and high-throughput Cre reporting and characterization system for the whole mouse brain. *Nat. Neurosci.* 13, 133–140. doi: 10.1038/nn.2467

Martinez-Monedero, R., Liu, C., Weisz, C., Vyas, P., Fuchs, P. A., and Glowatzki, E. (2016). GluA2-containing AMPA receptors distinguish ribbon-associated from ribbonless afferent contacts on rat cochlear hair cells. *Eneuro* 3:ENEURO.0078-16.2016. doi: 10.1523/ENEURO.0078-16.2016

McGovern, M. M., Brancheck, J., Grant, A. C., Graves, K. A., and Cox, B. C. (2017). Quantitative analysis of supporting cell subtype labeling among CreER lines in the neonatal mouse cochlea. *J. Assoc. Res. Otolaryngol.* 18, 227–245. doi: 10.1007/s10162-016-0598-0

McGovern, M. M., Randle, M. R., Cuppini, C. L., Graves, K. A., and Cox, B. C. (2019). Multiple supporting cell subtypes are capable of spontaneous hair cell regeneration in the neonatal mouse cochlea. *Development* 146:dev171009. doi: 10.1242/dev.171009

Montgomery, S. C., and Cox, B. C. (2016). Whole Mount Dissection and Immunofluorescence of the Adult Mouse Cochlea. *J. Vis. Exp.* 107:53561. doi: 10.3791/53561

Morrison, A., Hodgetts, C., Gossler, A., Hrabé de Angelis, M., and Lewis, J. (1999). Expression of Delta1 and Serrate1 (Jagged1) in the mouse inner ear. *Mech. Dev.* 84, 169–172. doi: 10.1016/S0925-4773(99)00066-0

Oesterle, E. C., Campbell, S., Taylor, R. R., Forge, A., and Hume, C. R. (2008). Sox2 and jagged1 expression in normal and drug-damaged adult mouse inner ear. *J. Assoc. Res. Otolaryngol.* 9, 65–89. doi: 10.1007/s10162-007-0106-7

Prajapati-DiNubila, M., Benito-Gonzalez, A., Golden, E. J., Zhang, S., and Doetzlhofer, A. (2019). A counter gradient of Activin A and follistatin instructs the timing of hair cell differentiation in the murine cochlea. *eLife* 8:e47613. doi: 10.7554/eLife.47613

Qie, S., and Diehl, J. A. (2016). Cyclin D1, cancer progression, and opportunities in cancer treatment. *J. Mol. Med.* 94, 1313–1326. doi: 10.1007/s00109-016-1475-3

Raphael, Y., and Altschuler, R. A. (2003). Structure and innervation of the cochlea. *Brain Res. Bull.* 60, 397–422. doi: 10.1016/S0361-9230(03)00047-9

Reijntjes, D. O. J., and Pyott, S. J. (2016). The afferent signaling complex: Regulation of type I spiral ganglion neuron responses in the auditory periphery. *Hear. Res.* 336, 1–16. doi: 10.1016/j.heares.2016.03.011

Rose, M. F., Ren, J., Ahmad, K. A., Chao, H.-T., Klisch, T. J., Flora, A., et al. (2009). Math1 is essential for the development of hindbrain neurons critical for perinatal breathing. *Neuron* 64, 341–354. doi: 10.1016/j.neuron.2009.10.023

Rubel, E. W., Furrer, S. A., and Stone, J. S. (2013). A brief history of hair cell regeneration research and speculations on the future. *Hear. Res.* 297, 42–51. doi: 10.1016/j.heares.2012.12.014

Ryals, B. M., and Westbrook, E. W. (1994). TEM analysis of neural terminals on autoradiographically identified regenerated hair cells. *Hear. Res.* 72, 81–88. doi: 10.1016/0378-5955(94)90208-9

Schmitz, F. (2009). The making of synaptic Ribbons: How they are built and what they do. *Neuroscientist* 15, 611–624. doi: 10.1177/1073858409340253

Seal, R. P., Akil, O., Yi, E., Weber, C. M., Grant, L., Yoo, J., et al. (2008). Sensorineural deafness and seizures in mice lacking vesicular glutamate transporter 3. *Neuron* 57, 263–275. doi: 10.1016/j.neuron.2007.11.032

Sekerková, G., Zheng, L., Mugnaini, E., and Bartles, J. R. (2008). Espin actin-cytoskeletal proteins are in rat type I spiral ganglion neurons and include splice-isoforms with a functional nuclear localization signal. *J. Comp. Neurol.* 509, 661–676. doi: 10.1002/cne.21755

Shen, C.-N., Horb, M. E., Slack, J. M. W., and Tosh, D. (2003). Transdifferentiation of pancreas to liver. *Mech. Dev.* 120, 107–116. doi: 10.1016/S0925-4773(02)00337-4

Simmons, D. D., Tong, B., Schrader, A. D., and Hornak, A. J. (2010). Oncomodulin identifies different hair cell types in the mammalian inner ear. *J. Comp. Neurol.* 518, 3785–3802. doi: 10.1002/cne.22424

Spoendlin, H. (1969). Innervation patterns in the organ of Corti of the cat. *Acta Otolaryngol* 67, 239–254. doi: 10.3109/00016486909125448

Srinivasan, R. S., Dillard, M. E., Lagutin, O. V., Lin, F.-J., Tsai, S., Tsai, M.-J., et al. (2007). Lineage tracing demonstrates the venous origin of the mammalian lymphatic vasculature. *Genes Dev.* 21, 2422–2432. doi: 10.1101/gad.1588407

Stamataki, S., Francis, H. W., Lehar, M., May, B. J., and Ryugo, D. K. (2006). Synaptic alterations at inner hair cells precede spiral ganglion cell loss in aging C57BL/6J mice. *Hear. Res.* 221, 104–118. doi: 10.1016/j.heares.2006.07.014

Strenzke, N., Chakrabarti, R., Al-Moyed, H., Müller, A., Hoch, G., Pangrsic, T., et al. (2016). Hair cell synaptic dysfunction, auditory fatigue and thermal sensitivity in otoferlin Ile515Thr mutants. *EMBO J.* 35, 2519–2535. doi: 10.15252/embj.201694564

Sun, S., Li, S., Luo, Z., Ren, M., He, S., Wang, G., et al. (2021). Dual expression of Atoh1 and Ikzf2 promotes transformation of adult cochlear supporting cells into outer hair cells. *eLife* 10:e66547. doi: 10.7554/eLife.66547

Szarama, K. B., Gavara, N., Petralia, R. S., Kelley, M. W., and Chadwick, R. S. (2012). Cytoskeletal changes in actin and microtubules underlie the developing surface mechanical properties of sensory and supporting cells in the mouse cochlea. *Development* 139, 2187–2197. doi: 10.1242/dev.073734

Thiers, F. A., Nadol, J. B., and Liberman, M. C. (2008). Reciprocal synapses between outer hair cells and their afferent terminals: Evidence for a local neural network in the mammalian Cochlea. *J. Assoc. Res. Otolaryngol.* 9, 477–489. doi: 10.1007/s10162-008-0135-x

Tong, B., Hornak, A. J., Maison, S. F., Ohlemiller, K. K., Liberman, M. C., and Simmons, D. D. (2016). Oncomodulin, an EF-Hand Ca $^{2+}$ Buffer. Is critical for maintaining cochlear function in mice. *J. Neurosci.* 36, 1631–1635. doi: 10.1523/JNEUROSCI.3311-15.2016

Tong, L., Strong, M. K., Kaur, T., Juiz, J. M., Oesterle, E. C., Hume, C., et al. (2015). Selective Deletion of Cochlear Hair Cells Causes Rapid Age-Dependent Changes in Spiral Ganglion and Cochlear Nucleus Neurons. *J. Neurosci.* 35, 7878–7891. doi: 10.1523/JNEUROSCI.2179-14.2015

Uthaiah, R. C., and Hudspeth, A. J. (2010). Molecular anatomy of the hair Cell's ribbon synapse. *J. Neurosci.* 30, 12387–12399. doi: 10.1523/JNEUROSCI.1014-10.2010

Weisz, C., Glowatzki, E., and Fuchs, P. (2009). The postsynaptic function of type II cochlear afferents. *Nature* 461, 1126–1129. doi: 10.1038/nature08487

White, P. M., Doetzlhofer, A., Lee, Y. S., Groves, A. K., and Segil, N. (2006). Mammalian cochlear supporting cells can divide and *trans*-differentiate into hair cells. *Nature* 441, 984–987. doi: 10.1038/nature04849

Wiwatpanit, T., Lorenzen, S. M., Cantú, J. A., Foo, C. Z., Hogan, A. K., Márquez, F., et al. (2018). Trans-differentiation of outer hair cells into inner hair cells in the absence of INSM1. *Nature* 563, 691–695. doi: 10.1038/s41586-018-0570-8

Yanger, K., Zong, Y., Maggs, L. R., Shapira, S. N., Maddipati, R., Aiello, N. M., et al. (2013). Robust cellular reprogramming occurs spontaneously during liver regeneration. *Genes Dev.* 27, 719–724. doi: 10.1101/gad.207803.112

Yu, H. V., Tao, L., Llamas, J., Wang, X., Nguyen, J. D., Trecek, T., et al. (2021). POU4F3 pioneer activity enables ATOH1 to drive diverse mechanoreceptor differentiation through a feed-forward epigenetic mechanism. *Proc. Natl. Acad. Sci. U.S.A.* 118:e2105137118. doi: 10.1073/pnas.2105137118

Yu, Y., Weber, T., Yamashita, T., Liu, Z., Valentine, M. B., Cox, B. C., et al. (2010). *In vivo* proliferation of Postmitotic cochlear supporting cells by acute ablation of the retinoblastoma protein in neonatal mice. *J. Neurosci.* 30, 5927–5936. doi: 10.1523/JNEUROSCI.5989-09.2010

Advantages of publishing in Frontiers

Frontiers
Avenue du Tribunal-Fédéral 34
1005 Lausanne | Switzerland

Visit us: www.frontiersin.org
Contact us: frontiersin.org/about/contact